Additive manufacturing of affinity hydrogels for controlled biomacromolecule delivery in early osteoarthritis

George Loxley

Thesis submitted to the University of Nottingham

for the degree of Doctor of Philosophy

May 2023

Abstract

Osteoarthritis (OA) is a disease that is characterised by the progressive erosion of articular cartilage, synovial inflammation, subchondral bone remodelling, and osteophyte formation. Osteoarthritis is a leading cause of disability and affects over 500 million people world-wide. There is a lack of disease modifying anti-osteoarthritic drugs (DMAODs) which means the disease pathobiology cannot be stopped, resulting in existing treatments having transient efficacy and being focused mainly on symptom management. Pro-inflammatory signalling is a key driver of OA progression at the early stages of the disease and is the result of an imbalance in M1 and M2 macrophage signalling. Regenerative medicine approaches for OA have historically neglected to target inflammation and osteochondral tissue engineering still remains elusive. An early intervention therapy promoting M2 macrophage polarisation may balance immune signalling in the osteoarthritic joint and decelerate OA progression to retain cartilage tissue that would otherwise be irreversibly lost.

The controlled release of cytokines from an implantable biomaterial to promote M2 macrophage polarisation in-vivo is a possible strategy to achieve this goal. The aims of this thesis were to generate hydrogels that exhibited the controlled release of an M2 promoting cytokine for a clinically relevant period of time, that were a synthetic, 3D printable material with the capacity to be up-scale manufactured.

The work in this thesis was subdivided into three sections. Firstly, affinity hydrogels were cast using ultraviolet (UV) photocrosslinking and protein release was characterised for 70 days using the model protein lysozyme. A

linear release trend was observed in hydrogels containing 5% w/v 3-sulfopropyl acrylate (SPAK) and 10% w/v poly (ethylene glycol) diacrylate (PEGDA), with the bioactivity of released lysozyme being over 50% after 2 months of in-vitro release.

Hydrogel size and loading concentration were then scaled down for the in-vitro release of interleukin-4 (IL-4), in which 5% SPAK 10% PEGDA exhibited sustained release in the ng/mL concentration range for 73 days. To assess the bioactivity of released IL-4, conditioned media from IL-4 in-vitro release time points was used to promote M2 polarisation of THP-1 macrophages to model immunomodulation in osteoarthritis. It was determined that IL-4 released from as late as 53 days was capable of inducing an M2-like polarisation state as evidenced by secretion of CCL-18, CCL-22 and increased Mannose receptor surface expression. Media conditioned by 5% SPAK 10% PEGDA hydrogels did not decrease the viability of THP-1 macrophages in comparison to monolayer controls. In the presence of an M1 promoting stimulus, direct incubation of IL-4 releasing SPAK PEGDA hydrogels with THP-1 macrophages enhanced the secretion of TNF-α and IL-6.

Finally, 5% SPAK 10% PEGDA hydrogels were 3D printed using digital light projection additive manufacturing. The release rate of lysozyme from a porous hydrogel design was compared to that of a non-porous design in effort to show proof-of-concept for the fine tuning of protein release rate using 3D printed hydrogel architecture with different surface area to volume ratios.

In summary, SPAK PEGDA hydrogels have been shown to be a promising material for electrostatic controlled protein release. Future studies may further

utilise 3D printing for controlled release targeting immunomodulation in osteoarthritis and in other broader regenerative medicine applications such as implantation into large animal models of osteoarthritis.

Acknowledgements

The work in this thesis would not have been possible without the help and support of some key people, and I would like to take some time to formally acknowledge them.

I would like to thank my supervisors Dr. Jing Yang and Professor Amir Ghaemmaghami for their continued support throughout the project. The learning opportunities experienced in this project have been pivotal in my development as a research scientist.

I would like to thank all members in the division of Regenerative Medicine and Cellular Therapies, and also all members of the Immuno Bioengineering group. In particular, the familiar faces seen on a daily basis in the Biodiscovery Institute PhD student office C214, BDI-3 laboratory B211, BDI-1/2 Additive BioFabrication laboratory A64, School of Life Sciences laboratories B137 and B145, and Boots Science Building laboratory D36. The collaborative and interesting conversations with regular lab users both in and out of work helped to solve many problems encountered during these years and facilitated the progression of this project.

I would like to thank the EPSRC & MRC Centre for Doctor Training in Regenerative Medicine for the opportunity to study this PhD and for the funding provided on this project. A special thanks goes to Dr. Karen Coopman for providing funding during the difficult Covid-19 extension phase of this project. I will also thank the other members of CDT-11 who have been with me since the beginning of this journey all the way back in 2018 at Loughborough and all

other CDT students encountered at CDT events, mini project rotations, conferences, and during PhD studies at Nottingham.

I would like to thank Dr. Chris Parmenter, Haneen Packeer Ally, and Kristian Plender for carrying out Cryo-SEM on my hydrogel samples at the Nanoscale and Microscale Research Centre.

I would like to give a final, special thanks to my loving family. You have all been able to provide support in ways that nobody else can, and you were all there at times when I have needed you the most. Without you, this long and demanding PhD journey would not have been possible. Thank you.

Impact statement: Covid-19 and logistical delays

From the formal start of this project in October 2019, there have been multiple interruptions that negatively impacted its progress. The interruptions can be subdivided into three events. The first was a building move occurring at the very start of the project which took multiple months to complete and delayed the start to data collection. The second was the global Covid-19 pandemic in March 2020 which caused the shutdown of the entire university and meant that laboratory and campus access was lost for 6 months. The third was working with Covid-19 restrictions including reduced laboratory and office access, shortages of personal protective equipment and consumables, and logistical delays in training and inductions which all reduced the maximum productivity that was achievable in the academic year 2020-2021.

A 6 month extension was added to the project by the University Of Nottingham School Of Pharmacy, but the total amount of time lost is an estimated 9-12 months. The exact delays caused by these events are described in more detail within this section.

Building move to Biodiscovery institute 3

From mid October 2019 the Regenerative Medicine and Cellular Therapies division moved from the Centre for Biomolecular Sciences to the Biodiscovery institute 3 (BDI3). The moving process and time taken for laboratories to become operational was originally expected to be 4 weeks.

In actuality most laboratories were not operational until the middle of December 2019 or New Year 2020. Each lab had to “go live” for work to be started in it and each room required a separate induction as well as an induction for each

floor. Many rooms took a great deal of time longer to “go live” than expected. Many groups moved to the BDI3 simultaneously and all workers needed inductions, the room and floor inductions were oversubscribed and it was common to wait multiple weeks for popular room inductions (D and B floors).

All existing Risk assessments needed to be re-written using the new BDI template with amendments for new BDI waste disposal routes. Each new RA then had to be individually approved which also resulted in delays for specific experiments to be started.

In totality the building move to BDI3 and time taken for most main laboratories to be live with new workers fully inducted and RAs signed off took until Christmas of 2020. This process delayed laboratory work for approximately 8 weeks.

Covid-19 lockdown and university closure

On 17.3.20 the University of Nottingham shut down for the Covid-19 pandemic. During this period of time there was no laboratory or university access and the only work possible was to read or write from home.

There was a phased return to work at the BDI based on a system of priority in which high priority workers returned to work as soon as possible, medium priority workers returned in June 2020 and low priority workers returned in September 2020. PhD students who started in October 2019 were categorised as “low priority” and were only allowed to return at the latest possible stage.

The total time spent without university access was approximately 6 months from 17.3.20 to 14.9.20. This meant that at the start of 2nd year PhD less than 3 months of laboratory work had been possible.

Restricted lab access and reduced hours

Upon the return to work there was a number of Covid-19 safety measures in place including social distancing, reduced building occupancy, restricted working hours, restricted lab access and the closure of shared offices.

To adhere to the 2m social distancing safety measure, all university laboratories were divided into zones which were bookable by one lab user at a time. This meant that laboratories previously containing 10-15 workers when full had the maximum reduced to 4 or even 3 workers for much of the year (B211 BDI3, D36 BSB). After multiple months the maximum number of workers for each lab was eventually increased by 1 when distancing was reduced to 1m+ which slightly improved accessibility.

Working hours for BDI3 and Boots Science Building (BSB) were reduced to 0700-2200 and 0800-1600 respectively. BDI3 had a finite number of bookable out-of-hours slots but shortages of first aid staff meant that at times the number of out-of-hours access slots was suddenly reduced. BSB had no available out-of-hours, making the planning of experiments difficult with reduced occupancy also limiting access.

Training for equipment that would have previously taken place in groups had to be done one-to-one, meaning trainers had to conduct separate training sessions for each new student. To adhere to the reduced lab occupancy rules this required the booking of two laboratory zones simultaneously which made the potential times training could be done even less available. Some equipment trainers were described as “isolating” which meant there was lesser availability and remaining

trainers were oversubscribed. This resulted in students waiting much longer to receive training on new equipment and techniques.

In winter 2020, the bay containing the glove box was unable to be booked for 3 weeks because the booking system for D36 has been fully booked up in advance. The glove box is used to create hydrogels used for every experiment in this project, so this delay prevented the start of any new data collection for 3 weeks.

In May 2021, training for ELISA was delayed for 1 week because training couldn't be provided at the same time as another student due to Covid-19 lab occupancy restrictions.

Delays in procurement of reagents and assay kits

The purchasing of chemicals and assay kits required for experimental output was often delayed during the Covid-19 period.

Prior to the pandemic, orders from large scale suppliers such as Sigma Aldrich often arrived within the same week of ordering. After returning from lockdown, orders often took multiple weeks to arrive which significantly hinders the start of new experiments and the finishing of ongoing experiments.

Throughout all of 2020 and 2021 the University of Nottingham finance team were "under-staffed due to Covid-19", resulting in the approval of requisitions and the sending of orders to suppliers being delayed in a backlog.

Delays are also likely to have arisen from inefficiencies in the supply chain. Delivery drivers who have contracted Covid-19 having to isolate would mean there is an understaffing at choke points in the supply chain.

In February 2021, the procurement of PEGDA from Sigma Aldrich took over 3 weeks. This chemical is used to form hydrogels for all experiments in this project and the start of new experiments had to be delayed until its arrival. Prior to Covid-19, orders would often come within the same week of ordering.

In March 2021 the procurement of TGF-β1 ELISA assays took over 2 weeks which delayed the analysis of on-going controlled release experiments. Without analysing the data from this experiment it was not possible to refine the plan for upcoming experiments as this was during a period of process optimisation.

Consumable shortages

At multiple points since the pandemic, there has been shortages of consumables required for almost all experiments in the BDI and some of which were essential PPE for Covid-19. This included industrial methylated spirits, 1mL pipette tips, 200uL pipette tips, nitrile gloves, assay plates, centrifuge tubes, and Eppendorf tubes.

Other than supply chain issues, the likely cause of these shortages is that the supply of laboratory consumables was being redirected to high throughput Covid-19 testing laboratories which have been performing quantitative-PCR en masse throughout the year to diagnose Covid-19 at the University testing service, in which all the aforementioned one-time-use consumables are needed for PPE and for the PCR test itself.

Notable instances when consumable shortages delayed data acquisition were:

Booking the lab to do ELISA on a day when there was no 200uL tips in all of BDI3. The lab then had to be re-booked at the next possible slot which caused multiple days of delay

Booking the lab on days with severe IMS shortages in BDI3. This was used to clean each work station before and after use as a Covid-19 safety measure, work was considered as unsafe and students were told to reschedule their experiments which caused multiple days of delay. This happened multiple times.

Delays in joining Life sciences lab

As a Covid-19 safety measure, all new starters in School of Life sciences laboratory B137 had to order labcoats new from the supplier. The rationale being that the spare coats which would have previously been worn by other new starters had increased risk of Covid-19 transmission.

Supply chain issues in receiving the new labcoats meant that there was a 2 month wait for the delivery (11/6/21 – 26/8/21). This resulted in a 2 month delay in starting work in B137 when prior to Covid-19 measures, work would have been able to start immediately.

Contraction of Covid-19 and subsequent isolation

On Friday the 25th of February 2022 I tested positive for Covid-19 via the university testing service. Following direct advice from the University of Nottingham Covid-19 testing service, I isolated at home for a minimum of 5 days and until testing negative twice by lateral flow.

It took 7 days to test negative by lateral flow and for symptoms to disappear, resulting in 1 week of lost time in the lab.

Table of contents

List of figures

List of abbreviations

% w/v: Percentage weight by volume

^{o}C: Degrees Celsius

3D: Three-dimensional

ACI: Autologous chondrocyte implantation

ADAMTS: A Disintegrin And Metalloprotease with Thrombospondin Motifs (4 and 5)

AK: Adenylate Kinase

ANOVA: Analysis Of Variance

BMP: Bone Morphogenic Protein (2 and 7)

BSA: Bovine Serum Albumin

CAD: Computer Aided Design

CCL: C-C motif Chemokine Ligand (2, 18 and 22)

CHO: Chinese Hamster Ovary cell

CO_2: Carbon Dioxide

Cryo-SEM: Cryo-Scanning Electron Microscopy

Da: Dalton

DAMPs: Danger Associated Molecular Patterns

DAPI: 4′,6-diamidino-2-phenylindole

DLP: Digital Light Projection

DMAOD: Disease Modifying Anti-Osteoarthritic Drug

DMSO: Dimethyl sulfoxide

ECM: Extra-cellular Matrix

E-Coli: Escherichia coli

ELISA: Enzyme-Linked Immunosorbent Assay

FBGCs: Foreign Body Giant Cells

FBR: Foreign Body Response

FBS: Foetal Bovine Serum

FDA: Food and Drug Administration

FGF: Fibroblast Growth Factor (2 and 18)

FGFR3: Fibroblast Growth Factor Receptor 3

g: grams

GAGs: Glycosaminoglycans

Gel-MA: Gelatin methacrylate

GM-CSF: Granulocyte-macrophage colony-stimulating factor

HEK: Human embryonic kidney

HEPA: High efficiency particulate air

HRP: Horse radish peroxidase

I2959: Irgacure-2959 (2-Hydroxy-4'-(2-hydroxyethoxy)-2 methylpropiophenone)

IC: Immuno complex

IFN: Interferon (alpha and gamma)

IgG: Immunoglobulin G

IL: Interleukin (1β, 2, 4, 6, 10, and 13)

IL4RA: Interleukin 4 receptor alpha

Inos: Inducible nitric oxide synthase

JAK/STAT: Janus kinase/signal transducers and activators of transcription

kDa: Kilodalton

kPa: Kilopascal

Kv: Kilovolt

LAP: Lithium phenyl (2,4,6-trimethylbenzoyl) phosphinate

LOD: Limit of Detection

LOQ: Limit of Quantification

LPS: Lipopolysaccharide

MACI: Matrix-Assisted Autologous Chondrocyte Implantation

M-CSF: Macrophage Colony Stimulating Factor

Mg: Milligram

mg/Ml: Milligram per millilitre

micro-RNA: Micro-ribonucleic acid

mL: Millilitre

MMP: Matrix metalloprotease

MRI: Magnetic resonance imaging

MSC: Mesenchymal stromal cell

ng: Nanogram

ng/mL: Nanograms per millilitre

NHS : National Health Service

NSAID: Non-Steroidal Anti-Inflammatory Drugs

OA: Osteoarthritis

PBMCs: Peripheral Blood Mononuclear Cells

PBS: Phosphate Buffered Saline

PCL: Polycaprolactone

PDGF: Platelet Derived Growth Factor

PEG: Poly(Ethylene Glycol)

PEGDA: Poly(Ethylene Glycol) Diacrylate

PEGT/PBT: poly(ethylene glycol)-terephthalate/poly(butylene terephthalate)

PEO-PPO-PEO: polyethylene oxide – polypropylene oxide – polyethylene oxide

PF127: Pluronic-F127

PFA: Paraformaldehyde

pg/mL: Picogram per millilitre

PLGA: Poly Lactic-co-Glycolic Acid

PMA: Phorbol 12-myristate 13-acetate

PPAR-γ: Peroxisome proliferator- activated receptor gamma

Ppm: Parts per million

PRG4: Proteoglycan 4

PRP: Platelet Rich Plasma

PTFE: Polytetrafluoroethylene

R&D: Research and Development

RNA: Ribonucleic acid

RT: Room Temperature

SA:V: Surface area to Volume ratio

SD: Standard Deviation

SEM: Standard Error of the Mean

SPAK: 3-Sulfopropyl acrylate potassium salt

STAT: Signal transducer and activator of transcription (1 and 6)

TCP: Tri-calcium Phosphate

TGF-β1: Transforming Growth Factor Beta 1

Th: T-Helper

TLRs: Toll-like Receptors

TMB: Tetramethylbenzidine

TNFR1: Tumour Necrosis Factor Receptor (1 and 2)

TNF-α: Tumour Necrosis Factor Alpha

USA: United States of America

UV: Ultra-Violet

VEGF: Vascular-Endothelial Growth Factor

μg/mL: Micrograms per Millilitre

μL: Microlitre

Chapter 1 - Introduction

1.1 Osteoarthritis

Osteoarthritis (OA) is a debilitating, painful[1] and incurable disease[2] that is characterised by the progressive degradation of articular cartilage[3], synovial inflammation, subchondral bone remodelling, and osteophyte formation[4–7]. OA patients frequently feel stiffness and pain in affected joints and OA in the hip, knee or ankle causes pain during weight bearing which significantly reduces mobility[8]. OA is considered a leading cause of disability[9], affecting over 20% of people aged over 40[10], and close to 50% of people over 65[11], with an estimated 500 million cases worldwide[12].

Generally, the risk factors for developing OA are increasing age and obesity[13–16]. OA may also be induced by joint injury[17,18], and women are more likely to develop OA than men[19]. There is thought to be a genetic component to increased risk in OA development[20] but this has previously been observed more in hand OA in comparison to symptomatic knee OA[21,22]. There is a lack of disease modifying anti-osteoarthritic drugs (DMAODs)[23,24] which means the pathobiology of OA cannot be actively stopped[25], making OA treatment options more focused to pain and symptom management[26]. OA patients frequently rely on analgesics to relieve mechanically induced pain during movement and also to relieve neuropathic pain that can be felt even while sedentary[27,28]. The financial cost of treating OA puts a significant burden on healthcare, in 2010 it was estimated that hip and knee replacements cost over £850 million in the UK[29] and that the use of non-steroidal anti-inflammatory drugs (NSAIDs) cost close

to £50 million. OA also has indirect financial costs that affect the patient individually and have larger socio-economic ramifications[30]. Such costs occur from the days of work missed by OA sufferers due to disability and the cost of providing social care to OA patients[30–32].

The cost burden of OA is expected to increase with every passing year because we have an increasingly aged society which means age related diseases will continue to become more frequently seen[33–35], and the obesity epidemic means more people have a high risk of developing OA[35,36]. In Australia alone, predictive modelling expects the cost of hip and knee replacements to reach over 5 billion dollars by 2030[37].

Considering the prevalence, socio-economic cost, lack of DMAODs, and predictive modelling associated with OA, it is imperative that continued research and development is carried out in order to produce advanced osteoarthritis therapies to improve patient quality of life.

1.2 The role of Inflammation in the pathobiology of osteoarthritis

The exact events that initially trigger OA pathobiology are still not fully understood on a molecular level. Synovial inflammation is present at the early and late stages of the disease and is associated with increased risk of disease progression[38,39]. Synovitis is thought to occur before visible signs of cartilage loss are seen and persistent pro-inflammatory signalling from cells in the innate immune system actively drives the pathobiology of OA[40,41]. The macrophage is the most abundant immune cell in the synovium and has a pivotal role in

orchestrating immune signalling based on its polarisation state[42]. In a quiescent state macrophages are described as M0. M1 and M2 was historically used to describe conventional and alternative activation states of macrophages following exposure to T-helper 1 (Th1) or T-helper-2 (Th2) cytokines[43]. M1 and M2 are now used to describe the extreme ends of a spectrum of polarisation states that are exhibited in response to environmental stimuli (polarisation states discussed in more detail in section 1.7). Polarisation states that are M1-like and M2-like then promote pro-inflammatory and anti-inflammatory signalling respectively[44].

In 2018, Liu et al. reported that there was an imbalance in M1 and M2 macrophages in synovial fluid from OA patients compared to healthy controls. The imbalance favoured pro-inflammatory M1 signalling and correlated to the Kellgren-Lawrence grading score of OA severity[45]. Similarly, Gómez-Aristizábal reported increased CD16 positive macrophages in OA synovial fluid that correlated with pro-inflammatory C-C motif chemokine ligand 2 (CCL-2) and symptom severity of the affected joint[46]. In 2019, Wang et al. used computational modelling and publicly available transcriptomic data to estimate the cellular composition of synovial tissue in osteoarthritic joints. They found M2 macrophages to be the predominant type in the synovium accounting for 26.9% of total cells in OA and 21.9% in healthy synovium. M1 macrophages were reported as less than 1% of the cell population in healthy synovium and were raised to 1.2% in OA[47,48]. A schematic showing the affected tissues in the osteoarthritic joint is shown below (Figure 1.1).

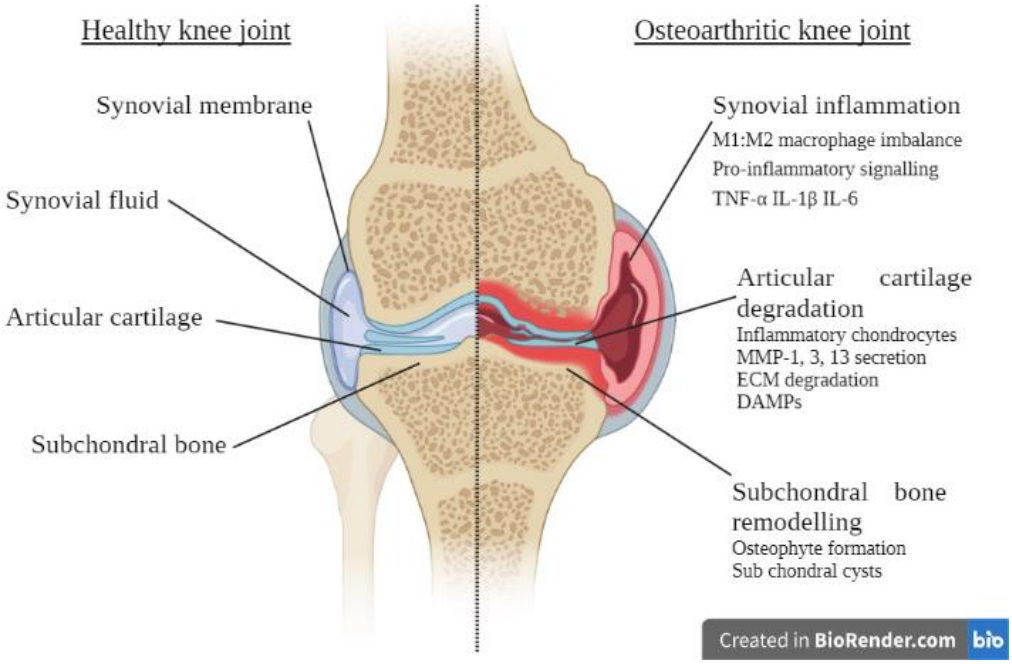

Figure 1.1 Schematic showing the affected tissues in the osteoarthritic knee joint. Osteoarthritis (OA) is characterised by synovial inflammation, the degradation of articular cartilage, subchondral bone remodelling, and osteophyte formation. In OA, dysregulated pro-inflammatory signalling orchestrated by M1 macrophages causes chondrocytes to adopt an inflammatory phenotype and secrete matrix metalloproteases (MMPs) that enzymatically degrade the cartilage extracellular matrix. Fragments of extracellular matrix (ECM) then act as danger associated molecular patterns (DAMPs) to induce more M1 macrophage recruitment and perpetuate the catabolic pro-inflammatory cycle. Image created at www.BioRender.com.

Pro-inflammatory signalling causes chondrocytes to adopt an inflammatory phenotype[49] following exposure to Tumour necrosis factor-alpha (TNF-α)[50], Interleukin-1 beta (IL-1β)[51] and Interleukin-6 (IL-6)[52]. Inflammatory chondrocytes then secrete matrix metalloproteases (MMPs) which enzymatically degrade the cartilage extracellular matrix (ECM)[53]. MMP

activity is usually balanced in tissue homeostasis but their dysregulation is linked to multiple pathobiologies[54]. In OA, the dysregulated activity of MMP-1, MMP-3, and MMP-13 are implicated in the destruction of cartilage ECM[55–58]. The destruction of type 2 collagen in articular cartilage extracellular matrix by MMPs is regarded as the point of irreversible damage in the pathobiology of OA[59]. Inflammatory chondrocytes also exhibit increased IL-1β secretion[60,61] which further propagates inflammatory signalling in an autocrine and paracrine manner, affecting other chondrocytes and immune cells to sustain inflammation[62]. TNF-α can directly induce apoptosis of chondrocytes by binding to Fas receptors and initiating caspase induced apoptosis[63,64]. Aggrecan, a major constituent of cartilage ECM[65,66] is degraded by the aggrecanases ADAMTS-4[67] and ADAMTS-5[68] and both are implicated in OA[69]. ADAMTS-4 expression is increased in chondrocytes following exposure to pro-inflammatory cytokines[70] and it has been observed as increased in the superficial cartilage zone[71] and in the serum of patients with early OA[72]. ADAMTS-5 was observed as raised in patients with intermediate and late OA and knockout of both previously prevented OA progression in model mice[73]. Fragments of degrading cartilage then act as danger associated molecular patterns (DAMPs)[74] which activates more macrophage polarisation towards M1 and induces further pro-inflammatory signalling in a self-propagating catabolic cycle[75].

Articular cartilage has a low natural regenerative capacity because it is avascular and requires nutrient diffusion from the synovial fluid and subchondral bone[76,77]. The pathobiology of OA is chronic which means cartilage is then irreversibly lost. Without cartilage, abnormal mechanical loading leads to

subchondral bone sclerosis and damage to bone tissue[78,79]. The normal cross-talk between subchondral bone and cartilage is disrupted and pro-inflammatory cells infiltrate the bone and stimulate osteoclast resorption of bone to produce lesions[80,81]. Osteophytes form in regions of high bone turnover in effort to stabilise the joint and are then a noticeable symptom of OA as ectopic bone outgrowths[82].

1.3 Limitations of traditional surgical treatments for osteoarthritis

Microfracture is a common surgical intervention for late-stage OA and has been considered a gold standard since its development in the 1980s[83,84]. During the procedure, multiple small incisions are made on the subchondral bone to allow bleeding from the bone marrow into the joint and over the cartilage defect[85]. The intention of microfracture is for mesenchymal stromal cells (MSCs) from bone marrow to enter the defect site and differentiate into chondrocytes to replace lost cartilage[86]. MSCs are multipotent cells capable of differentiating into chondrogenic, adipogenic, and osteogenic lineages[87,88]. However, following microfracture the new forming tissue is fibrocartilage which has low durability in comparison to the hyaline articular cartilage lost in OA[89]. Fibrocartilage repair tissue is mainly composed of collagen type 1 instead of the collagen type 2 mainly found in hyaline cartilage. It has poor integration into surrounding tissue and lacks the specialised mechanical properties of articular cartilage[90]. For this reason microfracture only provides beneficial effects for approximately 2-5 years[91], after which time OA symptoms return. Microfracture can be administered arthroscopically for reduced invasiveness[92]

and has a relatively long recovery period of 4-6 months before patients can resume exercise and sporting activities[93].

Total joint replacement is a procedure in which the diseased joint is surgically removed and replaced with a prosthetic that is traditionally made of titanium. Knee and hip replacements are frequently administered for treatment of late stage OA with 2.4 million procedures reported in the United States in 2021[94]. Previously, a review of multiple reports found that around 80% of patients have reported satisfaction with total knee replacements[95]. Patient dissatisfaction is likely to occur due to the limitations of total joint replacements. A major limitation is stress shielding, a phenomenon that occurs due to the difference in mechanical properties between the titanium implant and surrounding bone[96]. This results in reduced bone density and eventually bone resorption in tissue surrounding the implant which can lead to loosening and further complications including implant failure[97,98]. Decreasing the stiffness of the implant neck has been shown to reduce stress shielding but bone loss is still considered to be unavoidable[99]. The high frequency use of hip and knee joints can also lead to wear particles fragmenting from the prosthetic implant[100,101]. Titanium wear particles have been reported to induce pro-inflammatory signalling from M1 macrophages that contributes to further loss of bone around implants[102,103]. Pro-inflammatory signalling is already present in the pathobiology of OA and its enhancement from wear particles may increase the pain already felt by OA patients. Another limitation is that joint replacement implants have a finite lifespan of approximately 20-25 years[104,105] which means elderly patients who have OA for multiple decades may require multiple invasive surgeries.

Autologous chondrocyte implantation (ACI) is a surgical procedure in which the patient's articular cartilage tissue is harvested arthroscopically from a joint region that has a low weight bearing burden and that is unaffected by OA[106]. Chondrocytes are then isolated from the tissue and are expanded in-vitro for multiple weeks[107]. The cell suspension of chondrocytes is then injected into the defect site which is then sealed using a periosteal patch. In 2014, a 10 year follow up report on ACI observed positive clinical outcomes in the majority of patients which shows the therapeutic potential of ACI[108]. Negative outcomes were seen in 25% of patients which included failed engraftment of the implant and the need for subsequent operations. The main limitations of ACI are donor site morbidity[109], that chondrocytes dedifferentiate in-vitro and lose their chondrogenic potential which means only a relatively small amount of cells can be used for ACI[110], the need for multiple operations, and the long patient recovery time of up to 1 year[111]. Because of this, ACI is recommended for younger patients[112], patients with a single cartilage defect, and for relatively small cartilage lesions[113].

Matrix-assisted autologous chondrocyte implantation (MACI) is an adaptation of ACI in which patient derived chondrocytes are seeded onto a 3D scaffold in-vitro and the cell laden scaffold is implanted into the defect site[114]. Commonly used scaffold materials are hyaluronic acid and collagen type 2 as they are both present in cartilage ECM[115,116]. MACI has the advantages of having fewer surgical complications to traditional ACI because the scaffold is fixed in place with fibrin glue which is a quicker surgical process than the manual suturing of the periosteal patch required in traditional ACI[117]. The culture of chondrocytes in 3D is also reported to reduce their capacity to dedifferentiate and lose

chondrogenic potential following extended culture in-vitro[118]. Clinical trials comparing MACI with traditional ACI have found both techniques to produce similar results at 2 years and at 8-12 years follow-up[119–121]. The lack of improvement by MACI has been attributed to the immaturity of engineered cartilage tissue due to the short time chondrocytes are cultured on the scaffolds. Efforts have been made to mature seeded chondrocytes in-vitro with extended time periods of culture and the use of bioreactors to stimulate the cell laden scaffolds mechanically[122] or by culturing under hypoxia[123]. MACI has the same drawbacks as ACI and such ex-vivo methods would add more time to what is already a lengthy product generation time.

Intra-articular injection of corticosteroids is routinely performed to alleviate pain in osteoarthritic joints[124,125]. The process reduces inflammation and ameliorates OA symptoms for approximately 2 weeks[126] but does not prevent further progression of the disease. High frequency and high dose corticosteroid injection is associated with corticosteroid induced osteonecrosis which exacerbates OA, meaning the dosing and frequency must be carefully considered[127]. For these reasons, the National Health Service (NHS) in Britain recommends no more than 3 cortisone injections per year in the same joint.

1.4 Osteoarthritis treatments in clinical trials

Platelet rich plasma (PRP) is a relatively new treatment option for OA and has had considerable interest towards it in the last decade[128]. PRP is derived from whole blood by centrifugation and contains high concentrations of growth factors and platelets. Activated platelets secrete transforming growth factor beta-1 (TGF-β1), platelet derived growth factor (PDGF), and vascular-

endothelial growth factor (VEGF) that exert anabolic and angiogenic signalling respectively which could promote repair in damaged articular cartilage[129–131]. The literature surrounding PRP treatment is controversial[132], with some clinical trials showing positive results[133] and others showing no significant improvement over existing OA treatments or even compared to saline placebo[134]. There have been concerns into bias in some PRP trials pertaining to blinding, which are thought to have favoured PRP[135]. Currently, PRP is available to buy off-label in the USA but is not recommended for use in OA by international OA treatment guidelines. Such inconsistencies in PRP reports may be due to there being no standardised protocol for its preparation, meaning the content of PRP may vary from study to study.

Anti-TNF antibodies have been developed which bind to free TNF-α and prevent its binding to the receptors Tumour necrosis factor receptor 1 and 2 (TNFR1 and TNFR2) in order to reduce the pro-inflammatory signalling cascade[136]. Anti-TNFs have been used clinically for over 10 years for treatment of inflammatory conditions and have shown success in treating rheumatoid arthritis[137], but clinical trials have not shown the same effectiveness in treating OA[138]. In 2018, double-blind clinical trials using etanercept and adalimumab for treatment of hand OA found no improvement in pain alleviation or improvement of other OA related symptoms[139,140].

Sprifermin is a recombinant fibroblast growth factor-18 (FGF-18) drug that is in clinical trials as a possible DMAOD. FGF-18 binds with high affinity to the FGF receptor 3[141] (FGFR3) and is reported to induce chondroprotective effects in surgically induced OA model rats, as evidenced by a reduction in MMP-13 expression and an increase in collagen II expression in response to intra-

articular FGF-18 injection twice per week for 8 weeks[142]. In 2021, a clinical trial using sprifermin had mixed results. Patient groups were given 4 different dosing regimens and were monitored for a total of 5 years. The majority of patients had no difference in pain scoring compared to placebo, but a patient subgroup labelled "At risk of progression" did see a significant improvement after 5 years but these represented less than 30% of participants[143]. Overall, sprifermin shows potential as an anti-osteoarthritic drug but more consideration into the frequency of dosing should be implemented in future studies.

1.5 The need for early osteoarthritis detection

A major challenge in treating OA is that patients are only diagnosed at a relatively late stage of the disease. Patients may be suspected of having OA when they are more than 40 years of age and experience joint tenderness, reduced mobility, stiffness and pain during weight bearing[144,145]. OA is diagnosed by physical examination and by viewing X-rays for visible signs of joint space narrowing, osteophyte formation, subchondral bone remodelling, and subchondral cysts[146]. Symptoms are then considered in the 4 point Kellgren-Lawrence grading system according to disease severity[147].

These physical symptoms are only present when irreversible cartilage loss has occurred and early joint damage is not visible on X-rays[148]. It is therefore a goal of the field to generate detection methods for early osteoarthritis so that early intervention therapies may be utilized to modify the disease and retain articular cartilage tissue that would otherwise be irreversibly lost[149].

Attempts have been made to develop machine learning technologies to detect risk of OA at presymptomatic stages by viewing large volumes of

presymptomatic images of joints and then identifying image signatures between images from people who later went on to develop OA[150,151]. In the future, such technologies could be paired with increased monitoring of people identified as high risk and testing for biomarkers associated with inflammation. Previously, it has been suggested that biomarkers for OA may be found in serum, urine and the synovial fluid[152]. Ideally, samples that can be collected with minimal invasiveness would be used such as urine, but it is known in OA that inflammation is localised to the joint so it is likely that synovial fluid would give the most accurate result.

Biomarkers associated with inflammation could include pro-inflammatory proteins such as TNF-α, IL-1β, IL-6[153,154], and proteins thought to contribute directly to cartilage degradation such as MMP-13 and ADAMTS4[72,155]. Other biomarkers suggested in the literature are micro-RNAs which are small non-coding RNAs that regulate gene expression by inhibiting translation. Altered expression of a micro-RNAs has been associated with multiple diseases including OA[156,157], and a number of micro-RNAs have been identified as potential biomarkers for early OA identification[158]. Recently, the C terminal crosslinked telopeptide of type 2 collagen (CTX-II) has been used as a urinary biomarker for early OA in which urinary CTX-II correlated with radiographic grading of OV severity[159,160]. CTX-II detection in combination with increased patient monitoring for early OA development may be pivotal for timing a possible early OA intervention therapy.

Early intervention therapies would also need minimal invasiveness such as injection into the affected joint. Evidence to suggest early intervention could improve the prognosis of OA is that the “at risk of progression” group in the

sprifermin clinical trial responded best to the treatment[143], indicating that progression may be delayed if treatments are timed correctly.

1.6 Challenges faced in tissue engineering of articular cartilage and osteochondral Tissue engineering

Tissue engineering

The field of tissue engineering aims to regenerate tissue that is lost due to damage or disease, and utilises scaffolds to provide a site for cells to adhere to in new forming tissue and also provides mechanical support to the defect site[161]. Tissue engineering scaffolds may be manufactured using three-dimensional (3D) printing technologies which gives more control over material geometry in comparison to conventional casting and moulding methods. In particular, extrusion 3D printing has been used frequently to generate scaffolds with microscale pores. In this technique the material is extruded through a needle using temperature or pressure and the print head moves in the X-Y plane according to computer aided design (CAD) to produce a scaffold layer[162]. After each layer is printed the print head raises in the Z plane and the subsequent layer is extruded on top of the previous layer in an additive fashion to form multi-layered free standing materials. Generally, publications often print interconnected lattice scaffolds to facilitate the invasion of cells into the scaffold core [163] and control over the diameter of lattice pores has been explored as a method to induce cell fate[164,165]. 3D printing has also been used to generate patient specific implants with anatomically relevant geometries to match defect sites[166]. (3D printing for controlled release is reviewed in section 1.10)

The engineering of articular cartilage and osteochondral tissue has been a goal of the field for decades but significant advances have been slow due to the challenges faced in osteochondral tissue engineering which arise due to the complexity of articular cartilage and the environmental factors in the osteoarthritic joint[167–169].

The structure of articular cartilage

Articular cartilage is highly specialized tissue that is avascular, capable of heavy weight bearing and is resistant to wear and tear from high frequency use. Articular cartilage contains mature chondrocytes and its ECM is primarily made up of collagen II and aggrecan[170]. The tissue environment is hydrophilic and contains up to 80% water which aids its shock absorbing ability. Articular cartilage has complex hierarchical architecture that is split into three main layers, each with distinct mechanical properties, cell density, cell orientation, collagen fibre diameter, and ECM density[171,172].

The superficial layer contains a high density of chondrocytes that are elongated in morphology, horizontally orientated, and have a low density of ECM[173]. The superficial layer faces into the joint space and is highly resistant to sheer stress[174]. The intermediate layer contains a medium density of chondrocytes with a round morphology and both ECM and cells are randomly organised[175]. The deep layer contains chondrocytes that have a round morphology and are organised in a columnar orientation[176]. This layer has a low density of chondrocytes and the highest ECM density which enables it to exhibit the greatest resistance to compressive force[173]. Beneath this is the calcified layer which contains a sparse amount of hypertrophic chondrocytes and

hydroxyapatite crystals[177]. Calcified cartilage is separated from the deep layer by a basophilic tide mark and it acts as an intermediate between articular cartilage and the subchondral bone beneath[178]. During cartilage compression, chondrocytes and their surrounding pericellular matrix receive depth dependent mechanical stimuli which results in varying chondrocyte deformation and metabolism in each articular cartilage zone[179,180]. The zone specific responses to mechanostimulation are essential for the homeostasis of healthy cartilage[181,182] and demonstrate the requirement for specific control over zonal architecture in osteochondral tissue engineering attempts.

A schematic showing the multi-layered hierarchical structure of osteochondral tissue is included for convenience (Figure 1.2)

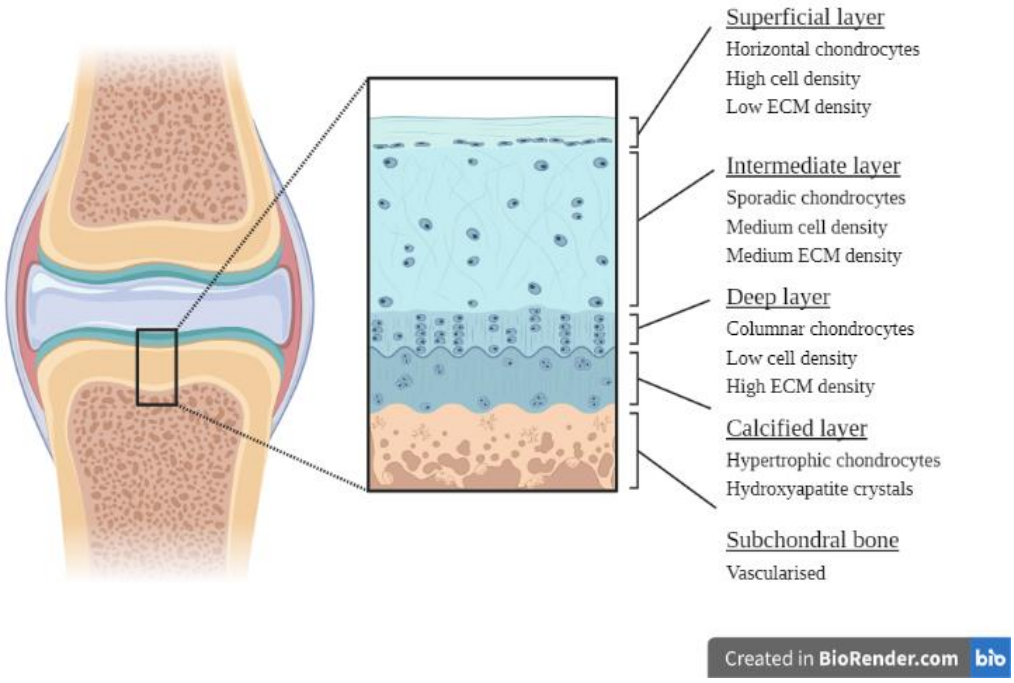

Figure 1.2: The hierarchical structure of the osteochondral unit. Articular cartilage is composed of superficial, intermediate, and deep layers. Each layer has unique chondrocyte density, chondrocyte orientation, extracellular matrix density, and compressive modulus that are essential for biomechanical function.

Calcified cartilage is deep to articular cartilage and contains hypertrophic chondrocytes and hydroxyapatite crystals. Beneath this is the subchondral bone which consists of cortical and trabecular bone. Image created at www.BioRender.com.

Osteochondral tissue engineering

When considering the complexity of osteochondral tissue, a major challenge in tissue engineering is the fabrication of scaffolds that can give rise to neotissue that recapitulates all of the aforementioned layers of articular cartilage and subchondral bone underneath. To be considered tissue engineering the new forming tissue must be functionality matched to naturally occurring osteochondral tissue and should be indistinguishable from the tissue formed during development.

Notable publications focusing on articular cartilage and osteochondral regenerative medicine are reviewed below:

A major challenge in auricular cartilage tissue engineering has been the inability to expand mature chondrocytes in-vitro due to their dedifferentiation and loss of chondrogenic potential after multiple population doublings. A multipotent, chondroprogenitor cell population has previously been identified in the superficial zone of bovine articular cartilage[183]. Chondroprogenitors are isolated by differential binding to fibronectin due to their high expression of integrin alpha 5. In 2009, long-term culture was compared between chondroprogenitors and freshly isolated chondrocytes, with chondroprogenitors exhibiting significantly increased telomerase activity and a reduced telomere erosion rate up to 22 population doublings which indicates they are less prone to senescence

in-vitro[184]. After 30 population doublings, high density pellets of chondroprogenitors were cultured in chondrogenic media. The resulting pellets shows positive staining for aggrecan at the periphery and notch-1 in the core which showed evidence of chondrogenic differentiation[185] (Figure 1.3).

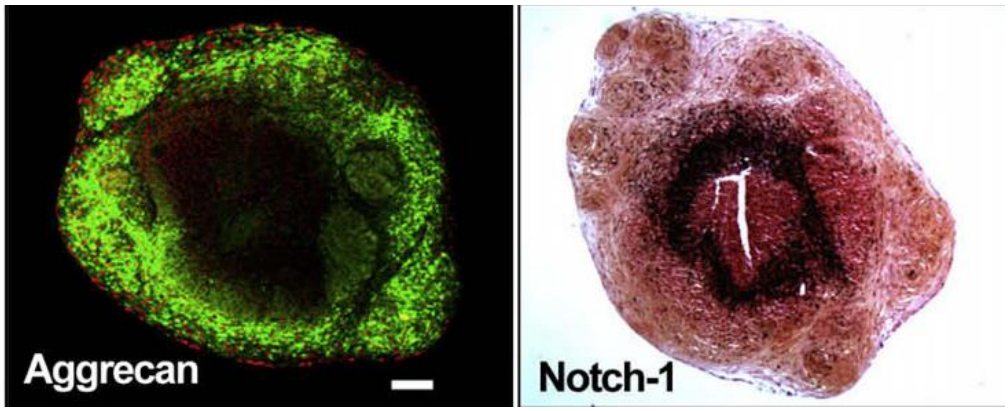

Figure 1.3: Chondroprogenitors grown in chondrogenic culture medium for 21 days. Aggrecan staining (left) indicates chondrogenic differentiation at the periphery of the cell pellet and Notch-1 staining (right) indicates undifferentiated chondroprogenitors in the core of the pellet. Scale bar = 100μm. Figure adapted with permission from the Osteoarthritis and Cartilage journal[184].

In 2017, the chondrogenic differentiation was compared between equine chondroprogenitors, bone marrow derived MSCs, and passage 1 chondrocytes when cultured in gelatin methacrylate (Gel-MA) hydrogels[186]. Following 8 weeks culture, the compressive modulus of cell laden hydrogels had increased to 186.6kPa for MSCs, 125.5kPa for chondrocytes and 101.4kPa for chondroprogenitors in comparison to the 18-23kPa cell free Gel-MA hydrogel. Previously the compressive modulus of human articular cartilage was reported as 1.16MPa in the superficial zone and 7.75MPa in the deep zone which is significantly higher than the cell laden hydrogels[187]. This low modulus is likely

due to the immaturity of chondrocytes in culture but the increase in modulus after 8 weeks compared to the Gel-MA control is a positive sign of chondrocyte viability and differentiation within 3D cultures. Greatly increased transcription of the superficial zone marker proteoglycan 4 (PRG4)[188] was observed in chondroprogenitor containing hydrogels and slightly increased transcription of collagen type X was observed in MSC containing hydrogels which is a marker of hypertrophic chondrocytes in the calcified zone[189]. This result suggested that the original source of each multipotent cell type may have a priming effect on its differentiation capacity. Chondroprogenitor laden Gel-MA was 3D printed using extrusion as proof of concept to show its potential for generating multi-layered, multi-material constructs in the future for articular cartilage regeneration. The use of chondroprogenitor cells is likely to improve procedures such as ACI and MACI in the future where currently only a finite amount of chondrocytes can be autologously harvested and their expansion potential is severely limited. The future generation of articular cartilage tissue engineering scaffolds may utilise chondroprogenitor cells with multi-layered materials with material cues in each layer tailored to promote neo-tissue with defined superficial, intermediate and deep zones.

Osteochondral tissue engineering attempts aim to generate multi material scaffolds with separate cartilage and bone promoting regions in order to heal full thickness osteochondral defects.

In 2013, Da et al. produced an osteochondral plug scaffold containing decellularized bovine cartilage with a bone phase of poly(Lactic-co-Glycolic) acid with tricalcium phosphate (PLGA/TCP) that was surrounded by collagen I that was produced by core-shell extrusion printing[190]. Implantation into a

surgically excised osteochondral defect in the rabbit knee showed generally promising regeneration as evidenced by histological staining after 3 and 6 months implantation. New forming tissue looked uniform in structure and had positive staining for glycosaminoglycans by safranin-O and light staining for collagen type 2 (Figure 1.4).

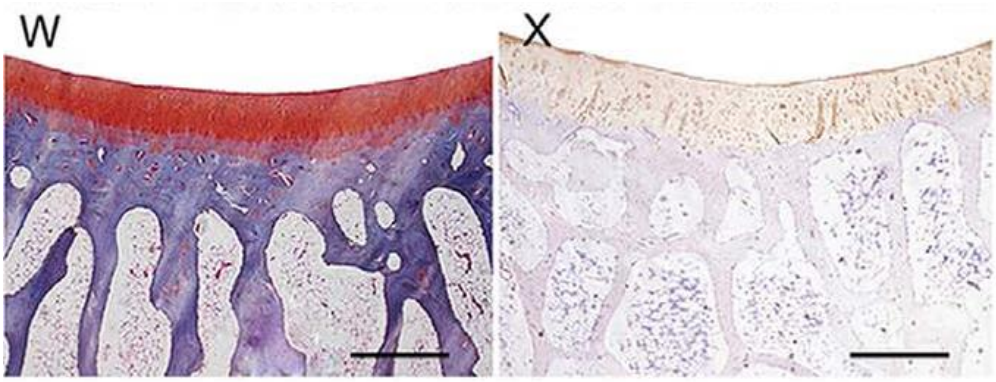

Figure 1.4: Immunohistostaining of neotissue following the 6 month implantation of a biphasic osteochondral plug into a surgically induced rabbit osteochondral defect model. The biphasic scaffold was composed of decellularized bovine articular cartilage chondrogenic region and a core-shell poly(Lactic-co-Glycolic) acid with tricalcium phosphate (PLGA/TCP) – collagen type 1 osteogenic region. W) Safranin O staining of glycosaminoglycans. X) Collagen type 2 staining. Scale bar 1mm. Figure adapted in accordance with the PLOS ONE journal policy[190].

The authors remarked on how including a compact layer of PLGA/TCP to separate the bone and cartilage scaffold regions significantly improved regeneration by mimicking the calcified layer of cartilage. This improvement was attributed to providing independent environments for bone and cartilage to form in and yielded significantly higher glycosaminoglycan and collagen type 2 content in neocartilage compared to a control where the separating layer was

not included. A major limitation of this approach is that the rabbit defect model does not actually suffer from osteoarthritis, meaning that regeneration took place in absence of the pro-inflammatory signalling and other hostile environmental factors present in OA which are almost certain to negatively impact the success of the implant.

In 2016, Shim et al. produced a biphasic scaffold consisting of a 3D printed Polycaprolactone (PCL) lattice with chondrogenic and osteogenic hydrogels printed into the macropores of the lattice to form cartilage and bone phases[191]. The osteogenic phase contained collagen type I laden with MSCs and Bone Morphogenic Protein-2 (BMP-2), and the chondrogenic phase contained hyaluronic acid laden with MSCs and TGF-β1. Similarly to Da et al., implantation into a surgically excised rabbit defect model showed some signs of articular cartilage regeneration after 8 weeks as evidenced by histology staining for Collagen type 2 and Collagen type X (Figure 1.5). Neocartilage showed visibly low staining for GAGs compared to native cartilage and there was a visible lack of integration into native tissue. The in-vivo model is still too simplistic to accurately represent regeneration under hostile conditions in OA.

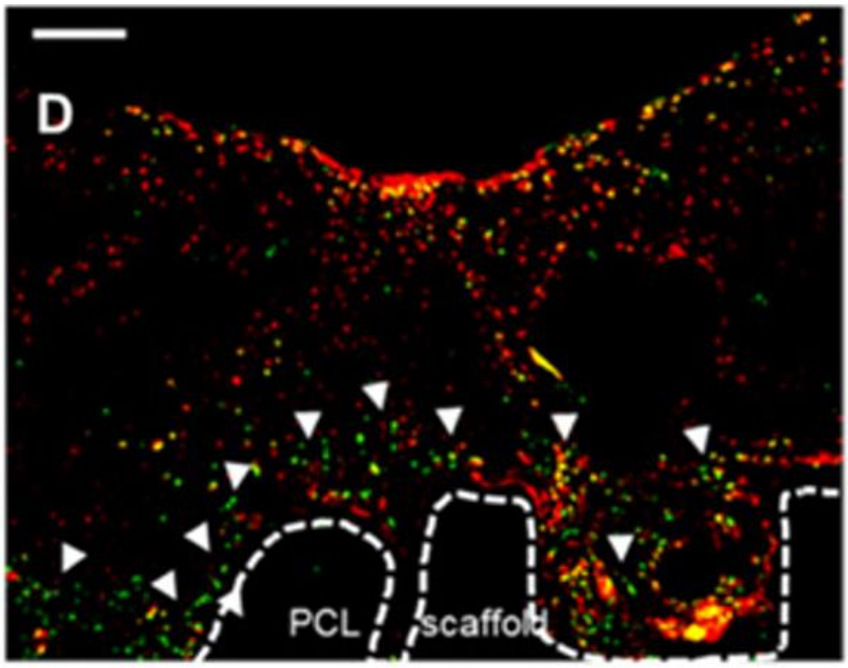

Figure 1.5: Immunohistochemistry staining for Collagen type 2 (red) and collagen type X (green) in neotissue following 8 week implantation of a mesenchymal stromal cell laden biphasic osteochondral scaffold into a surgically induced rabbit osteochondral defect model. The chondrogenic region contained hyaluronic acid, TGF-β1, and mesenchymal stromal cells. The osteogenic region contained type 1 atelocollagen, mesenchymal stromal cells, and BMP-2. The hydrogels were mechanically supported by a 3D printed polycaprolactone lattice. Figure adapted with permission from the Biofabrication journal[191].

In 2018, Mekhileri et al. used a custom bio-assembly system to automatically inject chondrocyte aggregates and Gel-MA hydrogels into the macropores in each layer of a 3D printed lattice scaffold[192]. At the time it was remarked that this mechanism could be used to produce 3D osteochondral tissue constructs scaling up to the size of a joint resurfacing prosthetic. In 2022, the same research group used bio-assembly to fabricate a biphasic scaffold with Gel-MA

microspheres placed within the macropores in a poly(ethylene glycol)-terephthalate/poly(butylene terephthalate) (PEGT/PBT) lattice[193]. The chondrogenic region contained MSCs encapsulated within Heparin sulfate-Gel-MA microspheres and an osteogenic region contained strontium nanoparticles encapsulated within Gel-MA microspheres. Following 35 days of culture, increased transcription of Collagen type 2 was seen in the chondrogenic region and increased collagen type 1 transcription was seen in the osteogenic region which shows promising potential for the method in-vitro, but in-vivo studies relevant to OA need to be carried out to continue this line of research.

In 2021, Liu at al. produced a multiphasic scaffold with a 3D printed lattice of PCL containing tricalcium phosphate as the bone region, a cartilage region of 3D printed methacrylated hyaluronic acid laden with bone marrow derived MSCs intercalated with 3D printed PCL containing a chondrogenic small molecule drug called kartogenin[194]. The scaffold contained a third immunomodulatory region of methacrylated hyaluronic acid loaded with the NSAID diclofenac. 7 day in-vitro culture of the kartogenin releasing layer with the MSC containing layer showed evidence of chondrogenic differentiation by increased transcription of TGF-β1, Collagen type 2, Sox9, and aggrecan and decreased transcription of MMP-13 compared to untreated monolayer control. Following TNF-α stimulation, MSCs secreted significantly less IL-1β in the presence of the diclofenac containing layer which suggests it may be exert anti-inflammatory signalling in-vivo. After 12 week implantation into a surgically excised osteochondral defect with subsequent joint destabilisation in rats, a reduction in cartilage degradation was observed in groups that used the scaffold, MSCs, and kartogenin but the inclusion of diclofenac did not further improve

the outcome. Increased leg function was seen in groups containing MSCs, kartogenin, or diclofenac in comparison to empty scaffold and untreated controls.

In 2022, Steel et al. developed a polycaprolactone osteochondral scaffold with microstructured zonal architecture in attempt to mimic articular cartilage[195]. The superficial region consisted of horizontally oriented electrospun fibres, porogen leeching was used to generate micropores in the intermediate zone and directional freezing was used to generate vertical grooves to model the deep zone. Thermal extrusion was used to print a PCL lattice as the subchondral bone region which was then thermally fused to the articular cartilage scaffold. The resulting composite scaffold exhibited anisotropic mechanical stiffness in which the deep zone was more than 50 fold stiffer than the intermediate zone. The scaffold exhibited strain partitioning between intermediate and deep layers which models the mechanics of cartilage compression better than a homogenous scaffold. In-vitro culture of bovine chondrocytes on the scaffolds in chondrogenic media saw signs of glycosaminoglycan and collagen production by alcain blue and picrosirius staining respectively. 6 month implantation into a surgically excised osteochondral defect in porcine models induced fibrocartilage formation in both the chondrocyte seeded scaffold and a cell-free control. There was no integration of fibrocartilage tissue into native articular cartilage tissue but some evidence of osseointegration at the bone region (Figure 1.6).

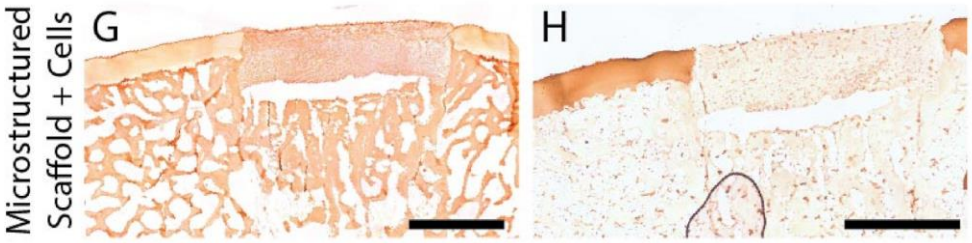

Figure 1.6: Immunohistostaining of collagen type 1 (left) and collagen type 2 (right) in neotissue following 6 month implantation of a multilayered microsturctured polycaprolactone scaffold into a porcine osteochondral defect model. Figure adapted in accordance with the policy of the Biomaterials journal[195].

It was concluded that the slow biodegradation rate of polycaprolactone meant there was inadequate space for matrix deposition and that a longer term study may yield improved results. This study did not consider the immune response to their biomaterial and while polycaprolactone is compatible with fabrication technologies such as extrusion printing, it is likely more complex material approaches with similar mechanical and chemical properties to articular cartilage will be required for improved in-vivo results in the future.

<u>The challenges still faced in the field of osteochondral tissue engineering</u>

Overall, the main challenges faced in osteochondral tissue engineering are:

The difficulty in producing cartilage tissue with zonal architecture resembling the layers of articular cartilage, with the majority of materials having a single "cartilage region" that is uniform in design. Producing scaffolds with 3D designs more closely matching the regions of articular cartilage may generate tissue with chondrocyte densities, chondrocyte orientations, and matrix

deposition more similar to naturally occurring hyaline cartilage and give greater efficacy in-vivo.

The lack of relevant animal models to accurately represent OA pathobiology in humans. Many studies simply excise osteochondral tissue and implant a scaffold into the site which mean any regeneration that occurs is an environment that is much less hostile than in an osteoarthritic joint. Surgical destabilisation of the joint to trigger osteochondral degradation is a much improved model but may be more useful in studying post traumatic osteoarthritis in comparison to the age related spontaneous OA that the majority of patients suffer from. Previous studies comparing surgically induced OA with spontaneous OA in mice have reported differences in the subsequent molecular pathobiology[196] and surgically induced OA occurs rapidly which may make studying the early disease more difficult[197]. Many osteochondral tissue engineering studies also use small model organisms such as mice and rats which are less anatomically similar to humans in comparison to larger models[198].

The lack of integration of new forming cartilage tissue into host tissue in-vivo. This is likely due to fibrocartilage formation and most attempts receiving an unfavourable immune response to scaffold implantation. Previous reports of bone tissue engineering have shown examples of osseointegration of new forming tissue into host bone, such as in the implantation of a 3D printed hydroxyapatite and polycaprolactone lattice scaffold into the skull of a rhesus monkey[199].

1.7 Approaches to modulate the OA immune environment

When considering the cellular and cell-free treatments for osteoarthritis that are approved by regulatory bodies[200], and the literature on osteochondral tissue engineering, the main focus has been repairing the osteochondral defect. Targeting the local immune environment in osteoarthritic joints has been less popular historically, but has garnered more attention in recent years. Given the major role of immune driven pro-inflammatory signalling in OA pathobiology (section 1.2), the absence of immunomodulation is likely a key reason as to why a lot of the data collected on osteochondral tissue engineering under favourable conditions has not translated into clinical products for OA. Approaches which primarily aim to modulate the immune environment and modify the pathobiology of OA will be critical in the generation of future therapies that have significantly improved clinical outcomes to those that are currently available.

The inflammatory chondrocytes responsible for MMP secretion in OA pathobiology have previously been a target for immunomodulatory drug delivery. Avidin functionalised nano carriers for small molecule drugs have been previously developed with the goal of diffusing through cartilage tissue to target inflammatory chondrocytes[201]. The carriers have been loaded with a biotinylated dexamethasone PEG conjugate that exhibited increased retention in bovine cartilage explant tissue and reduced cytokine induced GAG loss. The study only observed dexamethasone release for 13 days which limits its translatability as a clinically relevant controlled release device.

A major candidate cell target for an immunomodulatory OA therapy is the macrophage due to its ability to exhibit pro-inflammatory or anti-inflammatory signalling based on its polarisation state. The promotion of anti-inflammatory

signalling by controlling macrophage polarisation is a potential strategy for modifying the disease of OA, especially considering the pivotal role of M1 macrophages in driving OA progression. The potential to direct immune signalling through macrophage polarisation has made the generation of materials capable of promoting M2-like macrophage polarisation a popular goal in the fields of regenerative medicine and biomaterials[202]. Reported methods to induce macrophage polarisation states and their potential benefit in treating OA are reviewed below. Following the initial categorisation of M1 and M2 macrophage polarisation, the nomenclature surrounding M2 was subdivided into M2a, M2b M2c and M2d based on the method of stimulation[203]. A schematic summarising macrophage polarisation states is included which shows polarisation stimuli, secreted polarisation markers, gene expression markers, and cell surface markers (Figure 1.3)

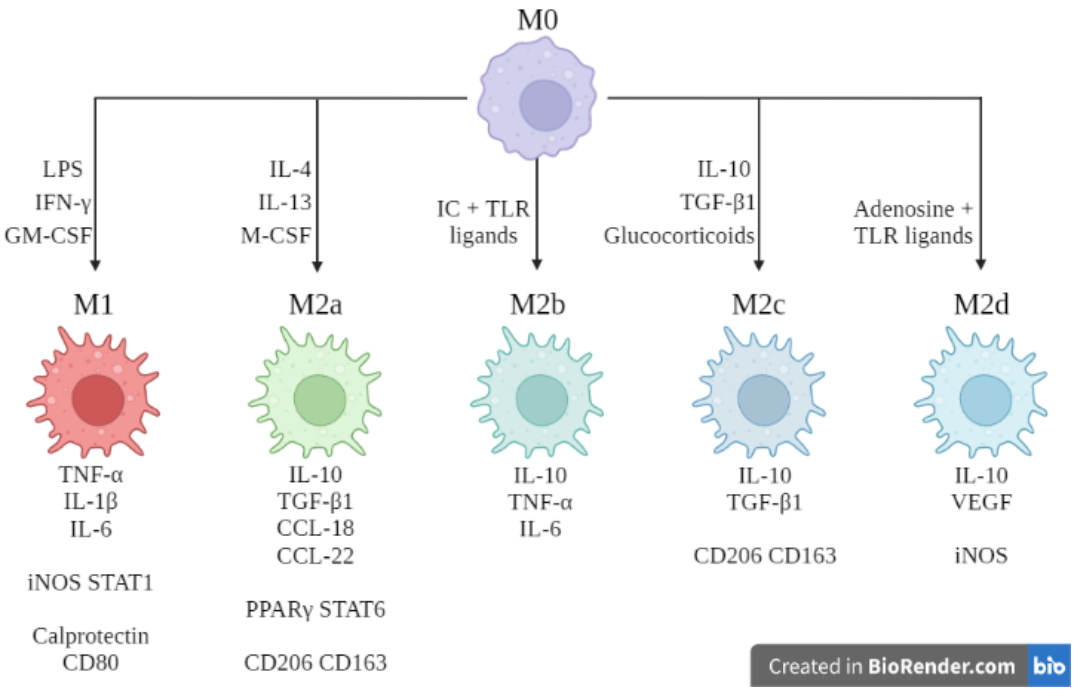

Figure 1.7: Summary of macrophage polarisation states. Macrophages are innate immune cells that become polarised in response to environmental stimuli.

M0 is used to describe a quiescent state, M1 describes classical activation and promotes pro-inflammatory signalling, M2 describes alternative activation and promotes anti-inflammatory signalling. M2 polarisation is subdivided into M2a (anti-inflammatory), M2b (immune regulatory), M2c (Immunosupressive), and M2d (Tumour associated). Commonly reported stimuli and polarisation markers for M1, M2a, M2b, M2c, and M2d are included. Image created at www.BioRender.com.

M2a is induced by IL-4[204] and may be enhanced by IL-13[205]. Following binding to the IL4RA, JAK/STAT signal transduction occurs in which STAT6 is activated by phosphorylation, enters the nucleus and acts as a transcription factor to upregulate expression of target genes[206]. M2a is considered as Anti-inflammatory and is associated with tissue repair. M2a secreted markers include IL-10, TGF-β1, IL-1 receptor antagonist (IL-1RA), C-C motif chemokine ligand 18 (CCL-18), and C-C motif chemokine ligand 22 (CCL-22)[207–209]. Previously known as alternative macrophage activation associated C-C chemokine, CCL-18 has a chemotactic role in promoting the migration of Th2 cells, monocytes, naïve CD4 T cells, and B lymphocytes. In-vitro application of CCL-18 is reported to induce M2-like polarisation of macrophages[210]. CCL-22 was previously known as macrophage derived chemokine and also has a chemotactic role in promoting migration of Th2 cells, monocytes, dendritic cells, and memory T cells[211]. CCL-22 has been observed as raised in the synovial fluid in certain subsets of OA patients and has been hypothesized to promote migration of fibroblast-like synovial cells in the pathobiology of OA[212]. Intracellular markers for M2a include PPAR-gamma and STAT6, and

associated surface markers are mannose receptor (CD206) and scavenger receptor (CD163)[213].

M2b is stimulated by immune complexes (IC) and toll-like receptor agonists (TLRs)[214]. M2b is considered to be a regulatory macrophage and expresses both pro-inflammatory and anti-inflammatory markers with high secretion of IL-10 and TNF-α[215,216].

M2c is stimulated by IL-10, TGF-β1, and by glucocorticoids such as dexamethasone which binds to the intracellular glucocorticoid receptor[217]. M2c exhibits immune suppressive signalling and is referred to as a deactivated macrophage. Secreted markers include high IL-10 and TGF-β1, and M2c has CD206 and CD163 expression[218].

M2d is stimulated by TLR agonists in the presence of adenosine. M2d secreted markers are IL-10 and Vascular-endothelial growth factor (VEGF). M2d is associated with angiogenesis and tumour progression[219].

In comparison, M1 is induced by IFN-γ, TNF-α, and lipopolysaccharide (LPS). M1 is characterised by high secretion pro-inflammatory cytokines including TNF-α, IFN-γ, IL-6, IL-1β and IL-12[220]. M1 Intracellular markers including inducible nitric oxide synthase (iNOS) and STAT1, and surface markers including calprotectin[221–223] (formerly known as S100A8/A9) and CD80[224].

Generally, M1 and M2 polarisation has been reported to be potentiated by GM-CSF and M-CSF respectively[225]. M-CSF is constitutively expressed in serum and both M-CSF and GM-CSF are elevated under conditions of inflammation[226]. For this reason, in-vitro macrophage polarisation experiments

routinely use combinations such as GM-CSF + IFN-γ for M1 and M-CSF + IL-4 for M2.

In recent years, this classification system has been criticized as inconsistent and there have been recommendations to update the nomenclature to M(stimulus) with the speculation that each stimulus or combination of stimuli can generate a unique polarisation state[227,228].

In addition to traditional cytokine application, M2-like macrophage polarisation has also been promoted using microscale grooves that induce an elongated cell morphology[229]. Other reported methods for promoting M2 polarisation are nanotopography[230,231], micro RNAs[232], silicate ions[233], copper ions[234], and magnesium ions[163]. Large scale material arrays have been carried out to identify acrylate polymers that promote M2-like polarisation following macrophage adhesion as candidates for advanced biomaterials[235].

In the context of osteoarthritis, promoting M2-like polarisation at the early stages of the disease is likely to be an ideal method to restore M1 and M2 balance and prevent the pro-inflammatory signalling that is the key driver of OA progression. If paired with improved early detection, an M2 promoting immunomodulatory therapy could modify the pathobiology of OA to retain articular cartilage tissue and prevent OA from reaching the late stage that is associated with disability.

Targeting M2-like polarisation would also be beneficial in treating late OA by reducing foreign body response (FBR) to scaffold implantation and by improving osteogenesis in the bone regions of osteochondral scaffolds. Following biomaterial implantation there is an acute inflammatory response by

the innate immune system[236]. Macrophages are recruited to the site and adhere to the material, FBR occurs when adhered macrophages fuse into multinucleated foreign body giant cells[237,238] (FBGCs) and encapsulate the material in fibrous matrix in a process called frustrated phagocytosis. Encapsulation is associated with implant failure[239] as the material cannot interact with surrounding cells and the low pH environment in the capsule facilitates material biodegradation[240]. While FBR contains complex cross-talk between a myriad of immune cell types, reports have shown that promoting M2 polarisation reduces its severity as evidenced by a decrease in fibrotic capsule thickness[241,242]. The reduction of FBR in OA tissue engineering would allow new forming tissue to integrate into surrounding tissue and would allow new tissue to form in less hostile conditions.

In bone tissue engineering, reports have shown enhanced osteogenic differentiation of MSCs with sequential M1 and M2 polarisation as evidenced by increased osteocalcin and alkaline phosphatase expression[243,244]. Sequential activation is also reported to stimulate angiogenesis in new forming bone by VEGF secreted from M1 macrophages and subsequent endothelial maturation by platelet derived growth factor (PDGF) secreted by M2[233]. Similarly, in epithelial wound healing the promotion of M1 polarisation in the early stages of repair followed by M2 polarisation at later stages is associated with reduced scar tissue formation and accelerated healing[245,246]. In OA, enhanced osteogenesis would offer improved osseointegration in the subchondral bone scaffold region.

It is likely that more successful attempts at osteochondral tissue engineering in the future will need to exhibit long-term immunomodulation as well as

osteogenic and chondrogenic regeneration in order to preserve new forming tissue. Promoting immunomodulation for 6 months may be a desirable period of efficacy because in-vivo models have shown maximal regeneration after 6 months compared to 3 months[190]. 6 months is also comparable to the recovery time following ACI and is considerably longer than the efficacy period of corticosteroid injections[126]. With the presence of pro-inflammatory signalling and the lack of immunomodulation, new forming tissue would be expected to degenerate by the same mechanism as natural tissue due to the pathobiology of OA. It is likely that more successful attempts would include multi-material osteochondral plug scaffolds laden with mature chondrocytes in the cartilage region and osteoblasts in the bone region, and it would need to be co-administered with a long term anti-inflammatory immunomodulatory therapy such as a controlled release device.

The future generation of multi-layered biomaterials for osteochondral tissue engineering that have properties such as complex 3D printed architecture, the use of autologous or allogeneic cells, exhibit immunomodulation by controlled drug release, and use multiple materials to promote osteogenesis and chondrogenesis will require the use of specialised laboratory settings. The scaling up of manufacturing of such materials in order to treat potentially millions of OA patients will be logistically challenging when rare equipment, skillsets, and considerable man hours will likely be needed.

In-vitro experiments that model immunomodulation using macrophages often use immortalised cell lines or peripheral blood mononuclear cells (PBMCs) from donor blood. THP-1 is a naturally immortalised cell line isolated from a 1 year old patient with acute myeloid leukaemia[247]. THP-1 monocytes can be

differentiated into macrophage-like cells using Phorbol 12-myristate 13-acetate (PMA) and are a popular choice for in-vitro polarisation experiments[248–252]. THP-1 have the benefits of being more clinically relevant than murine cell lines[253] and are logistically convenient to use, but as a cell line derived from a single patient they still have limited clinical relevance. Comparisons between THP-1 and PBMC derived macrophages have shown that not all polarisation markers for a given stimulus are the same between the two cell types and that THP-1 can be used as a more simplistic model for in-vitro immunomodulation[254–256]. PBMC derived macrophages have greater clinical relevance than cell lines, but donor to donor variation can make it difficult to acquire statistically significant in-vitro data when triplicate donors are used.

1.8 Challenges faced in controlled protein drug delivery

Proteins are biomacromolecules composed of polypeptide chains that are folded into secondary, tertiary and quaternary structures. During folding, hydrophobic regions are internalised and hydrophilic regions are exposed on the surface[257]. Proteins have a structure-function relationship in which the 3D structure must be maintained for its biological functionality, for example the active sites of enzymes[258]. Protein structure may become denatured due to harmful environmental stimuli such as high temperature, hydrophobicity, pH changes out of the active range for a protein, and ultraviolet (UV) light exposure[259–262]. Such changes in 3D structure often reduce bioactivity and render the protein non-functional[263].

The biological potency of cytokines and growth factors, and the ability to mass produce them in cell factories such as Chinese hamster ovary (CHO) cells[264],

Human embryonic kidney (HEK) cells[265], and Escherichia coli (E-Coli)[266] using recombinant expression vectors has led to increased interest in protein based drugs in the biopharmaceutical industry[267]. In OA, the delivery of cytokines that promote M2-like macrophage polarisation is an attractive strategy to modify the disease pathobiology using immunomodulation. However, the clinical administration of peptide and protein based drugs relies mainly on systemic injection methods which have undesirable side effects and limited efficacy due to the short half-life of proteins in-vivo. In 2017, a report combining multiple databases found there to be 239 peptide and protein based drugs that have FDA approval with a total of 380 drug variants[268]. When considering the routes of administration 158 were administered systemically by intravenous injection, 116 were injected subcutaneously, 49 were injected intramuscularly, 13 were administered orally, 4 used as external ointments, and only few injected directly into defect sites. Such methods are likely to only give transient efficacy due to the rapid enzymatic degradation by proteases in-vivo.

In bone regeneration therapies, the only three growth factors that have had FDA approval are BMP-2, BMP-7 and PDGF[269]. Infuse™ is a recombinant human BMP-2 treatment that is administered in a collagen sponge. Infuse has been shown to induce bone regeneration but there have also been adverse effects in clinical trials including ectopic bone formation, cancer risk, and severe swelling around implants for spinal cord injury[270–272]. Infuse™ remains controversial as it is available off-label in the USA[273] but there has been over $460 million in legal settlements by Medtronic from over 10,000 patients who received Infuse. After a period of time with FDA approval, the BMP-7 product OP-1 was withdrawn from the market due to safety concerns[274,275]. Overall, the main

issues surrounding BMP use historically can be attributed to the lack of controlled release from implants which exposes surrounding tissues to dosages far above the therapeutic range. In 2013, a randomised controlled trial reported positive outcomes after 36 months following the application of PDGF for periodontal osseous defects[276].

The only recombinant cytokines that have had FDA approval are IFN-α and IL-2 for cancer treatment[277,278]. Their clinical application has had limited efficacy due to the short half-life in vivo of the cytokines and that their systemic administration has severe off target toxicity at clinical doses for anti-cancer therapy. Attempts to improve the half-life of protein drugs have by conjugating them to poly(ethylene glycol) (PEG)[279,280], but this does not address the issue of off target effects that are associated with the systemic injection used for the majority of FDA approved protein drugs.

Experimental attempts at protein release from biomaterials often suffer from common shortcomings, the most notable of which is burst release. Burst release occurs when the cargo of a drug loaded material is released uncontrollably and the majority of the payload is released in a short period of time[281]. In-vivo, the consequences of uncontrolled protein release rate would mean that cells are exposed to supraphysiological concentrations which can lead to undesirable outcomes[282] such as the ectopic bone formation seen with BMP-2 in Infuse clinical trials. It would also mean that attempts at a long-term therapy would fail as majority of the protein payload is released in a short period of time.

A second common shortcoming is incomplete release, in which a significant amount of the drug payload is entrapped within the biomaterial[283]. A high dose

of entrapped protein can be problematic as damaging dose dumping can occur upon biodegradation of the material[284,285].

When taking into account the size of the recombinant protein industry and the complications observed in in-vivo growth factor and cytokine delivery pertaining to safety and efficacy, alternative approaches need to be taken to achieve the delivery of therapeutic dosages of proteins that is localised to the intended target area in the body and for a controllable period of time. A possible approach is the controlled release of proteins from advanced materials such as hydrogels.

1.9 Hydrogels for immunomodulatory cytokine delivery in OA

Hydrogels are hydrophilic polymers that are capable of absorbing large amounts of water to generate a swollen network. The hydrophilic environment within hydrogels is thought to promote the stability of biological cargo including proteins and has therefore generated interest into their feasibility as controlled release devices[286].

Poly(ethylene glycol) diacrylate

Poly(ethylene glycol) diacrylate (PEGDA) hydrogels are formed by photocrosslinking[287], in which a photoinitiator is activated by a select wavelength of light and cleaved into reactive free radicals[288]. Free radicals then attack the acrylate functional groups and initiate chain polymerisation between PEGDA macromers. Crosslinking between PEGDA chains then forms the polymer network[289]. Photocrosslinking is inhibited by oxygen which scavenges

the free radical species from the activated photoinitiator to terminate the chain reaction[290,291]. The residual monomer remaining from acrylate polymer generation needs to be considered for biological applications because they are often be cytotoxic[292,293]. PEGDA hydrogels have a slow biodegradation rate by hydrolysis of the ester linkage and the mesh size of the network depends on the molecular weight and concentration of the PEGDA macromer, in which low molecular weights and high PEGDA concentrations both reduce the mesh size[294,295].

Protein diffusion through the PEGDA polymer mesh has been previously studied with focus on the relationship between mesh size and the size of encapsulated proteins[296], in which relatively low molecular weight proteins such as 16.7kDa myoglobin can diffuse through a given mesh size of PEGDA but larger proteins like 66.4kDa bovine serum albumin (BSA) remain entrapped[297]. Introducing hydrolysable domains is an approach to achieve the release of protein that would otherwise be trapped in the hydrogel. First reported in 1993 by Sawhney et al. who showed the addition of lactic acid residues was able to extend the release of BSA for 50 days[298]. Similarly in 2015, Tong et al. show that the incorporation of rapidly degrading mercaptoacetic ester linkages into PEGDA enabled the release of BSA for 60 days and basic-FGF for 35 days[299]. In 2021, Lau et al. incorporated thiol residues in a photocrosslinkable dextran hydrogel and observed sustained release of 150kDa IgG antibody for 8 months[300]. Generally, the main limitations of controlled hydrogel degradation reports are that degradation is characterised using simple in-vitro incubation in PBS and this is unlikely to represent the biodegradation that would be observed in-vivo where many more chemical, enzymatic, and mechanical stimuli are

subject on the hydrogel. Stillman et al. reported increased biodegradation rate of PEGDA nanogels in comparison to bulk hydrogels. They also demonstrated that the addition of a biodegradable co-monomer containing disulfide bridges enhanced the biodegradation rate in the presence of glutathione and that this was further accelerated at pH 5.0 in comparison to 7.4 and 10.0[301]. Together, this shows potential for the fine tuning of PEGDA biodegradation to suit biological applications such as controlled cytokine delivery in osteoarthritis. A limitation in previous reports on protein release form PEGDA is that many of the reports with the longest periods of in-vitro release have either used BSA which has no measurable bioactivity, or have not obtained bioactivity data. Such data must be considered for translation to biological applications.

Pluronic-F127

Pluronic-F127 (PF127) is a tri block co-polymer with repeating units of polyethylene oxide – polypropylene oxide – polyethylene oxide (PEO-PPO-PEO)[302]. PF127 forms hydrogels in a temperature dependent mechanism by forming amphiphilic micelles and the sol-gel behaviour enables PF127 to be injected as a cool solution and form a gel in-situ at body temperature[303]. In-vitro characterisation of PF127 degradation has observed the majority of the hydrogel weight to be lost after 14 days which would limit its capacity as a long-term controlled release device[304]. Protein release attempts using PF127 usually rely on simple diffusion as the main release mechanism are extremely prone to burst release. Studies using simple protein encapsulation in PF127 have shown rapid burst release of IL-2 in 8 hours[305], VEGF after 3 days[306], and insulin in 24 hours[307]. Pre-encapsulation of VEGF in PLGA microspheres before loading into

PF127 improved the In-vitro release of VEGF from 4 day burst release up to 60 days[308].

Heparin mimics

Affinity based protein release approaches utilise electrostatic attraction between the protein and the hydrogel to decrease the rate of release. A naturally occurring example of this mechanism is the binding of heparin to a group of proteins collectively named heparin binding proteins including FGF-2, VEGF and PDGF[309]. Heparin binds to its binding proteins via electrostatic attraction between its carboxyl and sulfate groups with proteins that have a positive net charge at physiological pH. The iso-electric point of a protein is the pH at which it has no net charge and is determined by the amino acid sequence on its surface[310], meaning any protein with an iso-electric point above 7.3 would be electrostatically attracted to heparin.

The sequestration of heparin binding proteins by heparin prevents their degradation by proteases and increases their otherwise short half-life in vivo[311]. For this reason, incorporation of heparins into hydrogels has been a strategy to achieve controlled protein release. For example, Jeon et al. incorporated methacrylated heparin into alginate methacrylate hydrogels and observed 3 weeks sustained release of BMP-2[312]. Noushi et al. reported reduced burst release of neurotrophin-3 from alginate microspheres containing heparin[313]. Claaßen et al. reported 7 day burst release of VEGF from gelatin hydrogels containing 1% heparin which was followed by a plateau until 21 days[314]. The use of heparin does have several practical limitations. Firstly, there is considerable heterogeneity in large molecular weight heparin which leads to

batch-to-batch variability[315]. The production of low molecular weight heparins reduces variation but is expensive[316]. Heparin is animal derived which may promote adverse effects such as immunogenicity and may also prompt safety and ethical concerns[317–319]. In-vivo heparins are degraded by heparinases[320] which means biomaterials functionalized with heparin at the surface may lose their cargo and become ineffective for controlled release. Heparin detachment from biomaterials may also cause unwanted anti-coagulant effects at the site intended for controlled protein release.

The limitations of heparin gave rise to the fabrication of heparin mimicking materials which are intended to exhibit the beneficial effects of heparin but circumvent the drawbacks. In the field of protein release, sulfated alginate hydrogels have been produced as heparin mimics. Alginate is a naturally occurring polysaccharide that is isolated from algae. Alginate hydrogels are formed using calcium ions to crosslink alginate monomers; alginate hydrogels degrade by calcium ion dissipation[321]. In 2008, Freeman et al. produced sulfated alginate microspheres that showed reduced release rate of basic FGF over 5 days with 0.1% sulfation, in which the unsulfated alginate released 100% of basic FGF after 5 days and the 0.1% sulfated alginate released 50% after 5 days[322]. They also found increased vascularisation following 2 week subcutaneous implantation of basic FGF releasing alginate sulfate scaffolds in comparison to FGF releasing alginate scaffolds. In 2018, Park at al. showed an improvement in the release trend of BMP-2 from sulfated alginate in comparison to alginate over a 10 day period[323] but increasing the concentration of sulfated alginate had diminishing returns in further improving the release trend.

Interleukin-4 in-vitro release

When considering protein delivery in early osteoarthritis, IL-4 is a promising candidate biomacromolecule because its ability to promote M2a macrophage polarisation to promote anti-inflammatory signalling may combat the pro-inflammatory signalling associated with OA progression. Evidence to support this has been seen in IL-4 injection into OA model rats.

In 2008, Yorimatsu et al. showed that daily intra-articular injection of IL-4 into OA model rats elicited a chondroprotective effect as evidenced by reduced cartilage and aggrecan degradation, and reduced nitric oxide production[324].

In 2021, Zhao et al. studied foreign body response in response following the subcutaneous implantation of a titanium biomaterial coated in calcium-strontium-zinc-phosphate[325]. They found that daily injection of IL-4 into the site of implant between days 3-7 of implantation increased the expression of M2 markers in the tissue surrounding the implant. When this method was applied to a rat femoral defect model, daily IL-4 injection also enhanced new bone formation. While not directly related to chondroprotection in OA, this finding does demonstrate that repeated IL-4 delivery is capable of eliciting immunomodulation in-vivo.

Helvoort et al. showed that weekly injection of an IL-4 and IL-10 fusion protein into the knee of OA model rats for 10 weeks significantly reduced cartilage degradation[326]. The authors said this fusion protein may be a potential DMAOD but remarked on how future approaches need to generate delivery methods that avoid frequent intra-articular injection.

Kaeppler et al. studied OA progression following joint destabilisation in IL-4 knockout mice and saw a significantly worse phenotype by histological scoring

after 20 weeks compared to wild type mice[327]. IL-4 priming of macrophages in-vitro increased phagocytosis of cartilage degradation products derived from human osteoarthritic joints, which would be expected to reduce the DAMPs that new macrophages are exposed to in-vivo and reduce the promotion of M1 macrophage polarisation.

Reports of in-vitro IL-4 release from biomaterials have typically shown quantifiable release for 1-2 weeks with poor control over release trend:

In 2015, Reeves et al. reported rapid burst release from silk biomaterials in which all of the IL-4 was released within one day followed by a plateau for the rest of the 5 day experiment[328]. In 2018, Li et al. showed 10 day controlled release from titanium nanotubes functionalised with carboxymethyl chitosan hydrogels[329]. Kumar et al. showed 14 day release from injectable silk hydrogels[330]. In 2020, Li at al. reported 9 day IL-4 release from graphene oxide coated titanium[331]. In 2020, Gong et al. showed 7 day burst release from a digital light projection (DLP) 3D printed Methacrylated gelatin (Gel-MA) hydrogel as part of an attempted biphasic osteochondral scaffold[332]. Gel-MA is also formed by photocrosslinking and is popularly used for tissue engineering research due to its RGD domains that promote cell attachment[333,334]. In-vivo, Gel-MA is degraded by collagenases which means it is likely unsuitable for long term protein release purposes[335].

When considering the aforementioned literature surrounding in-vivo IL-4 delivery there is substantial evidence to suggest that repeated IL-4 delivery can promote M2 macrophage polarisation in-vivo, and that repeated delivery can significantly improve the phenotype in moderately hostile environments such

as surgically induced OA in rats. In-vitro reports of IL-4 release from biomaterials have been limited in their capacity to produce either controlled IL-4 release or IL-4 release for a sustained period of time that would be comparable to current injectable therapeutic options for OA such as corticosteroids. IL-4 has an isoelectric point of 9.4[336] which means it has a net positive charge at physiological pH and would be electrostatically attracted to heparin or heparin mimicking materials. Affinity based approaches may therefore offer improvement in the release of IL-4 to generate advanced biomaterial therapies for OA that have an increased time periods of efficacy and may elicit chondroprotective effects.

The loading of proteins into hydrogels typically uses one of two methods. The first is loading of the protein into the hydrogel precursor solution prior to gelation. This method has the benefits of having precise control over the loading of each hydrogel but has the drawback of proteins then being exposed to the gelation conditions such as UV light in photocrosslinking. Previous reports using PEGDA have shown the release of bioactive basic FGF using this method[299] but have also the reduction of lysozyme bioactivity from activated photoinitiator[337]. Lin et al. showed reduced percentage release of BSA at higher photoinitiator to protein ratios which suggests that the activated initiator interacts with proteins and cause its entrapment within PEGDA[338]. The second method is to load protein onto hydrogels post fabrication by immersion in a protein containing solution[339]. This method has the benefit of reducing protein exposure to environmental factors but has less control over the loading dosage onto each material. Requiring a separate bathing solution for each hydrogel is also wasteful and likely to require more experimental costs.

1.10 3D printing of hydrogels for controlled protein release

The generation of an early osteoarthritis therapy that utilises the controlled release of M2 promoting cytokines from affinity hydrogels would need minimal invasiveness, such as a single injection into the synovial joint. The clinical administration of cortisone into osteoarthritic knee joints uses 25 gauge needles[340] that have a 260µm inner diameter[341], which means the diameter of cytokine loaded hydrogels must be below 250µm to travel through the aperture.

Digital light projection (DLP) is an additive manufacturing technique that is capable of 3D printing photocrosslinkable polymers in the micro-scale[342]. During DLP, the 3D object file is sliced layers with thicknesses in the µm range, a build platform then enters a vat of photocrosslinkable precursor solution and is positioned at the first layer height away from a light projector. The light source projects the image of the first layer and initiates photocrosslinking of the first layer onto the build platform. The platform then moves in the Z-axis to the second layer height and the projection of the second layer builds onto the first layer. Subsequent layers are printed onto previous layers until the entire object is manufactured.

In the field of controlled release, DLP printing has previously been used to generate orally administered tablets for the release of small molecule drugs such as ibuprofen and dexamethasone[343,344]. The use of 3D printing to influence paracetamol drug elution has also been explored by printing PEGDA hydrogels with varying surface area to volume ratios (SA:V) using conventional laser

stereolithography, in which hydrogels with the highest SA:V had increased drug release rate[345].

In 2020, Wang at el. produced a DLP printed hydrogel using thiol conjugated heparin and glycidyl methacrylate conjugated hyaluronic acid for the purpose of VEGF and PDGF release to model the promotion of angiogenesis[346]. The photocrosslinking method used was thiol-ene which is a photoinitiated reaction that takes place between alkene and thiol containing molecules forms a covalent bond between them[347,348]. A 2-step approach was used to print a core-shell material with PDGF as the core and VEGF as the shell. In-vitro release had an approximately linear release trend for 28 days but there was no observable sequential release from the shell and core. A major limitation of the study was that the authors did not collect any biological data to investigate the bioactivity of released growth factors such as cell culture or the use of in-vivo models. They also did not report the concentration range that each factor was being released in or if it was close to the therapeutic range.

In 2018, there were 11 FDA approved injectable microsphere drug release therapies with particle sizes between 1-300μm[349]. The ejection of microparticles from medical needles is often met with challenges such as blockage due to particle aggregation and subsequent wasting of product in the syringe[350]. Previously, microparticle geometry has been studied with regard to improving injectability[351]. The use of DLP 3D printing to produce affinity hydrogel microparticles may allow for the optimisation of injectability using geometries that do not aggregate and block the needle. 3D particle design may also be investigated to optimise cytokine loading if particles are loaded post fabrication by immersion. Future studies should also consider the ideal particle size of

injection into the knee so that the particle is easily and efficiently injected but is not endocytosed by the native cells of the joint.

1.11 Conclusion

In conclusion, osteoarthritis remains an incurable disease with limited treatment options and hundreds of millions of sufferers worldwide. Tissue engineering of articular cartilage and osteochondral tissue remains elusive due to the complexity of native tissue and the hostile environment in the osteoarthritic joint. Osteoarthritis treatment strategies have historically focused on the repair of the osteochondral defect and not on modulating the osteoarthritic immune environment. Pro-inflammatory signalling orchestrated by M1 macrophages is present at the early stages of osteoarthritis and is a key driver of OA progression. Animal models of osteoarthritis have shown the repeated delivery of IL-4 to elicit chondroprotective effects by promoting M2 macrophage polarisation but controlled protein release remains challenging in the field. Affinity based methods for in-vitro protein release have utilised electrostatic attraction between heparin and positively charged proteins but heparins have multiple limitations. Heparin mimicking materials have been developed to utilise the beneficial effects of heparins but circumvent their limitations. Synthetic acrylates with charged chemical groups may be used as heparin mimics for controlled protein release and are commercially available, are able to be upscale manufactured for mass production, and are compatible with modern 3D printing technologies to enable the fabrication of biomaterials with defined architecture. Such technologies may be used to manufacture injectable IL-4 controlled release hydrogels for minimal invasiveness and could be a potential DMAOD

if administered in early osteoarthritis. The ideal injectable system would exhibit sustained release for a period of 6 months followed by controlled material biodegradation so that multiple surgical procedures are not required.

Thesis aims

The overall aim of this project was to generate 3D printed affinity hydrogels that exhibited the controlled release of anti-inflammatory cytokines to modulate immune signalling in the osteoarthritic joint at the early stage of the disease. Controlled release was intended to be sustained for a period of 6 months, and affinity hydrogels were envisaged to be injectable and undergo biodegradation once cytokine release was complete.

To address this overall aim, the research carried out in this thesis was sub-divided into three sections which each addressed a separate objective:

1) Achieve controlled protein release for multiple months from cast affinity hydrogels using photocrosslinkable synthetic materials that are an alternative to heparin. The model protein lysozyme and cytokines capable of promoting M2 macrophage polarisation were considered.
2) Show the bioactivity of released cytokines in promoting M2 macrophage polarisation in-vitro to model immunomodulation in the osteoarthritic joint.
3) Demonstrate the 3D printability of the selected affinity hydrogels using digital light projection 3D printing. Investigate if 3D printed hydrogel geometry may be used as an additional mechanism to fine-tune release behaviour.

Statement of novelty

This research focuses on controlled protein release from affinity hydrogels that are produced from commercially available synthetic acrylates, are compatible with modern 3D printing technology, and have the capacity to be upscale manufactured in the future. Such technology may be capable of generating long term immunomodulation in the osteoarthritic joint and bring improved therapy to many patients worldwide who currently have limited treatment options.

Chapter 2 - Materials and Methods

2.1 Materials

2.1.1 Laboratory consumables

Name	Supplier
Pipette tips 10µL – 1mL	TipOne® Pipette Tips
Pipette tips (filtered) 10µL – 1mL	TipOne® Pipette Tips
Serological pipettes (filtered) 5mL – 50mL	Star Lab
Eppendorf tubes 1.5mL, 0.7mL	Eppendorf™
Bijou 7mL	Sterilin™
Centrifuge tubes 15mL, 50mL	Corning™ Falcon™
Spectrophometry Cuvettes	Fisher Scientific 10663852
Assay plate 96-well flat bottom (Transparent)	Corning™ UV-Transparent Microplates 10288521
Assay plate 96 well flat bottom (White)	Fisher Scientific 10479501

Nunc-Immuno™ MicroWell™ 96 well solid plates	Sigma Aldrich M9410
ELISA plate sealer	R&D Systems DY992
Tissue culture flasks (T25, T75)	Corning™ Cell Culture Treated Flasks
Tissue culture treated plates (24-well, 12-well, 6-well)	Corning® Costar® TC-Treated Multiple Well Plates
Glass 20mL Scintillation Vials: Polypropylene Caps	Fisher Scientific 11768819
Aluminium foil	Scientific laboratory supplies
Glass microscopy slides	Sigma Aldrich S8902-1PAK
Thermo Scientific™ Nalgene™ System 100™ Cryogenic Vials	Fisher Scientific 13417659
Dulbecco′s Phosphate Buffered Saline	Sigma Aldrich D8537-500ML

2.1.2 Hydrogel fabrication and in-vitro protein release materials

Name	Supplier
Irgacure-2959 (2-Hydroxy-4′-(2-hydroxyethoxy)-2-methylpropiophenone)	Sigma Aldrich 410896-10G

LAP (Lithium phenyl-2,4,6-trimethylbenzoylphosphinate)	Sigma Aldrich 900889-5G
PEGDA 575Da	Sigma Aldrich 437441-500ML
PEGDA 4kDa	Sigma Aldrich 907227-1G
PEGDA 6kDa	Sigma Aldrich 701963-1G
PEGDA 20kDa	Sigma Aldrich 767549-1G
3-Sulfopropyl acrylate potassium salt	Sigma Aldrich 251631-500G
Lysozyme from chicken egg white	Sigma Aldrich L6876-10G
Micrococcus lysodeikticus ATCC No. 4698	Sigma Aldrich M3770-5G
Pierce™ Detergent Compatible Bradford Assay Kit	Thermo Fisher Scientific 23246
Recombinant Human TGF-β1 (CHO derived)	PeproTech 100-21C
Human TGF-β1 Pre-Coated ELISA Kit	PeproTech BGK01137
Gelatin from porcine skin	Sigma Aldrich G6144-500G

Hydrochloric acid	Fisher Scientific 12943544
Tartrazine	Sigma Aldrich T0388-500G
Isopropanol	Fisher Scientific 149320250
Tissue-Tek® OCT embedding compound	Fisher Scientific 12351753

2.1.3 Cell culture materials

Name	Supplier
RPMI 1640 media	Thermo Fisher Scientific 21870076
Foetal bovine serum	Sigma Aldrich F2442-500ML
GlutaMAX	Thermo Fisher Scientific 35050061
Glucose solution	Thermo Fisher Scientific A2494001
HEPES buffer (4-(2-hydroxyethyl)-1-piperazineethanesulphonic acid)	Thermo Fisher Scientific 15630080
Sodium pyruvate	Thermo Fisher Scientific

	11360070
Penicillin-streptomycin	Sigma Aldrich P4333-20ML
Trypan blue	Thermo Fisher Scientific 15250061
Phorbol 12-myristate 13-acetate (PMA)	Sigma Aldrich P8139-1MG
Macrophage Colony-Stimulating Factor human	Sigma Aldrich M6518-10UG
Granulocyte-Macrophage Colony-Stimulating Factor human	Sigma Aldrich G5035-4X5UG
Interferon-γ human	Sigma Aldrich I17001-100UG
Interleukin-4 human	Sigma Aldrich I4269-50UG
Paraformaldehyde Solution, 4% in PBS, Thermo Scientific™	Fisher Scientific 15670799
TWEEN® 20	Sigma Aldrich P1379-100ML
PBS, Phosphate Buffered Saline, 10X Solution, Fisher BioReagents™	Fisher Scientific 12899712
Tris buffered saline	Sigma Aldrich

	94158-10TAB
Deionized water	Sigma Aldrich 38796-1L
Bovine serum albumin (BSA, solid)	Sigma Aldrich A9418
Bovine serum albumin (BSA, liquid, sterile)	Sigma Aldrich A7284-50ML
Glycine	Sigma Aldrich G8898
Goat Serum Donor Herd	Sigma Aldrich G6767-500ML
Calprotectin Mouse anti-human	Thermo Fisher Scientific 27E10
Anti-Mannose Receptor anti-human antibody	Abcam ab64693
Goat anti-Mouse IgG (H+L) Cross-Adsorbed Secondary Antibody, Rhodamine Red™-X	Thermo Fisher Scientific R-6393
Goat anti-Rabbit IgG (H+L) Cross-Adsorbed Secondary Antibody, Alexa Fluor™ 488	Thermo Fisher Scientific A-11008

Recombinant Alexa Fluor 488 Anti-CD68 antibody [KP1]	Abcam ab222914
DAPI (4',6-Diamidino-2-Phenylindole, Dihydrochloride)	Thermo Fisher Scientific D1306
Human TNF-alpha DuoSet ELISA	R&D Systems DY210-05
Human IL-6 DuoSet ELISA	R&D Systems DY206-05
Human CCL18/PARC DuoSet ELISA	R&D Systems DY394-05
Human CCL22/MDC DuoSet ELISA	R&D Systems DY336
Human IL-4 DuoSet ELISA	R&D Systems DY204-05
Thermo Scientific™ 1-Step™ Ultra TMB-ELISA Substrate Solution	Thermo Fisher Scientific 10647894
Sulfuric acid	Thermo Fisher Scientific 15644920
ToxiLight™ 100% Lysis Control Set, 200 Test	Lonza LT07-517

ToxiLight™ Non-Destructive Cytotoxicity BioAssay Kit, 500 test	Lonza LT07-217
Antibiotic-Antimycotic (100X)	Thermo Fisher Scientific 15240096
Cell Freezing Medium-DMSO 1×	Sigma Aldrich C6164-50ML
Water bath protective media Aqua Stabil 6 x 100 ML	Julabo BAT5584
Ethanol, Absolute (200 Proof), Molecular Biology Grade, Fisher BioReagents™	Fisher Scientific 16685992
Tristel™ Distel™ Surface Disinfectant	Fisher Scientific 12879357

2.2 Methods

2.2.1 Hydrogel casting and characterisation

UV-photocrosslinking

Photoinitiator solutions were prepared in 20mL glass scintillation vials covered in aluminium foil to protect from light. Photosensitive chemicals were weighed out or pipetted with the nearest overhead light switched off. 0.5% w/v Irgacure-2959 (2-Hydroxy-4′-(2-hydroxyethoxy)-2-methylpropiophenone) was dissolved in phosphate buffered saline (PBS) by heating to 80^{o}C on a hotplate

for 20 minutes. The photoinitiator solution was left to stand for 10 minutes to equilibrate to room temperature. Acrylate monomers were then dissolved into the solution by vortexing. Solutions for lysozyme or BSA in-vitro release experiments had the solid protein added as the final ingredient.

TGF-β1 containing solutions were prepared from a stock solution which was reconstituted according to supplier's instructions. Photoinitiator and acrylates were first prepared at 2X the desired concentrations. TGF-β1 stock solution was diluted to 2X the desired concentration with PBS containing 1mg/mL BSA. The 2X photoinitiator and TGF-β1 solutions were mixed 1:1 to produce a final solution containing the desired concentration of photoinitiator, acrylates and TGF-β1.

UV photocrosslinking was carried out in a custom made glove box under argon atmosphere. Hydrogel precursor solutions, polytetrafluoroethylene (PTFE) moulds, well-plates, pipettes and tips were placed into an airtight antechamber. Air was purged from the antechamber until a pressure of -90kPa was reached. The antechamber was then filled with argon gas until a gauge pressure of 0kPa was reached. The gas was then purged and refilled with argon two more times. The main glove box chamber was filled with argon gas until an oxygen concentration of below 2000ppm was reached. From inside the glove box, the inner antechamber door was opened and samples were prepared for photocrosslinking. 500µL hydrogels were formed in square PTFE moulds measuring 15x15mm and 100µL hydrogels were formed as droplets on a single piece of flat PTFE. To initiate the reaction, a 365nm UV lamp was suspended 10cm above the samples and switched on for 10 minutes (UVP XX-15 Series UV Bench Lamp, 15 Watt). Following UV irradiation the lamp was switched

off and hydrogels were placed into well-plates for subsequent experimentation. All experimental groups used hydrogels in triplicate and a separate pipette tip was used for each condition.

In-vitro hydrogel swelling

Following photocrosslinking, hydrogels were weighed to obtain the initial gel weight. Hydrogels were then immersed in PBS at 37^{o}C and the change in gel weight was measured at multiple time points over a 5 day period. 500μL hydrogels were incubated in 6mL of PBS and 100μL hydrogels were incubated in 5mL. To prevent evaporation, well-plates were sealed with laboratory tape during incubation. In each condition the swelling was expressed as the average percentage weight increase from the initial hydrogel weight immediately after photocrosslinking.

Hydrogel compressive testing

Mechanical testing was carried out on swollen hydrogels using a texture analyser (Stable bio systems TA.HD plus). A 5kg load cell and 32mm diameter cylindrical probe were used as attachments. Load cell force and probe height were calibrated at the start of each experiment. Hydrogel dimensions were measured using digital callipers and input into the software (Exponent TEE32) to calculate stress area. Target mode was set to strain, test speed was set to 0.1mms^{-1} and the target position was set to 50% strain. Following material compression the stress and strain data was exported to Microsoft Excel and plotted as a scatter graph. The compressive modulus was calculated as the gradient of the linear section of the stress - strain curve.

2.2.2 In-vitro protein release from cast hydrogels

Direct loading method (Lysozyme, BSA and TGF-β1)

The protein of interest was loaded into the hydrogel precursor solution and exposed to 365nm UV light for photocrosslinking (2.2.1). Protein containing hydrogels were then immersed in PBS (6mL for 500µL hydrogels and 5mL for 100µL hydrogels) and incubated at 37°C with well-plates sealed using laboratory tape. At each controlled release time point the entire volume of PBS was aspirated and replaced with fresh PBS to re-establish the diffusion gradient. For each hydrogel the PBS at every time point was stored in a separate 7mL bijou at -20°C until the time for analysis.

Core-shell method (Gelatin –PEGDA)

A 6% w/v gelatin solution (Type A from porcine skin 100 bloom) was dissolved in PBS at 80°C. Simultaneously, 0.5% w/v Irgacure-2959 ((2-Hydroxy-4′-(2-hydroxyethoxy)-2-methylpropiophenone) was dissolved at 80°C for 20 minutes while protected from light. After equilibrating to room temperature, 10% w/v 4kDa PEGDA was dissolved into the photoinitiator solution. 400µL of was pipetted into custom made square PTFE moulds measuring 15x15mm with a raised 5x5x1mm square in the base of each mould so that the raised square was covered. 365nm UV light was applied to the moulds for 10 minutes to form PEGDA hydrogels (UVP XX-15 Series UV Bench Lamp, 15 Watt). During this time the 6% w/v gelatin solution was taken off the hot plate and allowed to cool. Once reaching approximately 37°C the gelatin solution was mixed 1:1 with a 100µg/mL stock solution of TGF-β1 to form a solution containing 3% w/v gelatin and 50µg/mL TGF-β1. The 400µL PEGDA hydrogels were removed from the moulds and inverted to expose a 5x5x1mm indentation. 20µL of the

combined gelatin and TGF-β1 was pipetted into the indentation and the hydrogels were left to incubate at room temperature for 15 minutes followed by 15 minutes incubation at 4^{o}C. Hydrogels were then placed into square moulds measuring 15x15mm with a flat base and 400μL of PEGDA photoinitiator solution was applied over the gelatin filled indentation and exposed to 365nm UV light for 10 minutes to encapsulate the TGF-β1 loaded gelatin hydrogel between two layers of 10% 4kDa PEGDA. Composite gelatin-PEGDA hydrogels were then immersed in 5mL PBS for a controlled release study with matched time points to the original TGF-β1 release attempt. A control group was included with a 3% gelatin core containing no TGF-β1.

Indirect loading method (Interleukin-4 release into THP-1 culture media)

100μL hydrogels were formed containing 10% PEGDA (4kDa) and 0%, 1% and 5% w/v 3-sulfopropyl acrylate using 10 minutes 365nm UV light exposure in a custom made glove box with oxygen concentration below 2000 ppm (2.2.1 UV photocrosslinking). Hydrogels were each immersed in 5mL PBS for 5 days to investigate in-vitro swelling (2.2.1 in-vitro hydrogel swelling).

Hydrogels were sterilised using 254nm UV light irradiation for 20 minutes (Benchmark UV-Clave UltraViolet Chamber) followed by a 30 minute wash in antibiotic antimitotic antibody (Sigma Aldrich) in a class 2 biological safety cabinet. Hydrogels were then washed three times each in 1mL sterile PBS for 5 minutes per wash. From this point onwards, hydrogels were only handled with sterilised implements (By 70% ethanol wash and UV irradiation) within a class 2 biological safety cabinet. At the start of each use the cabinet airflow was switched on. Once a sufficient air flow was reached to protect the inner

environment of the cabinet, the cabinet and all its contents were washed thoroughly with 70% ethanol. The vessels containing either hydrogel samples, new reagents or consumables were washed with 70% ethanol prior to entering the cabinet. Only filtered pipette tips were used within the cabinet and vessels containing sterile hydrogels, reagents or consumables were only opened within the cleaned cabinet after sufficient air flow was reached to protect the sample and the user.

To load hydrogels with IL4, each gel was immersed in 500μL of a 2.2μg/mL sterile solution of IL-4 in a 24-well plate. Hydrogels were incubated at 37^{o}C for 24 hours in the IL-4 solution before being transferred to a 12-well plate with one gel per well. 2mL of THP-1 complete cell culture media (2.2.5 THP-1 culture conditions) was added to each well to cover each hydrogel for a controlled release study. At each time point the entire 2mL of media was removed from each gel and replaced with 2mL fresh THP-1 complete media. For each hydrogel at every time point, 1mL of the collected media was stored in a sterile Eppendorf tube at -20^{o}C for future cell culture experiments. The remaining 1mL was stored at -20^{o}C in a separate Eppendorf tube to be assayed by ELISA in non-sterile conditions (R&D systems IL-4 Duoset) to quantify the IL-4 released at each time point for each hydrogel.

To estimate the dosage of IL-4 loaded onto each hydrogel a sample of the bathing solution after 24 hours incubation with each hydrogel was diluted by serial dilution and quantified by ELISA. The difference in IL-4 dosage calculated between the initial IL-4 solution and the solution after 24 hours incubation with the hydrogel was used as the estimated amount loaded for each

gel. A control group was included with 10% 4kDa PEGDA and 5% SPAK and was incubated for 24 hours in PBS containing 1mg/mL BSA with no IL-4.

2.2.3 Protein detection assays

Bradford assay

Bradford reagent (Pierce™ Detergent Compatible Bradford Assay Kit) was left to equilibrate at room temperature while controlled release samples were thawed at 37ºC. Bradford assay was carried out in transparent flat-bottom 96-well assay plates using the micro microplate protocol. Protein standards were made for the protein of interest (Lysozyme or BSA as appropriate) by serial dilution in PBS to produce standards with the concentrations 25µg/mL, 20 µg/mL, 15 µg/mL, 10 µg/mL, 5 µg/mL, 2.5 µg/mL, 1.25µg/mL and PBS was used as a blank.

150µL of each standard was pipetted the 96-well assay plate in triplicate using a separate pipette tip for each standard. Controlled release samples were assayed in duplicate at 150µL. 150µL of Bradford reagent was then added into each well using a multichannel pipette, aspirating up and down 5 times to gently mix the sample and reagent. Plates were incubated at room temperature for 10 minutes.

Absorbance was read at 595nm using a plate reader (TECAN infinite 200 PRO) and exported to Microsoft Excel (Office 365). As per supplier's instructions, the average absorbance of the blank was subtracted from each well and a standard curve was used to calculate the protein concentration of controlled release wells. Samples with absorbance below the calculated LOD (3 standard deviations above the average blank)[352] were assigned a zero value[353] and samples with absorbance values above 25µg/mL were diluted in PBS and assayed again until

they were within the linear dynamic range of the assay. The LOQ was calculated as 10 standard deviations above the blank and was considered during interpretation of the data[354].

For each hydrogel the average concentration at each time point was multiplied by the volume of release buffer to calculate the dosage released. The dosage was then expressed as a percentage of the total amount of protein estimated to be in the hydrogel. For each condition, cumulative protein release was calculated by adding together the percentage release at each time point chronologically until the end of the experiment.

Enzyme-linked immunosorbent assay (ELISA, TGF-β1 in-vitro release)

TGF-β1 controlled release samples were thawed at 37ºC. During this time the pre-coated TGF-β1 ELISA plate (PeproTech BGK01137) was thawed at room temperature and a 10ng vial of TGF-β1standard was reconstituted in 1mL of sample dilutant and left to equilibrate for 10 minutes with gentle agitation.

A serial dilution was performed on the assay standard to generate TGF-β1 standards with the concentrations: 1000pg/mL, 500pg/mL, 250pg/mL, 125pg/mL, 62.5pg/mL, 31.25pg/mL, 15.625pg/mL, and the reagent dilutant was used as a blank.

100µL of each standard or sample was pipetted into each well. Standards were assayed in triplicate and protein release samples were assayed in duplicate. The plate was sealed and incubated at 37ºC for 90 minutes. The seal was removed and the plate was inverted over a waste container and agitated by repeated flicking to empty the liquid content of the wells. The plate was blotted onto laboratory paper towel until all excess liquid was removed.

The 100x biotinylated anti-TGF-β1 detection antibody was diluted with antibody dilutant and mixed thoroughly. 100µL of biotinylated antibody was pipetted into each well using a multichannel pipette. The plate was sealed and incubated at 37°C for 60 minutes. The seal was removed and the plate was inverted over a waste container and agitated by repeated flicking to empty the liquid content of the wells. Wash buffer concentrate was dissolved in 1 litre of deionized water and 300µL of wash buffer was pipetted into each well using a multichannel pipette. The plate was inverted and agitated over a waste container to remove wash buffer. The plate was washed two more times and blotted onto paper towel after the final wash.

The 100x Avidin-Biotin-Peroxidase complex was diluted with the Avidin-Biotin-Peroxidase dilutant. 100µL was pipetted into each well using a multichannel pipette and the plate was sealed and incubated at 37°C for 30 minutes. The plate was inverted, blotted and washed with wash buffer 5 times. After the final wash the plate was blotted with paper towel to remove excess wash buffer.

90µL of colour developing reagent was pipetted into each well with a multichannel. The plate was sealed and incubated in the dark for 20-30 minutes. During this time the plate was checked at regular intervals for visible colour change from colourless to dark blue. At the time when the highest 4 standards were visibly dark blue and the lowest standards remained colourless by eye, 100µL of stop solution was added to each well using a multichannel which immediately caused blue wells to yellow.

The absorbance at 450nm was immediately read using a platereader (TECAN infinite 200 PRO) with reference wavelength set to 570nm. The data was exported to Microsoft Excel (Office 365) and the average absorbance of the blank was subtracted from each well. A standard curve was used to calculate the TGF-β1 concentration of controlled release wells. Samples with absorbance below the calculated LOD (3 standard deviations above the average blank) were assigned a zero value[352,353] and samples with absorbance values above 1000pg/mL were diluted in reagent dilutant and assayed again until they were within the linear dynamic range of the assay. The LOQ was calculated as 10 standard deviations above the blank and was considered during interpretation of the data[354].

For each hydrogel the average concentration at each time point was multiplied by the volume of release buffer to calculate the dosage released. The dosage was then expressed as a percentage of the total amount of TGF-β1 estimated to be in the hydrogel. For each condition, cumulative TGF-β1 release was calculated by adding together the percentage release at each time point chronologically until the end of the experiment.

2.2.4 Protein bioactivity assays

Lysozyme bioactivity assay

Lysozyme substrate (Micrococcus lysodeikticus) was dissolved in PBS at a concentration of 0.15mg/mL. For each lysozyme controlled release time point to be tested, a control sample of lysozyme was prepared in PBS with a matched concentration to what was determined in the controlled release sample by Bradford assay (2.2.2 Direct loading method, 2.2.3 Bradford assay). The

number of freeze-thaw cycles was matched between the control samples and their corresponding controlled release sample. Lysozyme bioactivity was determined using a UV-Vis spectrophotometer (Agilent Cary UV-Vis Multicell Peltier). 1.5mL of lysozyme substrate was pipetted into a disposable cuvette followed by 100μL of either controlled release sample or control solution. Cuvettes were mixed once by immersion and immediately placed into the spectrophotometer chamber. The absorbance was read at 450nm and was then read again every minute for 5 minutes. Samples were read in triplicate and the average decrease in absorbance in 5 minutes for controlled release samples was expressed as a percentage of the decrease in absorbance in 5 minutes in its corresponding control.

2.2.5 Cell culture

THP-1 culture conditions

Unless otherwise stated, all cell culture experiments were carried out in class 2 biological safety cabinets with functioning High-Efficiency Particle Absorbing (HEPA) filters. At the start of each use the air flow was activated. Once a velocity was reached that protected the inner environment and the user, the entire cabinet and its contents were thoroughly cleaned with 70% ethanol. All vessels containing cells, reagents and consumables were washed with 70% ethanol before being placed into the cleaned cabinet. Only sterile reagents, filtered pipette tips and serological pipettes were used within the cabinet and all consumables were only used once before being discarded. Vessels containing sterile reagents, consumables or cells were only opened within the cleaned

cabinet. All reagents were warmed to 37°C in a water bath before being applied to cells.

THP-1 cells were purchased from ATCC (ATCC TIB-202). Cryopreserved THP-1 cells were thawed in a 37°C water bath for 3 minutes. Thawed cells were centrifuged at 350g for 5 minutes and resuspended in THP-1 complete media consisting of RPMI-1640 supplemented with 10% foetal bovine serum (FBS), 1% sodium pyruvate, 1% GlutaMAX, 1% HEPES, 1.25% glucose solution and 1% penicillin-streptomycin (Thermo Fisher Scientific). All media supplements were 0.2μm sterile filtered. THP-1 cells were cultured in the concentration range of 200,000 – 1000,000 cells per mL in T25 and T75 flasks as appropriate. During culture, T-flasks were stood upright in a humidified 37°C incubator with 5% CO_2.

Cells were split every 3 days. During this process, cells were aspirated into sterile centrifuge tubes and centrifuged at 350g for 5 minutes. The supernatant was discarded and the cell pellet was resuspended in 1-5mL of fresh THP-1 complete media based on the initial volume prior to centrifugation. 50μL of cell suspension was pipetted into an Eppendorf tube and mixed 1:1 with Trypan blue outside of the cabinet. 10μL was pipetted under the cover slip of a cleaned haemocytometer and counted using an automated cell counter (Life technologies Countess II FL). For continued culture the cell suspension was diluted down to 200,000 cells per mL in new T-flasks or diluted to 500,000 cells per mL for seeding in subsequent macrophage polarisation experiments.

<u>THP-1 cell seeding</u>

THP-1 cells were centrifuged at 350g for 5 minutes and then resuspended at 500,000 cells per mL. 50ng/mL of PMA (Phorbol 12-myristate 13-acetate) was added from a stock solution and the cell suspension was mixed gently. THP-1 cells were then seeded in triplicate in 24-well culture plates with 1mL of cell suspension per well. After seeding, each plate was agitated gently and incubated at 37^{o}C for 6 hours. Each plate of cells was viewed by Brightfield microscopy to confirm cell adhesion and confluency of approximately 70%. PMA containing media was aspirated from each well and cells were washed once with sterile PBS for 5 minutes. PBS was removed and 1mL of fresh THP-1 complete media was added to each well. THP-1 cells were then left to rest for 24 hours at 37^{o}C with 5% CO_2 before subsequent polarisation using either cytokine application or incubation with IL-4 releasing hydrogels.

THP-1 macrophage polarisation (cytokine application)

Polarisation cocktails were prepared in THP-1 complete media for each experimental condition. For experiments investigating the controlled release of IL-4, the following control groups were used as examples of M0 and M1 macrophage polarisations:

M0: 50ng/mL M-CSF

M1: 50ng/mL GM-CSF + 20ng/mL IFN-γ

For experimental groups using “Released IL-4” the 1mL sterile aliquots from IL-4 controlled release time points were used as the polarisation stimuli (2.2.2 indirect loading method). M-CSF was added to each aliquot to a final concentration of 50ng/mL. For each experiment, an “M2” control group was included with the polarisation cocktail containing 50ng/mL M-CSF and a

matched IL-4 concentration to what was estimated in the corresponding "Released IL-4" time point.

THP-1 cells were cultured in polarisation cocktails for 6 days. 50μL of media was collected from each well at day 3 for a cell viability timepoint. After 6 days the media from each sample was collected in 1.5mL Eppendorf tubes and stored at -20^{o}C for subsequent ELISA and viability assays.

THP-1 macrophage polarisation (hydrogel incubation)

100μL hydrogels were formed containing 10% 4kDa PEGDA and 5% 3-sulfopropyl acrylate in a custom glovebox using 10 minutes 365nm UV light exposure with oxygen concentration below 2000ppm (as described 2.2.1 UV photocrosslinking). Hydrogels were sterilised and loaded with IL-4 by overnight immersion in a 2.2μg/mL solution of IL-4 (as described 2.2.2 indirect loading method).

THP-1 cells were seeded at 500,000 cells per mL using 6 hours exposure to 50ng/mL PMA (as described 2.2.5 THP-1 cell seeding). Well size was increased to 12-well with 2mL of seeded cells to match the media volume to what was used for IL-4 controlled release. A single IL-4 loaded gel was added to each well as appropriate. A control group containing 5% SPAK 10% PEGDA hydrogels with no IL-4 loading was included. A control group modelling an IL-4 bolus injection was included which had a dose of IL-4 matched to what was estimated to be released by 5% SPAK 10% PEGDA after 6 days from the cumulative release curve (202ng/mL) (2.2.2 Interleukin-4 release into THP-1 culture media).

50µL of media was collected from each well at day 3 for a cell viability timepoint. After 6 days 1mL of the media from each sample was collected in 1.5mL Eppendorf tubes and stored at -20^{o}C for subsequent ELISA and viability assays.

ELISA (THP-1 secreted cytokines, IL-4 controlled release)

Upon purchase of all R&D Duoset ELISA kits, antibodies and standards were reconstituted according to supplier's instructions and were stored as aliquots at -80^{o}C. The general method for each ELISA was the same for each cytokine target. ELISA was carried out in non-sterile conditions.

Capture antibody was appropriately diluted in PBS and 50µL was pipetted into each well of a 96-well ELISA plate with a multichannel pipette. The plate was agitated gently to ensure full coverage of capture antibody in each well. The plate was then sealed and incubated on a rocker at room temperature overnight.

The plate was inverted over the sink and repeatedly flicked to empty the wells. The plate was washed 3 times with wash buffer (0.05% Tween-20 in PBS). During each wash 400µL of wash buffer was added to every well, the plate was inverted over the sink with repeated flicking and then was blotted onto laboratory paper towel to remove excess wash buffer. 300µL of blocking buffer (1% w/v BSA in PBS) was pipetted into each well. The plate was sealed and incubated on a rocker at room temperature for 1 hour.

Cytokine standards were prepared by serial dilution using reagent dilutant in the specified concentration range of each ELISA kit. Reagent dilutant was used as a blank. Samples were thawed to room temperature. The ELISA plate was washed 3 times with washing buffer. 50µL of each standard or sample was

pipetted into each well. Standards were assayed in triplicate and samples were assayed in duplicate. The plate was sealed and incubated on a rocker at room temperature for 1 hour.

The ELISA plate was washed 3 times with washing buffer. 50µL of appropriately diluted detection antibody was pipetted into each well with a multichannel. The plate was sealed and incubated at room temperature on a rocker for 1 hour.

The ELISA plate was washed 3 times with wash buffer. 50µL of appropriately diluted Streptavidin-HRP was pipetted into each well with a multichannel pipette. The plate was sealed and incubated at room temperature for 20 minutes while being protected from light.

The ELISA plate was washed 3 times with wash buffer. TMB substrate was brought to room temperature. 50µL of TMB substrate was pipetted into each well with a multichannel pipette. The plate was sealed and incubated at room temperature for 20 minutes while being protected from light.

25µL of sulfuric acid was pipetted into each well using a multichannel pipette as stop solution. The absorbance at 450nm was immediately read on a plate reader with 570nm reference wavelength (Promega GloMax explorer). The data was exported to Microsoft Excel (Office 365). The average absorbance of the blank was subtracted from each well and a standard curve was used to calculate the concentration of target cytokine in each sample. Samples with absorbance below the calculated LOD (3 standard deviations above the average blank)[352] were assigned a zero value[353] and samples with absorbance values above the highest standard for a given kit were diluted in reagent dilutant and assayed

again until they were within the linear dynamic range of the assay. The LOQ was calculated as 10 standard deviations above the blank and was considered during interpretation of the data[354].

For IL-4 controlled release, the dosage released at each time point was calculated and expressed as a percentage of the total IL-4 estimated to be loaded onto each hydrogel for each condition (2.2.2 Interleukin-4 release into THP-1 culture media). For each condition, cumulative IL-4 release was calculated by adding together the percentage release at each time point chronologically until the end of the experiment.

Immunostaining

THP-1 cells were washed twice with 37°C PBS using 1mL for 24-well plates and 2mL for 12-well plates. The remainder of the immunostaining protocol was carried out in non-sterile conditions. Cells were fixed with 4% PFA in PBS for 15 minutes using 300µL per well for 24-well plates and 600µL per well for 12-well.

Cells were washed 3 times with washing buffer (0.2% Tween-20 in PBS). Wells were blocked with a solution containing 3% w/v BSA and 1% w/v glycine for 30 minutes. Cells were washed 3 times with washing buffer and were then incubated in 5% goat serum for 30 minutes.

A primary antibody solution was prepared containing 2µg/mL mouse anti-human calprotectin (Thermo fisher 27E10) and rabbit anti-human mannose receptor/CD-206 (Abcam ab64693) in 5% goat serum. Cells were incubated in primary antibody solution overnight at 4°C using 300µL for 24-well plates and 600µL for 12-well. For CD-68 the primary antibody solution contained 5µg/mL

recombinant anti-human CD-68 conjugated to Alex Fluor-488 in 5% goat serum.

Cells were washed 3 times with wash buffer. A secondary antibody solution was prepared containing 8μg/mL Rhodamine red x goat anti-mouse IgG (Thermo Fisher R-6393) and 8μg/mL Alex Fluor 488 x goat anti-rabbit (Thermo Fisher A-11008) antibodies in 5% goat serum. Cells were incubated in secondary antibody solution for 1 hour at room temperature while protected from light. 300μL was used for 24-well plates and 600μL for 12-well. For CD-68 no secondary antibody was required.

Cells were washed twice with wash buffer. 200ng/mL DAPI solution was added to each well using 300μL for 24-well plates and 600μL for 12-well plates. The plates were incubated at room temperature for 5 minutes while protected from light. Cells were washed with PBS 3 times and stored at 4^{o}C with 1mL PBS per well while protected from light for future fluorescent imaging.

Fluorescent cell imaging

Immunostained cells were imaged using a fluorescent cell imager (ZOE, Bio-Rad) in the dark. During imaging, equal settings for gain, exposure, LED intensity and contrast were used for green and red channels. Merged images were generated in ImageJ (Fiji) by merging the blue, green and red channels for a given region of interest.

Viability assay

Viability was assayed using the ToxiLight™ assay. Adenylate kinase (AK) detection reagent was resuspended in 10mL of AK assay buffer per vial. At the time of use, AK detection reagent was left to equilibrate at room temperature.

10µL of THP-1 polarisation media was pipetted into flat bottom white 96-well assay plates in duplicate using a separate pipette tip for each sample. A control group was included which contained M0 macrophages seeded at 500,000 cells per mL that were lysed on day 6 of culture. The control group was lysed with ToxiLight™ 100% lysis reagent by pipetting 500µL of lysis reagent into 1mL of culture media in each well. The plate was left to incubate at room temperature for 30 minutes with repeated mixing by pipetting at 15 and 30 minutes.

50µL of AK detection reagent was pipetted into each well using a multichannel pipette. The plate was incubated at room temperature for 5 minutes and then the luminescence was read using a plate reader (Promega GloMax explorer). The data was exported to Microsoft Excel (Office 365). To estimate the percentage of dead cells in experimental groups the average magnitude of luminescence for each group was divided by the average magnitude of luminescence in the lysed control group. The percentage of dead cells was subtracted from 100 to estimate the percentage of viable cells for each condition.

Cryopreservation

THP-1 cells were centrifuged at 350g for 5 minutes and resuspended in THP-1 complete media for counting. Cells were counted using Trypan blue and an automated cell counter (Life technologies Countess II FL). An appropriate amount of freezing medium was prepared containing 10% DMSO and 90% FBS. THP-1 cells were centrifuged at 350g for 5 minutes and resuspended in freezing medium at 1,000,000 cells per mL. 1mL of cell suspension was pipetted into each cryogenic storage vial and all vials were placed into an insulated "Mr Frosty" box to allow the freezing process to take place at 1^{o}C per minute. The

insulated box was stored at -80^{o}C overnight. The next day each vial was transferred to -190^{o}C liquid nitrogen storage.

2.2.6 Additive manufacturing

Computer aided design (CAD)

3D objects were designed at www.Tinkercad.com and were exported as .STL files. Object files were sliced in Photon workshop 64 software (Anycubic) to generate .pwma files. Photon mono 4k was selected from the machine list. Slice parameters were set to 25µm z thickness, 5mm Z lift distance, 4mms^{-1} Z lift speed and 6mms^{-1} Z retract speed.

Digital light projection 3D printing

Photoinitiator solutions were prepared in 20mL scintillation vials covered in aluminium foil to protect from light. 0.5% w/v LAP, 10% w/v 575Da PEGDA, 0%, 2% or 5% w/v 3-sulfopropyl acrylate (SPAK), 0%-1% tartrazine and 0mg/mL, 2mg/mL or 10mg/mL lysozyme were dissolved into PBS as appropriate for each experimental condition. Printing was carried out on a Photon Mono 4k printer (Anycubic). Before and after each use the printer vat and platform were removed and cleaned with isopropanol.

In-vitro lysozyme release from 3D printed hydrogels

Lysozyme containing hydrogels were 3D printed, each immersed in 4mL PBS and incubated at 37^{o}C with well-plates sealed using laboratory tape. At each controlled release time point the entire volume of PBS was aspirated and replaced with fresh PBS to re-establish the diffusion gradient. For each hydrogel

the PBS at every time point was stored in a separate 7mL bijou at -20^{o}C until the time for analysis by Bradford assay (2.2.3 Bradford assay).

Brightfield microscopy

3D printed hydrogels were gently removed from the printing platform with a paint scraper. Hydrogels were gently dried with laboratory tissue to remove excess monomer and were then placed onto glass slides for microscopy. Hydrogel pores were viewed by Brightfield microscopy at 5X magnification and were imaged using an AmScope camera attachment (AmScope MU1403). To estimate pore diameter, 5 pores were imaged from 5 separate hydrogels for each condition. Pore diameter was measured in AmScope software. A known distance of 250 μm was also imaged and measured to establish a pixel to μm ratio. For each condition the length in pixels for each pore diameter was converted into μm.

Cryo-scanning electron microscopy (Cryo-SEM)

5% SPAK 10% PEGDA hydrogels were cut into small sections using a scalpel. The sections were then mounted onto an SEM specimen stub using stabilising glue (Tissue-Tek O.C.T Compound). The stub was then plunge frozen and transferred into the cryo-preparation chamber. The specimen was then fractured, sublimed at -90^{o}C for 30 minutes, and sputter coated with platinum using a current of 10 mA for 60 seconds. Imaging was performed at 10 kV under cryo conditions. Cryogenic scanning electron microscopy was performed on an FEI Quanta 200 3D (FEI, Hillsboro Oregon, USA) electron microscope equipped with a Quorum 3010 (Quorum Technologies, Loughton, UK) cryogenic stage and preparation stage.

2.2.7 Statistical analysis

All hydrogel characterisation and controlled release data is presented as mean ± standard deviation (SD) with each experimental condition tested in triplicate (n=3). All cell culture ELISA and viability data is presented as mean ± standard error of the mean (SEM) from two independent experiments which each contained three experimental repeats per condition (N=2, n=3). Statistical analysis was carried out in GraphPad PRISM 9.0. One-way ANOVA was performed to determine significant differences between experimental conditions when three or more were present on a column graph (α=0.05). Tukey's post hoc multiple comparisons test was performed for pair-wise comparisons. Student's t-test was used to determine significant differences between the mean of two experimental groups. Pairs with significant differences were labelled as ns $P>0.05$, * $P\leq0.05$, ** $P<0.01$, *** $P<0.001$ and **** $P<0.0001$. In instances with an excessive amount of pairwise comparisons, only the ones which were discussed were included in the figure.

Chapter 3 - Characterisation of protein release from photocrosslinkable affinity hydrogels

3.1 Introduction

The controlled delivery of biomacromolecules to localised biological systems is an attractive approach to modify disease by influencing cell behaviour due to the natural potency of growth factors and cytokines. The generation of implantable biomaterials which are capable of exhibiting controlled protein release has remained a challenging branch of the field for years. Commonly encountered issues are: burst release, in which the majority of the protein payload is rapidly released followed by little to no further release[281]. A phenomenon likely to lack efficacy due to the short time period of release and one which may also be cytotoxic due to cells being exposed to a supraphysiological dosage of protein. Incomplete release, occurring when a significant amount of the payload is entrapped within the material which may lead to drug dumping at the point of material degradation[283]. Protein denaturation occurs when its structural integrity is diminished, often leading to a lack of functionality and is caused by damaging environmental conditions[260,261,263]. Taken together, measures must be put in place to minimise burst release, avoid incomplete release and maintain the bioactivity of released proteins.

Affinity based approaches to improve protein release are modelled on the ability of heparins to sequester heparin binding proteins by electrostatic attraction[355]. The electrostatic attraction takes place between the negatively charged sulfate and carboxyl groups on heparins and the positive surface charge of heparin binding proteins as determined by their iso-electric point[309,310]. The sequestration by heparin increases the in-vivo half-life of heparin binding proteins which has led to the functionalisation of biomaterial surfaces with heparins being a previous strategy to approach controlled protein release in-vitro[356].

However, heparins do have multiple practical limitations such as batch to batch variability in high molecular weight heparin, high cost in the production of low molecular weight heparin, and the need for it to be harvested from animal tissue[315–318]. Heparins are also degraded in-vivo by heparinises and heparin containing hydrogels have previously been observed to be degraded by the same mechanism which would limit their capacity as a long term controlled release material[320]. To this end, so called "Heparin mimics" have been fabricated with the aim to utilise the positive attributes of heparins while circumventing their limitations[357–359].

A routinely administered anti-inflammatory therapy for osteoarthritis is the intra-articular injection of corticosteroids such as cortisone. Corticosteroid injections alleviate the symptoms of osteoarthritis for approximately 2 weeks[125,126]. Repeated intra-articular injections are painful for patients and can damage host tissue at the injection site[360]. An alternative anti-inflammatory therapy utilising controlled protein release would therefore be required to

exhibit controlled release for a period of multiple months to be a significant improvement over what is currently administered in the clinic.

Macrophages are cells of the innate immune system that are considered to be a main orchestrator of immune cell signalling during inflammation. Macrophages exist on a polarisation spectrum in which M1 promotes pro-inflammatory signalling and M2 promotes anti-inflammatory signalling[44]. Macrophages become polarised in response to environmental stimuli and M2 polarisation has historically been subdivided into M2a, M2b, M2c, and M2d based on the stimulus used[203]. In the pathobiology of osteoarthritis, pro-inflammatory signalling is a key driver of disease progression and is the product of an M1:M2 macrophage imbalance that favours M1[45,361]. A therapeutic approach that aims to prevent osteoarthritis progression using controlled protein release should therefore use cytokines that promote the anti-inflammatory M2a polarisation using either Interleukin-4 (IL-4) or Interleukin-13 (IL-13), or promote immune suppressive M2c function using Transforming growth factor beta 1 (TGF-β1) or Interleukin-10 (IL-10)[204,205,217].

This chapter aims to investigate protein release from Poly (ethylene glycol) diacrylate (PEGDA) hydrogels containing acrylate monomers with charged chemical groups in order to elicit electrostatic attraction to proteins similarly to heparin, with the goal of achieving controlled release. Ideally, controlled release of the anti-inflammatory cytokines associated with M2 macrophage polarisation will be observed for a period of multiple months in order to show potential benefit over currently administered injectable corticosteroids that have approximately 2 weeks efficacy.

Acrylate monomers typically have low cost and may be easily integrated into PEGDA hydrogels during ultraviolet (UV) photocrosslinking[287]. Acrylate monomers are often 3D printable which would allow the possible large scale manufacturing of protein release products in the future. The fine control over hydrogel architecture by additive manufacturing has been previously explored as a controlled drug release parameter in small molecule drug release from tablets[345], an approach which has not been significantly explored in controlled protein release but may be a valuable tool for future applications.

3.2 Chapter specific Methods

Detailed materials and methods can be found in Chapter 2. Chapter specific methods are briefly outlined below for convenience with experimental design schematics where appropriate.

3.2.1 Hydrogel UV photocrosslinking

As described (2.2.1 UV photocrosslinking). Briefly, hydrogel precursor solutions were prepared in Phosphate buffered saline (PBS) while protected from light. Hydrogels were formed by 10 minutes 365nm UV light exposure under argon with oxygen concentration below 2000ppm. 500µL hydrogels were cast in 15x15mm square Poly (tetrafluoro ethylene) (PTFE) moulds and 100µL hydrogels were formed as droplets on a flat piece of PTFE.

3.2.2 In-vitro hydrogel swelling

As described (2.2.1 In-vitro hydrogel swelling). Briefly, hydrogels were immersed in PBS and weighed multiple times over a 5 day period. The swollen

weight was expressed as a percentage increase from the initial hydrogel weight after UV photocrosslinking.

3.2.3 Hydrogel compressive testing

As described (2.2.1 hydrogel compressive testing). Briefly, compressive modulus was characterised by compressing swollen hydrogels using a texture analyser with a 5kg load cell. The compressive modulus was calculated as the gradient of the linear section from the stress-strain curve.

3.2.4 In-vitro protein release (direct loading method)

As described (2.2.2 Direct loading method). A schematic of the experimental design has been included for convenience (Figure 3.1). Briefly, the protein of interest was dissolved into the hydrogel precursor solution as the final ingredient. Following UV photocrosslinking, hydrogels were immersed in PBS for in-vitro protein release experiments. At each time point the PBS was completely aspirated and an equal volume of fresh PBS was applied to each gel. PBS collected from each time point was stored at -20^{o}C until the appropriate time for analysis by Bradford assay for lysozyme and BSA, or ELISA for TGF-β1 and IL-4.

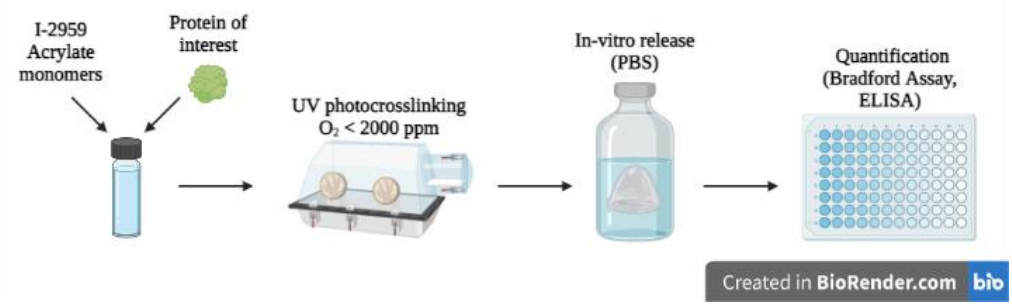

Figure 3.1: Schematic of direct loading protein release method. The protein of interest was dissolved into the photoinitiator solution. Hydrogels were cast

under argon and immersed in PBS for in-vitro protein release. Controlled release samples were quantified using Bradford assay or ELISA as appropriate. Image created at www.BioRender.com

3.2.5 In-vitro protein release (core-shell method)

As described (2.2.2 core-shell method). A schematic of the loading method has been included for convenience (Figure 3.2). Briefly, custom PTFE moulds were used to position a 3% gelatin hydrogel loaded with TGF-β1 in between two layers of 10% 4kDa PEGDA. Core-shell gels were then immersed in PBS for in-vitro TGF- β1 release.

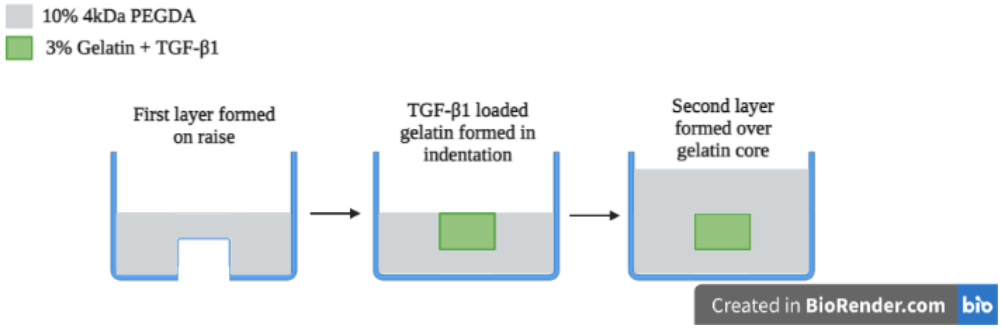

Figure 3.2: Schematic of core-shell protein loading method. A 20µL core hydrogel was used that contained 3% gelatin and a matched TGF- β1 dosage to the initial experiment using 10µg/mL TGF- β1 from 10% 4kDa PEGDA. The core was placed in between two 400µL layers of 10% 4kDa PEGDA. Image created at www.BioRender.com

3.2.6 Bradford assay

As described (2.2.3 Bradford assay). Briefly, standards of the protein of interest were prepared in PBS from 25µg/mL to 1.25µg/mL. Controlled release samples were thawed at 37°C and Bradford reagent was left to equilibrate to room

temperature. In a 96-well plate, 150µL of either standard or sample was mixed with 150µL of Bradford reagent. After 10 minutes incubation at room temperature the absorbance at 595nm was read using a plate reader. A standard curve was used to calculate the dosage of protein released at each time point. Each standard curve assayed standards in triplicate and each experimental repeat was assayed in duplicate.

3.2.7 Enzyme linked immunosorbent assay (ELISA)

TGF-β1 ELISA was carried out as described (2.2.3 TGF-β1 in-vitro release), IL-4 ELISA was carried out as described (2.2.5 THP-1 secreted cytokines, IL-4 controlled release). Each standard was assayed in triplicate and each experimental repeat was assayed in duplicate.

3.2.8 Lysozyme bioactivity assay

As described (2.2.4 lysozyme bioactivity assay). 100µL of controlled release sample was added to 1.5mL of Micrococcus lysodeikticus and mixed by inversion. The decrease in absorbance at 450nm was measured once per minute for 5 minutes using a UV-Vis spectrophotometer. For each sample, a control was run simultaneously which was prepared from stock lysozyme with a matched concentration. The decrease in absorbance of controlled release samples was expressed as a percentage of the decrease in absorbance measured in its matched control.

3.2.9 Statistical analysis

All numerical data is presented as mean ± standard deviation from 3 repeats per experimental condition. When quantifying protein release from hydrogels the Limit of detection (LOD) and Limit of quantification (LOQ) were calculated as

3 and 10 standard deviations above the average blank standard respectably[352,354]. One-way ANOVA with Tukey's post hoc multiple comparisons test (α=0.05) was used to determine significant differences between experimental groups where three or more are present on a column graph. Student's t-test was used to determine significant differences between the means of two groups of data. Pairs with significant differences were labelled as * $P \leq 0.05$, ** $P < 0.01$, *** $P < 0.001$ and **** $P < 0.0001$.

3.3 Results

3.3.1 Swelling and compressive characterisation of PEGDA hydrogels containing 3-sulfopropyl acrylate

500µL hydrogels were cast in 15mm x 15mm PTFE moulds using UV photocrosslinking containing 10% w/v 575Da PEGDA and 0%, 5%, 10%, and 15% w/v 3-sulfopropyl acrylate (SPAK, 232.3Da). SPAK was selected as a negatively charged acrylate to electrostatically attract the candidate proteins of interest for M2 macrophage polarisation IL-4, IL-10 and TGF- β1 which have iso-electric points of 9.2[336], 8.3[362] and 9.51[363] respectively.

The in-vitro swelling behaviour of SPAK containing PEGDA hydrogels was investigated over 5 days and showed approximately a dose dependent increase of hydrogel weight increase with increasing SPAK concentration Figure (3.3 A). The increase in water absorption is likely due to the negatively charged SO_3^- groups attracting bipolar water molecules. 0% SPAK 10% PEGDA showed a decrease in hydrogel weight at all swelling time points after initial weighing (Figure 3.3 A). The decrease in hydrogel weight seen in 0% SPAK 10% PEGDA is likely indicative of residual PEGDA monomer diffusing out of the gel.

Compressive testing on swollen hydrogels showed all groups to have a modulus in the low kPa range with a general increasing trend as SPAK concentration increased. A significantly higher modulus was measured at 15% SPAK 10% PEGDA compared to 0% SPAK 10% PEGDA when analysed with 1 way ANOVA with Tukey's post hoc multiple comparisons test (Figure 3.3 B). The increasing trend seen with increasing SPAK concentration is likely due to increasing overall hydrogel concentration.

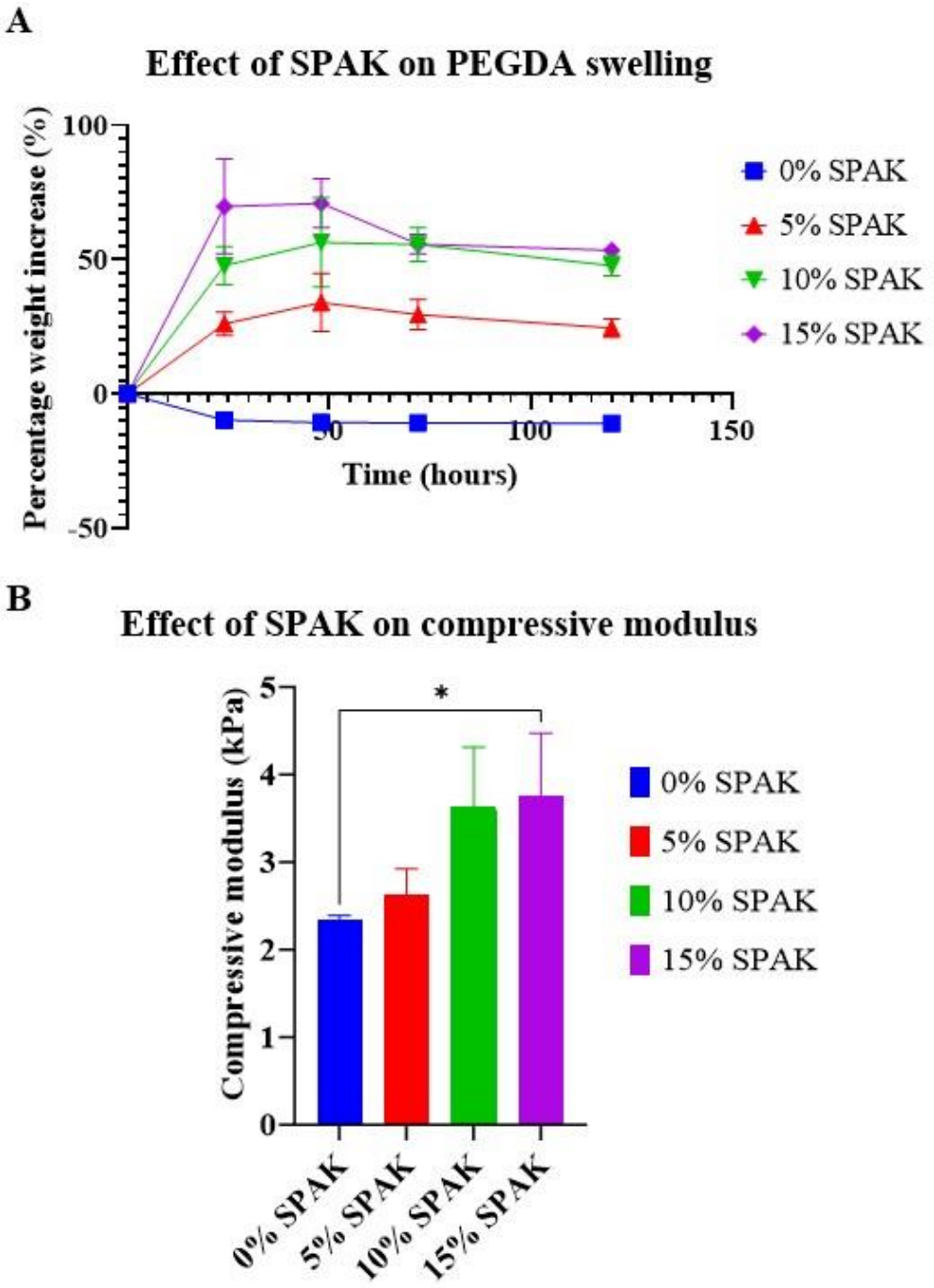

Figure 3.3: Swelling and compressive characterisation of SPAK PEGDA hydrogels cast by UV photocrosslinking. A) 5 day in-vitro swelling of 10% 575Da PEGDA hydrogels containing 0-15% SPAK. B) Compressive modulus of 10% 575Da PEGDA hydrogels containing 0-15% SPAK. Values presented as mean ± standard deviation (n=3). * denotes a statistical difference with

$P \leq 0.05$ determined by 1 way ANOVA with Tukey's post hoc multiple comparisons.

3.3.2 Characterisation of lysozyme release from cast SPAK PEGDA hydrogels

Initial protein release experiments used lysozyme from chicken egg whites as a low cost model protein. Lysozyme was chosen because its iso-electric point of 11.35[364,365] means it has a net positive charge at neutral pH and would be electrostatically attracted to SPAK to model the estimated interaction of SPAK with the M2 promoting cytokines IL-4, IL-10 and TGF- β1. Lysozyme was also chosen because its molecular weight of 14-15kDa[364] is similar to that of the aforementioned M2 promoting cytokines which are 15kDa, 18kDa and 13kDa respectively[366–368].

10mg/mL lysozyme was dissolved into hydrogel precursor solutions containing 10% w/v 575Da PEGDA and 0%, 5%, 10% and 15% w/v SPAK. 500µL hydrogels were cast using UV photocrosslinking and hydrogels were each immersed in PBS for a 70 day in-vitro protein release study. During analysis, seven standard curves for the Bradford assay were averaged to generate a master standard cure (Supplementary Figure S.1 Appendix 1) with a calculated LOD and LOQ of 1.46µg/mL and 4.94µg/mL respectively. Cumulative lysozyme release (Figure 3.4 A, B) and the lysozyme concentration released at each time point (Figure 3.4 C) were considered.

0% SPAK 10% PEGDA exhibited rapid burst release with a measured percentage release of 100% after 3 days and 110% after 13 days (Figure 3.4 A blue line). The first 7 days of time points were diluted to fit the assay concentration range (Figure 3.4 C blue line). There was then a plateau until day

70 at in which the majority of time points were below the LOD with a final percentage release at 111% (Figure 3.4 A, C blue lines). The cumulative release reaching over 100% may be explained by the total loading dosage being an estimate based off the hydrogel volume, and that the first 7 days of time points had to be diluted for quantification by Bradford assay.

The addition of SPAK had a potent effect in reducing the burst release of lysozyme from 10% PEGDA and groups 5%, 10% and 15% SPAK showed a dose dependent decrease in the release rate of lysozyme which demonstrates control over lysozyme release rate using electrostatic affinity (Figure 3.4 A red, green and purple lines).

5% SPAK 10% PEGDA had an approximately zero order release trend for the first 31 days followed by a slight decrease in release rate until day 70 at which 31% of lysozyme had been released (Figure 3.4 B red line). The lysozyme concentration released was below LOQ until day 2 of release and was then above LOQ at every time point until day 64, after which it fell slightly below LOQ until day 70 (Figure 3.4 C red line).

10% SPAK 10% PEGDA had a linear release trend reaching 14% release at day 70. The released lysozyme concentration was below LOQ until day 13 and was then above LOQ until day 28. After this time point the released concentration was between LOD and LOQ until day 70 (Figure 3.4 C green line).

Lysozyme release from 15% SPAK 10% PEGDA was below LOD until day 13, followed by an increased release rate that reached 5% release at day 70 (Figure 3.4 B purple line) with remaining time points having concentrations between LOD and LOQ (Figure 3.4 C purple line).

A control group containing 15% SPAK 10% PEGDA with no lysozyme loading was included. This group had no response above the LOD at any time point which demonstrates no cross reactivity of any species such as residual monomer or hydrogel degradation products with the Bradford assay (Figure 3.4 A, B, C orange line).

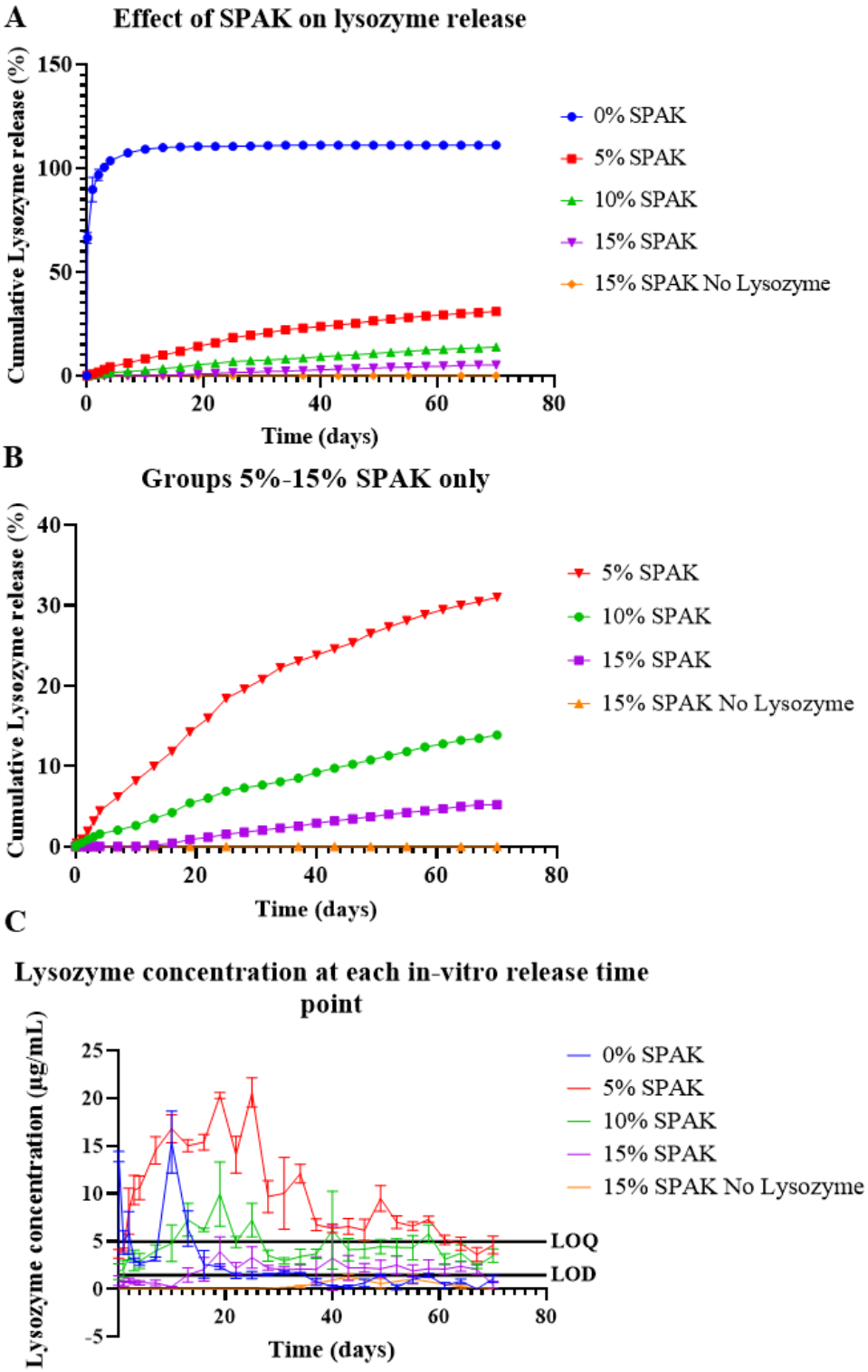

Figure 3.4: Lysozyme release from SPAK PEGDA affinity hydrogels. A) Effect of SPAK on lysozyme release from 500µL, 10% 575Da PEGDA hydrogels loaded with 10mg/mL lysozyme. B) Effect of SPAK on lysozyme release showing only 5-15% SPAK experimental groups. C) Concentration of

lysozyme at each in-vitro release time point. Lysozyme was quantified using Bradford assay, the first 7 time points from 0% SPAK 10% PEGDA were diluted to fit the assay range. Values presented as mean ± standard deviation, where error bars cannot be seen they are smaller than the marker at each plotted point (N=2, n=3).

3.3.3 Investigating the bioactivity of lysozyme released from SPAK PEGDA hydrogels

The bioactivity of lysozyme released from 5% SPAK 10% PEGDA was measured at days 2, 10, 31 and 61 of release and showed a reduction in comparison to controls across all groups with approximately 37% bioactivity at day 2 and between 52-62% for days 10, 31 and 61 (Figure 3.5 A). To investigate the effect of UV exposure on lysozyme bioactivity, the bioactivity of a 10μg/mL sample that had been exposed to 365nm UV for 10 minutes was compared to a 10μg/mL control sample. The bioactivity of the UV irradiated sample was found to be 96 ± 1.52% of the 10μg/mL control sample (Figure 3.5 B). A 2 tailed, unpaired Student's t-test found there to be no statistical difference between the mean bioactivity of UV irradiated lysozyme and the 10μg/mL control (P=0.3817). This result suggests that the UV dosage used in the experimental design of this experiment was not the main reason for reduced bioactivity.

The reduced bioactivity of lysozyme released from 5% SPAK 10% PEGDA at days 2, 10, 31 and 61 (Figure 3.5 A) indicates that protein structure is damaged during the UV photocrosslinking reaction. Interestingly, the bioactivity did not decrease further at the later time points tested (days 31 and 61). The electrostatic sequestration of lysozyme by SPAK may be the reason why bioactivity is

maintained at an estimated 55%, 57% and 56% at days 10, 31 and 61 respectively, with no deterioration at later time points. The reduction in bioactivity in comparison to stock lysozyme may be due to free radicals produced from UV activation of Irgacure-2959. Free radicals have previously been reported to damage biologics including proteins. This effect may be reduced in future experiments by using an alternative photoinitiator, by reducing photoinitiator concentration, or by modifying the protein loading method.

A

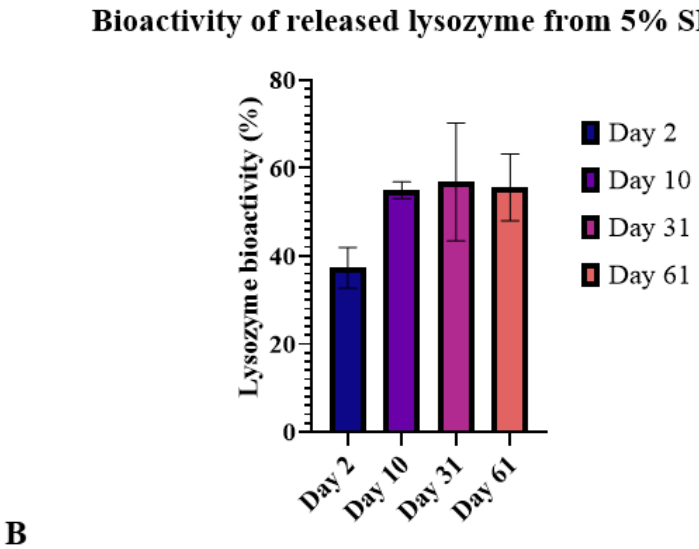

B

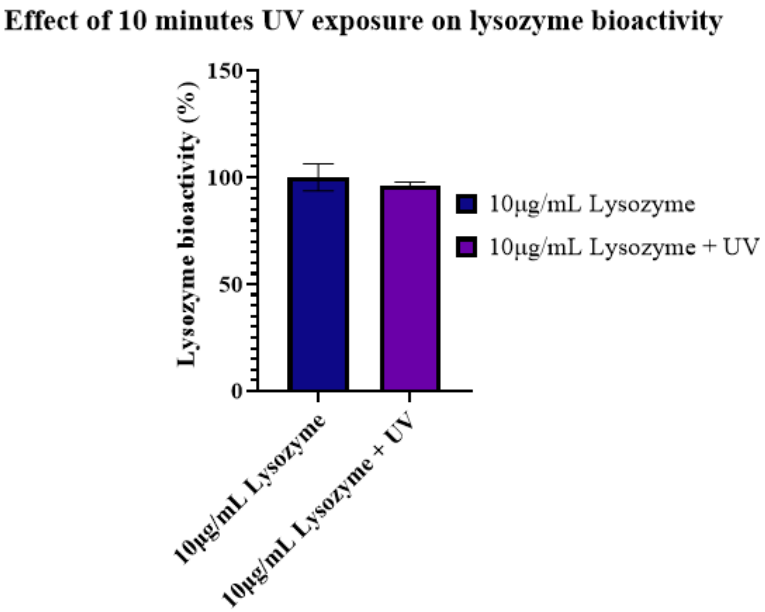

Figure 3.5: Bioactivity of lysozyme released from 5% SPAK 10% PEGDA. A) Calculated bioactivity of lysozyme released from 5% SPAK 10% PEGDA at 4 time points during a 70 day controlled release experiment. At each time point tested the bioactivity was compared to a stock solution of lysozyme with a matched concentration to what was quantified in the controlled release time point by Bradford assay. B) Bioactivity of 10µg/mL lysozyme after exposure to 365nm UV light for 10 minutes in comparison to a stock 10µg/mL lysozyme solution. Values presented as mean ± standard deviation (N=3, n=3).

3.3.4 Investigating protein loading and mesh size parameters

Following the initial characterisation of lysozyme release from SPAK PEGDA hydrogels loaded with 10mg/mL lysozyme, experimental parameters pertaining to protein loading conditions and PEGDA mesh size were investigated.

To investigate protein loading parameters, protein loading concentration was decreased from 10mg/mL to 1mg/mL. 500µL hydrogels were cast containing 10% 575Da PEGDA with 1mg/mL lysozyme or 1mg/mL bovine serum albumin (BSA). In-vitro protein release was compared between the two proteins in a 10 day study. It was observed that after 10 days the lysozyme group had reached approximately 50% cumulative release and the BSA group had reached a plateau at 9% (Figure 3.6 A). The low cumulative release of BSA is likely due to its large molecular weight of 66kDa[369] in comparison the considerably smaller lysozyme which is 15kDa[364]. The larger protein size would be expected to hinder its diffusion through the PEGDA polymer mesh.

PEGDA mesh size was previously reported to be dependent on the molecular weight of the PEGDA macromer in which larger molecular weights produce a larger mesh to enable increased protein diffusion[296]. In effort to increase lysozyme cumulative release, PEGDA molecular weight was increased to from 575Da to 4kDa to increase polymer mesh size. Cumulative release from 10% 4kDa PEGDA hydrogels increased to approximately 100% after 10 days (Figure 3.6 B).

PEGDA mesh size is also reported to be dependent on concentration[295]. To further investigate mesh size parameters, a 5% 4kDa PEGDA group was

included which showed increased percentage release at each time point and reached an estimated 100% cumulative release at day 6 (Figure 3.6 C).

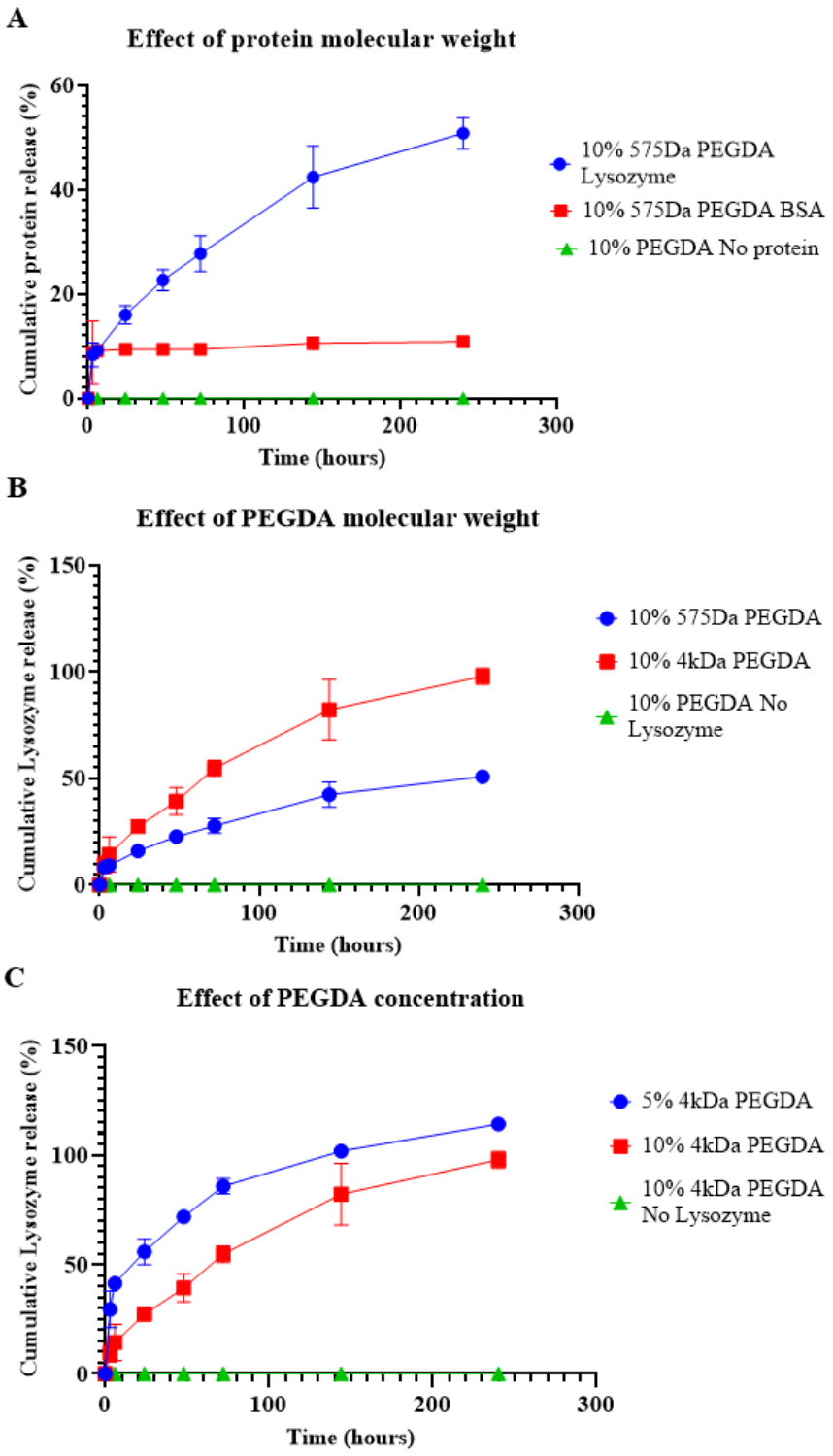

Figure 3.6: Characterisation of protein release parameters pertaining to mesh size. 500µL hydrogels were loaded with 1mg/mL of the protein of

interest. A) Comparison of BSA and lysozyme release from PEGDA. B) Effect of PEGDA molecular weight on lysozyme release rate. C) Effect of PEGDA concentration on lysozyme release rate from 4kDa PEGDA. Values presented as mean ± standard deviation (N=2, n=3).

3.3.5 TGF-β1 release from 10% 4kDa PEGDA hydrogels

The method was adapted in attempt to release the M2 promoting anti-inflammatory cytokine TGF-β1. To conserve experimental costs when using TGF-β1 cytokine, hydrogel volume was decreased from 500µL to 100µL. A TGF-β1 loading concentration of 10µg/mL was chosen with the intention of releasing TGF-β1 in the ng/mL concentration range that is relevant for biological growth factor action. The molecular weight of PEGDA selected was 4kDa because of its observed improvement seen in lysozyme release (Figure 3.6 B).

100µL hydrogels were cast by UV photocrosslinking containing 10% 4kDa PEGDA with 10µg/mL TGF-β1 and a 5 day in-vitro protein release experiment was carried out in PBS. The TGF-β1 concentration at each time point was quantified using ELISA. After 5 days the cumulative release of TGF-β1 was less than 0.1% (Figure 3.7 A) and at day 5 the TGF-β1 concentration released became lower than the calculated LOQ of 12.5pg/mL (Figure 3.7 B). This result suggested that the majority of loaded TGF-β1 is entrapped within 10% PEGDA and is unable to be released by diffusion after 5 days.

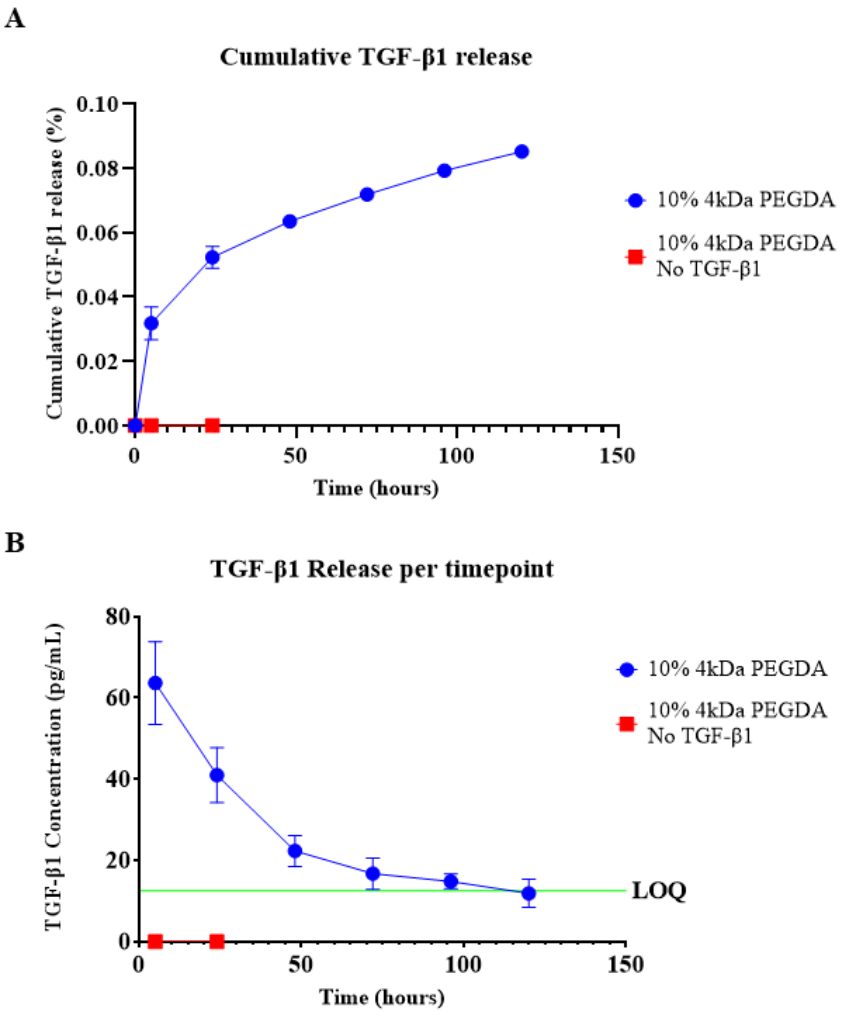

Figure 3.7: TGF-β1 release from 10% 4kDa PEGDA hydrogels. Hydrogel volumes were 100µL and were loaded with 10µg/mL TGF-β1. A) Cumulative release of TGF-β1. B) TGF-β1 concentration released at each time point. Values presented as mean ± standard deviation (N=2, n=3).

3.3.6 Optimisation of TGF-β1release parameters

In attempt to improve TGF-β1 release, experimental parameters were modified. The data from lysozyme release experiments (Figures 3.4 and 3.6) was used to aid decision making for the optimisation of TGF-β1 release parameters. Due to the increase in PEGDA molecular weight from 575Da to 4kDa improving lysozyme cumulative release (Figure 3.6 B), the molecular weight of PEGDA

was further increased in TGF-β1 release experiments in effort to improve cumulative release.

PEGDA molecular weight was increased from 4kDa to 6kDa, and then to 20kDa to increase polymer mesh size. For 20kDa hydrogels the volume of PBS release buffer was increased to 30mL to accommodate the large in-vitro swelling exhibited by the hydrogels (Supplementary Figure S.2, Appendix 1). Increasing PEGDA molecular weight improved TGF-β1 cumulative release but the release from 6kDa PEGDA only reached 1.5% after 5 days and 20kDa PEGDA plateaued at 8.5% after 9 days (Figure 3.8 A). This indicated that parameters other than mesh size needed to be considered in order to optimise TGF-β1 cumulative release enough for biological applications or for SPAK to be reintroduced.

In sections 3.3.2 and 3.3.4, the cumulative lysozyme release exhibited from 10% 575Da PEGDA had greater percentage release when loaded with 10mg/mL lysozyme in comparison to 1mg/mL lysozyme (Figure 3.4 A 0% SPAK, and Figure 3.6 A lysozyme). This showed that protein loading concentration considerably influenced release rate. With this previous result considered, TGF-β1 loading concentration was increased from 10μg/mL to 50μg/mL and the in-vitro release was compared. Cumulative release of TGF-β1 was increased at every time point but after 13 days the total percentage release was still less than 2% (Figure 3.8 B). The increased TGF-β1 release rate in relation to protein loading dosage is consistent with lysozyme data but the lower overall percentage release suggests that a dosage of TGF-β1 remains entrapped within the hydrogel and this phenomenon is particularly noticeable at lower loading concentrations because it represents a larger proportion of the total loading dose.

To investigate if low percentage release was specific to TGF-β1, 10% 4kDa PEGDA hydrogels were loaded with 50μg/mL IL-4 and the percentage release was compared over 5 days. IL-4 percentage release was greater than TGF-β1 at every time point but after 5 days the cumulative release was still less than 1% (Figure 3.8 C). This suggests that the low percentage release observed at 50μg/mL cytokine loading is not specific to TGF-β1.

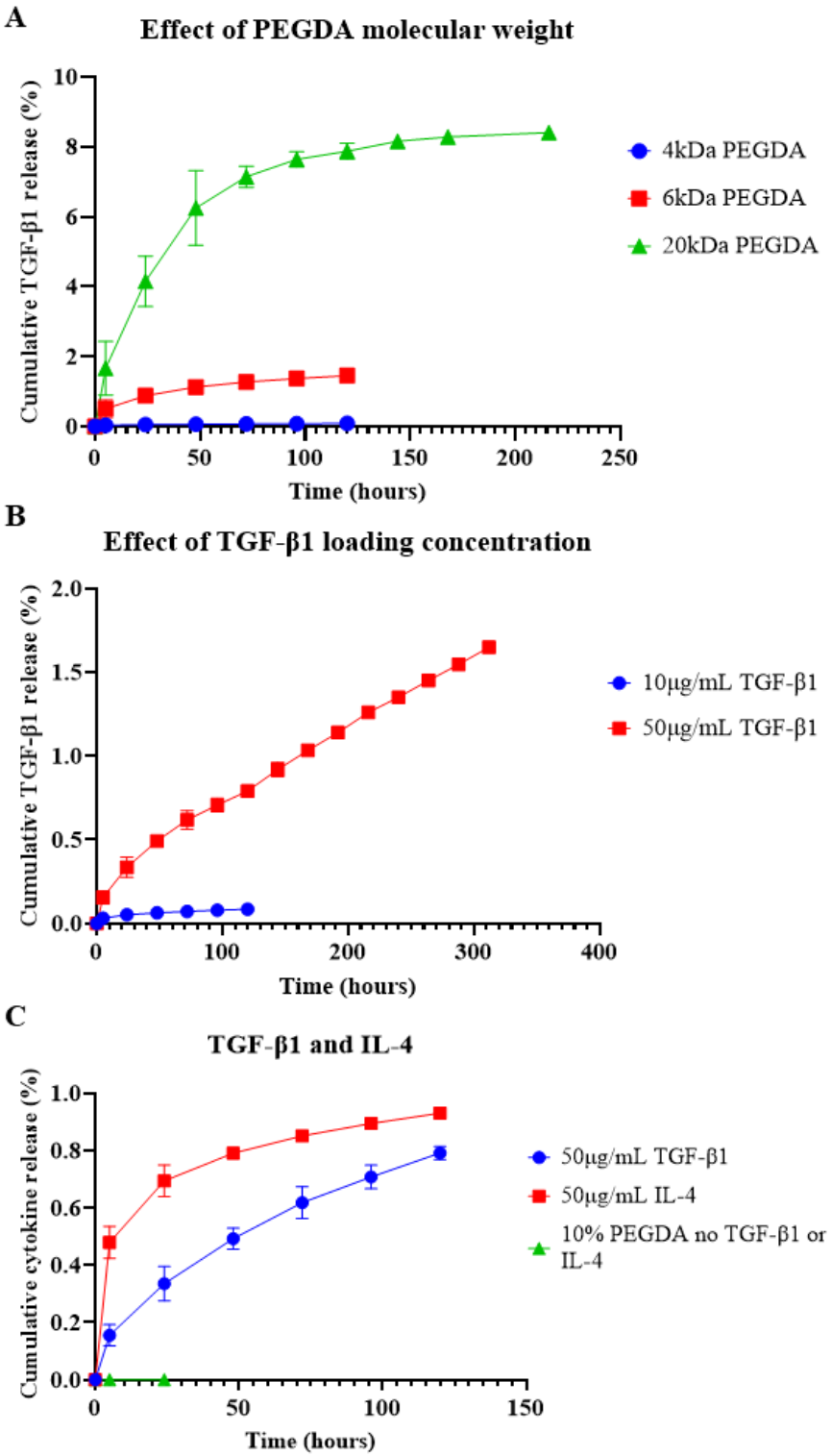

Figure 3.8: Modification of TGF-β1 release parameters to improve percentage release. A) Increasing PEGDA molecular weight. B) Increasing TGF-β1 loading concentration. C) Comparison of TGF-β1 and IL-4 loaded with

equal concentrations in 10% 4kDa PEGDA. Values presented as mean ± standard deviation (N=2, n=3).

3.3.7 Trouble shooting low TGF-β1 cumulative release from 10% 4kDa PEGDA

A series of trouble shooting experiments were carried out to determine the cause of low TGF-β1 cumulative release from PEGDA.

To determine if low TGF-β1 cumulative release was due to inaccurate loading, the 100µg/mL stock solution used for in-vitro release experiments was diluted to 1ng/mL using a 3 step serial dilution. Standards with concentrations matching the ELISA kit standards were then prepared from the 1ng/mL solution by serial dilution. TGF-β1 standards diluted from the stock were then assayed on the same plate as the ELISA kit standards and the standard curves were compared. The standard curve generated from the stock derived solution had approximately half the ELISA response compared to the curve generated using standards supplied with the kit (Figure 3.9 A). The gradient of the two curves were approximately the same when viewed by eye (Figure 3.9 A). The discrepancy in ELISA absorbance values between the stock standards and the kit standards is likely due to the large dilution factor required to dilute the 100µg/mL stock TGF-β1 solution down to 1ng/mL to fit the assay range.

To investigate whether UV photocrosslinking conditions were decreasing the quantification of TGF-β1 by ELISA, a set of TGF-β1 standards was exposed to 365nm UV light for 10 minutes and its standard curve was compared to normal standards. A second experimental condition was included with TGF-β1 standards which contained 0.5% w/v Irgacure-2959 (I2959) that were also

exposed to 365nm UV for 10 minutes. Following UV irradiation, standards containing I2959 had a noticeable colour change from transparent to white, which was not observed in other conditions (Figure 3.9 B). At the final stage of ELISA, no colour change was observed in photoinitiator containing standards (Figure 3.9 C iii). Standard curves from the control group and UV irradiated standards were approximately the same, but absorbance values from the photoinitiator containing group were all below the LOD (Figure 3.9 D). This result indicates that TGF-β1 is denatured by the free radicals from the activated photoinitiator, and the change in its structure renders it unquantified by ELISA. This would occur if the epitope recognised by ELISA capture antibodies is covered by the change in TGF-β1 structure. The white colour change observed in photoinitiator containing standards may be indicative of aggregates formed by photocrosslinking between proteins. This possibility was considered further in the discussion section of this chapter (3.4 Discussion). Following this result, the experimental approach was then modified to reduce protein exposure to photoinitiator.

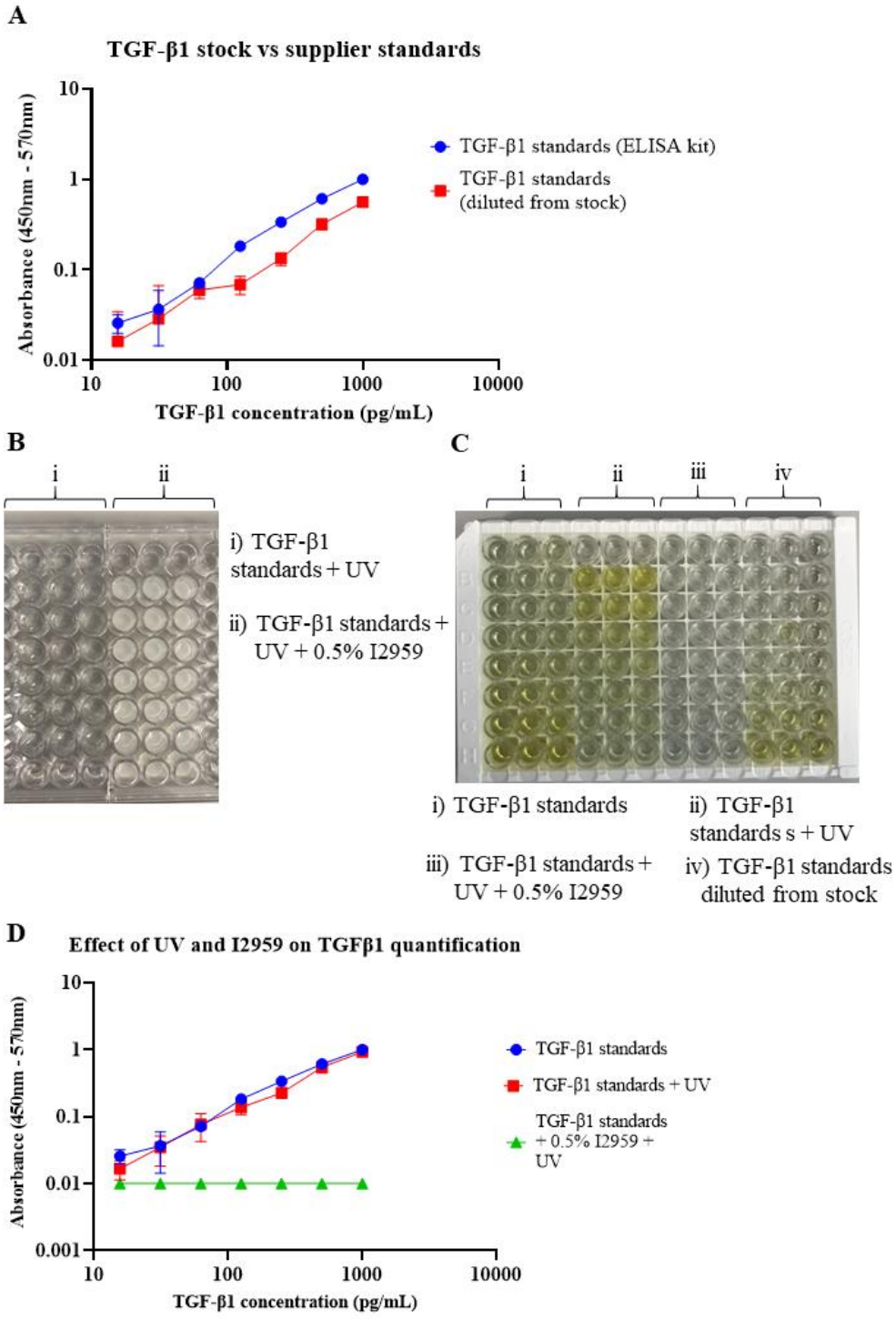

Figure 3.9: Troubleshooting low TGF-β1 percentage release. A) Comparison of ELISA detection of kit standards with standards diluted from the TGF-β1 stock solution used for in-vitro release. B) Visible colour change of UV irradiated TGF-β1 standards containing 0.5% w/v Irgacure-2959 (I2959). C) No visible colour change in UV irradiated I2959 containing standards at the

final stage of ELISA detection. In rows B-H, standards were input from low-to-high in Ci and high-to-low in Cii. D) UV irradiated I2959 containing standards were all below the ELISA LOD. Values presented as mean ± standard deviation (n=3).

3.3.8 Generation of core-shell PEGDA-Gelatin hydrogels for TGF-β1 release

After observing diminished TGF-β1 ELISA quantification in the presence of activated photoinitiator, the protein loading method was modified to separate TGF-β1 from Irgacure-2959 using a core-shell hydrogel in which TGF-β1 was loaded into a gelatin core that is surrounded by a 10% 4kDa PEGDA shell. A schematic of the core-shell fabrication concept is included for convenience in the methods section of this chapter (Figure 3.2 section 3.2.5).

1μg of TGF-β1 was loaded into a 3% gelatin core to give an equal total dosage to the initial TGF-β1 in-vitro release experiment using (Figure 3.7). The gelatin core was encapsulated between two sheets of 10% 4kDa PEGDA using custom made PTFE moulds with a raised 5x5x1mm square at the base of each 15x15mm square mould (Figure 3.10 A).

Following fabrication, the 20μL gelatin core was visible within the hydrogel and the thickness of core-shell hydrogels was approximately 5mm (Figure 3.10 B). A TGF-β1 release in-vitro experiment was performed for 5 days using core-shell hydrogels, no detectable TGF-β1 was released at any time point (Figure 3.10 C). The 5mm total thickness of the hydrogel is likely the reason for no TGF-β1 release. The large distance between the gelatin core and the periphery of the PEGDA shell means TGF-β1 is more likely to be entrapped by

mechanisms such as intermolecular forces of attraction between the PEGDA network and TGF-β1[339].

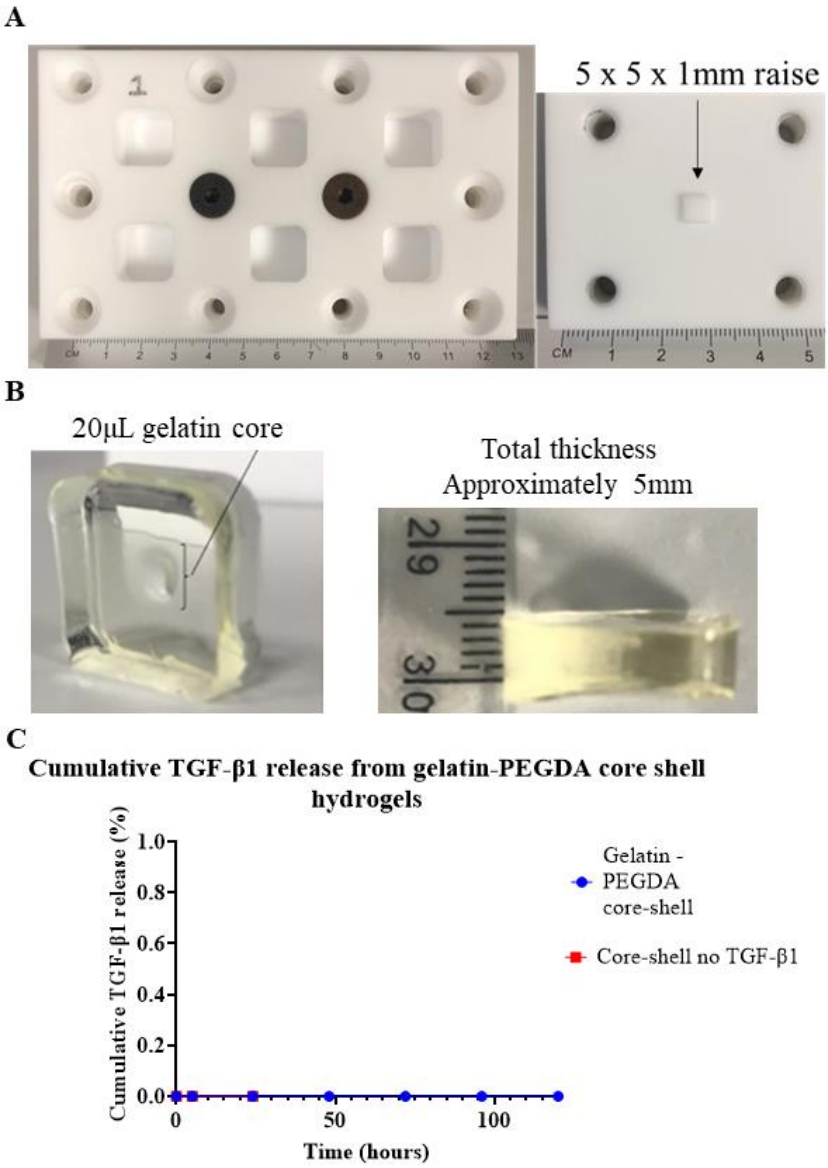

Figure 3.10: TGF-β1 release from core-shell gelatin-PEGDA hydrogels. A) Custom made PTFE moulds were used to generate core-shell hydrogels. A schematic of the core-shell fabrication method is included in section 3.2.5 B) Macroscopic images of core-shell hydrogels from front and side view. C) Cumulative TGF-β1 release from core-shell hydrogels. Values presented as mean ± standard deviation (N=2, n=3).

3.4 Discussion

The aims of this chapter were to generate affinity hydrogels for the purpose of controlled protein release that were synthetic, low cost and had a high manufacturing capacity. A clinical application for controlled protein release from biomaterials is immunomodulation in osteoarthritis by the promotion of M2 macrophage polarisation to reduce the inflammation associated with disease progression. With this in mind, a controlled release period of multiple months was assigned as a goal in order to be clinically relevant in comparison to clinically administered anti-inflammatory drug therapies that have an efficacy period of multiple weeks.

Within this study, lysozyme was selected as a model protein based on its iso-electric point and molecular weight. The initial characterisation of lysozyme release from 5% SPAK 10% PEGDA hydrogels saw a linear release trend for 70 days (Figure 3.4 A, B, C). This controlled release data has superior controlled release period and release trend to previous affinity based methods using heparin functionalised materials and sulfated alginate hydrogels which report protein release for days to weeks range[312–314,322,323,356,370].

The 70 day controlled protein release is comparable to reports with the longest periods of sustained release. Such reports have used controlled material degradation and have and have been limited by often not presented bioactivity data and have often not considered how simple biodegradation in simple in-vitro conditions may be translatable to complex in-vivo conditions [298–300].

Taken together, the lysozyme release data has shown promising potential for SPAK PEGDA hydrogels as an affinity protein release material. The data set in

this chapter may be further improved with the optimisation of experimental parameters. The 56% bioactivity of lysozyme released after 61 days could be increased by optimising photocrosslinking conditions including photoinitiator type, concentration, and UV photocrosslinking time (Figure 3.5 A). Increasing PEGDA molecular weight from 575Da may allow a higher percentage release to be achieved before plateau (Figure 3.4 A, B).

Compressive testing showed the modulus of SPAK PEGDA hydrogels to all be in the low kPa range (Figure 3.3 B) which is within reported range for PEGDA hydrogels[371]. Material stiffness in the kPa range is much lower than the MPa range reported in osteochondral tissue[372]. This difference must be considered if future studies intend to administer controlled release hydrogels as scaffolds into osteoarthritic defect sites. Future studies that use SPAK PEGDA hydrogels for tissue engineering purposes may use a stiffer scaffold as a supporting material for the hydrogel such as a 3D printed polycaprolactone lattice to generate a composite biomaterial with a more in-keeping modulus to surrounding osteochondral tissue.

A limitation of this experimental design is that released lysozyme was in the μg/mL range which is an order of magnitude above the therapeutic concentration of most cytokines and growth factors that are typically in the low ng/mL range. The release of protein far above the therapeutic dose into biological systems is expected to cause undesirable effects such as cytotoxicity and has previously caused ectopic bone formation when an uncontrolled release of BMP-2 occurred in clinical trials for intervertebral disc implants[373].

A second limitation is that lysozyme was used as a model protein instead of an actual M2 associated cytokine. Lysozyme has the benefit of being a low cost protein with a molecular weight and iso-electric point that is reasonably close to IL-4, IL-10, and TGF- β1 but its iso-electric point of 11.35 is still the highest out of the group which means the controlled release effect of SPAK may not be as potent when using an actual M2 promoting cytokine. To load hydrogels with an equal dosage of any of the three aforementioned cytokines to what was used in this experiment would cost thousands British sterling per gel which makes direct comparison using the same parameters logistically challenging.

Finally, the 500μL hydrogel volume used in this experiment is larger than what would be expected in a biomaterial that is implanted into a synovial joint. The implantation of a 500μL hydrogel into the knee joint would require invasive surgery and an early osteoarthritic controlled release therapy would need to be smaller and ideally injectable for minimal invasiveness.

The identified limitations were the rationale for scaling down protein loading concentration to 10μg/mL and hydrogel volume to 100μL for subsequent TGF-β1 release experiments. Following initial experimentation with lysozyme it was assumed that the primary mechanism for protein release was based on electrostatic charge and that with decreased protein loading concentration the release behaviour would remain similar from uncharged PEGDA hydrogels. It was therefore unexpected to see the extremely low percentage release of TGF-β1 from 10% 4kDa PEGDA (Figure 3.7 A). This finding highlights the difficulty and in extrapolating data collected from systems using cost effective model proteins to systems using low concentrations of biologically relevant cytokines and growth factors.

With previous literature on protein diffusion from polymers often focusing on the relationship between protein size and the mesh size of the network as the main factor governing release, this phenomenon was explored in this chapter when characterising lysozyme release parameters and when attempting to improve TGF-β1 release. Indeed, BSA appeared to be entrapped in 10% 575Da PEGDA with 10% release at the first time point followed by a plateau for 10 days whereas the smaller lysozyme showed 50% cumulative release over 10 days (Figure 3.6 A). Similarly, increasing PEGDA molecular weight from 575Da to 4kDa improved lysozyme cumulative release which indicates that increasing mesh size can improve diffusion of protein out of the polymer (Figure 3.6 B). While PEGDA concentration is also reported to affect mesh size, reducing 4kDa PEGDA from 10% to 5% did not have as potent as an effect as the increase of molecular weight from 575Da to 4kDa did (Figure 3.6 C).

Increasing PEGDA molecular weight did improve TGF-β1 percentage release but by a lower magnitude than expected which indicates that simple entrapment due to size is not the main reason for low percentage release (Figure 3.8 A). When investigating low TGF-β1 release the UV irradiated standards containing photoinitiator had a visible colour change to white and became opaque which indicates photocrosslinking occurred between proteins (Figure 3.9 B). The appearance was the same for all wells despite containing different concentrations of TGF-β1, however; each standard contained 1mg/mL BSA as dilutant for the ELISA kit. If a finite amount of protein is photocrosslinked into the PEGDA network it would offer an explanation as to why PEGDA hydrogels loaded with lower initial dosages of protein exhibit reduced fractional release before reaching plateau.

When considering the chemical groups present on BSA, TGF-β1, and PEGDA it is possible thiol-ene reaction took place during UV photocrosslinking to covalently bond the proteins to the PEGDA network. Thiol-ene reaction occurs between a thiol containing molecule and an alkene in the presence of a photoinitiator and results in the thiol becoming covalently bonded to the carbon atom from the vinyl group[348]. In the UV photocrosslinking reaction thiol-ene may occur between the vinyl groups on the acrylate terminals of PEGDA and thiol groups present on cysteine amino acids in the structure of proteins. The thiol side chain of cysteine amino acids usually form disulfide bonds during protein folding and cysteines are therefore usually internal[374]. However, BSA is reported to have a free cysteine group on its surface which means it could take part in thiol-ene[375,376]. BSA crosslinked into PEGDA may then have a sequestering effect on TGF-β1 to render it trapped within the hydrogel. BSA has an iso-electric point of 4.7[377] which would make it electrostatically attracted to TGF-β1 at neutral pH such as in the PBS used for photocrosslinking of PEGDA.

While TGF-β1 doesn't have a surface cysteine, the TGF-β1 homodimer used for protein release experiments is connected together by a disulfide bond[378,379]. If the dimer were to detach it would leave free thiol groups available for thiol-ene integration into the PEGDA network. For this to occur the disulfide bond would need to be broken by either 365nm UV light irradiation for 10 minutes or by the free radicals generated from activated Irgacure-2959. Previously the disulfide bond has been reported to be broken by 266nm UV light irradiation[380]. If TGF-β1 is significantly denatured it is likely that cysteines which were originally internal could be exposed on the surface and then take part in thiol-

ene. Evidence that TGF-β1 is denatured was the lack of ELISA detection for all standards that were UV irradiated in the presence of photoinitiator (Figure 3.9 C, D). Changes to folding due to denaturation would prevent detection by ELISA if the epitopes required for antibody recognition are covered.

When comparing different protein loading concentrations in 10% PEGDA for both lysozyme (10mg/mL and 1mg/mL Figure 3.4 A and 3.6 A) and TGF-β1 (Figure 3.8 B) there was a decrease in both release rate and the percentage release in the lower loading concentrations. In consideration of the suspected interaction between protein and photoinitiator, hydrogels loaded with a higher protein concentration have a greater protein to photoinitiator ratio and it is likely that after 10 minutes UV irradiation a significant proportion of protein remains unreacted with the photoinitiator and is therefore unaffected. This would explain why at 10mg/mL lysozyme loading there was no noticeable effect from the photoinitiator in the release trend (Figure 3.4 A 0% SPAK). At lower protein loading concentrations almost all of the protein is likely to be affected by the photoinitiator which would explain why less than 0.1% of TGF-β1 was released after 5 days when loading at 10μg/mL whereas at 50μg/mL almost 1% was released after 5 days with a continued linear release trend up to nearly 2% after 13 days (Figure 3.8 B).

Reduced percentage release due to photocrosslinking by thiol-ene would also offer an alternative explanation as to why increasing PEGDA molecular weight from 4kDa to 6kDa and 20kDa increased TGF-β1 cumulative release (Figure 3.8 A). In 10% w/v of PEGDA there is a higher molar concentration for lower molecular weight PEGDAs which means there are more acrylate groups free to react with proteins during photocrosslinking. Increasing the molecular weight

would then reduce the amount of acrylate groups present and would leave a larger proportion of protein unreacted and free to diffuse out of the hydrogel.

Few publications have focused on photoinitiator interaction with proteins in controlled protein release. Lin et al. also reported reduced lysozyme bioactivity and fractional release from PEGDA. They found changing from Irgacure-2959 to the more hydrophobic Irgacure-651 increased lysozyme percentage release and bioactivity[337]. They hypothesized that in the gel precursor solution Irgacure-651 localises to the hydrophobic acrylate groups whereas Irgacure-2959 localises to the more hydrophilic environment and is in close proximity to lysozyme and the PEG chains. The same research group also reported incomplete release of BSA from PEGDA and showed that the addition of a BSA binding ligand, iminodiacetic acid, improved cumulative release and that this effect was further enhanced in the presence of copper[338]. At the time of publication the molecular mechanism for this effect remained unknown. When considering thiol-ene, the binding ligand could interact with or cover the free thiol group and reduce its availability for thiol-ene conjugation to PEGDA. Copper (I) ions have been reported to bind strongly to thiol when interacting with cysteine[381] which would offer an explanation as to why BSA release was further improved when copper was added to iminodiacetic acid.

The core-shell gelatin-PEGDA hydrogels generated in effort to separate photocrosslinking from TGF-β1 loading exhibited no detectable TGF-β1 release (Figure 3.10 C). This is likely due to the limitations of the PTFE moulds used because the resulting hydrogel had approximately 5mm total thickness but had a small core and large shell (Figure 3.10 B). A considerably thick shell component would mean TGF-β1 has to diffuse through a large distance of

PEGDA to be released from the hydrogel and during this time, intermolecular forces of attraction between TGF-β1 and PEGDA likely prevent TGF-β1 form being released. Future attempts at generating core-shell hydrogels for this purpose should use more sophisticated approaches to generate constructs with a larger core to shell ratio in which the bulk of the material cross section is the cytokine loaded core with a relatively thin PEGDA shell to act as a filter for diffusion that could then be charged by addition of SPAK once a high percentage release is observed from PEGDA alone. Such approaches may utilize co-axial extrusion 3D printing which has previously been shown to generate core-shell hydrogels where an IgG loaded Gel-MA core was printed with an alginate and PEGDA shell[382].

Future studies utilising the direct loading method should optimise the photoinitiator type used, the concentration of photoinitiator and the UV exposure time to minimise protein entrapment within the hydrogel. It is likely that when using this approach cytokine loading concentrations will have to be in the mg/mL or high μg/mL range to get predictable protein release which could then be controlled by the addition of charged acrylates such as SPAK. If optimised, this approach could produce in-situ forming control release hydrogels for minimally invasive administration into the knee joint in osteoarthritis.

Protein damage and entrapment during UV photocrosslinking may also be avoided if hydrogels are loaded by immersion in cytokine containing solution after fabrication and processing. This approach would expose proteins to the least amount of possibly damaging environmental conditions possible but would have the drawbacks of high cost due to requiring a bath of cytokine to

immerse each material into and there would also be less control over the dosage of cytokine loaded onto each hydrogel.

Once in-vitro cytokine release data is obtained with sustained release close to the therapeutic range of growth factor action, in-vitro experiments should be carried out to model immunomodulation in osteoarthritis to transition simple in-vitro protein release data into more clinically relevant scenarios.

3.5 Conclusion

In summary, this chapter has shown:

Incorporation of SPAK into 10% 575Da PEGDA hydrogels resulted in the controlled release of lysozyme for 70 days with linear trends in all experimental groups loaded with SPAK and 10mg/mL lysozyme.

The bioactivity of lysozyme released from 5% SPAK 10% PEGDA at 2 days, 10 days, 31 days and 61 days was decreased compared to controls but was still estimated at 56% at day 61 of in-vitro release.

The scaling down of hydrogel volume and loading concentration for TGF-β1 release from 10% 4kDa PEGDA resulted in an extremely low percentage release.

Attempted optimisation by increasing PEGDA molecular weight and TGF-β1 loading concentration did increase percentage release but by a lower magnitude than expected.

Investigation into how UV photocrosslinking conditions may affect encapsulated proteins found that UV exposure had no effect but that activated photoinitiator diminished ELISA quantification. It was suspected that thiol-ene

reaction was responsible for protein entrapment within PEGDA and that this was less noticeable at higher protein loading concentrations.

A core-shell hydrogel was fabricated in effort to separate TGF-β1 loading from the photocrosslinking reaction but it failed to improve percentage release. The limitations of the approach were discussed along with recommendations for future work.

Chapter 4 - Promotion of M2 macrophage polarisation using sustained IL-4 release from affinity hydrogels

4.1 Introduction

Osteoarthritis (OA) is a debilitating disease that is characterised by the irreversible degradation of articular cartilage, synovial inflammation, subchondral bone remodelling, and osteophyte formation[3,5–7,145]. OA is a leading cause of disability and affects over 500 million people globally[12]. There is a lack of disease modifying osteoarthritic drugs (DMAODs) which means that existing therapeutics options are limited to pain and symptom management[23,24,26]. Pro-inflammatory signalling is present in the early stages of osteoarthritis and is a key driver of OA pathobiology[40,41]. Promoting M2 polarisation to restore M1 and M2 macrophage balance may be a possible approach to prevent further progression of OA by stopping the cycle of pro-inflammatory signalling.

Interleukin-4 (IL-4) promotes M2a polarisation which has surface markers CD206 and CD163[204,213], and has secreted markers including IL-10, TGF-β1, CCL-18 and CCL-22[207–209]. Previously, repeated IL-4 injection has shown beneficial effects in OA animal models in-vivo. Daily intra-articular injection of IL-4 has been shown to elicit a chondroprotective effect in a murine model of OA and it was attributed to the reduction of nitric oxide synthesis by chondrocytes at the time[324]. Similarly, another study showed that weekly

injection of an IL-4 and IL-10 fusion protein into the knee of OA model mice for 10 weeks significantly reduced cartilage degradation[326].

Data from Chapter 3 of this thesis showed hydrogels containing 3-sulfopropyl acrylate potassium salt (SPAK) and poly (ethylene glycol) diacrylate (PEGDA) to control the release of lysozyme for 70 days with a linear release trend and over 50% lysozyme bioactivity after 61 days. This showed promising potential for SPAK PEGDA hydrogels as a synthetic, low cost controlled release material with a slow biodegradation rate and a high manufacturing capacity[294,343,344]. The scaling down of hydrogel volume and loading concentration for TGF-β1 and IL-4 release was met with extremely low percentage release (Chapter 3 figure 7). After a series of optimisation and troubleshooting experiments, it was found that the activated photoinitiator was likely causing photocrosslinking between cytokines and the polymer network to cause incomplete release from PEGDA (Chapter 3 figures 8 and 9).

This chapter aims to modify the protein release method to fully decouple protein loading from Ultraviolet (UV)-photocrosslinking using material loading by immersion in order to achieve the controlled release of IL-4.

This method will separate the conditions of the UV photocrosslinking reaction from protein loading and also avoid protein exposure to the sterilisation steps required for aseptic cell culture work. The bioactivity of released IL-4 will be investigated by using it to promote M2-like polarisation of THP-1 macrophages to model immunomodulation in osteoarthritis.

THP-1 is an immortalised human monocyte derived from a 1 year old patient with acute myeloid leukaemia. THP-1 monocytes can be differentiated using

phorbol 12-myristate 13-acetate (PMA) into macrophage-like cells. THP-1 are a popular choice for in-vitro models of immunomodulation because they share many key functional properties of peripheral blood monocyte derived macrophages[255,383,384].

4.2 Chapter specific methods

Detailed materials and methods can be found in Chapter 2. Chapter specific methods are briefly outlined below for convenience with experimental design schematics where appropriate.

4.2.1 UV-photocrosslinking

As described (2.2.1 UV photocrosslinking). Briefly, hydrogel precursor solutions were prepared in Phosphate buffered saline (PBS) while protected from light. Hydrogels were formed by 10 minutes 365nm UV light exposure under argon with oxygen concentration below 2000ppm. 100µL hydrogels were formed as droplets on a flat piece of polytetrafluoroethylene (PTFE).

4.2.2 In-vitro hydrogel swelling

As described (2.2.1 In-vitro hydrogel swelling). Briefly, hydrogels were immersed in PBS and weighed multiple times over a 5 day period. The swollen weight was expressed as a percentage increase from the initial hydrogel weight after UV photocrosslinking.

4.2.3 Hydrogel compressive testing

As described (2.2.1 hydrogel compressive testing). Briefly, the compressive modulus was characterised by compressing swollen hydrogels using a texture

analyser with a 5kg load cell. The compressive modulus was calculated as the gradient of the linear section from the stress-strain curve.

4.2.4 In-vitro IL-4 release

As described (2.2.2 indirect loading method). A schematic of the loading method has been included for convenience (Figure 4.1). Briefly, 100μL hydrogels were cast by UV photocrosslinking containing 10% w/v 4kDa PEGDA with 0%, 1% and 5% w/v SPAK.

Hydrogels were swelled in 5mL PBS for 5 days and then sterilized for cell culture using 20 minutes 254nm UV irradiation and a 30 minute wash with antibiotic-antimitotic antibody followed by 3 washes with sterile PBS. Each hydrogel was immersed in 500μL of a 2.2μg/mL IL-4 solution for 24 hours at 37^{o}C.

For in-vitro IL-4 release, each hydrogel was immersed in 2mL of THP-1 complete culture media. At each time point the entire 2mL of media was collected and replaced. This was done to re-establish the diffusion gradient for IL-4 release to mimic the short half-life of IL-4 in-vivo. 1mL of the collected media was stored at -20^{o}C for quantification by ELISA and the remaining 1mL was stored at -20^{o}C as a sterile aliquot to investigate bioactivity by in-vitro THP-1 macrophage polarisation.

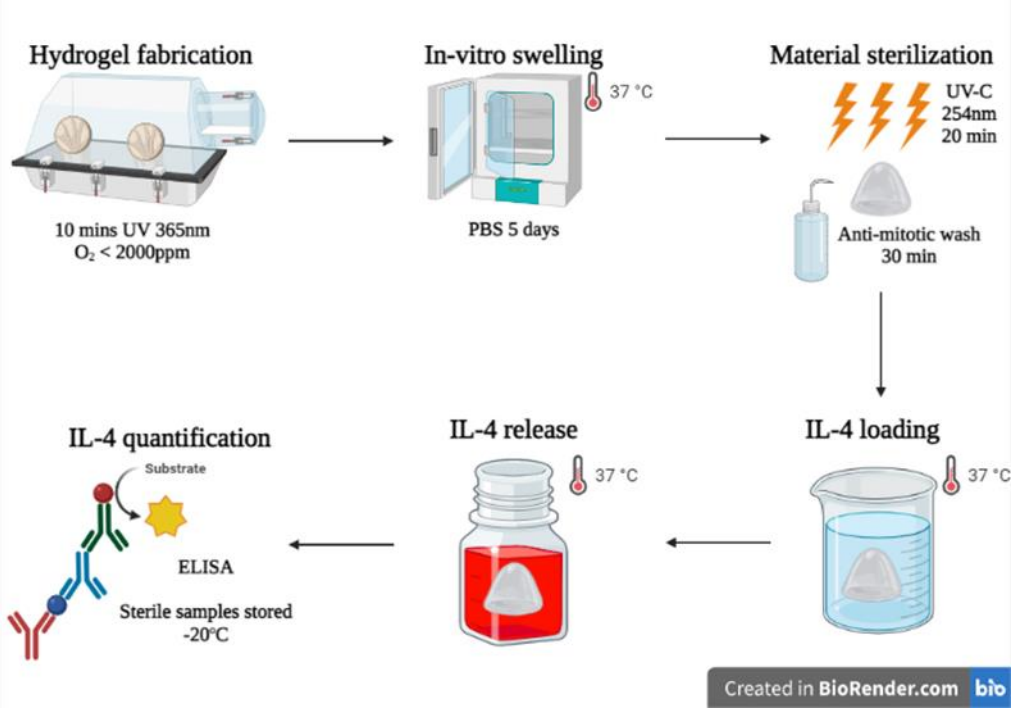

Figure 4.1: Schematic of indirect IL-4 loading method. IL-4 was loaded by immersion after UV photocrosslinking and hydrogel sterilization. IL-4 loaded hydrogels were immersed in 2mL of THP-1 complete culture media for a 73 day controlled release experiment. Image created at www.BioRender.com.

4.2.5 THP-1 culture conditions

THP-1 monocytes were cultured in RPMI-1640 media supplemented with 10% Foetal bovine serum (FBS), 1% GlutaMAX, 1% Sodium pyruvate, 1% HEPES buffer, 1.25% glucose solution and 1% penicillin-streptomycin. THP-1 cells were cultured in the concentration range of 200,000-1,000,000 cells per mL at 37^{o}C with 5% CO_2.

4.2.6 THP-1 seeding

THP-1 cells were seeded at 500,000 cells per mL and differentiated into macrophages by exposure to 50ng/mL PMA for 6 hours. THP-1 macrophages were then washed with PBS and incubated in THP-1 complete media for 24

hours. Cells were then polarised with cytokine containing cocktails, IL-4 controlled release media or by incubation with IL-4 releasing hydrogels.

4.2.7 THP-1 polarisation (IL-4 controlled release media)

As described (2.2.5 THP-1 macrophage polarisation (cytokine application)). Sterile aliquots of SPAK IL-4 controlled release media were thawed and warmed to 37^{o}C. Following THP-1 seeding, 1mL of controlled release media was used to polarise THP-1 macrophages towards M2a for 6 days. For each IL-4 release time point that was tested, an "M2" control group was included with a matched IL-4 concentration to directly compare the polarisation effect of IL-4 released from SPAK PEGDA hydrogels with a matched dose of stock IL-4. M2 polarisation using Released IL-4 and control IL-4 included 50ng/mL macrophage colony stimulating factor (M-CSF). Control groups were included as examples quiescent and conventionally activated polarisation states. "M0" contained 50ng/mL M-CSF, and "M1" contained 50ng/mL granulocyte macrophage colony stimulating factor (GM-CSF) and 20ng/mL Interferon gamma (IFN-γ). After 6 days culture in polarisation media, cells were fixed for immunostaining and culture media was stored at -20^{o}C for future analysis.

4.2.8 THP-1 polarisation (Incubation with IL-4 releasing hydrogel)

As described (2.2.5 THP-1 macrophage polarisation (hydrogel incubation)). Briefly, 5% SPAK 10% PEGDA hydrogels were fabricated, sterilized and loaded with IL-4 with the same method as IL-4 in-vitro release. THP-1 cells were seeded at 500,000 cells per mL with 2mL per well in a 12-well plate to match the media volume used for IL-4 in-vitro release. IL-4 loaded 5% SPAK 10% PEGDA hydrogels were placed in the appropriate wells for 6 days. To

compare repeated IL-4 delivery to a single large IL-4 injection, a control group named “IL-4 bolus” was included which contained the IL-4 dose estimated to be released from 5% SPAK 10% PEGDA in 6 days (404ng). Following 6 days polarisation the viability and secreted markers were compared between the IL-4 bolus and IL-4 releasing hydrogel groups when applied to M0 cells and in the presence of an M1 stimulus.

4.2.9 Enzyme linked immunosorbent assay (ELISA)

As described (2.2.5 ELISA (THP-1 secreted cytokines, IL-4 controlled release)). Briefly, ELISA plates were coated with capture antibody overnight on a rocker at room temperature (RT). ELISA plates were washed and blocked with 1% w/v BSA for 1 hour at RT. Media samples from THP-1 macrophage polarisation or IL-4 in-vitro release were thawed and brought to room temperature. Plates were washed and incubated with sample media for 1 hour on a rocker at room temperature. Plates were washed and incubated with appropriately diluted detection antibody for 1 hour on a rocker at room temperature. Plates were washed and incubated with appropriately diluted streptavidin-HRP for 20 minutes while protected from light. Plates were washed and incubated with TMB substrate for 20 minutes while protected from light. Sulfuric acid was added as stop solution and absorbance was read at 450nm with 570nm reference wavelength. The cytokine concentration in sample media from macrophage polarisation or IL-4 in-vitro release was quantified using a standard curve.

4.2.10 Immunostaining

As described (2.2.5 Immunostaining). Briefly, Cells were washed twice with PBS and then fixed with 4% PFA in PBS for 15 minutes. Cells were washed 3 times with wash buffer and were then blocked with a solution containing 3% BSA and 1% glycine in PBS for 30 minutes. Cells were washed 3 times and blocked a second time with 5% goat serum for 30 minutes. Cells were incubated with appropriately diluted primary antibody overnight at 4ºC. Cells were washed 3 times and incubated with appropriately diluted secondary antibody for 1 hour at RT while protected from light. Cells were washed twice and were then incubated with appropriately diluted DAPI solution for 5 minutes at RT while protected from light. Cells were washed twice and viewed using a fluorescent cell imager. For CD-68, the conjugated primary antibody was incubated for 1 hour at RT while protected from light followed by DAPI staining.

4.2.11 Viability assay

As described (2.2.5 Viability assay). Briefly, viability was measured at days 3 and 6 of culture in polarisation media by the ToxiLight™ viability assay. Media collected at days 3 and 6 were mixed with adenylate kinase detection reagent and luminescence was read after 5 minutes on a plate reader. For each experiment a control group of M0 cells seeded at 500,000 cells per mL was cultured in parallel to other experimental groups. After 6 days the control group was lysed with ToxiLight™ lysis reagent and luminescence generated from analysing this group was treated as the value for 100% cell death.

4.2.12 Statistical analysis

For hydrogel characterisation and IL-4 in-vitro release all numerical data is presented as mean ± standard deviation from 3 repeats per experimental

condition. When quantifying IL-4 release from SPAK PEGDA hydrogels the limit of detection (LOD) and limit of quantification (LOQ) of ELISA were calculated as 3 and 10 standard deviations above the average blank standard respectably[352,354]. In THP-1 macrophage polarisation experiments, ELISA and viability data is presented as mean ± standard error of the mean from 2 biological repeats (N=2), which each contained 3 replicates per experimental condition (n=3). One-way ANOVA with Tukey's post hoc multiple comparisons test (α=0.05) was used to determine significant differences between experimental groups where three or more are present on a column graph. Pairs with significant differences were labelled as * $P \leq 0.05$, ** $P < 0.01$, *** $P < 0.001$ and **** $P < 0.0001$. In instances with many pairwise comparisons on a single graph, only ones that are discussed are presented.

4.3 Results

4.3.1 Swelling and compressive characterisation of SPAK PEGDA hydrogels

100µL hydrogels were cast by UV photocrosslinking that contained 10% w/v 4kDa PEGDA and 0%, 1% and 5% w/v SPAK. 5% w/v was selected as the highest concentration of SPAK due to the potent effect of it seen in controlling the release rate of lysozyme in Chapter 3 when 5%, 10%, and 15% were compared (Chapter 3 Figure 4). 4kDa PEGDA molecular weight was selected to keep consistent with IL-4 release data from Chapter 3.

The in-vitro swelling of SPAK PEGDA hydrogels was characterised in PBS for 5 days. At day 5, the increase in hydrogels weights from the initial weight after photocrosslinking for 0% SPAK, 1% SPAK and 5% SPAK were 5.1 ± 4.1%, 8.5 ± 2.4% and 58.2 ± 1.5% respectively (Figure 4.2 A). The increased swelling

exhibited by 5% SPAK 10% PEGDA may be explained by the charged sulfate groups attracting bipolar water molecules.

Three extra replicates for each condition were included for compressive testing. Compressive testing was performed on swollen hydrogels following 5 days in-vitro swelling. 0% SPAK, 1% SPAK and 5% SPAK had average modulus values of 8.5 ± 1.1kPa, 11.9 ± 3.0kPa and 10.9 ± 0.6kPa respectably. One-way ANOVA and Tukey's post hoc multiple comparisons test finding no significant difference between the groups (Figure 4.2 B).

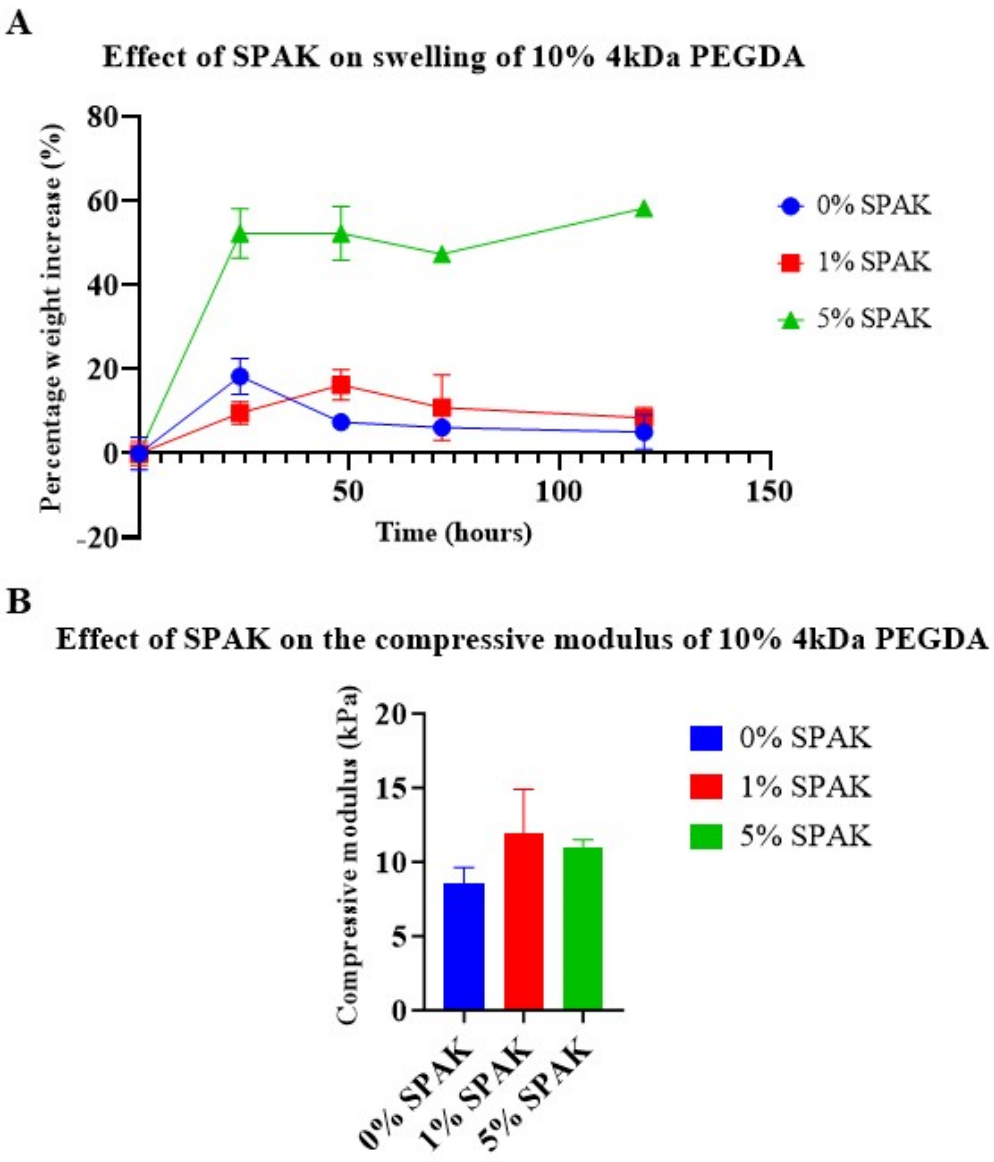

Figure 4.2: Swelling and compressive characterisation of SPAK containing 10% 4kDa PEGDA hydrogels. A) 5 day in-vitro swelling of 10% 4kDa PEGDA hydrogels containing 0%, 1% and 5% SPAK. B) Compressive modulus of 100µL 10% 4kDa PEGDA hydrogels containing 0%, 1% and 5% SPAK. No statistical difference was observed between modulus values for 0%, 1% and 5% SPAK when tested using one-way ANVOA with Tukey's post hoc multiple comparisons test. Values presented as mean ± standard deviation (n=3).

4.3.2 Sustained Intelreukin-4 release from SPAK PEGDA hydrogels

Following in-vitro swelling and material sterilization, hydrogels were loaded with IL-4 by 24 hour immersion in a 2.2μg/mL IL-4 solution at 37^{o}C. 2.2μg/mL was selected as the concentration for the loading solution as it was intended to release IL-4 in the low ng/mL range that is appropriate for the biological action of cytokines.

IL-4 loading dosage was estimated as the difference between the IL-4 dose in the starting solution and the dosage in the solution after 24 hour incubation with the hydrogel as determined by ELISA. 5% SPAK 10% PEGDA had an estimated 0.91 ± 0.02μg load which was significantly higher than 0% SPAK 10% PEGDA and 1% SPAK 10% PEGDA which had IL-4 loads of 0.37 ± 0.03μg and 0.37 ± 0.06μg respectively (Figure 4.3 A). IL-4 loading dosage was normalised to the swollen hydrogel weight after 5 days of in-vitro swelling. The normalised loading dose for 0% SPAK, 1% SPAK, and 5% SPAK were 4.2 ± 0.45μg/g, 3.9 ± 0.52μg/g, and 6.6 ± 0.26μg/g.

Increased IL-4 loading in 5% SPAK 10% PEGDA hydrogels can be explained by the increased electrostatic attraction between the negative charge of SPAK and the positive net charge of IL-4, and the increased volume from the swelling of 5% SPAK 10% PEGDA hydrogels.

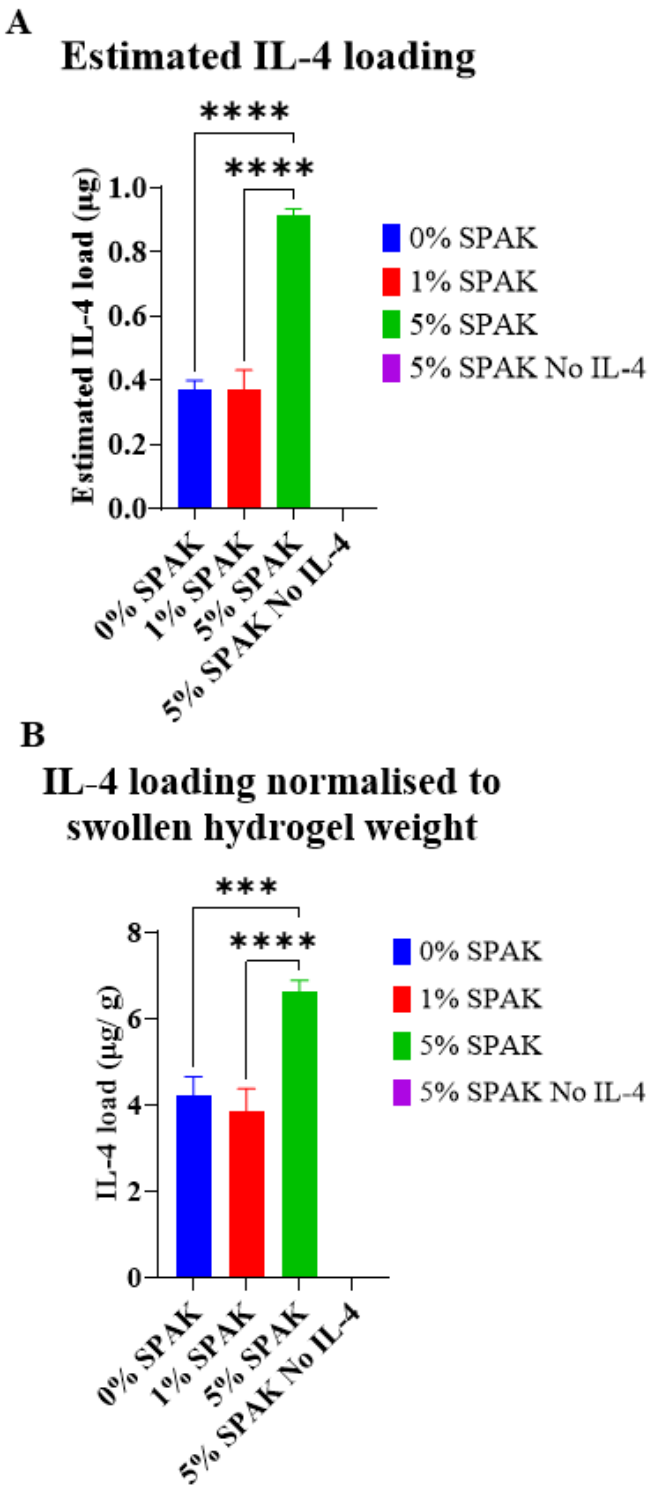

Figure 4.3: Estimated IL-4 loading dosage. A) The loading dosage for each gel estimated as the difference between the IL-4 dose before and after incubation with the hydrogel. B) Estimated IL-4 loading dosage normalised to swollen hydrogel weight on day 5 of in-vitro swelling. Values presented as

mean ± standard deviation (N=2, n=3). Pairs with significant differences were labelled as * P≤0.05, ** P<0.01, *** P<0.001 and **** P<0.0001

IL-4 loaded hydrogels were immersed in THP-1 complete culture media for a 73 day controlled release experiment. Each hydrogel was immersed in 2mL of fully supplemented culture media. 2mL was selected as the volume of release media as it is the approximate volume of synovial fluid in the knee.

At each controlled release time point the entire 2mL was collected and replaced with 2mL of fresh media to re-establish the diffusion gradient for IL-4 release. On the first day the time points were 2 hours, 4 hours, and 6 hours. The media was then changed every day until day 5, every two days until day 9, every three days until day 33, and then every 5 days until day 73.

The IL-4 dose released at each time point was calculated by ELISA and expressed as a percentage of the estimated total load in each condition. The cumulative release was then calculated over the duration of the experiment.

0% SPAK 10% PEGDA reached 55% cumulative release after 2 days, 66% after 15 days and 69% at day 73 (Figure 4.4 A blue line). 1% SPAK 10% PEGDA reached 60% cumulative release after 2 days, 72% after 15 days and 76% at day 73 (Figure 4.4 A red line). 5% SPAK 10% PEGDA reached 28% cumulative release after 2 days, 48% after 15 days and 61% at day 73 (Figure 4.4 A green line).

The concentration of IL-4 released at each time point was considered in relation to in-vitro M2a macrophage polarisation. Commonly used IL-4 concentrations used for in-vitro macrophage polarisation are 20ng/mL[248,385] and 10ng/mL[386,387].

0% SPAK 10% PEGDA released 68ng/mL after 2 hours, after 2 days the released concentration was 12ng/mL and after 24 days the released IL-4 concentration fell below 1ng/mL for all remaining time points (Figure 4.4 B blue line). 1% SPAK 10% PEGDA released 65ng/mL after 2 hours, after 2 days the concentration released was 14ng/mL and after 27 days the concentration fell below 1ng/mL in all remaining time points (Figure 4.4 B red line). 5% SPAK 10% PEGDA released 32ng/mL after 2 hours, 30ng/mL after 2 days, after 18 days the concentration released fell below 10ng/mL and after 53 days the released concentration fell below 5ng/mL. After 73 days the final concentration released was 1ng/mL (Figure 4.4 B green line).

The average limit of detection (LOD) and limit of quantification (LOQ) from 5 standard curves were 31.1pg/mL and 127.4pg/mL respectively (Supplementary Figure S.3 Appendix 1). These values were not visible on the ng/mL scale for IL-4 concentration released per time point (Figure 4.4 B). Samples testing above the highest ELISA standard of 2000pg/mL were diluted and re assayed as appropriate.

A control group containing 5% SPAK 10% PEGDA with no IL-4 loading was included and had no detectable response at any time point which demonstrated that there were no interfering substances present in the release media from FBS (Figure 4.4 A, B Purple line). The sustained release trend exhibited by 5% SPAK is likely due to the increased electrostatic attraction between SPAK and IL-4, and due to the higher total IL-4 loading dosage which is a limitation of the loading method.

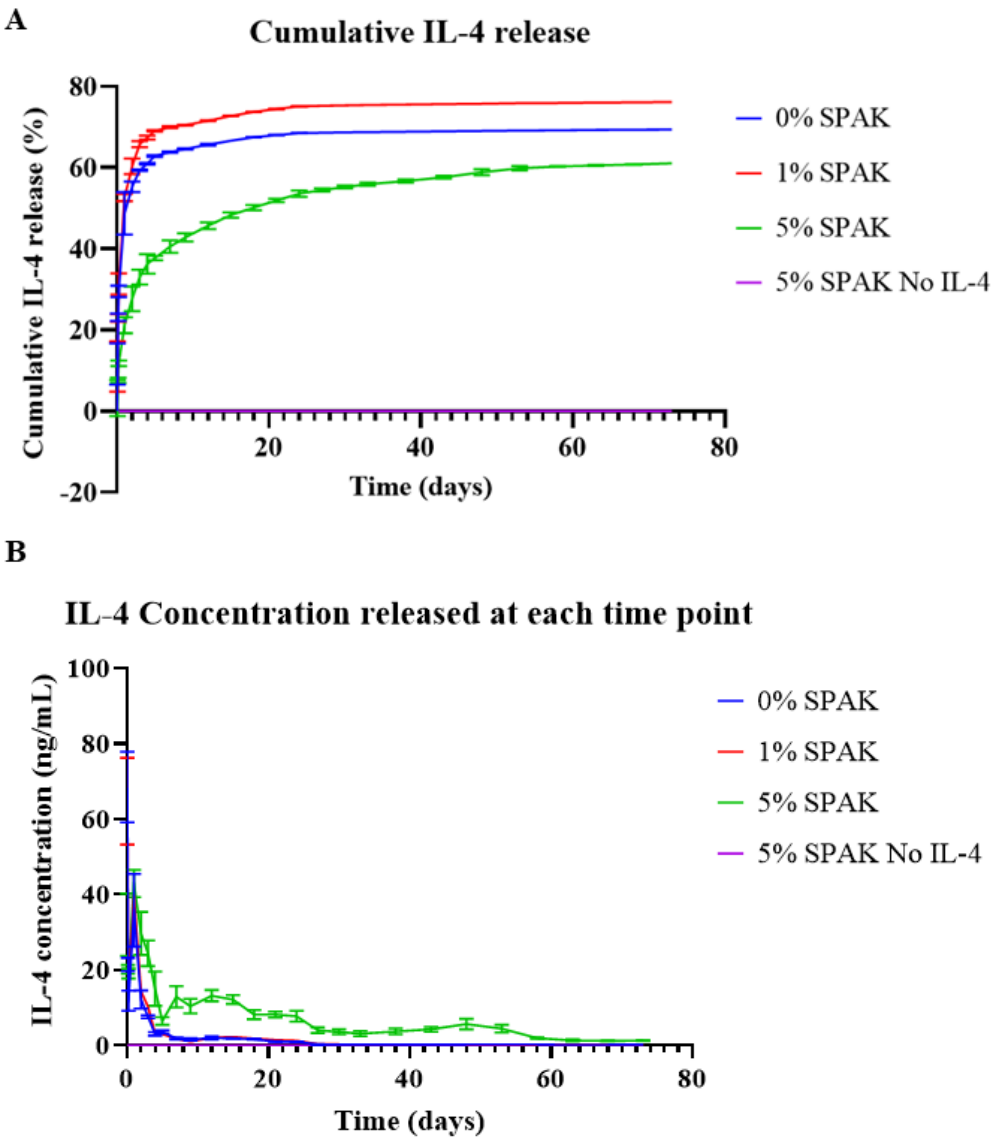

Figure 4.4: IL-4 release from SPAK containing PEGDA hydrogels. A) Cumulative IL-4 release expressed as a percentage of the IL-4 estimated to be loaded in each condition. B) IL-4 concentration released at each time point over 73 days. The entire 2mL of media was collected and replaced at each time point. Highly cited IL-4 concentrations for in-vitro macrophage polarisation are 20ng/mL and 10ng/mL. Values presented as mean ± standard deviation (N=2, n=3).

4.3.3 Characterisation of THP-1 macrophages

PMA differentiation of THP-1 monocytes into macrophage-like cells was characterised using immunostaining for the pan macrophage marker CD68[388] at three time points (Figure 4.5).

The Day 0 timepoint was immediately after PMA removal in which the cells were aggregated with a small morphology and low CD68 staining (Figure 4.5 Day 0). The second time point was after PMA removal, 24 hours rest in THP-1 complete media and 3 days culture in M0 promoting media containing 50ng/mL M-CSF. The cells were more evenly distributed, had a larger morphology and showed a small increase in CD68 staining (Figure 4.5 Day 3). The third time point was after PMA removal, 24 hours rest and 6 days culture in M0 promoting media containing 50ng/mL M-CSF. The highest amount of CD68 staining was visibly present, indicating a macrophage-like phenotype (Figure 4.5 Day 6).

Prior to fixing and staining confluency was approximately 80% at day 6 but it was noticed that more cells became detached during the washing steps of immunostaining than at other time points (Figure 4.5 Day 6). Detachment of cells is likely due to dedifferentiation from a macrophage-like phenotype to a less adherent monocytic phenotype following PMA withdrawal. This phenomenon has previously been reported in THP-1 cells in which dedifferentiation was seen following 7 days of PMA removal[389].

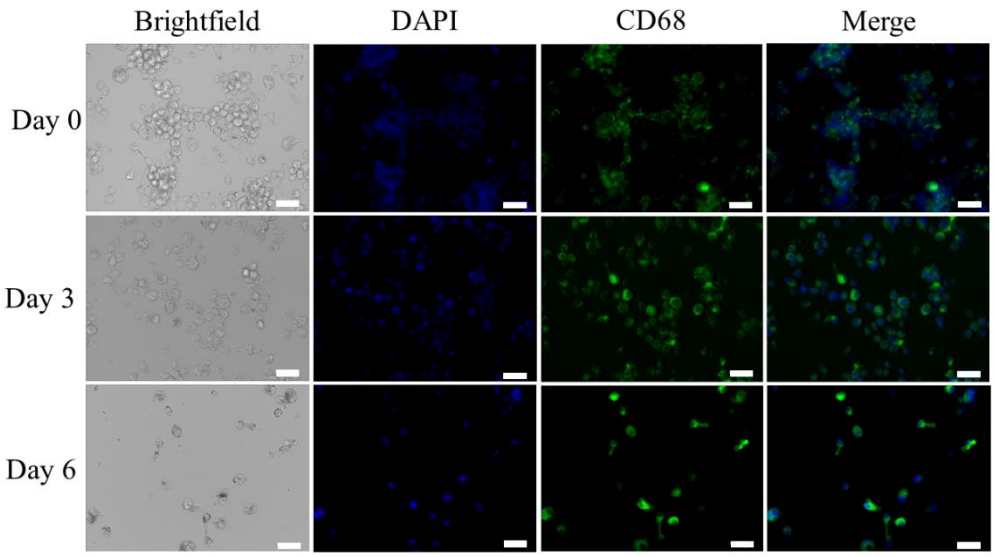

Figure 4.5: CD68 immunostaining of PMA differentiated THP-1 cells. THP-1 cells were exposed to 50ng/mL PMA for 6 hours and were then fixed and stained for the surface marker CD68 at three time points of subsequent culture. The time points chosen were immediately after PMA removal (Day 0), after 24 hours of rest with a following 3 and 6 days of culture in 50ng/mL M-CSF which are labelled as Day 3 and Day 6. Scale bar = 40μm.

4.3.4 Macrophage polarisation using IL-4 from 5% SPAK 10% PEGDA controlled release time points

To investigate the bioactivity of IL-4 released from SPAK PEGDA hydrogels, media from IL-4 controlled release time points was used to promote M2a polarisation of THP-1 macrophages in monolayer culture. Samples from 5% SPAK 10% PEGDA release were selected because it had the most time points within the reported 10-20ng/mL range[248,385–387] and was the only experimental group to remain in the ng/mL range at time points later than one month (Figure 4.4 B).

The bioactivity of released IL-4 was investigated at multiple time points in the long term sustained release experiment to investigate if bioactivity reduced over time or was maintained in later stages of the experiment. The time points selected were split into three groups which were Early (Days 1 and 2), Medium (Days 12 and 15), and Late (Days 48 and 43).

At each time point tested, the macrophage response to "Released IL-4" was compared to an equal concentration of stock IL-4. Due to the concentration of IL-4 in controlled release time points decreasing over the course of the experiment, separate controls with matched concentrations of IL-4 to the corresponding controlled release time points were included as the "M2" control. 50ng/mL M-CSF was included in "Released IL-4" and "M2" groups because it is frequently used in conjunction with IL-4 to promote M2 polarisation in-vitro. Control groups of M0 (50ng/mL M-CSF) and M1 50ng/mL (GM-CSF + 20ng/mL IFN-γ) polarisation were also included.

To investigate the bioactivity of released IL-4 at early time points, controlled release media from days 1 and 2 from 5% SPAK 10% PEGDA were used to promote M2 polarisation of THP-1 macrophages. Independent experiments were carried out using controlled release media from day 1 and day 2 which both contained 20ng/mL IL-4.

The secretion of four polarisation markers was quantified by ELISA following six days of culture in polarisation media. TNF-α and IL-6 were selected as M1 markers, CCL-18 and CCL-22 were selected as M2 markers. Preliminary investigations used IL-10 as a secreted M2 marker but its secretion was not observed in response to 20ng/mL IL-4 + 50ng/mL M-CSF (Supplementary

Figures S.9 and S.10), which is consistent with previous reports comparing the secreted markers between THP-1 macrophages and macrophages derived from primary peripheral blood monocytes[255,390,391].

The values from independent experiments using day 1 and day 2 controlled release samples were averaged. Statistical analysis was performed using one-way ANOVA with Tukey's multiple comparisons post hoc test. THP-1 macrophages polarised by "Released IL-4 20ng/mL" had significantly lower secretion of TNF-α and IL-6 in comparison to the "M1" control (Figure 4.6 A, B), and a significantly higher secretion of CCL-18 and CCL-22 in comparison to "M0" and "M1" (Figure 4.6 C, D). All four secretion markers were statistically the same between "Released IL-4 20ng/mL" and the "M2 20ng/mL" control group (Figure 4.6 A-D). This indicates that IL-4 released from 5% SPAK 10% PEGDA was bioactive at days 1 and 2 of in-vitro release and that media conditioned by SPAK PEGDA hydrogels did not elicit a pro-inflammatory response.

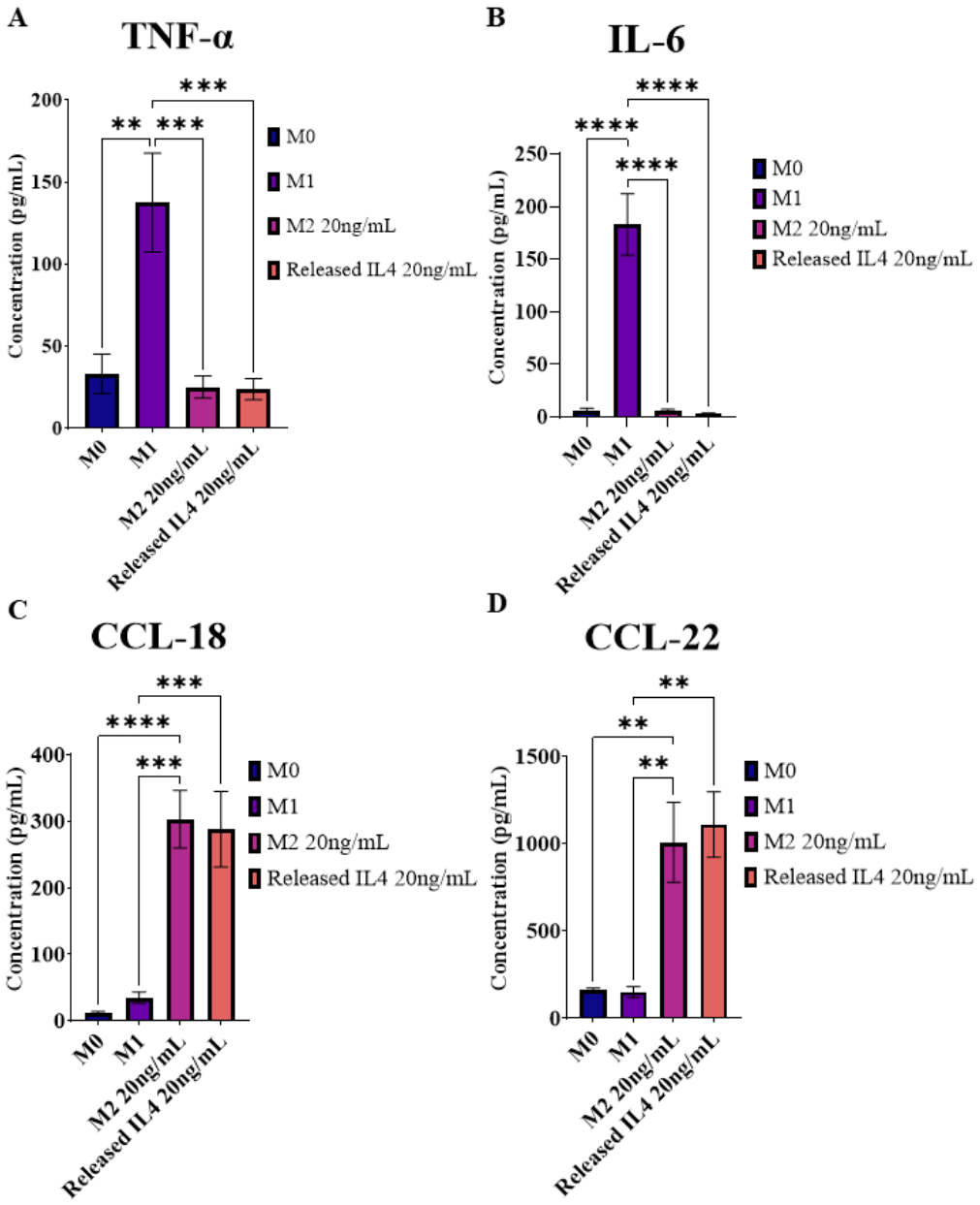

Figure 4.6: Secreted polarisation markers of THP-1 macrophages polarised with IL-4 released from 5% SPAK 10% PEGDA at days 1 and 2 of in-vitro release. TNF-α and IL-6 were selected as M1 markers (A + B). CCL-18 and CCL-22 were selected as M2 markers (C + D). Secreted markers were compared between released IL-4 and stock IL-4 at a concentration of 20ng/mL. Control groups of M0 and M1 polarisation were included. Data presented as mean ± standard error of the mean from two independent experiments which

used media samples from day 1 and day 2 of controlled release respectively. (N=2, n=3). Following one-way ANOVA and Tukey's post hoc multiple comparisons test, pairs with significant differences were labelled as * $P \leq 0.05$, ** $P < 0.01$, *** $P < 0.001$ and **** $P < 0.0001$.

To further investigate polarisation, THP-1 macrophages polarised by day 2 controlled IL-4 release media were fixed and stained for M1 and M2 surface markers after 6 days of culture. Calprotectin was selected as an M1 surface marker and mannose receptor (CD206) was selected as an M2 surface marker.

The "M0" group had very low staining for both mannose receptor and calprotectin (Figure 4.7 row one). The "M1" group had high staining for calprotectin (Figure 4.7 row 2). Both the "M2 20ng/mL" and "Released IL-4" had low calprotectin staining and lower mannose receptor staining than expected (Figure 4.7 rows 3 and 4). This is consistent with previous reports showing no CD206 expression in THP-1 macrophages[392,393] and CD206 expression to be lower in THP-1 macrophages than in PBMC derived macrophages[255].

During the immunostaining process fewer cells became detached during wash steps in the M1 experimental group. This can be explained by M1 macrophages having stronger adherence to tissue culture plastic than other groups. Previous reports found M1 cells to be less motile than M0 and M2 which could indicate stronger adherence[394].

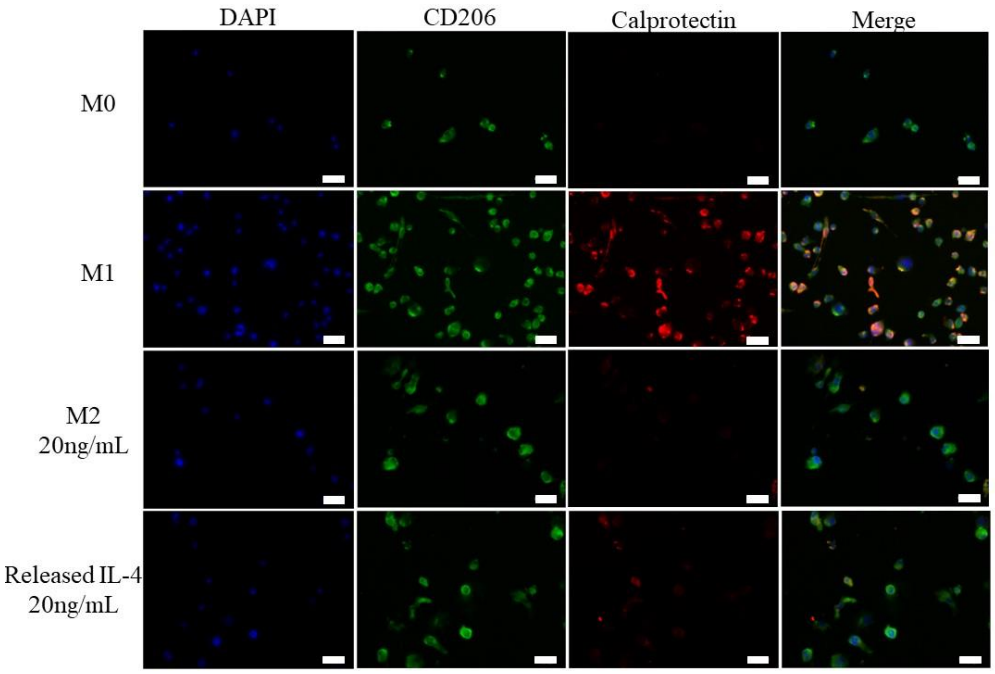

Figure 4.7: Immunostaining for M1 and M2 surface markers on THP-1 macrophages polarised by 20ng/mL IL-4 released from 5% SPAK 10% PEGDA on day 2 of in-vitro release. CD206 / Mannose receptor was chosen as an M2 surface marker, Calprotectin was chosen as an M1 surface marker. DAPI was used as a nuclear stain. Scale bar = 40μm.

During polarisation with 20ng/mL released IL-4 the viability of cells was tested on days 3 and 6 by ToxiLight™ bioassay. The ToxiLight™ assay measures adenylate kinase that is released from dying cells, the adenylate kinase detected in experimental groups is then expressed as a percentage of a control group that is 100% lysed to calculate the percentage of dead cells.

At day 3, it was observed that M0, M2 (20ng/mL) and Released IL-4 (20ng/mL) had viability values of 96.1%, 96.3% and 96.0% respectably with no significant difference between groups (Figure 4.8). The M1 control had significantly reduced viability at 93% (Figure 4.8) which is consistent with reports showing pro-inflammatory cytokines to lower cell viability[395,396].

At day 6, all groups had viability values in the range of 82%-86% with no significant difference between groups as determined by one-way ANOVA. The decrease in viability from day 3 to day 6 can be explained by nutrients in the media becoming exhausted. This shows media conditioned by 5% SPAK 10% PEGDA hydrogels was not cytotoxic to THP-1 cells, which indicates that residual monomer was sufficiently washed away during the PBS washes prior to IL-4 loading (Figure 4.8).

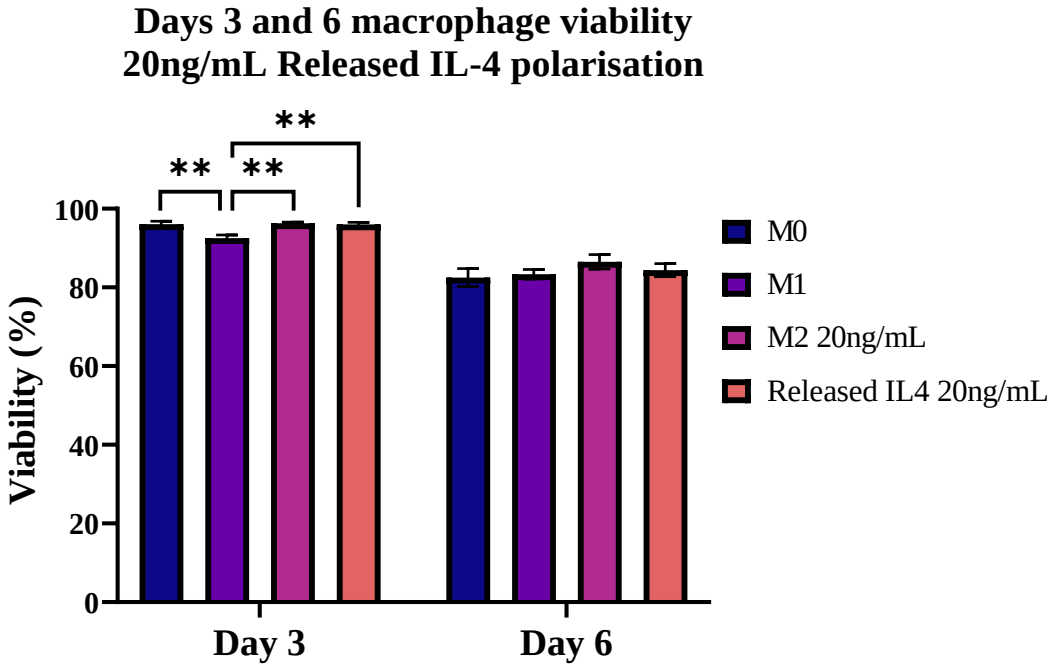

Figure 4.8: Viability of THP-1 macrophages polarised with 20ng/mL IL-4 released from 5% SPAK 10% PEGDA on days 1 and 2 of in-vitro release. Viability was tested using ToxiLight™ viability assay on days 3 and 6 of culture. Data presented as mean ± standard error of the mean from two independent experiments which each had three experimental repeats per conditions (N=2, n=3). Following one-way ANOVA and Tukey's post hoc

multiple comparisons test, pairs with significant differences were labelled as * $P \leq 0.05$, ** $P < 0.01$, *** $P < 0.001$ and **** $P < 0.0001$.

To investigate the bioactivity of released IL-4 at medium time points, controlled release media from days 12 and 15 from 5% SPAK 10% PEGDA were used to promote M2 polarisation of THP-1 macrophages. Independent experiments were carried out using controlled release media from day 12 and day 15 which both contained 12ng/mL IL-4. “Released IL-4 12ng/mL” had significantly lower secretion of TNF-α and IL-6 in comparison to the “M1” control (Figure 4.9 A, B) and significantly higher secretion of CCL-18 and CCL-12 in comparison to “M0” and “M1” controls. “Released IL-4 12ng/mL” had CCL-18 secretion that was statistically the same as and “M2 12ng/mL” (Figure 4.9 C) and CCL-22 secretion that was statistically higher than “M2 12ng/mL” (Figure 4.9 D). This result indicates that IL-4 released from 5% SPAK 10% PEGDA is still bioactive at 12 and 15 days of in-vitro release.

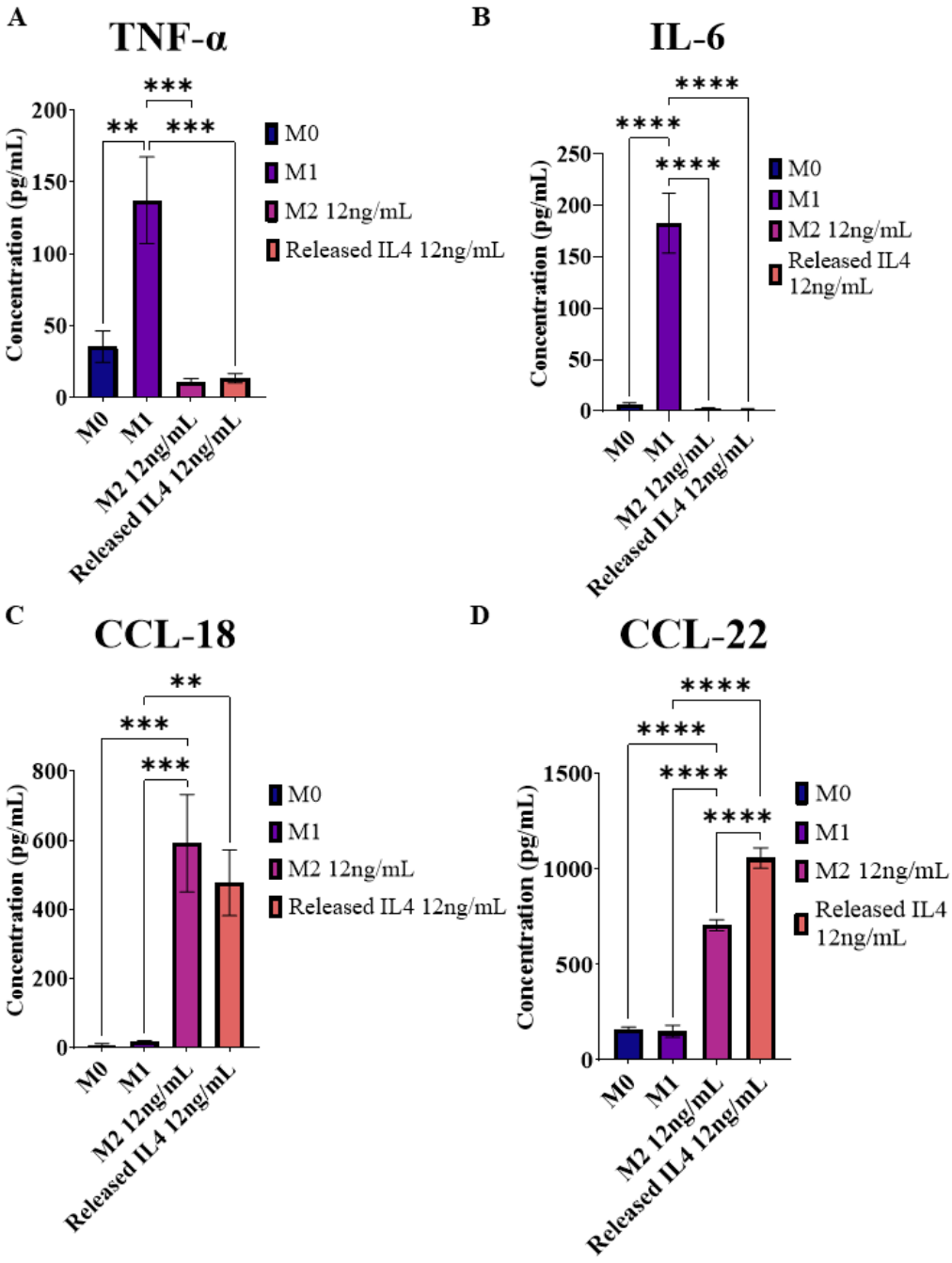

Figure 4.9: Secreted macrophage polarisation markers of THP-1 cells polarised with IL-4 released from 5% SPAK 10% PEGDA at days 12 and 15. TNF-α and IL-6 were selected as M1 markers (A + B). CCL-18 and CCL-22 were selected as M2 markers (C + D). Secreted markers were compared between released IL-4 and stock IL-4 at a concentration of 12ng/mL. Control groups of M0 and M1 polarisation were included. Data presented as mean ±

standard error of the mean from two independent experiments which used media samples from day 12 and day 15 of controlled release respectively (N=2, n=3). Following one-way ANOVA and Tukey's post hoc multiple comparisons test, pairs with significant differences were labelled as * $P \leq 0.05$, ** $P < 0.01$, *** $P < 0.001$ and **** $P < 0.0001$.

To further investigate polarisation, THP-1 cells were stained for M1 and M2 surface markers after 6 days of culture. M0 cells had very low staining for both CD206 / mannose receptor and calprotectin. M1 cells showed high staining for calprotectin. Both "M2 12ng/mL" and "Released IL-4 12ng/mL" also had low staining for CD206 / mannose receptor (Figure 4.10) which is consistent with the immunostaining data from day 2 (Figure 4.7).

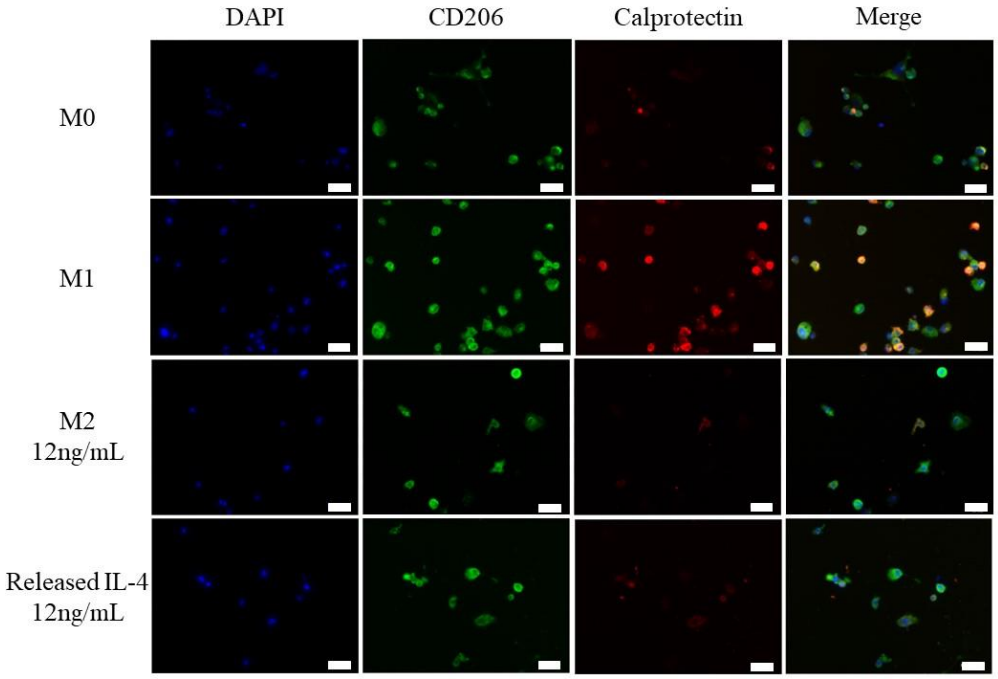

Figure 4.10: Immunostaining for M1 and M2 surface markers on THP-1 macrophages polarised by IL-4 released from 5% SPAK on day 15. CD206 / mannose receptor was chosen as an M2 surface marker, Calprotectin was

chosen as an M1 surface marker. DAPI was used as a nuclear stain. Scale bar = 40μm.

During polarisation with 12ng/mL released IL-4 the viability of cells was tested on days 3 and 6 by ToxiLight™ bioassay. At day 3 there was no significant difference between all groups, with M0, M1, M2 (12ng/mL) and Released IL-4 (12ng/mL) having 96%, 93%, 96% and 95% viability respectably (Figure 4.11). At day 6 there was no significant difference between all groups, with M0, M1, M2 (12ng/mL) and Released IL-4 (12ng/mL) having 76%, 83%, 80% and 80% viability respectably (Figure 4.11).

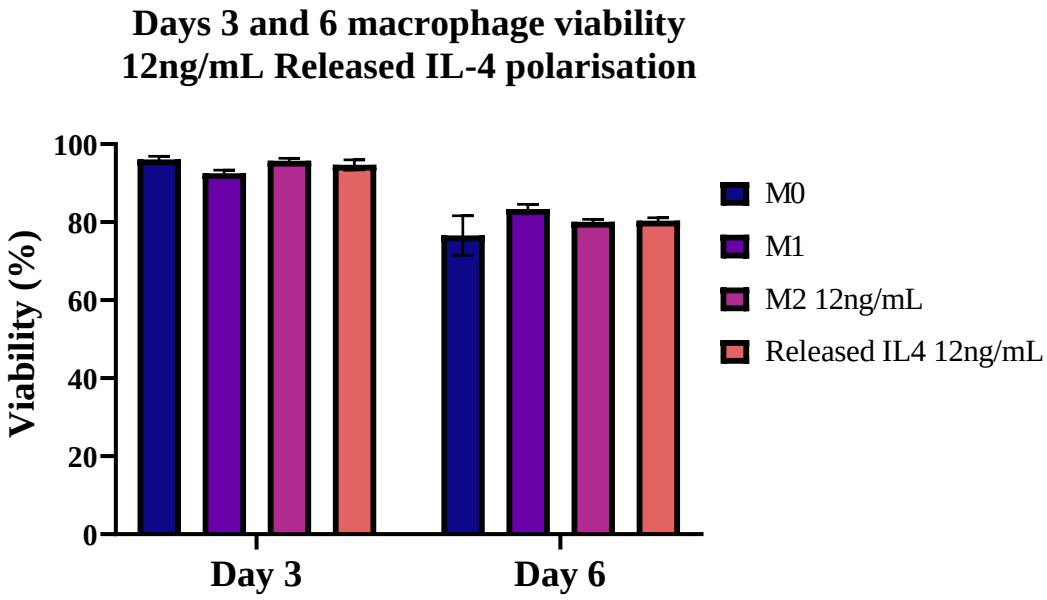

Figure 4.11: Viability of THP-1 macrophages polarised with 12ng/mL IL-4 released from 5% SPAK on days 12 and 15 of in-vitro release. Viability was tested using ToxiLight™ viability assay on days 3 and 6 of culture. Data presented as mean ± standard error of the mean from two independent experiments which each had three experimental repeats per condition (N=2, n=3).

To investigate IL-4 bioactivity at late time points, 5% SPAK 10% release samples from days 48 and 53 were used to polarise THP-1 macrophages.

The IL-4 concentration was 4ng/mL at both time points and independent experiments were carried out using media from day 48 and day 53 time points. THP-1 macrophages polarised by “Released IL-4 4ng/mL” had significantly lower secretion of TNF-α and IL-6 in comparison to “M1” (Figure 4.12 A, B), and a significantly increased secretion of CCL-18 and CCL-22 in comparison to “M0” and “M1” (Figure 4.12 C, D). “Released IL-4 4ng/mL” had CCL-22 secretion that was statistically the same between “M2 4ng/mL” (Figure 4.12, D) and CCL-18 secretion that was slightly lower (Figure 4.12, C, $0.01<P<0.05$). This indicates that IL-4 is still bioactive at days 48 and 53 of in-vitro release.

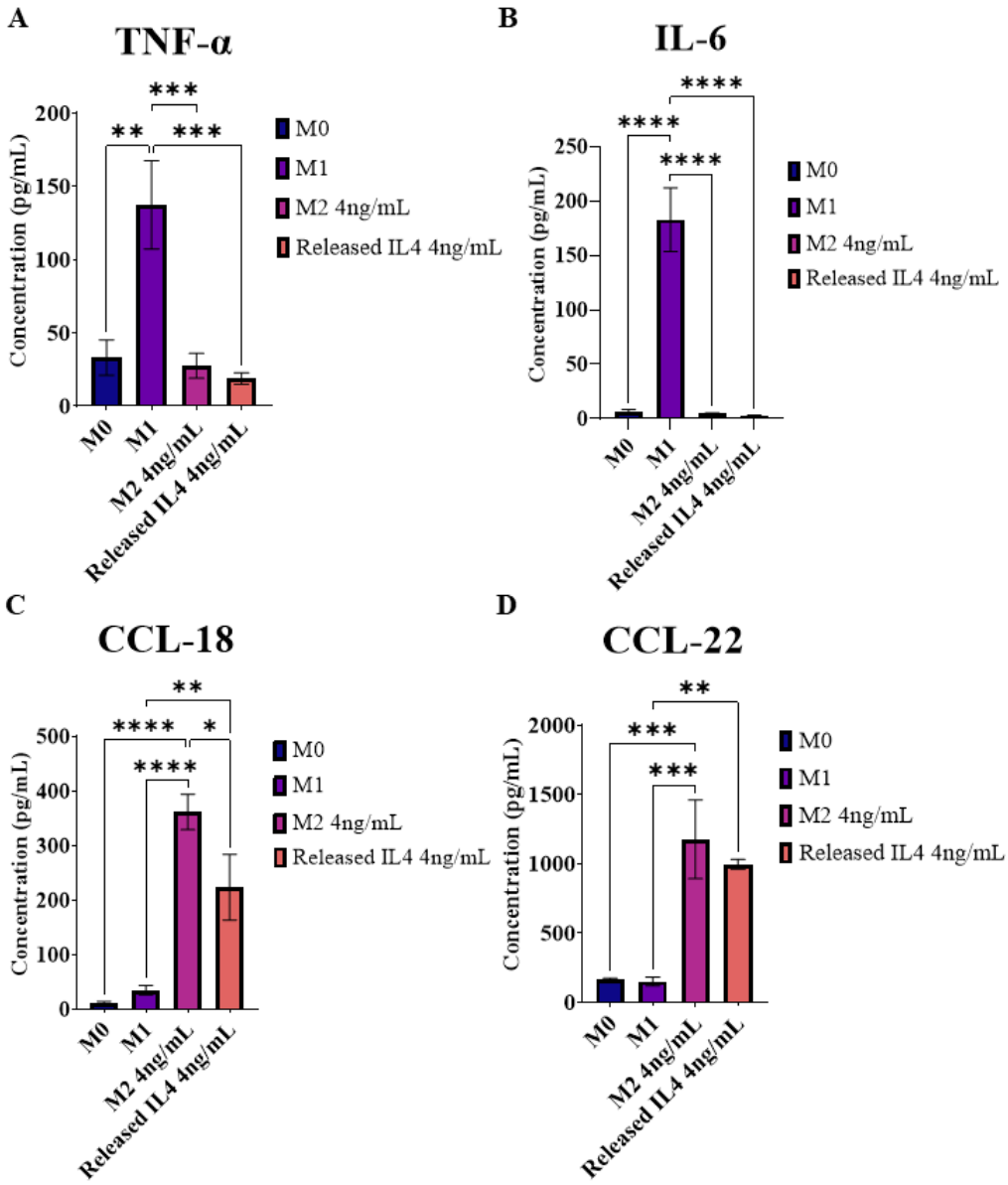

Figure 4.12: Secreted macrophage polarisation markers of THP-1 cells polarised with IL-4 released from 5% SPAK 10% PEGDA at days 48 and 53. TNF-α and IL-6 were selected as M1 markers (A + B). CCL-18 and CCL-22 were selected as M2 markers (C + D). Secreted markers were compared between released IL-4 and stock IL-4 at a concentration of 4ng/mL. Control groups of M0 and M1 polarisation were included. Data presented as mean ± standard error of the mean from two independent experiments which used media samples from day 48 and day 53 of controlled release respectively. (N=2, n=3).

Following one-way ANOVA and Tukey's post hoc multiple comparisons test, pairs with significant differences were labelled as * $P \leq 0.05$, ** $P < 0.01$, *** $P < 0.001$ and **** $P < 0.0001$.

To further investigate polarisation using day 53 IL-4 controlled release media, THP-1 cells were stained for M1 and M2 surface markers after 6 days of culture in polarisation media. "M0" cells had very low staining for both CD206 and calprotectin. "M1" cells showed high staining for calprotectin. Both "M2 4ng/mL" and "Released IL-4 4ng/mL" had visibly raised CD206 staining compared to "M0" and "M1" controls (Figure 4.13). High staining for CD206 and low staining for calprotectin indicates an M2-like polarisation and shows IL-4 was still bioactive at day 53 of in-vitro release.

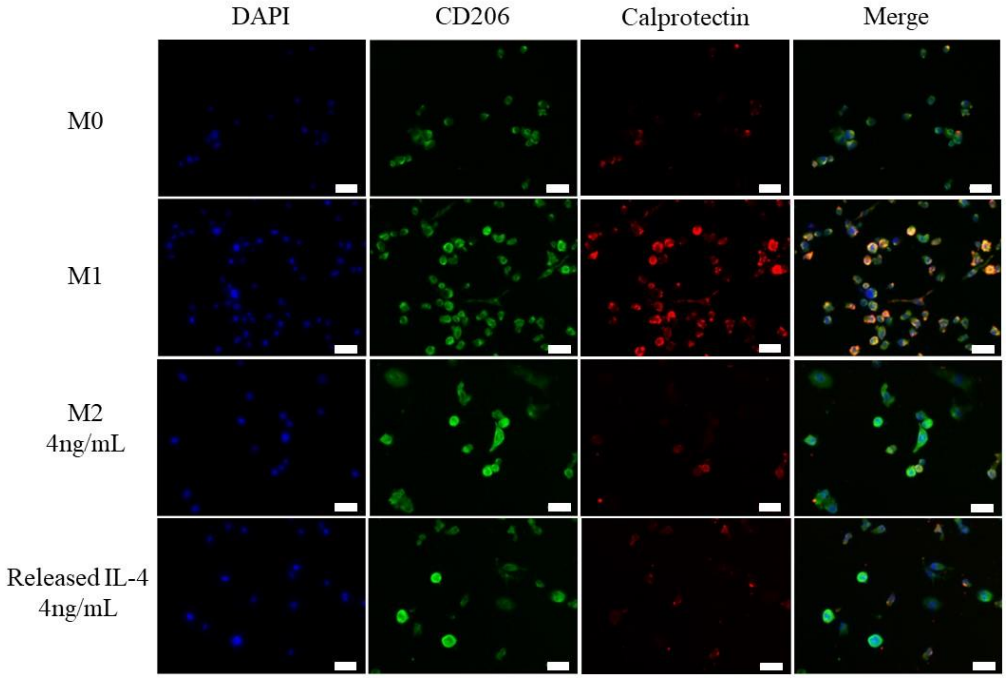

Figure 4.13: Immunostaining for M1 and M2 surface markers on THP-1 macrophages polarised by IL-4 released from 5% SPAK on day 53. CD206 was chosen as an M2 surface marker, Calprotectin was chosen as an M1 surface marker. DAPI was used as a nuclear stain. Scale bar = 40μm.

During polarisation with 4ng/mL released IL-4 the viability of cells was tested on days 3 and 6 by ToxiLight™ bioassay. At day 3 there was no significant difference between all groups, with M0, M1, M2 (4ng/mL) and Released IL-4 (4ng/mL) having 96%, 93%, 95% and 94% viability respectably (Figure 4.14). At day 6 there was no significant difference between all groups, with M0, M1, M2 (4ng/mL) and Released IL-4 (4ng/mL) having 82%, 83%, 84% and 82% viability respectably (Figure 4.14). This indicates that any degradation products that may be present in the conditioned media at days 48 and 53 of in-vitro release are not cytotoxic.

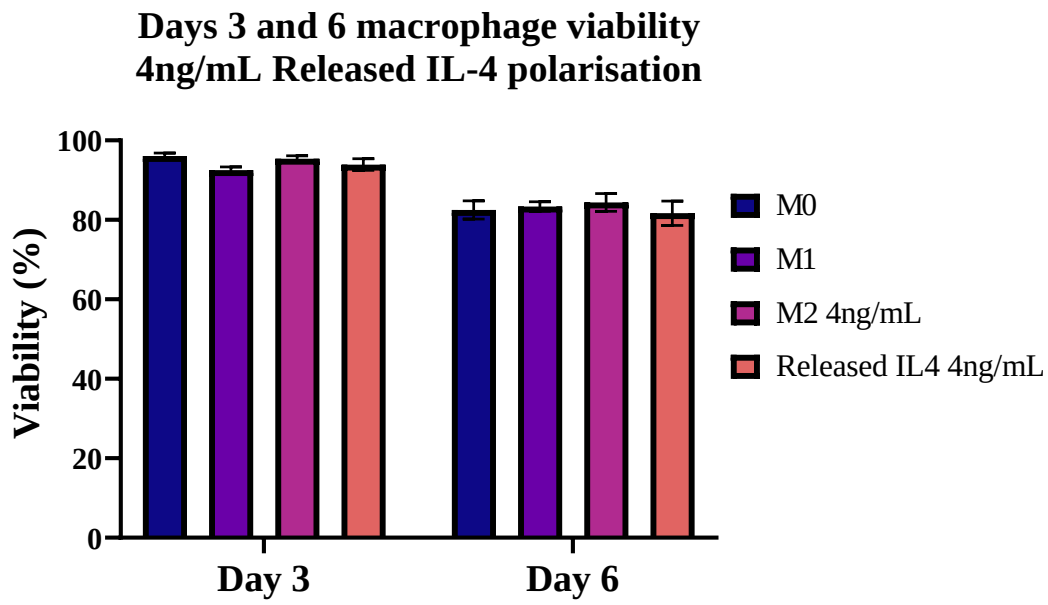

Figure 4.14: Viability of THP-1 macrophages polarised with 4ng/mL IL-4 released from 5% SPAK on days 48 and 53 of in-vitro release. Viability was tested using ToxiLight™ viability assay on days 3 and 6 of culture. Data presented as mean ± standard error of the mean from two independent experiments which each contained three experimental repeats per condition (N=2, n=3).

4.3.5 Investigating sustained IL-4 delivery to THP-1 macrophages from 5% SPAK 10% PEGDA Vs a large bolus IL-4 dose

Due to controlled drug release from biomaterials being a possible alternative to high dose bolus drug injection, an experiment was designed to compare IL-4 sustained delivery to THP-1 macrophages from SPAK PEGDA hydrogels with a single large IL-4 dose to model a bolus injection.

To investigate if the sustained delivery of IL-4 from 5% SPAK 10% PEGDA was more beneficial than a single large IL-4 injection, IL-4 loaded hydrogels were incubated directly with THP-1 cells for 6 days. The well size was scaled up to 6-well with one million cells seeded at 500,000 cells per mL to match the 2mL volume used for IL-4 in-vitro release. Following 6 hours exposure to 50ng/mL PMA and 24 hours rest in THP-1 complete media, IL-4 loaded 5% SPAK 10% PEGDA hydrogels were placed in the well with THP-1 macrophages. 100μL SPAK PEGDA hydrogels were hemispherical in shape and were placed upside-down with the apex in contact with monolayer cells so that minimal hydrogel area was in contact with monolayer cells (Supplementary Figure S.11 Appendix 1).

An IL-4 bolus group was included with a matched total IL-4 dosage to what was estimated to be released from 5% SPAK 10% PEGDA in 6 days (404ng). Secreted polarisation markers and cell viability were compared between IL-4 releasing 5% SPAK 10% PEGDA hydrogels (IL4 Gel) and the 404ng bolus dose of IL-4 (IL4 bolus). IL-4 Gel and the IL-4 bolus were compared in the presence of an M0 promoting stimulus (50ng/mL M-CSF) to investigate the delivery methods in benign conditions.

The IL-4 delivery methods were also compared in presence of an M1 promoting stimulus (20ng/mL IFN-γ + 50ng/mL GM-CSF) to model IL-4 delivery to macrophages in hostile environments such as the pro-inflammatory osteoarthritic joint (IL-4 gel + M1, IL-4 bolus + M1).

A control group was included that contained 5% SPAK 10% PEGDA hydrogels without any IL-4 loading and was cultured with THP-1 macrophages with 50ng/mL M-CSF (Control gel).

Control groups containing "M0" (50ng/mL M-CSF) and "M1" (20ng/mL IFN-γ + 50ng/mL GM-CSF) in monolayer were included as comparisons to typical culture conditions.

"Control gel" had low secretion of all markers which was expected (Figure 4.15 A-D). When cultured with 50ng/mL M-CSF, IL-4 releasing SPAK PEGDA hydrogels (IL-4 Gel) elicited a small but non-significant increase in CCL-18 secretion compared to the "Control gel" group (Figure 4.15 C). In the presence of 20ng/mL IFN-γ + 50ng/mL GM-CSF, IL-4 releasing hydrogels (IL-4 Gel) elicited statistically higher secretion of CCL-18, TNF-α and IL-6 in comparison to "Control Gel" (Figure 4.15 A, B, C).

When cultured with 50ng/mL M-CSF, the "IL-4 bolus + M0" group had increased CCL-18 and CCL-22 secretion that was significantly than the "IL-4 gel + M0" group (Figure 4.15 C, D). In the presence of 20ng/mL IFN-γ + 50ng/mL GM-CSF, the "IL-4 bolus + M1" group had increased secretion of all 4 markers (Figure 4.15 A-D), IL-6 and CCL-18 were significantly lower than the "IL-4 gel + M1" group and CCL-22 was significantly higher in bolus groups than all others (Figure 4.15 C, D). The "IL-4 gel + M1" condition showed

enhanced TNF-α and IL-6 secretion in comparison to the M1 control condition as well as high CCL-18 secretion (Figure 4.15 A, B, C).

This result indicates that neither IL-4 delivery method was able to reduce the M1 promoting stimulus. This experimental design was limited by the finite amount of time THP-1 macrophages can be cultured in-vitro which then limited the dosage of the comparative IL-4 bolus model. (Limitations discussed further in section 4.4)

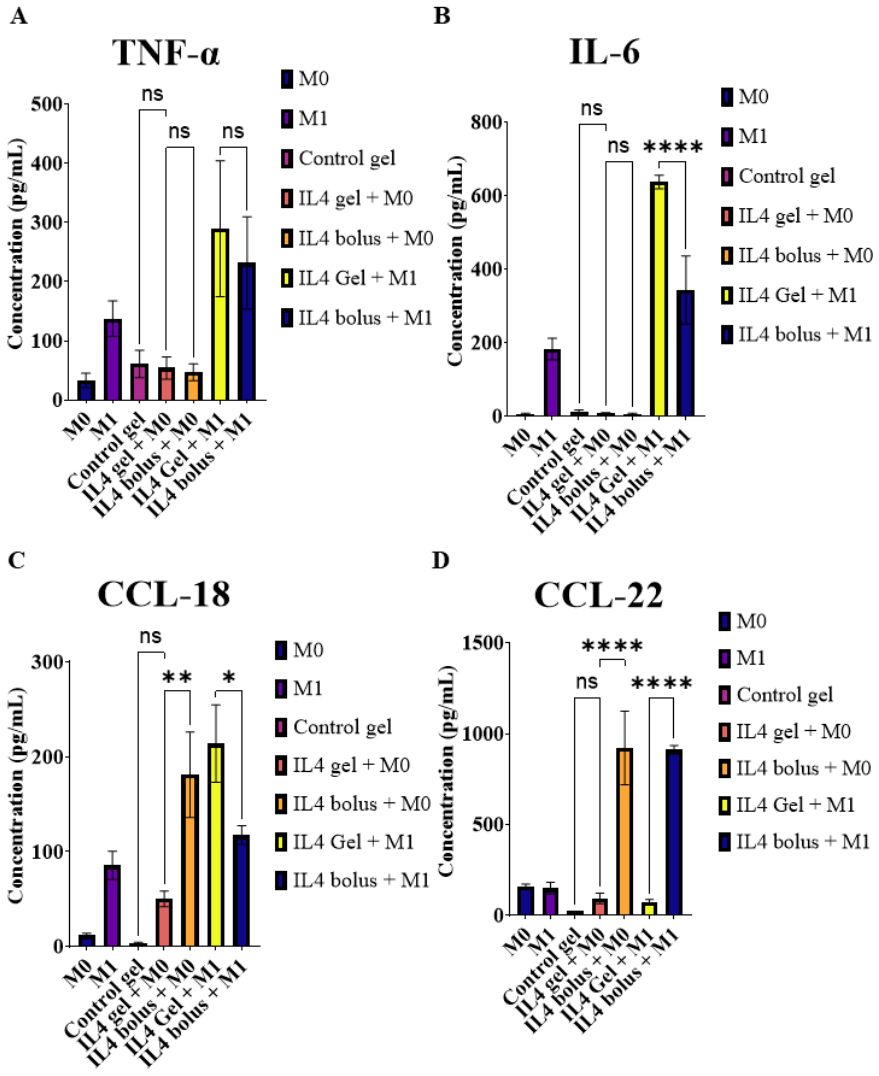

Figure 4.15: Secreted macrophage polarisation markers of THP-1 cells polarised by direct incubation with an IL-4 releasing 5% SPAK 10%

PEGDA hydrogel and with a large IL-4 bolus injection model. TNF-α and IL-6 were selected as M1 markers (A +B). CCL-18 and CCL-22 were selected as M2 markers (C + D). Control groups of M0 and M1 in monolayer were included. A 5% SPAK 10% PEGDA with no IL-4 loading condition was included as "Control Gel" group. Sustained IL-4 delivery from 5% SPAK 10% PEGDA hydrogels was compared to a single large IL-4 bolus dose with a matched total dose of 404ng in its ability to promote M2 polarisation when applied to THP-1 macrophages. IL-4 delivery methods were compared in the presence of M0 (50ng/mL M-CSF) and M1 (20ng/mL IFN-γ + 50ng/mL GM-CSF) promoting conditions. Data presented as mean ± standard error of the mean from two independent experiments (N=2, n=3). Pairs with significant differences using one-way ANOVA with Tukey's post hoc multiple comparisons test were labelled as ns $P>0.05$, * $P\leq0.05$, ** $P<0.01$, *** $P<0.001$ and **** $P<0.0001$.

On day 1 of polarisation cells were viewed by brightfield microscopy. It was observed that cells culturing under the hydrogel apex had a flattened morphology (Figure 4.16 C, centre of image) in comparison to typical monolayer which highlights a limitation of this experimental method (Figure 4.16 A, B). At the periphery of the area of contact between hydrogel apex and monolayer cells, detached cells could be seen (Figure 4.16 D, bottom left corner). This observation was considered when interpreting the viability data.

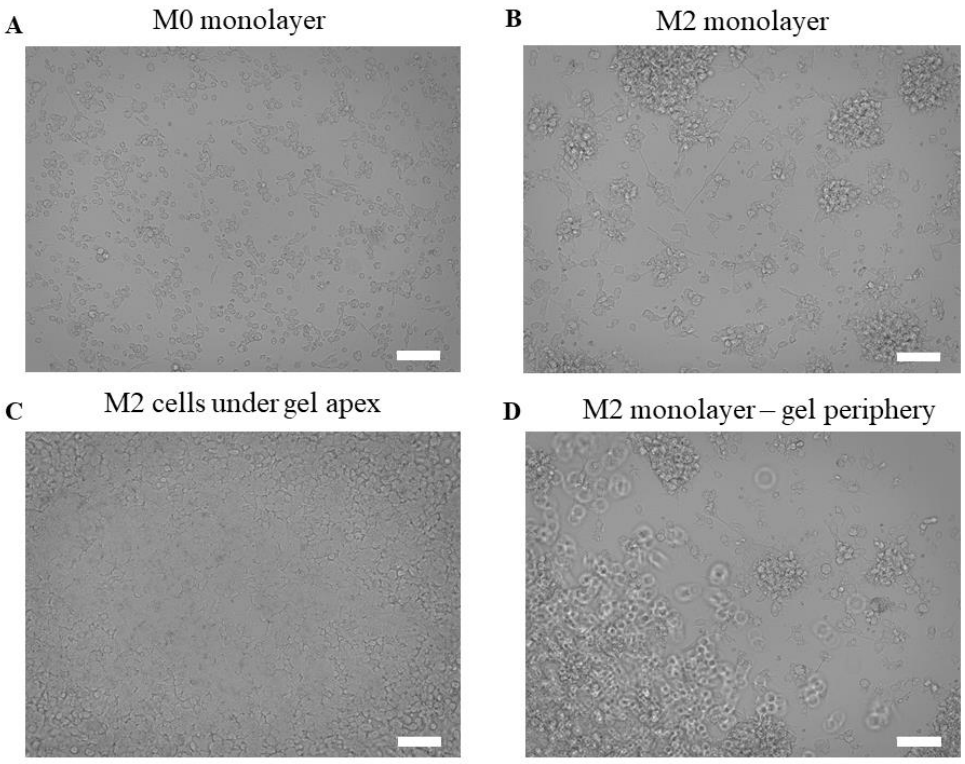

Figure 4.16: Characterisation of THP-1 cell morphology in culture beneath 5% SPAK hydrogels. Cells were viewed on day 1 of polarisation. Scale bar = 100μm.

During polarisation with 5% SPAK hydrogels and IL-4 bolus models, the viability of cells was tested on days 3 and 6 by ToxiLight™ bioassay. At day 3 there was significantly reduced viability in M1, IL-4 Gel + M1, and IL-4 bolus + M1 groups which had 93%, 92% and 92% viability in comparison to M0, Control Gel, IL-4 Gel + M0, and IL-4 bolus + M0 groups which had 96%, 96%, 97% and 97% viability respectably (Figure 4.17 A). At Day 6 there was no significant difference between any experimental groups (Figure 4.17 B). The scaling up of well size for hydrogel incubation experiments meant that one million cells were present in each well, the population of cells seen to be flattened under SPAK PEGDA hydrogels was likely a statistically insignificant amount out of the total population in the well.

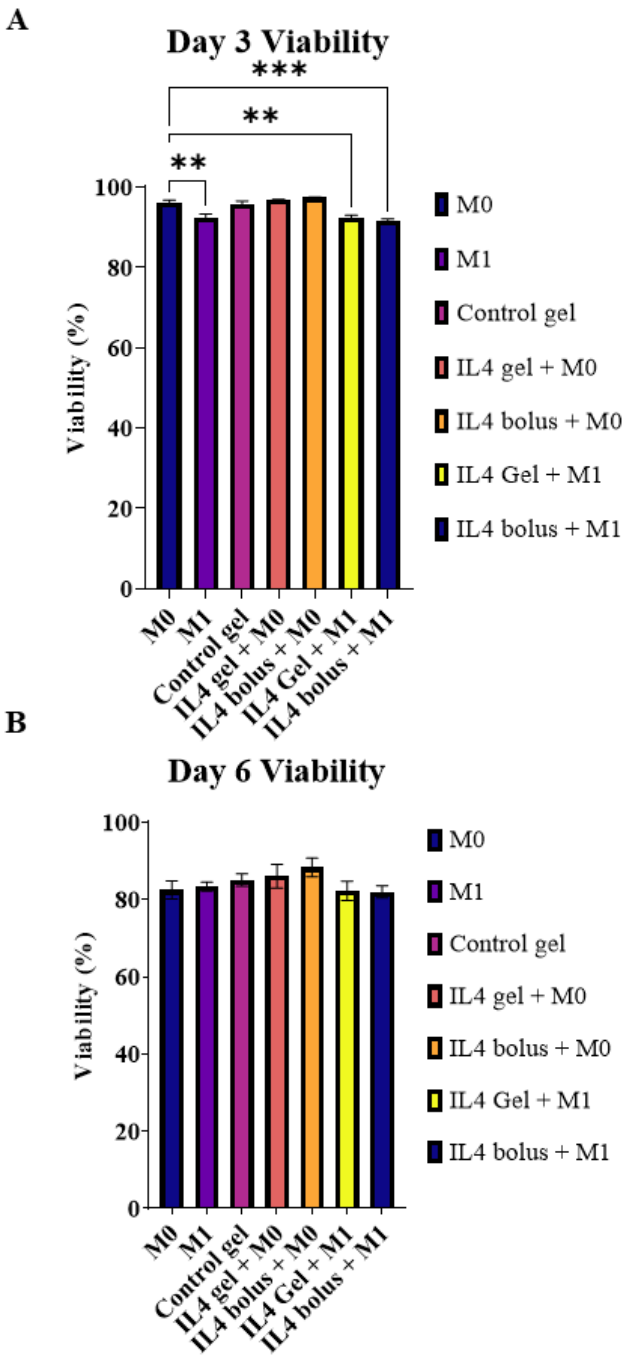

Figure 4.17: Viability of THP-1 cells polarised by incubation with IL-4 releasing 5% SPAK and IL-4 bolus injection models. Viability was tested using ToxiLight™ viability assay on days 3 and 6 of culture. Data presented as mean ± standard error of the mean from two independent experiments (N=2, n=3). Pairs with significant differences were labelled as * P≤0.05, ** P<0.01, *** P<0.001 and **** P<0.0001.

4.4 Discussion

This chapter aimed to modify the protein loading method for SPAK PEGDA hydrogels in order to separate cytokine loading from photoinitiator with the goal of achieving controlled release of IL-4 for multiple months in the ng/mL concentration range that is used for in-vitro macrophage polarisation. IL-4 was selected as the cytokine for controlled release because previous reports in OA animal models showed repeated injection of IL-4, or an IL-4 IL-10 fusion protein to elicit chondroprotective effects[324,326], suggesting that its controlled delivery to the osteoarthritic joint may delay progression of the disease as a possible DMAOD. Hydrogels containing SPAK and PEGDA were selected as the material of choice for IL-4 release because data from chapter 3 of this thesis showed the material combination to give a potent effect in controlling the release rate of lysozyme based on electrostatic affinity between SPAK and the net charge of lysozyme (Chapter 3 Figure 4).

Following IL-4 loading by hydrogel immersion, a non-linear release trend was observed from 5% SPAK 10% PEGDA which is consistent with previous reports that did not achieve a zero order release for IL-4. The IL-4 release from 5% SPAK 10% PEGDA was sustained in the ng/mL range for 73 days. This period of quantifiable release is considerably longer than previously affinity based cytokine and growth factor release methods using heparins and sulfated alginates which have typically shown release for 1-3 weeks[312–314,322,323,356,397].

73 days is less time than the longest reports for in-vitro protein release. In particular, the longest time period reported for in-vitro protein controlled release is 8 months by Lau et al. in 2021 which used controlled material degradation[300].

A major limitation of the aforementioned study and most other protein release studies is that the protein concentration released at each time point is far above the ng/mL therapeutic range for biological function. Long term protein release studies often use time points that are multiple days apart, given that the in vivo half-life of IL-4 is reported to be 19 minutes following systemic injection[311] and 45 minutes following injection into the knee[398], it is likely the dosage released from a hydrogel would be different in vivo due to the altered differentiation kinetics which makes extrapolating in-vitro data collected under simple conditions to in-vivo applications challenging. Release rate may have to be matched more closely to the in-vivo half-life and it may be the case that a higher release rate is needed to maintain the IL-4 concentration within the therapeutic range in the synovial fluid than would be estimated from simple in-vitro data.

The release trend was expected to be linear based off of the preliminary data in Chapter 3 showing SPAK to have a potent effect in controlling the release of lysozyme (Chapter 3 Figure 4). However, a biphasic release trend was observed with initial burst release followed by a moderately linear phase (Figure 4.4 A). A previous report by Weber et al. 2009 used a similar protein loading method and saw a burst release trend in PEGDA discs of 0.4mm thickness that were loaded by immersion[339]. The 100µL hydrogels used in this chapter are thicker than the discs used by Weber et al. which means it is likely that the IL-4 did not penetrate to the core of the hydrogels during loading. If the IL-4 was mostly near the surface then it would explain why the release trend was not as linear as expected because not all of the 5% w/v of SPAK present in the hydrogels would have come into contact with free IL-4 to sequester, whereas in the original loading method used in Chapter 3 it is likely all of the encapsulated protein had

come into contact with SPAK during the mixing and vortexing of the gel precursor solution.

When considering the IL-4 release from SPAK PEGDA hydrogels, the major limitation in the method used in this study was the reduced control over IL-4 loading onto 0%, 1% and 5% SPAK in which 5% had approximately triple the IL-4 dosage (Figure 4.3). Despite being incubated in identical IL-4 solutions for loading, the increased loading of 5% SPAK can be explained by multiple mechanisms. The increase in hydrogel weight of 58.2% by 5% SPAK 10% PEGDA during in-vitro swelling is expected to result in a larger surface area for IL-4 to diffuse through the swollen network of 5% SPAK 10% PEGDA would also have a larger mesh size to allow IL-4 to diffuse further into the core of the gel in comparison to 0% and 1% SPAK. Finally, IL-4 has an iso-electric point of 9.4 meaning it would be electrostatically attracted to the negatively charged chemical groups of SPAK in the 5% SPAK group. Future studies utilizing this method could achieve equal IL-4 loading in each condition by altering the concentration of IL-4 each group is incubated in.

The experimental parameters used in this chapter for IL-4 release should be optimised in the future in order to improve the IL-4 release trend. The IL-4 concentration used in the loading solution could be further optimised by using higher concentrations than the 2.2μg/mL used in this study. The incubation time for IL-4 loading could be increased from 24 hours to time periods of multiple days to further increase IL-4 loading. It is likely that a linear controlled release trend and a longer period of sustained release will be achieved with the combination of increased IL-4 loading paired with increased SPAK concentration to control the release rate. This optimisation process would be

financially expensive in preparing high concentration solutions of IL-4 with sufficient volumes to immerse each hydrogel in a separate bathing solution for loading, especially considering the number of different experimental groups if using multiple SPAK concentrations, IL-4 concentrations, and IL-4 loading times for full process optimisation. This process would also be time consuming because to determine if each experimental group had improved controlled release it would take multiple weeks or months before the release trend of each condition could clearly be seen. The repeated use of ELISA to quantify released IL-4 at each time point is time consuming, financially expensive and could be automated in the future if optimisation is pursued.

3D printing of SPAK PEGDA hydrogels could further improve IL-4 loading in comparison to the casting method used in this study. Hydrogels printed with macroporous architectures would allow more efficient penetration of IL-4 into the core of the hydrogel and the increased surface area to volume ratio would provide a larger area for IL-4 to diffuse into the hydrogel during loading. In the context of delivering IL-4 releasing hydrogels to patients with early osteoarthritis, 3D printing could also be utilised to generate microscale hydrogels containing SPAK and PEGDA that could be loaded with IL-4 and injected into the joint space with minimal invasiveness.

IL-4 released from 5% SPAK 10% PEGDA was shown to be bioactive for more than 50 days as evidenced by the secretion of M2a markers CCL-18 and CCL-22 by THP-1 macrophages polarised with “Released IL-4”, which were significantly higher than M0 and M1 controls in all six time points tested (Figure 4.12 C, D). Immunostaining showed CD206 / mannose receptor staining to be visibly raised in “Released IL-4” at the day 53 time point and in its matched

"M2 4ng/mL" control. However, Mannose receptor staining was lower than expected in Released IL-4 and M2 controls at the other time points tested (Figures 4.7, 4.10) which suggests it may not be a reliable marker in this cell line used in this study. Consistent with this, THP-1 have previously been reported to have low CD206 / mannose receptor expression[392,393] which indicates that an alternative M2 surface marker could be used for this cell line in the future such as CD-163.

The absence of IL-6 or TNF-α in the media of "Released IL-4" experimental groups indicates that degradation products from 5% SPAK 10% PEGDA hydrogels that may be in the conditioned media do not elicit a pro-inflammatory response (Figures 4.6, 4.9 and 4.12). The viability of THP-1 cells in "Released IL-4" experimental groups was not significantly reduced in comparison to corresponding M2 controls which suggests any gel degradation products that could be in controlled release conditioned media is not cytotoxic (Figures 4.8, 4.11 and 4.13).

THP-1 is a cell line originating from a single acute myeloid leukaemia patient which means sub populations are expected to have minimal batch to batch variation. Despite polarisation studies showing key similarities between THP-1 and peripheral blood monocyte differentiated macrophages (PBMCs)[255,390,391], there is also evidence showing differences including cytokine production in response to lipopolysaccharide[256]. Hence, data that is more clinically representative could be obtained using PBMCs isolated from multiple donors. However, a well-known drawback to this approach is the donor to donor variability in PBMCs which can make it challenging to obtain in-vitro data that shows statistical significance. A reason for this difficulty is the anonymisation

of donor blood samples that are available for research, given that OA is known to be age related, that immune cell signalling varies based on patient age, and that sex dependent differences in immune responses have been observed, it means the difference in cell response between biological repeats may be vastly different due to unknown variety in donor demographics.

In-vitro experiments using controlled release conditioned media could be modified to better model immunomodulation in osteoarthritis. Macrophages could be polarised with controlled release conditioned media and then be co-cultured with chondrocytes that have been primed with a pro-inflammatory stimulus. Secreted markers from inflammatory chondrocytes that are associated with the progression of OA, such as MMP-13[399] could be quantified in the media by ELISA to determine if the secretome of macrophages polarised by controlled release can significantly reduce the secretion of OA related factors such as MMP-13 from chondrocytes to model the avoidance of cartilage degradation in OA.

The direct incubation of IL-4 releasing SPAK PEGDA hydrogels with THP-1 macrophages in the presence of an M1 promoting stimulus resulted in enhanced secretion of TNF-α, IL-6 and CCL-18 in comparison to the M1 control (Figure 4.15). Presence of both M1 and M2 markers indicates that there is a heterogeneous population of THP-1 macrophages in which some macrophages are polarised towards M1 and others towards M2. In 2021, single cell RNA sequencing of murine bone marrow derived macrophages showed unique transcriptional states when treated with a combined M1 and M2 stimulus in comparison to either of the stimuli separately[400] which offers an alternative explanation.

This experimental approach had multiple limitations that could be reduced in the future by modifying the experimental design. Despite the direct contact of SPAK PEGDA hydrogels not significantly reducing the viability (Figure 4.18 B), this phenomenon could be easily avoided in the future by using a transwell insert to separate the IL-4 releasing hydrogel from a monolayer of macrophages beneath.

The IL-4 bolus injection model used in this experiment was more than ten times the reference concentration (202ng/mL) and was expected to significantly lower the viability of THP-1 macrophages but it was not observed. Due to being a cancer cell line, it is likely THP-1 cells are more resilient to high doses of cytokine than primary PBMCs. To confirm this, future experiments exploring macrophage polarisation from cytokine releasing hydrogels should use primary PBMCs and determine if sustained IL-4 delivery from controlled release maintains macrophage viability in comparison to a large bolus dosage.

The bolus dosage was chosen as a match the estimated cumulative dose released from 5% SPAK 10% PEGDA in six days because suspected dedifferentiation of THP-1 macrophages into non-adherent monocytes was observed if culture exceeded 6 days. This observation is consistent with a previous report that observed THP-1 dedifferentiation after 7 days[389]. Ideally the in-vitro comparison of sustained IL-4 delivery from a biomaterial to a bolus IL-4 injection would run for significantly longer than 6 days but it will always be limited by the in-vitro lifespan of macrophages. A comparison over a longer period of time would more likely see the difference between a single large bolus dose of IL-4 and the sustained delivery of IL-4 from a biomaterial in the therapeutic concentration range.

Immunomodulation should be studied in vivo by implanting IL-4 releasing SPAK PEGDA hydrogels subcutaneously in rats. Foreign body response can be investigated from IL-4 releasing hydrogels compared to unloaded controls containing no IL-4. While not directly related to treating early osteoarthritis, a significant reduction in the thickness of the fibrotic capsule surrounding hydrogels following foreign body response would demonstrate that released IL-4 from SPAK PEGDA has shifted macrophage polarisation towards M2 in-vivo which would be the first step in translating in-vitro data into more biologically relevant systems.

In-vivo osteoarthritis models usually use surgical joint destabilisation to initiate rapid onset of OA which may make studying early OA difficult. Model organisms that are genetically predisposed to OA may be more useful in modelling early intervention therapies such as injection with M2 inducing controlled release biomaterials into affected joints.

Future controlled release experimentation should also consider the release of multiple drugs that promote M2 polarisation as it is likely to be more potent in vivo than IL-4 alone. Multiple cytokine combinations such as IL-4, IL-10 and TGF-β1 may have greater potency in reducing the inflammation in OA than each one individually. The release of other types of M2 promoting drugs such as dexamethasone may be combined with cytokine release to increase potency in reducing inflammation in the knee and preventing OA progression.

4.5 Conclusion

In summary, this chapter has shown:

The loading of IL-4 onto 5% SPAK 10% PEGDA hydrogels by 24 hour immersion resulted in the sustained release of IL-4 in the ng/mL concentration range for 73 days.

When controlled release samples were applied to THP-1 macrophages it was observed that released IL-4 from as late as the day 53 time point was bioactive, as evidenced by increased secretion of the M2 markers CCL-18 and CCL-22, and increased surface expression of mannose receptor.

In the presence of an M1 stimulus, direct incubation of IL-4 releasing 5% SPAK 10% PEGDA hydrogels with THP-1 macrophages resulted in enhanced secretion of CCL-18, TNF-α and IL-6 in comparison to the M1 control which indicated the presence of a heterogeneous population of pro-inflammatory and anti-inflammatory macrophages.

When comparing IL-4 delivery from 5% SPAK 10% PEGDA hydrogels to a bolus injection model containing more than 10 times the reference concentration of IL-4, the bolus model did not significantly reduce the viability of THP-1 macrophages.

The limitations of the experimental approaches chosen were discussed and recommendations for future work were made.

Chapter 5 - Additive manufacturing of affinity hydrogels for controlled protein release

5.1 Introduction

Additive manufacturing technology enables the fabrication of materials with complex architectures that would be difficult or impossible to produce with traditional casting and moulding methods[162]. Three-dimensional (3D) printing technologies have gained much interest in the field of regenerative medicine for purposes such as generating scaffolds with interconnected pore networks that facilitate cell invasion into the scaffold core[163], printing topographic architecture and pores to influence cell attachment and differentiation[164,165], and to print patient specific implants with geometries matching anatomical defect sites[166].

In the field of controlled release, 3D printing has been used to produce tablets containing small molecule drugs including ibuprofen and dexamethasone[343,344]. 3D printing of geometries with varying surface area to volume ratios has been explored briefly as a mechanism to influence paracetamol elution rate from poly(ethylene glycol) diacrylate (PEGDA). The controlled release of biomacromolecules such as cytokines and growth factors from biomaterials remains challenging due to their requirement for structural integrity and the propensity of the structure to become denatured in damaging environmental conditions. Digital light projection (DLP) is a vat polymerisation technique that

is capable of 3D printing photocrosslinkable materials with microscale resolution[342]. Few publications have studied protein release from DLP 3D printed hydrogels and the reported data is limited. Gong et al. reported rapid burst release of Interleukin-4 (IL-4) from DLP printed gelatin methacrylate (Gel-MA)[332]. Wang et al. produced a DLP printed hydrogel using thiolated heparin and glycidyl methacrylate conjugated hyaluronic acid for the purpose of vascular-endothelial growth factor (VEGF) and platelet derived growth factor (PDGF) to model the stimulation of angiogenesis[346]. They reported an approximately linear release trend for 28 days but did not collect any bioactivity data or consider how their model may be clinically translatable.

Data from chapter 3 of this thesis showed potential for 3-sulfopropyl acrylate (SPAK) to control the release of lysozyme from 10% PEGDA hydrogels and data in chapter 4 showed IL-4 released from 5% SPAK 10% PEGDA hydrogels to be bioactive after more than 50 days of in-vitro release. Previously, hydrogels were formed by simple moulding and casting which has limited control over hydrogel architecture. The use of 3D printing to generate hydrogels complex architecture may be a useful tool to overcome challenges encountered in controlled release. For example, 3D printing hydrogels with increased surface area to volume ratio may avoid undesirable incomplete release that is often seen in protein and other drug release attempts[283–285] by providing increased total surface area for diffusion to take place out of the hydrogel.

This chapter aims to 3D print SPAK containing PEGDA hydrogels using digital light projection and investigate if the geometry of 3D printed hydrogels may be used to fine tune the release rate of lysozyme.

5.2 Chapter specific methods

Detailed materials and methods can be found in Chapter 2. Chapter specific methods are briefly outlined below for convenience.

5.2.1 Computer aided design (CAD)

3D objects were designed at www.Tinkercad.com and were exported as .STL files. Object files were sliced using Photon workshop 64 software (Anycubic) to generate .pwma files. Photon mono 4k was selected from the machine list. Slice parameters were set to 25µm z thickness, 5mm Z lift distance, 4mms^{-1} Z lift speed and 6mms^{-1} Z retract speed.

5.2.2 Digital light projection 3D printing

Photoinitiator solutions were prepared in Phosphate buffer saline (PBS) using 20mL glass scintillation vials covered in aluminium foil to protect from light. 3D printing solutions contained 0.5% w/v Lithium phenyl-2,4,6-trimethylbenzoylphosphinate (LAP) as photoinitiator, 10% w/v 575Da Poly(ethylene glycol) diacrylate (PEGDA), 2% or 5% w/v 3-sulfopropyl acrylate (SPAK) as appropriate, 0.0255% w/v tartrazine as photoabsorber. For protein release experiments, lysozyme was added at 0mg/mL, 2mg/mL and 10mg/mL as appropriate. Printing was carried out on a Photon Mono 4k printer (Anycubic). Before and after each use the printer vat and build platform were removed and cleaned with isopropanol.

5.2.3 Brightfield microscopy

3D printed hydrogels were gently removed from the printing platform with a paint scraper. Hydrogels were gently dried with laboratory tissue paper to

remove excess monomer and placed onto glass slides for microscopy. Hydrogel pores were viewed by brightfield microscopy at 5X magnification and imaged using an AmScope camera attachment (AmScope MU1403). To estimate pore diameter, 5 pores were imaged from 5 separate hydrogels for each condition. Pore diameter was measured in AmScope software. A known distance of 250 μm was also imaged and measured to establish a pixel to μm ratio. For each condition the length in pixels for each pore diameter was converted into μm.

5.2.4 In-vitro hydrogel swelling

As described (2.2.1 In-vitro hydrogel swelling). Briefly, hydrogels were immersed in PBS and weighed multiple times over a 5 day period. The swollen weight was expressed as a percentage increase from the initial hydrogel weight after UV photocrosslinking.

5.2.5 Hydrogel compressive testing

As described (2.2.1 hydrogel compressive testing). Briefly, compressive modulus was characterised by compressing swollen hydrogels using a texture analyser with a 5kg load cell. The compressive modulus was calculated as the gradient of the linear section from the stress-strain curve.

5.2.5 Cryo-Scanning electron microscopy (Cryo-SEM)

As described (2.2.6 Cryo-SEM). Briefly, 5% SPAK 10% PEGDA hydrogels were cut into small sections using a scalpel. Samples were mounted onto SEM stubs and were then plunge frozen and transferred into the cryo-preparation chamber and fractured, sublimed at -90 ^{o}C for 30 minutes. Samples were sputter coated with platinum using a current of 10 mA for 60 seconds. Imaging was performed at 10 kV under cryo conditions.

5.2.6 In-vitro lysozyme release from 3D printed hydrogels

Lysozyme containing hydrogels were 3D printed, each immersed in 4mL PBS and incubated at 37^{o}C with well-plates sealed using laboratory tape. At each controlled release time point the entire volume of PBS was aspirated and replaced with fresh PBS to re-establish the diffusion gradient. For each hydrogel the PBS at every time point was stored in a separate 7mL bijou at -20^{o}C until the time for analysis by Bradford assay (2.2.3 Bradford assay).

5.2.7 Lysozyme bioactivity assay

As described (2.2.4 lysozyme bioactivity assay). 100µL of controlled release sample was added to 1.5mL of Micrococcus lysodeikticus and mixed by inversion. The decrease in absorbance at 450nm was measured once per minute for 5 minutes using a UV-Vis spectrophotometer. For each sample, a control was run simultaneously which was prepared from stock lysozyme with a matched concentration. The decrease in absorbance of each controlled release sample was expressed as a percentage of the decrease measured in its matched control.

5.2.8 Statistical analysis

All numerical data is presented as mean ± standard deviation from 3 repeats per experimental condition. When quantifying protein release from hydrogels the limit of detection (LOD) and limit of quantification (LOQ) were calculated as 3 and 10 standard deviations above the average blank standard respectably[352,354]. One-way ANOVA with Tukey's post hoc multiple comparisons test (α=0.05) was used to determine significant differences between experimental groups where three or more are present on a column

graph. Student's t-test was used to compare the means between two experimental groups. Pairs with significant differences were labelled as * $P \leq 0.05$, ** $P < 0.01$, *** $P < 0.001$ and **** $P < 0.0001$.

5.3 Results

5.3.1 Computer aided design

To investigate the effect of hydrogel geometry on protein release, porous and non-porous 3D object designs were created at www.TinkerCAD.com that had high and low surface area to volume ratios respectively. The porous design was a cuboidal prism measuring 11mm x 11mm x 0.6mm that contained 25 pores measuring 1mm x 1mm x 0.6mm in a 5 by 5 grid (Figure 5.1 A). Each pore was spaced 1mm apart and 1mm from the periphery of the hydrogel. The non-porous design was a cuboidal prism measuring 9.79mm x 9.79mm x 0.6mm (Figure 5.1 B). The two designs have approximately equal volumes (57.60mm^3 and 57.51mm^3), but the increased surface area of the porous design meant that its surface area to volume ratio is approximately 1.35 times larger than the non-porous. 3D printing was carried out with 0.025mm layer height, a 30 second exposure for the bottom two layers was used to generate adhesion to the build platform. A 4 second exposure time was used for remaining layers. Default settings for build platform movement were used which were 5mm Z lift distance, 4mms^{-1} Z lift speed, and 6mms^{-1} Z retract speed (Figure 5.1 C). Parameters were chosen after initial process optimisation (Supplementary Table S.1 Appendix 1)

A

Porous design

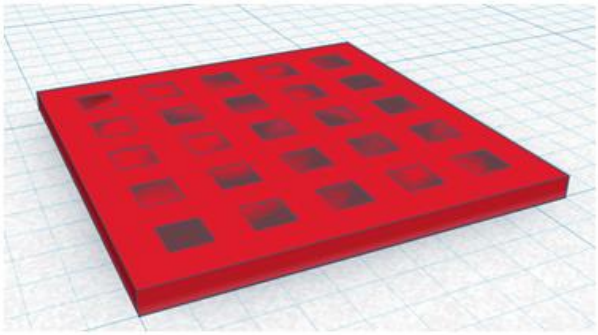

Length 11mm

Width 11mm

Height 0.6mm

Surface area 291.60mm^2

Volume 57.6mm^3

B

Non-porous design

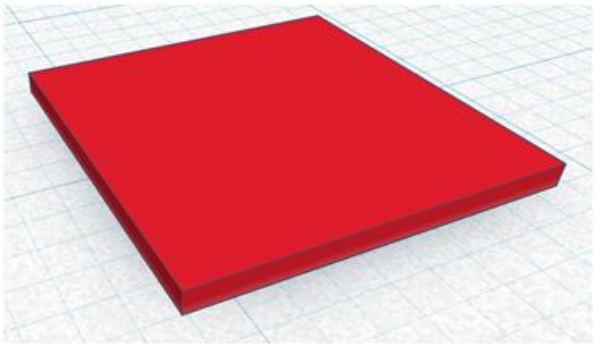

Length 9.79mm

Width 9.79mm

Height 0.6mm

Surface area 215.18mm^2

Volume 57.51mm^3

C Printing parameters

Layer thickness / mm	0.025
Z lift distance / mm	5.00
Z lift speed / mms^{-1}	4.00
Z retract speed / mms^{-1}	6.00
Bottom layer exposure / s	30.00 x 2 layers
Exposure / s	4.00
Power / Watt	45.00

Figure 5.1: 3D object designs were created using Tinker CAD to investigate the effect of surface area to volume ratio on protein release from SPAK PEGDA hydrogels. A) Porous design containing twenty five macropores each measuring 1mm x 1mm x 0.6mm in a 11mm x 11mm x 0.6mm cuboidal prism.

B) Non-porous design measuring 9.79mm x 9.79mm x 0.6mm. C) Parameters for digital light projection 3D printing.

5.3.2 3D printed SPAK PEGDA hydrogel characterisation

Hydrogels were printed with tartrazine (0.0255% w/v) to increase print fidelity (Figure 5.2 A). Tartrazine was used as a photoabsorber to prevent overexposure and improve print fidelity (Supplementary Table S.1, Appendix 1). Following 24 hours incubation in PBS, tartrazine had diffused out of SPAK PEGDA hydrogels as indicated by the visible colour change from yellow to transparent (Figure 5.2 A). Immediately after printing, hydrogel pores were viewed by Brightfield microscopy at 5X magnification (Figure 5.2 B). To estimate the average pore diameter, images of 5 pores from 5 separate hydrogels were taken and measured using AMscope software. Hydrogels containing 2% SPAK 10% PEGDA had a measured pore diameter of 1110.7 ± 36.3µm and 5% SPAK 10% PEGDA had a measured pore diameter of 1115.7 ± 35.4µm (Figure 5.2 C). This indicates that the material combination of SPAK and PEGDA is compatible with DLP 3D printing but that the printing parameters and material composition may be further optimised to increase the fidelity of printed architecture.

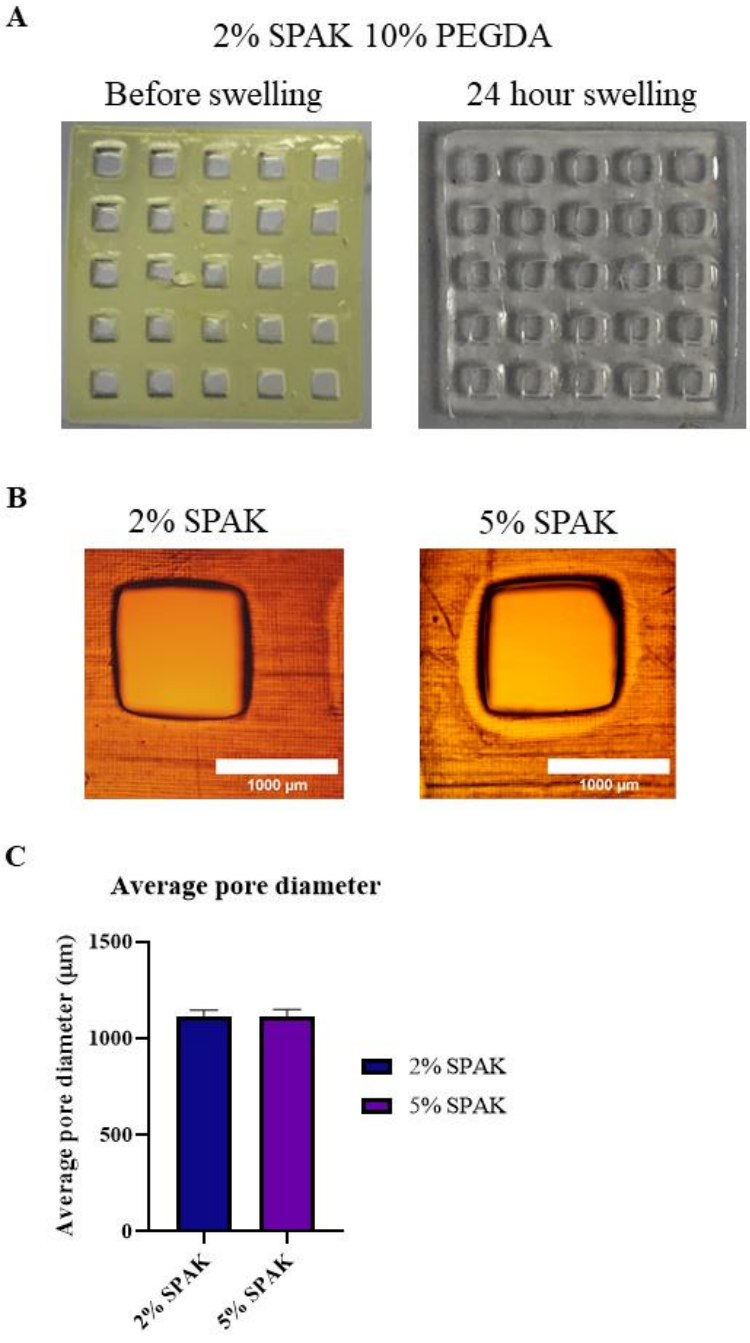

Figure 5.2: 3D printed SPAK PEGDA hydrogels. A) Macroscopic images of a porous 2% SPAK 10% PEGDA hydrogel immediately after printing, and after 24 hours incubation in PBS. B) Brightfield microscopy images showing representative pores from 2% SPAK 10% PEGDA and 5% SPAK 10% PEGDA

hydrogels. C) Average pore diameter estimated from measuring 5 pores from 5 separate hydrogels expressed as mean ± standard deviation (N=5 n=5).

In-vitro hydrogel swelling was characterised over 5 days in PBS. After 5 days, 2% SPAK 10% PEGDA hydrogels with porous and non-porous designs exhibited weight increases of 26.5 ± 10.4% and 28.6 ± 4.9% from the initial weight respectively. 5% SPAK 10% PEGDA hydrogels had weight increases of 51.4 ± 10.1% and 37.1 ± 9.7% for porous and non-porous designs respectively. The increase in swelling seen by 5% SPAK hydrogels can be attributed to there being a higher concentration of hydrophilic charged groups present in the polymer network.

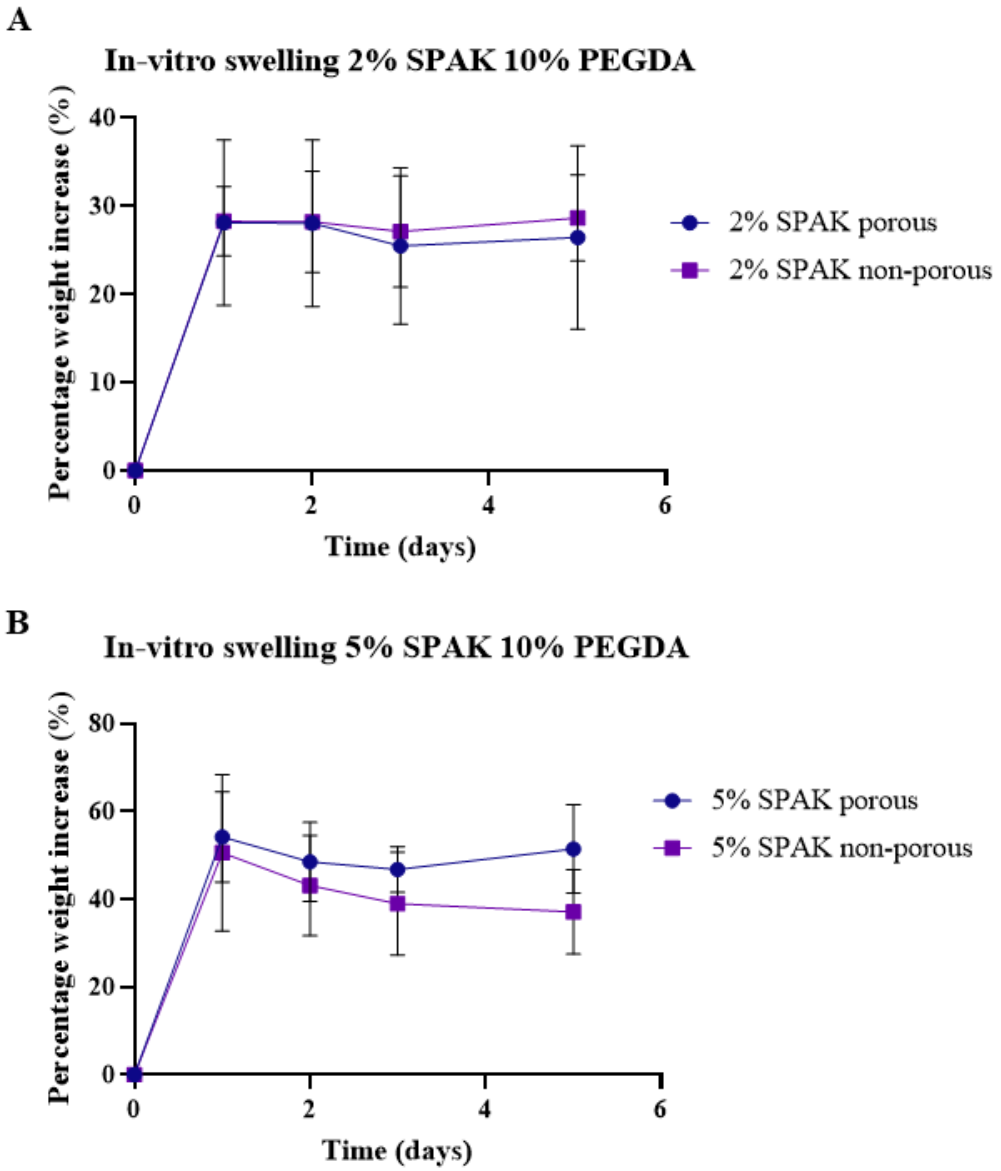

Figure 5.3: 5 day in-vitro swelling of 3D printed hydrogels. A) 2% SPAK 5% PEGDA. B) 5% SPAK 10% PEGDA. Values presented as mean ± standard deviation (n=3).

The thickness of SPAK PEGDA hydrogels was measured with digital callipers. It was determined that 2% SPAK 10% PEGDA hydrogels with porous and non-porous designs had average thicknesses of 0.577 ±0.02mm and 0.580 ± 0.01mm respectively. 5% SPAK 10% PEGDA hydrogels with porous and non-porous designs had average thicknesses of 0.590 ± 0.03 and 0.583 ± 0.02mm

respectively (Figure 5.4 A). A macroscopic image of a porous 5% SPAK 10% PEGDA hydrogel being measured from a side view is included for convenience (Figure 5.4 A). These results indicate complete printing of the 3D design, the slight decrease in the measured values in comparison to the 0.6mm value in the CAD design may be explained by the limitations of the measuring method. It's possible that the gels were pinched slightly while trying to delicately measure them using the callipers. After 5 day swelling in PBS, the compressive modulus of 3D printed hydrogels was characterised using a texture analyser. It was found that 2% SPAK 10% PEGDA hydrogels with porous and non-porous designs had average modulus values of and 2.63 ± 0.15 kPa and 3.2 ± 0.10 kPa respectively. 5% SPAK 10% PEGDA hydrogels with porous and non-porous designs had average modulus values of 2.77 ± 0.31 kPa and 4.3 ± 0.4 kPa respectively (Figure 5.4 B). The significantly increased modulus seen from the non-porous 5% SPAK 10% PEGDA may be explained by the difference in geometry.

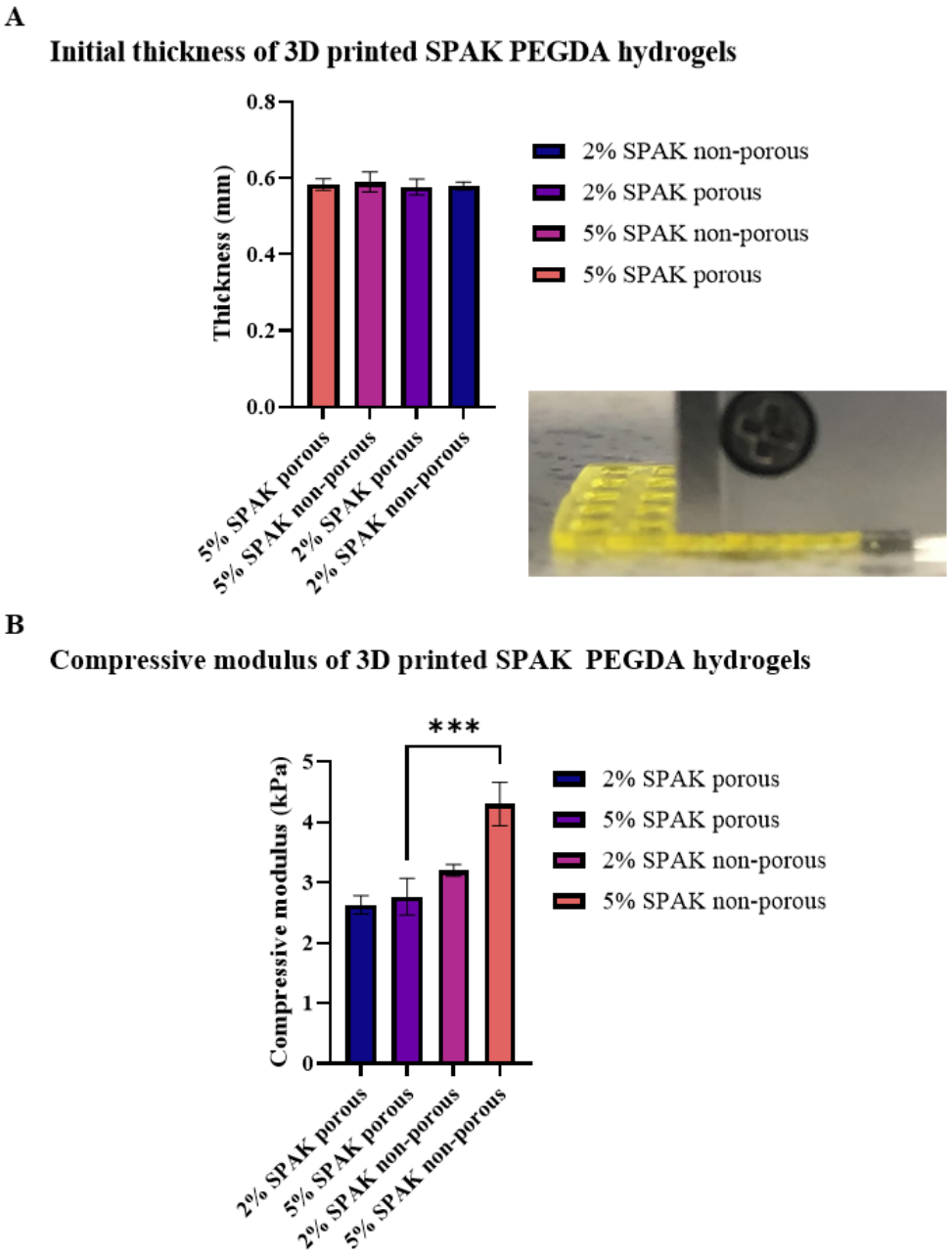

Figure 5.4: Mechanical characterisation of 3D printed SPAK PEGDA hydrogels. A) Average measured thickness of 3D printed hydrogels. B) Compressive modulus of SPAK PEGDA hydrogels with porous and non-porous designs. Following 1-way ANOVA and Tukey's post hoc test, pairs with significant differences were labelled as * P≤0.05, ** P<0.01, *** P<0.001 and **** P<0.0001. Values presented as mean ± standard deviation (n=3).

The surface and cross section of a porous 5% SPAK 10% PEGDA hydrogel was characterised using cryo-SEM (Figure 5.5 A, B). The surface and cross section had microporous architecture which is consistent with previous reports of the PEGDA polymer network formed by chain growth[295] (Figure 5.5 A, B). When viewed by eye, the porosity of the network was approximately consistent throughout the Z plane of the hydrogel which indicates consistent crosslinking in each 3D printed layer (Figure 5.5 B).

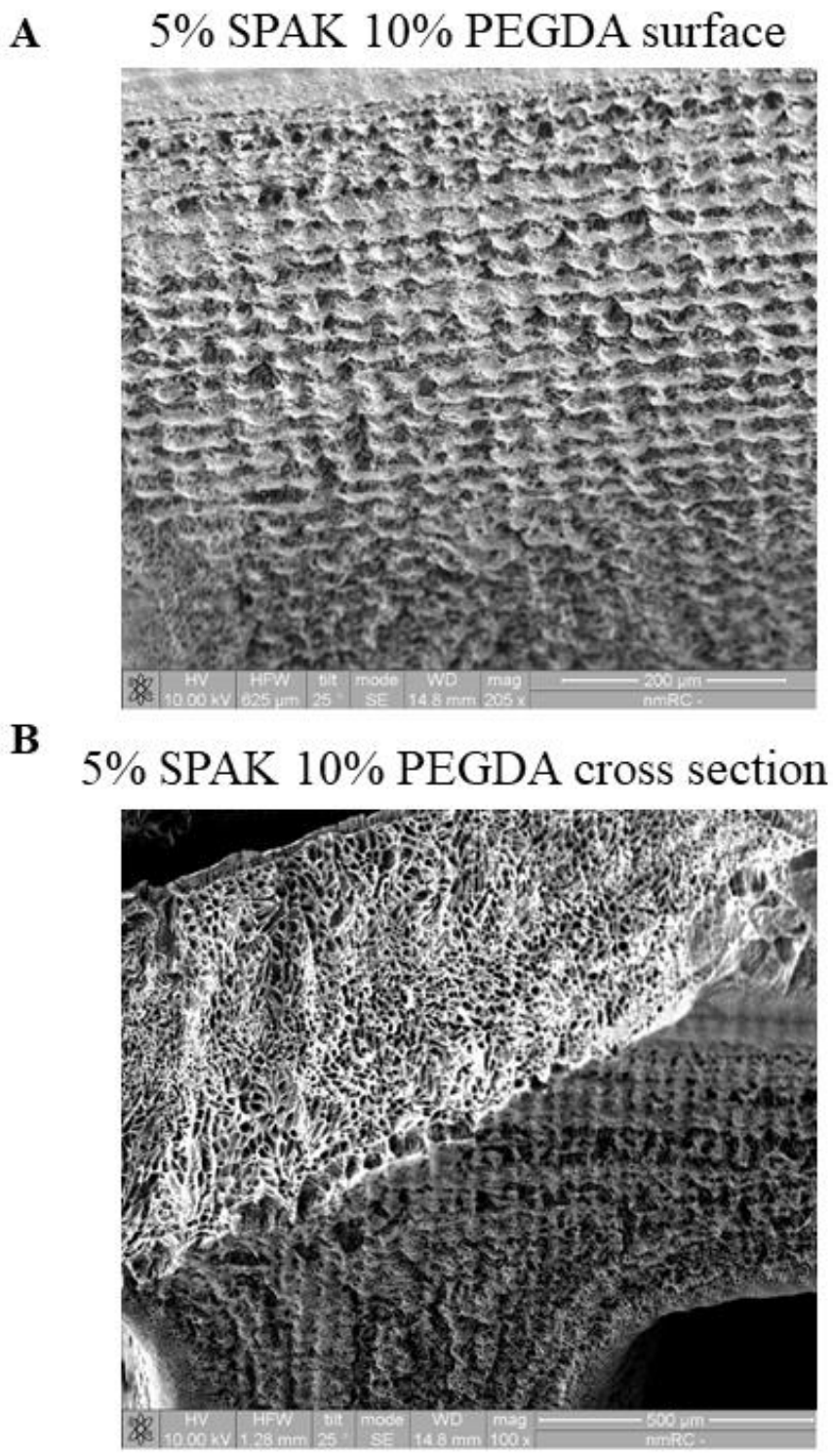

Figure 5.5: Cryo-SEM micrographs of 5% SPAK 10% PEGDA 3D printed hydrogels. A) 5% SPAK 10% PEGDA surface characterisation. B) 5% SPAK 10% PEGDA cross section view.

5.3.3 Lysozyme release from 3D printed SPAK PEGDA hydrogels

To investigate protein release from 3D printed hydrogels, lysozyme was loaded into the photoinitiator solution for 2% SPAK 10% PEGDA and 5% SPAK 10% PEGDA at 10mg/mL and 2mg/mL. Direct loading into the hydrogel precursor solution was chosen so that there was approximately even protein loading between experimental groups. Hydrogels were printed with the porous design and a 15 day lysozyme release experiment was conducted in PBS.

In 10mg/mL lysozyme groups, 2% SPAK 10% PEGDA had 60% release on day 1, 100% after 4 days and had an estimated 115% cumulative release after 15 days (Figure 5.6 A). 5% SPAK 10% PEGDA had 21% release after day 1, 64% release at day 4 and had 95% cumulative release after day 15 (Figure 5.6 A). The decreased release rate in 5% SPAK 10% PEGDA can be attributed to increased electrostatic attraction between lysozyme and the sulfate groups of SPAK. The 2% SPAK group reaching a cumulative release value of more than 100% may be explained by the loading dose being an estimate based on the 3D CAD design.

In 2mg/mL lysozyme groups, 2% SPAK 10% PEGDA had 55% release after day 1, 59% at day 7 and then plateaued until day 15 (Figure 5.6 B). 5% SPAK 10% PEGDA had 21% release after 1 day, 51% at day 7 and then plateaued at 52% from days 9 to 15 (Figure 5.6 B). Similarly to 10mg/mL groups, the decreased lysozyme release rate in 5% SPAK hydrogels may be attributed to electrostatic attraction. The plateau of cumulative released seen in 2mg/mL hydrogels indicates that a significant proportion of the loaded lysozyme is

entrapped within the gel or that the Bradford assay was not sensitive enough to quantify smaller dosages that could have been released at later time points.

The bioactivity of released lysozyme was investigated at the day 3 time point for 10mg/mL experimental groups. 5% SPAK 10% PEGDA had 34.8 ± 5.0% lysozyme bioactivity and 2% SPAK 10% PEGDA had 13.8 ± 2.3%. An unpaired Student's t-test determined this difference as significant ($P<0.01$). The decrease in bioactivity compared to stock lysozyme indicates that the conditions during DLP 3D printing have a damaging effect on lysozyme (Figure 5.6 C). The increase in bioactivity seen by 5% SPAK compared to 2% may be explained by SPAK exhibiting a protective effect on lysozyme by binding to it in the hydrogel precursor solution.

The bioactivity of lysozyme from 2mg/mL experimental groups was determined at day 1. 5% SPAK 10% PEGDA had 15.8 ± 3.5% and 2% SPAK 10% PEGDA had 9.72 ± 2.2% respectively. The reduced bioactivity in 2mg/mL experimental groups in comparison to the corresponding 10mg/mL condition may be explained by there being a higher photoinitiator to protein ratio in 2mg/mL in comparison to 10mg/mL, meaning that a larger proportion of the loaded protein is likely to come into contact with activated photoinitiator.

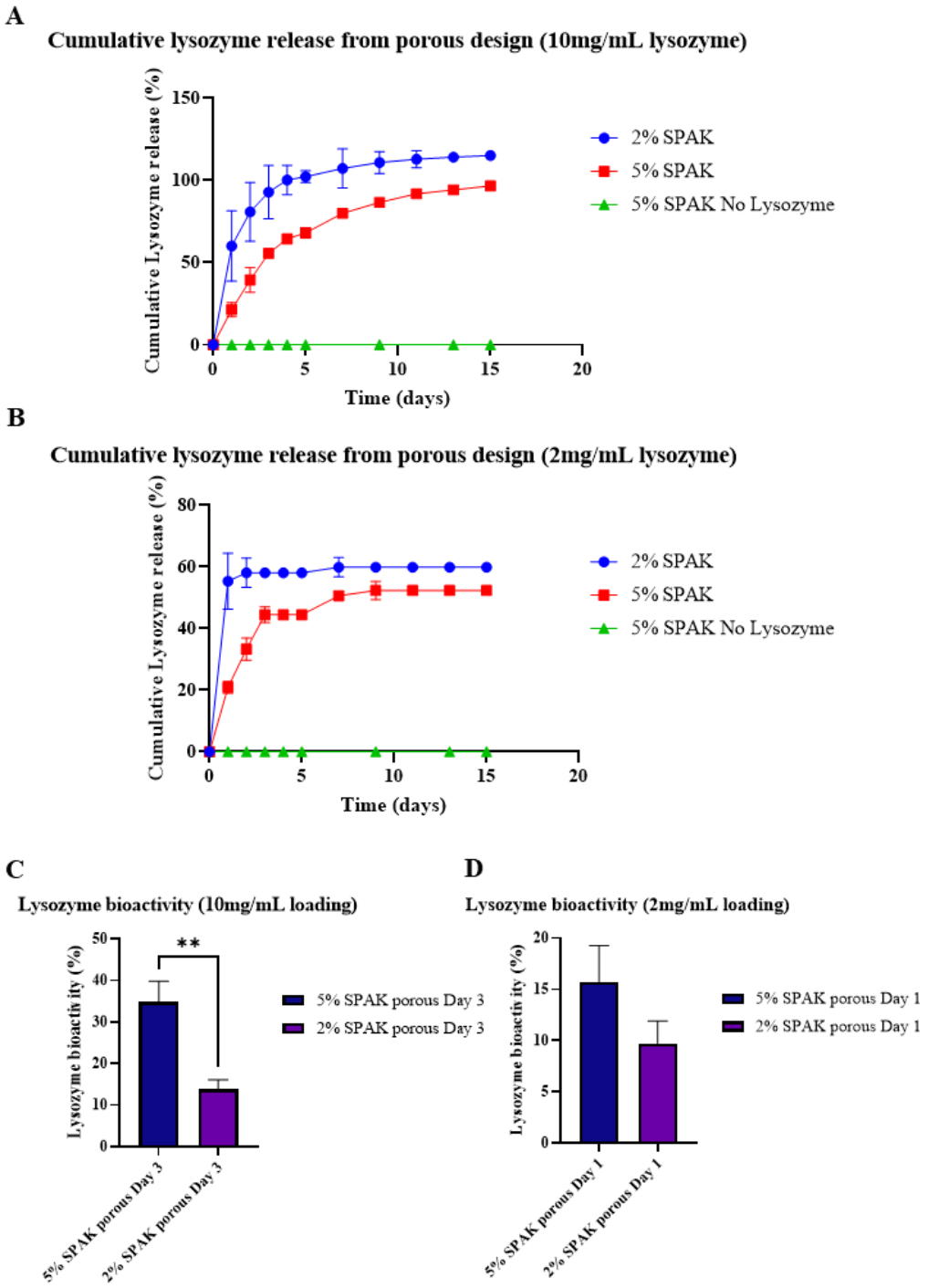

Figure 5.6: Lysozyme release from porous 3D printed SPAK PEGDA hydrogels. A) 15 day cumulative lysozyme release from 2% SPAK and 5% SPAK containing 10% PEGDA and 10mg/mL lysozyme. B) 15 day cumulative lysozyme release from 2% SPAK and 5% SPAK containing 10% PEGDA and 2mg/mL lysozyme. C) Bioactivity of lysozyme released on day 3 from

10mg/mL experimental groups. D) Bioactivity of lysozyme released on day 1 from 2mg/mL experimental groups. Values presented as mean ± standard deviation. Significant differences as determined by Student's t-test are labelled as * $P \leq 0.05$, ** $P < 0.01$, *** $P < 0.001$ and **** $P < 0.0001$. Three hydrogels were used per experimental condition, Bradford assay was carried out in duplicate (N=2, n=3) and lysozyme bioactivity assay was carried out in triplicate (N=3, n=3).

To investigate the effect of hydrogel geometry on lysozyme release, porous and non-porous designs were printed with 10mg/mL lysozyme. Direct loading into the hydrogel precursor solution was chosen so that each design would contain an approximately even dosage of lysozyme. Lysozyme release was characterised for 15 days in PBS.

In 5% SPAK 10% PEGDA hydrogels, lysozyme release from the porous design reached 56% at day 3, 80% at day 7 and had 97% at day 15 (Figure 5.7 A). Lysozyme release from the non-porous design reached 32% at day 3, 57% at day 7, and had 80% at day 15 (Figure 5.7 A). The increased release rate from the porous 5% SPAK 10% PEGDA hydrogels is likely due to the increase in surface area to volume ratio from the 3D printed design, which would give a larger total surface area for diffusion out of the hydrogel to take place.

In 2% SPAK 10% PEGDA hydrogels, there was no observable difference in lysozyme release rate between porous and non-porous designs (Figure 5.7 B). This may be an indication that at lower concentrations of SPAK, the reduced electrostatic attraction between the polymer network and the protein means that a burst release trend due to diffusion occurs regardless of hydrogel geometry.

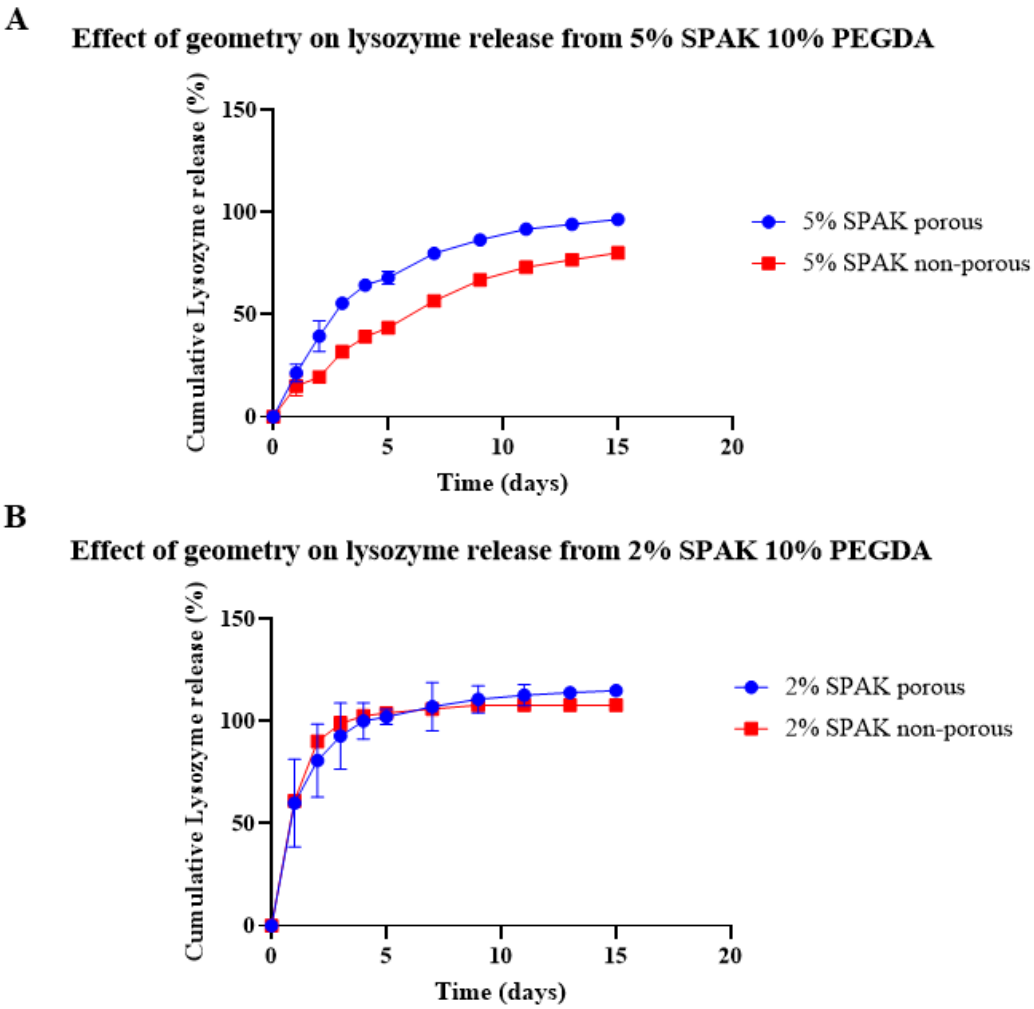

Figure 5.7: Effect of 3D printed hydrogel geometry on lysozyme release from SPAK PEGDA hydrogels containing 10mg/mL lysozyme. A) Lysozyme release from porous and non-porous 5% SPAK 10% PEGDA. B) Lysozyme release from porous and non-porous 2% SPAK 10% PEGDA. Values presented as mean ± standard deviation. Where error bars cannot be seen they are smaller than the marker of each plotted point. Three hydrogels were used per experimental condition, Bradford assay was carried out in duplicate (N=2, n=3).

Lysozyme release was compared from 3D printed 5% SPAK 10% PEGDA hydrogels and the cast 5% SPAK 10% PEGDA hydrogels from chapter 3 of this

thesis (Figure 5.8 A). In cast hydrogels, cumulative lysozyme release reached 1.9% after 2 days, 6.2% at day 7 and was 10.0% at day 13. Release from 3D printed hydrogels reached 19.4% after 3 days, 56.7% at day 7 and was 76.8% at day 13. The difference in lysozyme release rate may be due to the different photoinitiator and manufacturing method used. These possibilities were considered further in the discussion section of this chapter. The bioactivity of lysozyme released from each group was compared from day 2 of release for cast hydrogels and day 3 of release from 3D printed hydrogels. The bioactivity was 37.3 ± 4.7% for cast hydrogels and 34.7 ± 5.0% for 3D printed hydrogels (Figure 5.8 B).

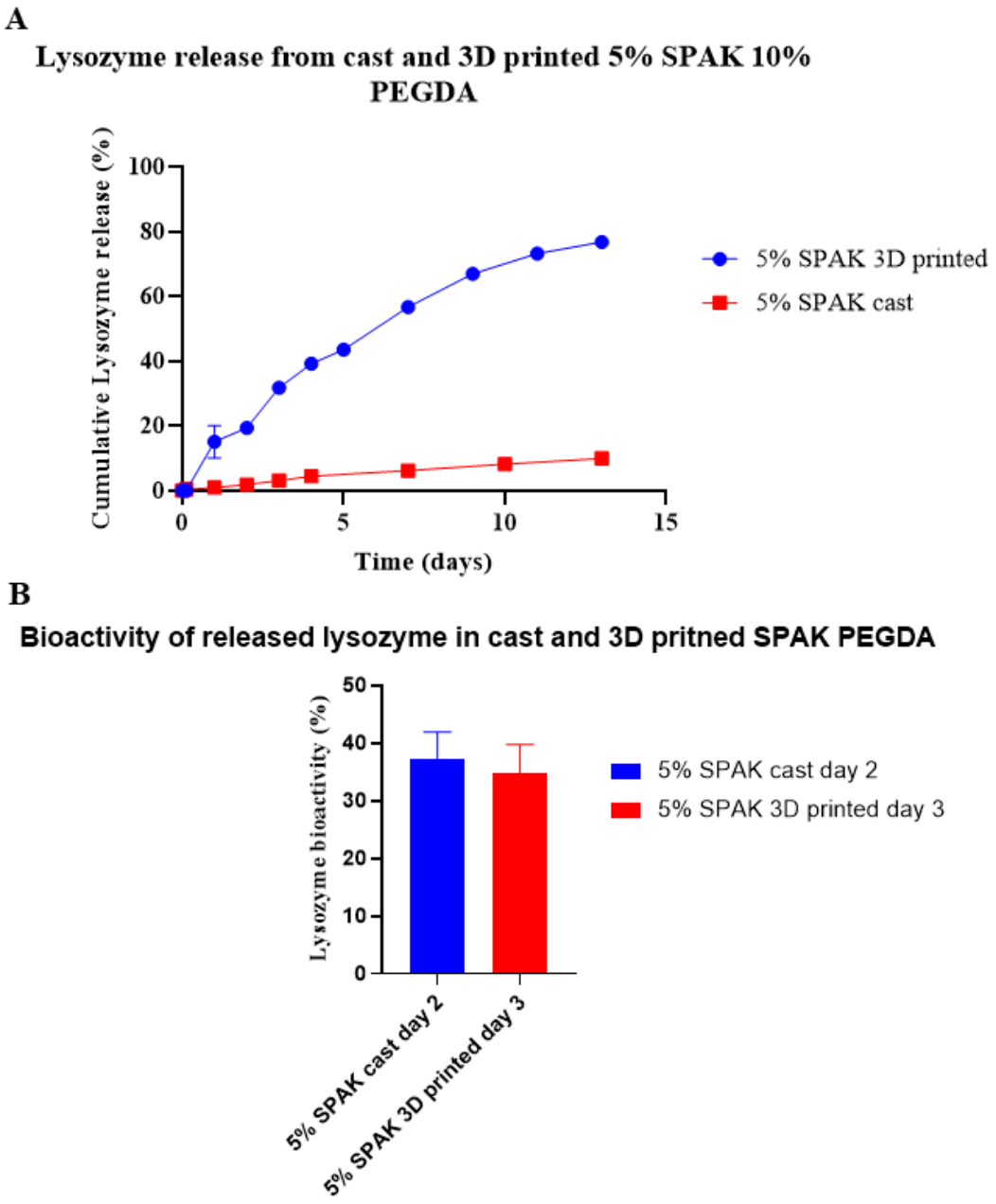

Figure 5.8: Lysozyme release from cast and 3D printed 5% SPAK 10% PEGDA. Hydrogels were loaded with 10mg/mL lysozyme. A) Cumulative lysozyme release. B) Lysozyme bioactivity tested at day 2 of release in cast hydrogels and day 3 of release for 3D printed hydrogels. Values presented as mean ± standard deviation. Where error bars cannot be seen they are smaller than the marker of each plotted point. Three hydrogels were used per experimental condition, Bradford assay was carried out in duplicate (N=2, n=3).

5.4 Discussion

Data in chapters 3 and 4 of this thesis showed evidence that hydrogels formed from SPAK and PEGDA are a promising material choice for affinity based controlled protein release. Data in chapters 3 and 4 was collected using hydrogels that were fabricated with traditional casting and moulding, this chapter sought to generate SPAK PEGDA hydrogels using additive manufacturing as proof of concept and investigate if 3D hydrogel geometry may be used as a tool to further optimise protein release. Previous literature has studied the effect of surface area to volume ratio of 3D printed PEGDA in the elution of small molecule drugs[345], but there is exceptionally limited literature on protein release from 3D printed materials and controlled protein release remains a challenging goal in the field overall.

In this work, digital light projection 3D printing was used to manufacture multi-layered, macroporous hydrogels containing 10% w/v PEGDA and 2% or 5% w/v SPAK for the purpose of controlled protein release (Figure 5.2 A). Consistent with data from chapter 3, increasing SPAK concentration decelerated the release rate of lysozyme which indicates protein release is governed by electrostatic affinity (Figure 5.6 A, B). The release period of 15 days is comparable to many protein release reports[328–330] but is sub optimal when considering therapeutic application in osteoarthritis. 3D printed 5% SPAK 10% PEGDA loaded with 10mg/mL lysozyme exhibited markedly different lysozyme release rate in comparison to the identical material composition from cast hydrogels in chapter 3 (Figure 5.8 A). The multiple months of controlled release observed in 5% SPAK 10% PEGDA from cast hydrogels in chapter 3

was not reproduced in the 3D printed counterparts. The difference in fabrication techniques may be responsible for the discrepancy in lysozyme release. 3D printing was performed under atmospheric air whereas hydrogel casting was performed under argon with oxygen < 2000ppm which may man there was lower crosslinking efficiency in 3D printed hydrogels[290]. Lower crosslinking efficiency would then mean more SPAK monomers remain uncrosslinked and diffuse out of the polymer, resulting in less electrostatic affinity towards lysozyme to control protein release and an increased release rate in comparison to SPAK PEGDA hydrogels formed by casting under argon. The normal exposure time of 4 seconds per layer chosen for 3D printing was selected based on visible scaffold fidelity during process optimisation, it is also possible that this UV dose resulted in less crosslinking efficiency throughout the bulk of the hydrogel in comparison to the 10 minutes of UV used during the initial hydrogel casting experiments in Chapter 3. The difference in crosslinking efficiency between the two techniques may be confirmed in the future by quantifying residual monomer from hydrogels with equal volume and approximately identical 3D geometries.

When comparing the bioactivity of lysozyme released from 3D printed hydrogels to cast hydrogels in 5% SPAK 10% PEGDA loaded with 10mg/mL lysozyme, the bioactivity at day 3 release from 3D printed gels was 34.5% and was 37.3% at day 2 release from cast gels (Figure 5.8 B). These values are comparable and were not significantly different when tested by Student's t-test, and further indicate that the photocrosslinking process is damaging to proteins. The later time points tested up to 2 months of release in cast gels were all above 50% bioactivity, but it was not possible to characterise the release from 3D

printed hydrogels up to this time due to the lack of optimisation in parameters and the time constraints of the experiment.

The comparison of lysozyme release from 5% SPAK 10% PEGDA saw evidence of material geometry affecting release rate in hydrogels loaded with 10mg/mL lysozyme in which the high SA:V design had increased release rate (Figure 5.7 A). Only simple 3D designs were printed in this chapter in attempt to show proof of concept, future experimentation in this line of research should print more complex designs with greater differences in surface area to volume ratio to investigate the magnitude of its influence over controlled lysozyme release.

The experimental approach used in this chapter had multiple other limitations. Firstly, direct protein loading into the hydrogel precursor solution was used to achieve approximately equal lysozyme loading into gels with varying SPAK concentration and different geometries. Loading post fabrication by immersion would have made it difficult to compare the release rate from porous and cuboidal hydrogels as it is likely a different amount of lysozyme would have been loaded onto the hydrogels due to the difference in surface area. As discussed in chapter 3, direct loading into the hydrogel precursor solution gave promising results when loaded with 10mg/mL lysozyme but loading at lower concentrations gave very limited protein release results due to the permanent entrapment of a significant amount of the loaded protein due to methods such as thiol-ene crosslinking of the protein into the polymer network (Chapter 3 discussion), a phenomenon which was also seen in the data from this chapter in 2mg/mL loaded hydrogels (Figure 5.6 B).

A second limitation is that the photoinitiator had to be change from Irgacure-2959 to LAP in order to be compatible with the wavelength of available 3D printers. It may be possible that the change in photoinitiator influenced lysozyme release rate or lysozyme bioactivity. Similarly, a third limitation is that the lysozyme release data collected from SPAK PEGDA cast hydrogels in chapter 3 used a 500µL total volume which was considerably larger than the total volume of 3D printed hydrogels and the resulting difference in total dosage when loaded at 10mg/mL. The difference in total volume makes comparing data from chapter 3 to chapter 5 difficult and arose due to the optimisation of 3D printing parameters being focused to achieving pore fidelity. At taller 3D printed heights there was a loss of pore fidelity in the lower layers due to overexposure and the optimisation of parameters to circumvent this issue was limited by time which restricted the maximum printable height of SPAK PEGDA hydrogels (Supplementary Table S.1 Appendix 1).

To confirm this, future experimental work on this topic should compare protein release from cast and 3D printed SPAK PEGDA hydrogels both using LAP and an approximately identical geometry to determine if the multiple months of controlled release observed in chapter 3 of this thesis in cast hydrogels is reproducible in ones that are DLP 3D printed.

3D printing parameters should be further optimised to achieve high fidelity of microscale architecture in SPAK PEGDA printed designs. Parameters such as exposure time, SPAK concentration, PEGDA concentration, photoabsorber concentration, and photoinitiator concentration will likely need to be modified to achieve this goal. It is also likely that the optimal material composition for

3D printing will not be the optimal composition for controlled release and a compromise may have to be made.

The work in this chapter used an Anycubic 4K Photon Mono 3D printer with a 250mL vat size. Future work related to this topic should aim to utilise DLP printers with micro vats to reduce the minimum volume of hydrogel precursor solution required for printing and conserve experimental costs.

3D printing of SPAK PEGDA hydrogels should be used to optimise the IL-4 release data obtained in Chapter 4 of this thesis. Increasing the surface area to volume ratio of the hydrogels may give increased IL-4 loading dosage and lead to improved controlled release rate and an improved time period of sustained release.

The work in this chapter used hydrogels that were in the millimetre scale in size and had two simplistic designs to show proof of concept. When considering the clinical translatability of a controlled protein release therapy for immunomodulation in early osteoarthritis, minimal invasiveness would be required such as a single injection into the knee. Clinical administration of corticosteroids via injection into the osteoarthritic knee uses medical syringes that have a 25 gauge needle with a 260μm inner diameter[340,341]. The microscale resolution of DLP 3D printing may be used to manufacture SPAK PEGDA microparticles with a diameter small enough for injectable administration through a 25 gauge needle. A previously reported issue with microparticle injection is particle aggregation which causes needle blockage[350]. Microparticle shape has been associated with injectability[351], therefore 3D printing could be

used to optimise microparticle geometry to maximise injectability to increase the efficiency of administration.

Following fabrication, the effect microparticles with multiple diameters on the in-vitro viability of chondrocytes and macrophages should be investigated. A particle diameter should then be chosen which has low cytotoxicity but is an appropriate size for high efficiency injection but that avoids rapid clearance from the synovial fluid. Protein release for a cytokine such as IL-4 should then be characterised and optimised from the microparticles. In-vivo testing should be done to investigate if injection of IL-4 releasing SPAK PEGDA 3D printed microparticles can significantly prevent the progression of osteoarthritis in large animal models.

The generation of a clinically translatable controlled protein release biomaterial remains challenging. Hydrogels formed from SPAK and PEGDA have shown promise as candidate materials for controlled protein release using electrostatic affinity and the utilisation of 3D printing may play a pivotal role in improving both the controlled release and clinical translatability of such a material in the future. An injectable controlled protein release therapy targeting M2 macrophage polarisation may be a viable therapy for early osteoarthritis in the future.

5.5 Conclusion

In conclusion, this chapter has shown

SPAK PEGDA hydrogels were successfully 3D printed using digital light projection 3D printing.

When comparing Lysozyme release rate from 2% and 5% SPAK hydrogels loaded with 10mg/mL lysozyme, the release rate of lysozyme was decreased with increasing SPAK concentration which is consistent with the original data collected using cast hydrogels in Chapter 3.

When comparing simple porous and non-porous hydrogel designs with differing surface area to volume ratio, increased lysozyme release rate was observed in porous scaffolds containing 5% SPAK hydrogels 10% PEGDA and 10mg/mL lysozyme.

The limitations of the current methodology were addressed and recommendations for future work in this line of experimentation

Chapter 6 – Conclusion and future work recommendations

6.1 Conclusion

The biological potency of growth factors and cytokines makes them attractive drug candidates for influencing cell behaviour in-vivo for purposes such as immunomodulation and directing cell fate in tissue engineering[191,324–327]. The ability to mass produce recombinant proteins has led to the expansion of the biopharmaceutical industry with 380 drugs and drug variants that are peptides, proteins or antibodies gaining FDA approval by 2017[268]. The most common methods of administration for these drugs is intravenous injection, subcutaneous injection, intramuscular injection, and oral administration. The short in-vivo half-life of proteins means frequent injections would be required for long term effect[279,280]. This has the negative impacts of repeatedly causing patient discomfort, causing tissue damage at injection sites[360], and systemic administration methods having undesirable off target effects such as the cytotoxicity seen when IFN-α and IL-2 were systemically administered in clinical trials as a cancer treatment[277].

The controlled release of protein drugs from biomaterials to therapeutically target cells in a localised biological niche has therefore been a goal in the field for decades but remains challenging due to the multiple difficulties commonly faced in the field such as burst release, incomplete release, and the release of denatured protein[263,281–283]. When inadequate consideration was given to the release of BMP-2 from collagen sponges during clinical trials for spinal cord

regeneration, severe adverse effects including ectopic bone formation and swelling around airways were observed[269–272] which highlights the need for control of release dosage over time so that cells are exposed to therapeutic concentrations of growth factors. A clinical application for a long term controlled protein release therapy is immunomodulation in early osteoarthritis by promoting M2 macrophage polarisation to reduce the pro-inflammatory signalling associated with progression of the disease[45,361]. Osteoarthritis has limited treatment options and regenerative medicine approaches are not clinically translatable at the current stage of the field[91,95,96,109]. Modification of the disease pathobiology at the early stages of osteoarthritis may retain articular cartilage tissue that would otherwise be irreversibly lost[149–151].

The work in this thesis has focused on achieving controlled protein release from photocrosslinkable affinity hydrogels, the promotion of M2-like macrophage polarisation using Interleukin-4 (IL-4) released from affinity hydrogels, and the additive manufacturing of affinity hydrogels used for controlled release. A material composition including Poly (ethylene glycol) diacrylate (PEGDA) and 3-sulfopropyl acrylate potassium salt (SPAK) was chosen as a synthetic alternative to heparin which has the advantages of having a slow biodegradation rate[294], low material cost, and increased manufacturing capacity[344,345] and also circumvents the limitations of heparin such as enzymatic degradation in-vivo, batch variability, and being derived from animal tissue[315–320].

In Chapter 3, the initial characterisation of protein release used lysozyme as a model protein because of its isoelectric point and molecular weight. 500µL hydrogels were formed using casting and moulding under argon containing 10mg/mL lysozyme. In-vitro release into Phosphate buffered saline (PBS) saw

rapid burst release from 10% PEGDA and a linear release trend from 5% SPAK 10% PEGDA for 70 days with quantifiable lysozyme release in the µg/mL range at every time point. Increasing SPAK concentration to 10% and 15% gave a dose dependent reduction in lysozyme release rate which demonstrated electrostatic control over protein release. The bioactivity of released lysozyme was tested at 4 time points from 5% SPAK 10% PEGDA and was still more than 50% after 2 months of in-vitro release when compared to stock lysozyme with a matched concentration.

With promising initial data, lysozyme was switched with the anti-inflammatory cytokine TGF-β1. To conserve experimental costs, hydrogel volume was reduced to 100µL and the loading concentration used for TGF-β1 was 10µg/mL. Extremely low cumulative percentage release of TGF-β1 was observed. A series of optimisation experiments were performed which increased TGF-β1 loading concentration and PEGDA molecular weight, which both saw an improvement in cumulative release but the total percentage release was still low. IL-4 was compared to TGF-β1 to investigate if determine if the low percentage release was specific to TGF-β1 but the results were similar. When investigating if UV photocrosslinking conditions could have affected TGF-β1 quantification, it was found that UV exposure in the presence of photoinitiator severely diminished TGF-β1 quantification by ELISA.

To separate TGF-β1 from photoinitiator, a core-shell hydrogel was fabricated using custom made Poly (tetrafluoro ethylene) (PTFE) moulds in which a TGF-β1 loaded gelatin core was encapsulated within 10% 4kDa PEGDA. No quantifiable TGF-β1 was released from core-shell hydrogels and it was concluded that this approach was too limited to continue with.

In Chapter 4, the protein release method was modified to completely separate protein loading from photocrosslinking conditions. Following photocrosslinking and sterilisation, 100µL SPAK PEGDA hydrogels were immersed in IL-4 solutions overnight for subsequent in-vitro release into complete THP-1 cell culture media. 5% SPAK 10% PEGDA hydrogels exhibited sustained release in the ng/mL range for 73 days. The bioactivity of released IL-4 was investigated at multiple controlled release time points by using it to promote M2-like polarisation of THP-1 macrophages. It was determined that IL-4 released up to the day 53 release time point was bioactive as evidenced by the secretion of M2 markers CCL-18 and CCL-22, and increased expression of mannose receptor seen by immunostaining. Media conditioned by IL-4 releasing SPAK PEGDA hydrogels gave no decrease in cell viability in comparison to monolayer controls generated using standard cytokine application. When comparing sustained IL-4 delivery from 5% SPAK 10% PEGDA hydrogels to a single large IL-4 dose to model bolus injection, no significant difference in cell viability was observed. When IL-4 delivery from 5% SPAK 10% PEGDA hydrogels was co-administered with an M1 promoting stimulus, increased secretion of TNF-α, IL-6 and CCL-18 was observed which indicated a heterogeneous macrophage population and that IL-4 delivery alone could not overpower the M1 stimulus applied.

In Chapter 5, SPAK PEGDA hydrogels were 3D printed using digital light projection additive manufacturing. 2% SPAK 10% PEGDA and 5% SPAK 10% PEGDA hydrogels were 3D printed with a porous design containing 10mg/mL lysozyme and protein release was characterised for 15 days. Lysozyme release rate was decreased in 5% SPAK in comparison to 2% SPAK which was

consistent with data collected from cast hydrogels in chapter 3. The release trend of 5% SPAK 10% PEGDA was not the same as it was for cast hydrogels with matched concentration in chapter 3. Hydrogels loaded with 2mg/mL lysozyme had noticeable incomplete release and plateaued after 1 week of release which indicates protein entrapment within the hydrogel. Lysozyme release was compared between 3D printed hydrogels with porous and non-porous designs to investigate if hydrogel geometry may be used to fine tune release behaviour. In 5% SPAK 10% PEGDA, lysozyme release rate was increased in porous hydrogels in comparison to non-porous which showed proof of concept towards using surface area to volume ratio to control protein release from hydrogels.

The limitations of the research in this thesis are as follows:

In-vitro cytokine release parameters were not fully optimised, the use of higher cytokine loading concentrations and optimisation of SPAK and PEGDA concentrations would yield the controlled release of M2 macrophage promoting cytokines for a period of at least 6 months which was the original goal of this project. Sustained release was only achieved with IL-4 when a combination of anti-inflammatory cytokines is likely to have greater efficacy in-vivo.

Macrophage polarisation data was collected using an immortal cell line which has limited clinical relevance, the use of primary PBMC derived macrophages will yield more clinically relevant results and the age of donors could be matched to the average age of onset for OA. More complex in-vitro models of immunomodulation in OA may then be used with chondrocytes, macrophages, and cytokine releasing affinity hydrogels that utilise transwell inserts instead of the method used in Chapter 5 of this thesis.

3D printing of SPAK PEGDA hydrogels was only briefly explored as proof of concept, ideally this fabrication method would have been used for an extended period of time to obtain optimised 3D print fidelity and cytokine release from microscale hydrogels to then be used for in-vitro immunomodulation experiments.

The biodegradation of SPAK PEGDA hydrogels was not characterised, the ideal system for clinical delivery would exhibit controlled material biodegradation after 6 months of sustained cytokine release. The incorporation of biodegradable co-monomers should be pursued in the future to match biodegradation rate with affinity based cytokine release and the release of cytokines due to degradation as a separate mechanism for release must be considered.

In summary, hydrogels containing PEGDA and SPAK have been shown to be promising carrier materials for controlled protein release applications. The generation of biomaterials that exhibit long-term controlled release of biologically active proteins would have multiple clinical applications such as immunomodulation in osteoarthritis. Additive manufacturing technology is a useful tool for the future generation of materials with optimised geometries for controlled protein release, hydrogel injectability, and for related applications in regenerative medicine.

6.2 Future work recommendations

Future studies should optimise the parameters used for IL-4 release in chapter 4 of this thesis so that a linear release trend is observed in-vitro for a period of more than 3 months with IL-4 concentration in the ng/mL range at each time

point. Parameters including the IL-4 concentration used for hydrogel immersion, hydrogel immersion time, SPAK and PEGDA concentrations, and PEGDA molecular weight will need to be considered for full optimisation. 3D printing should be used to increase the efficiency of IL-4 loading onto hydrogels by printing designs with high surface area to volume ratios in comparison to the simple hemispherical hydrogels used in chapter 5. The release of multiple immunomodulatory drugs should also be considered as a long term goal. It is likely that IL-4 release in combination with IL-10, TGF-β1, or dexamethasone will prove more efficacious in overcoming hostile pro-inflammatory signalling in-vivo in comparison to IL-4 alone.

The work in this thesis used THP-1 cells were used to model M2-like macrophage polarisation in-vitro which have limited clinical relevance. Future studies should use macrophages derived from peripheral blood mononuclear cells for in-vitro macrophage polarisation using controlled release. Primary cells isolated from three donors should be used to generate data with a greater level of clinical relevance[255].

The parameters of digital light projection 3D printing should be optimised to print SPAK PEGDA hydrogels with high fidelity microscale architecture. Parameters including exposure time, photoinitiator concentration, photoabsorber concentration, SPAK concentration, PEGDA molecular weight, and PEGDA concentration will need to be considered to achieve maximum print fidelity. The use of alternative UV 3D printing systems with smaller vat sizes and higher resolution printing capabilities should also be considered. Following optimisation, SPAK PEGDA microparticles should be 3D printed with diameters small enough for injection through needles used to clinically

administer drugs into the osteoarthritic knee joint[349]. 3D printing should then be used to generate microparticles with geometries that maximise injectability with minimal blocking and particle wastage within the needle[350,351]. 3D printed control over microparticle architecture should also be investigated to optimise the loading and release of anti-inflammatory drugs such as IL-4.

In-vivo studies should be carried out using the implantation of IL-4 releasing SPAK PEGDA hydrogels into large osteoarthritis model organisms. The type of organism chosen and method of osteoarthritis induction should be considered to model the human disease as much as possible. Animals with high anatomical joint similarity to humans such as primates and animals that are prone to naturally occurring osteoarthritis may give data that is more representative of the human disease in comparison to surgically induced small animal models[196–198].

Chapter 7 – References

1. Fu, K., Robbins, S. R. & McDougall, J. J. Osteoarthritis: The genesis of pain. *Rheumatology (United Kingdom)* **57**, (2018).

2. Wieland, H. A., Michaelis, M., Kirschbaum, B. J. & Rudolphi, K. A. Osteoarthritis - An untreatable disease? *Nature Reviews Drug Discovery* vol. 4 Preprint at https://doi.org/10.1038/nrd1693 (2005).

3. Tchetina, E. V. Developmental Mechanisms in Articular Cartilage Degradation in Osteoarthritis. *Arthritis* **2011**, (2011).

4. Abhishek, A. & Doherty, M. Diagnosis and Clinical Presentation of Osteoarthritis. *Rheumatic Disease Clinics of North America* vol. 39 Preprint at https://doi.org/10.1016/j.rdc.2012.10.007 (2013).

5. Felson, D. T. *et al.* Osteophytes and progression of knee osteoarthritis. *Rheumatology* **44**, (2005).

6. Goldring, M. B. Articular Cartilage Degradation in Osteoarthritis. *HSS Journal* **8**, (2012).

7. Li, G. *et al.* Subchondral bone in osteoarthritis: Insight into risk factors and microstructural changes. *Arthritis Research and Therapy* Preprint at https://doi.org/10.1186/ar4405 (2013).

8. Neogi, T. The epidemiology and impact of pain in osteoarthritis. *Osteoarthritis Cartilage* **21**, (2013).

9. Hunter, D. J. & Bierma-Zeinstra, S. Osteoarthritis. *The Lancet* Preprint at https://doi.org/10.1016/S0140-6736(19)30417-9 (2019).

10. Cui, A. *et al.* Global, regional prevalence, incidence and risk factors of knee osteoarthritis in population-based studies. *EClinicalMedicine* **29–30**, (2020).

11. Barbour, K. Prevalence of doctor-diagnosed arthritis and arthritis-attributable activity limitation--United States, 2010-2012. *MMWR Morb Mortal Wkly Rep* **62**, (2013).

12. Antony, B. & Singh, A. Imaging and biochemical markers for osteoarthritis. *Diagnostics* vol. 11 Preprint at https://doi.org/10.3390/diagnostics11071205 (2021).

13. Shane Anderson, A. & Loeser, R. F. Why is osteoarthritis an age-related disease? *Best Practice and Research: Clinical Rheumatology* vol. 24 Preprint at https://doi.org/10.1016/j.berh.2009.08.006 (2010).

14. O'Brien, M. S. & McDougall, J. J. Age and frailty as risk factors for the development of osteoarthritis. *Mechanisms of Ageing and Development* vol. 180 Preprint at https://doi.org/10.1016/j.mad.2019.03.003 (2019).

15. Raud, B. *et al.* Level of obesity is directly associated with the clinical and functional consequences of knee osteoarthritis. *Sci Rep* **10**, (2020).

16. Salih, S. & Sutton, P. Obesity, knee osteoarthritis and knee arthroplasty: A review. *BMC Sports Science, Medicine and Rehabilitation* vol. 5 Preprint at https://doi.org/10.1186/2052-1847-5-25 (2013).

17. Keenan, C. M. *et al.* Post-traumatic osteoarthritis development is not modified by postnatal chondrocyte deletion of Ccn2. *DMM Disease Models and Mechanisms* **13**, (2020).

18. Liu, P. *et al.* A mouse model of ankle-subtalar joint complex instability induced post-traumatic osteoarthritis. *J Orthop Surg Res* **16**, (2021).

19. Srikanth, V. K. *et al.* A meta-analysis of sex differences prevalence, incidence and severity of osteoarthritis. *Osteoarthritis Cartilage* **13**, (2005).

20. Zengini, E. *et al.* Genome-wide analyses using UK Biobank data provide insights into the genetic architecture of osteoarthritis. *Nat Genet* **50**, (2018).

21. Boer, C. G. *et al.* Genome-wide association of phenotypes based on clustering patterns of hand osteoarthritis identify WNT9A as novel osteoarthritis gene. *Ann Rheum Dis* **80**, (2021).

22. Magnusson, K., Turkiewicz, A., Haugen, I. K. & Englund, M. THE GENETIC CONTRIBUTION TO HAND OSTEOARTHRITIS. *Osteoarthritis Cartilage* **30**, (2022).

23. Makarczyk, M. J. *et al.* Current Models for Development of Disease-Modifying Osteoarthritis Drugs. *Tissue Engineering - Part C: Methods* vol. 27 Preprint at https://doi.org/10.1089/ten.tec.2020.0309 (2021).

24. Fajardo, M. & Di Cesare, P. E. Disease-modifying therapies for osteoarthritis: Current status. *Drugs and Aging* vol. 22 Preprint at https://doi.org/10.2165/00002512-200522020-00005 (2005).

25. Chen, D. *et al.* Osteoarthritis: Toward a comprehensive understanding of pathological mechanism. *Bone Research* vol. 5 Preprint at https://doi.org/10.1038/boneres.2016.44 (2017).

26. Knoop, J. *et al.* Analgesic use in patients with knee and/or hip osteoarthritis referred to an outpatient center: a cross-sectional study within the Amsterdam Osteoarthritis Cohort. *Rheumatol Int* **37**, (2017).

27. Zeng, C. *et al.* Initial analgesic prescriptions for osteoarthritis in the United Kingdom, 2000-2016. *Rheumatology (United Kingdom)* **60**, (2021).

28. Güngör Demir, U., Demir, A. N. & Toraman, N. F. Neuropathic pain in knee osteoarthritis. *Advances in Rheumatology* **61**, (2021).

29. Chen, A., Gupte, C., Akhtar, K., Smith, P. & Cobb, J. The Global Economic Cost of Osteoarthritis: How the UK Compares. *Arthritis* (2012) doi:10.1155/2012/698709.

30. Hochman, J. R., Gagliese, L., Davis, A. M. & Hawker, G. A. Neuropathic pain symptoms in a community knee OA cohort. *Osteoarthritis Cartilage* **19**, (2011).

31. Leardini, G. *et al.* Direct and indirect costs of osteoarthritis of the knee. *Clin Exp Rheumatol* **22**, (2004).

32. Salmon, J. H. *et al.* Economic impact of lower-limb osteoarthritis worldwide: a systematic review of cost-of-illness studies. *Osteoarthritis and Cartilage* vol. 24 Preprint at https://doi.org/10.1016/j.joca.2016.03.012 (2016).

33. Christensen, K., Doblhammer, G., Rau, R. & Vaupel, J. W. Ageing populations: the challenges ahead. *The Lancet* vol. 374 Preprint at https://doi.org/10.1016/S0140-6736(09)61460-4 (2009).

34. Jaul, E. & Barron, J. Age-Related Diseases and Clinical and Public Health Implications for the 85 Years Old and Over Population. *Frontiers in Public Health* vol. 5 Preprint at https://doi.org/10.3389/fpubh.2017.00335 (2017).

35. Prince, M. J. *et al.* The burden of disease in older people and implications for health policy and practice. *The Lancet* vol. 385 Preprint at https://doi.org/10.1016/S0140-6736(14)61347-7 (2015).

36. Reyes, C. *et al.* Association Between Overweight and Obesity and Risk of Clinically Diagnosed Knee, Hip, and Hand Osteoarthritis: A Population-Based Cohort Study. *Arthritis and Rheumatology* **68**, (2016).

37. Ackerman, I. N. *et al.* The projected burden of primary total knee and hip replacement for osteoarthritis in Australia to the year 2030. *BMC Musculoskelet Disord* **20**, (2019).

38. Benito, M. J., Veale, D. J., FitzGerald, O., Van Den Berg, W. B. & Bresnihan, B. Synovial tissue inflammation in early and late osteoarthritis. *Ann Rheum Dis* (2005) doi:10.1136/ard.2004.025270.

39. Sanchez-Lopez, E., Coras, R., Torres, A., Lane, N. E. & Guma, M. Synovial inflammation in osteoarthritis progression. *Nature Reviews Rheumatology* vol. 18 Preprint at https://doi.org/10.1038/s41584-022-00749-9 (2022).

40. Hill, C. L. *et al.* Synovitis detected on magnetic resonance imaging and its relation to pain and cartilage loss in knee osteoarthritis. *Ann Rheum Dis* **66**, (2007).

41. de Lange-Brokaar, B. J. E. *et al.* Evolution of synovitis in osteoarthritic knees and its association with clinical features. *Osteoarthritis Cartilage* **24**, (2016).

42. Thomson, A. & Hilkens, C. M. U. Synovial Macrophages in Osteoarthritis: The Key to Understanding Pathogenesis? *Frontiers in Immunology* vol. 12 Preprint at https://doi.org/10.3389/fimmu.2021.678757 (2021).

43. Lee, H. L. *et al.* Inflammatory cytokines and change of Th1/Th2 balance as prognostic indicators for hepatocellular carcinoma in patients treated with transarterial chemoembolization. *Sci Rep* **9**, (2019).

44. Martinez, F. O. & Gordon, S. The M1 and M2 paradigm of macrophage activation: time for reassessment. *F1000Prime Rep* (2014) doi:10.12703/P6-13.

45. Liu, B., Zhang, M., Zhao, J., Zheng, M. & Yang, H. Imbalance of M1/M2 macrophages is linked to severity level of knee osteoarthritis. *Exp Ther Med* **16**, (2018).

46. Gómez-Aristizábal, A., Gandhi, R., Mahomed, N. N., Marshall, K. W. & Viswanathan, S. Synovial fluid monocyte/macrophage subsets and their correlation to patient-reported outcomes in osteoarthritic patients: A cohort study. *Arthritis Res Ther* **21**, (2019).

47. Wang, W., Wang, L., Gulko, P. S. & Zhu, J. Computational deconvolution of synovial tissue cellular composition: Presence of adipocytes in synovial tissue decreased during arthritis pathogenesis and progression. *Physiol Genomics* **51**, (2019).

48. Mushenkova, N. V. *et al.* Phenotype Diversity of Macrophages in Osteoarthritis: Implications for Development of Macrophage Modulating Therapies. *International Journal of Molecular Sciences* vol. 23 Preprint at https://doi.org/10.3390/ijms23158381 (2022).

49. Pesesse, L. *et al.* Consequences of chondrocyte hypertrophy on osteoarthritic cartilage: Potential effect on angiogenesis. *Osteoarthritis Cartilage* **21**, (2013).

50. Ferrao Blanco, M. N. *et al.* Effect of Inflammatory Signaling on Human Articular Chondrocyte Hypertrophy: Potential Involvement of Tissue Repair Macrophages. *Cartilage* **13**, (2021).

51. Arra, M., Swarnkar, G., Alippe, Y., Mbalaviele, G. & Abu-Amer, Y. IκB-ζ signaling promotes chondrocyte inflammatory phenotype, senescence, and erosive joint pathology. *Bone Res* **10**, (2022).

52. Pearson, M. J. *et al.* IL-6 secretion in osteoarthritis patients is mediated by chondrocyte-synovial fibroblast cross-talk and is enhanced by obesity. *Sci Rep* **7**, (2017).

53. Loffek, S., Schilling, O. & Franzke, C.-W. Biological role of matrix metalloproteinases: a critical balance. *European Respiratory Journal* **38**, (2011).

54. Klein, T. & Bischoff, R. Physiology and pathophysiology of matrix metalloproteases. *Amino Acids* vol. 41 Preprint at https://doi.org/10.1007/s00726-010-0689-x (2011).

55. Leong, D. J. *et al.* Matrix metalloproteinase-3 in articular cartilage is upregulated by joint immobilization and suppressed by passive joint motion. *Matrix Biology* **29**, (2010).

56. Pengas, I. *et al.* MMP-3 in the peripheral serum as a biomarker of knee osteoarthritis, 40 years after open total knee meniscectomy. *J Exp Orthop* **5**, (2018).

57. Wang, M., Zhou, Y., Huang, W., Zeng, Y. & Li, X. Association between matrix metalloproteinase-1 (Mmp-1) protein level and the risk of rheumatoid arthritis and osteoarthritis: A meta-analysis. *Brazilian Journal of Medical and Biological Research* **54**, (2021).

58. Akhtar, N. *et al.* MicroRNA-27b regulates the expression of matrix metalloproteinase 13 in human osteoarthritis chondrocytes. *Arthritis Rheum* **62**, (2010).

59. Shingleton, W. D. Collagenase: A key enzyme in collagen turnover. *Biochemistry and Cell Biology* **74**, (1996).

60. Arra, M., Swarnkar, G., Alippe, Y., Mbalaviele, G. & Abu-Amer, Y. IκB-ζ signaling promotes chondrocyte inflammatory phenotype, senescence, and erosive joint pathology. *Bone Res* **10**, (2022).

61. Shimo, T. *et al.* Expression and role of il-1β signaling in chondrocytes associated with retinoid signaling during fracture healing. *Int J Mol Sci* **21**, (2020).

62. Goldring, M. B. & Berenbaum, F. The regulation of chondrocyte function by proinflammatory mediators: Prostaglandins and nitric oxide. in *Clinical Orthopaedics and Related Research* vol. 427 (2004).

63. Aizawa, T., Kon, T., Einhorn, T. A. & Gerstenfeld, L. C. Induction of apoptosis in chondrocytes by tumor necrosis factor-alpha. *Journal of Orthopaedic Research* **19**, (2001).

64. Strasser, A., Jost, P. J. & Nagata, S. The Many Roles of FAS Receptor Signaling in the Immune System. *Immunity* vol. 30 Preprint at https://doi.org/10.1016/j.immuni.2009.01.001 (2009).

65. Roughley, P. J. & Mort, J. S. The role of aggrecan in normal and osteoarthritic cartilage. *J Exp Orthop* **1**, (2014).

66. Dudhia, J. Aggrecan, aging and assembly in articular cartilage. *Cellular and Molecular Life Sciences* vol. 62 Preprint at https://doi.org/10.1007/s00018-005-5217-x (2005).

67. Tauchi, R. *et al.* The endogenous proteoglycan-degrading enzyme ADAMTS-4 promotes functional recovery after spinal cord injury. *J Neuroinflammation* **9**, (2012).

68. Kosasih, H. J. *et al.* A disintegrin and metalloproteinase with thrombospondin motifs-5 (ADAMTS-5) forms catalytically active oligomers. *Journal of Biological Chemistry* **291**, (2016).

69. Verma, P. & Dalal, K. ADAMTS-4 and ADAMTS-5: Key enzymes in osteoarthritis. *J Cell Biochem* **112**, (2011).

70. Xue, J., Wang, J., Liu, Q. & Luo, A. Tumor necrosis factor-α induces ADAMTS-4 expression in human osteoarthritis chondrocytes. *Mol Med Rep* **8**, (2013).

71. Cheung, K. S. C., Hashimoto, K., Yamada, N. & Roach, H. I. Expression of ADAMTS-4 by chondrocytes in the surface zone of human osteoarthritic cartilage is regulated by epigenetic DNA de-methylation. *Rheumatol Int* **29**, (2009).

72. Li, W., Du, C., Wang, H. & Zhang, C. Increased serum ADAMTS-4 in knee osteoarthritis: A potential indicator for the diagnosis of osteoarthritis in early stages. *Genetics and Molecular Research* **13**, (2014).

73. Majumdar, M. K. *et al.* Double-knockout of ADAMTS-4 and ADAMTS-5 in mice results in physiologically normal animals and prevents the progression of osteoarthritis. *Arthritis Rheum* **56**, (2007).

74. Lambert, C. *et al.* The Damage-Associated Molecular Patterns (DAMPs) as Potential Targets to Treat Osteoarthritis: Perspectives From a Review of the Literature. *Frontiers in Medicine* vol. 7 Preprint at https://doi.org/10.3389/fmed.2020.607186 (2021).

75. Hamasaki, M., Terkawi, M. A., Onodera, T., Homan, K. & Iwasaki, N. A Novel Cartilage Fragments Stimulation Model Revealed that Macrophage Inflammatory Response Causes an Upregulation of Catabolic Factors of Chondrocytes In Vitro. *Cartilage* **12**, (2021).

76. Wang, Y., Wei, L., Zeng, L., He, D. & Wei, X. Nutrition and degeneration of articular cartilage. *Knee Surgery, Sports Traumatology, Arthroscopy* **21**, (2013).

77. Jackson, A. & Gu, W. Transport Properties of Cartilaginous Tissues. *Curr Rheumatol Rev* **5**, (2009).

78. Donell, S. Subchondral bone remodelling in osteoarthritis. *EFORT Open Rev* **4**, (2019).

79. Iijima, H. *et al.* Subchondral plate porosity colocalizes with the point of mechanical load during ambulation in a rat knee model of post-traumatic osteoarthritis. *Osteoarthritis Cartilage* **24**, (2016).

80. Findlay, D. M. & Kuliwaba, J. S. Bone-cartilage crosstalk: A conversation for understanding osteoarthritis. *Bone Research* vol. 4 Preprint at https://doi.org/10.1038/boneres.2016.28 (2016).

81. Bertuglia, A. *et al.* Osteoclasts are recruited to the subchondral bone in naturally occurring post-traumatic equine carpal osteoarthritis and may contribute to cartilage degradation. *Osteoarthritis Cartilage* **24**, (2016).

82. Nagaosa, Y., Lanyon, P. & Doherty, M. Characterisation of size and direction of osteophyte in knee osteoarthritis: A radiographic study. *Ann Rheum Dis* **61**, (2002).

83. Steadman, J. R., Rodkey, W. G., Singleton, S. B. & Briggs, K. K. Microfracture technique for full-thickness chondral defects: Technique and clinical results. *Oper Tech Orthop* **7**, (1997).

84. Erggelet, C. & Vavken, P. Microfracture for the treatment of cartilage defects in the knee joint – A golden standard? *Journal of Clinical Orthopaedics and Trauma* vol. 7 Preprint at https://doi.org/10.1016/j.jcot.2016.06.015 (2016).

85. Steadman, J. R., Rodkey, W. G. & Rodrigo, J. J. Microfracture: Surgical technique and rehabilitation to treat chondral defects. in *Clinical Orthopaedics and Related Research* vol. 391 (2001).

86. Goldberg, A., Mitchell, K., Soans, J., Kim, L. & Zaidi, R. The use of mesenchymal stem cells for cartilage repair and regeneration: A systematic review. *Journal of Orthopaedic Surgery and Research* vol. 12 Preprint at https://doi.org/10.1186/s13018-017-0534-y (2017).

87. Caplan, A. I. Mesenchymal stem cells: Time to change the name! *Stem Cells Transl Med* **6**, (2017).

88. Horwitz, E. M. *et al.* Clarification of the nomenclature for MSC: The International Society for Cellular Therapy position statement. *Cytotherapy* **7**, (2005).

89. Mithoefer, K., Mcadams, T., Williams, R. J., Kreuz, P. C. & Mandelbaum, B. R. Clinical efficacy of the microfracture technique for articular cartilage repair in the knee: An evidence-based systematic analysis. *American Journal of Sports Medicine* vol. 37 Preprint at https://doi.org/10.1177/0363546508328414 (2009).

90. Armiento, A. R., Alini, M. & Stoddart, M. J. Articular fibrocartilage - Why does hyaline cartilage fail to repair? *Advanced Drug Delivery*

Reviews vol. 146 Preprint at https://doi.org/10.1016/j.addr.2018.12.015 (2019).

91. Gobbi, A., Karnatzikos, G. & Kumar, A. Long-term results after microfracture treatment for full-thickness knee chondral lesions in athletes. *Knee Surgery, Sports Traumatology, Arthroscopy* **22**, (2014).

92. Kan, H. *et al.* Arthroscopic Microfracture Technique for Cartilage Damage to the Lateral Condyle of the Tibia. *Case Rep Orthop* **2015**, (2015).

93. Weber, A. E. *et al.* Clinical Outcomes After Microfracture of the Knee: Midterm Follow-up. *Orthop J Sports Med* **6**, (2018).

94. Siddiqi, A., Levine, B. R. & Springer, B. D. Highlights of the 2021 American Joint Replacement Registry Annual Report. *Arthroplast Today* **13**, (2022).

95. Bourne, R. B., Chesworth, B. M., Davis, A. M., Mahomed, N. N. & Charron, K. D. J. Patient satisfaction after total knee arthroplasty: Who is satisfied and who is not? in *Clinical Orthopaedics and Related Research* vol. 468 (2010).

96. Van Lenthe, G. H., De Waal Malefijt, M. C. & Huiskes, R. Stress shielding after total knee replacement may cause bone resorption in the distal femur. *Journal of Bone and Joint Surgery - Series B* **79**, (1997).

97. Raffa, M. L., Nguyen, V. H., Hernigou, P., Flouzat-Lachaniette, C. H. & Haiat, G. Stress shielding at the bone-implant interface: Influence of

surface roughness and of the bone-implant contact ratio. *Journal of Orthopaedic Research* **39**, (2021).

98. Kusano, T. *et al.* Preoperative Canal Bone Ratio is Related to High-Degree Stress Shielding: A Minimum 5-Year Follow-Up Study of a Proximally Hydroxyapatite-Coated Straight Tapered Titanium Femoral Component. *Journal of Arthroplasty* **33**, (2018).

99. Yamako, G. *et al.* Improving stress shielding following total hip arthroplasty by using a femoral stem made of β type Ti-33.6Nb-4Sn with a Young's modulus gradation. *J Biomech* **63**, (2017).

100. Sakamoto, M., Watanabe, H., Higashi, H. & Kubosawa, H. Pseudotumor caused by titanium particles from a total hip prosthesis. *Orthopedics* **39**, (2016).

101. Quinn, J., McFadden, R., Chan, C. W. & Carson, L. Titanium for Orthopedic Applications: An Overview of Surface Modification to Improve Biocompatibility and Prevent Bacterial Biofilm Formation. *iScience* vol. 23 Preprint at https://doi.org/10.1016/j.isci.2020.101745 (2020).

102. Jämsen, E. *et al.* Effect of Aging on the Macrophage Response to Titanium Particles. *Journal of Orthopaedic Research* **38**, (2020).

103. Zhao, Y. P. *et al.* Progranulin suppresses titanium particle induced inflammatory osteolysis by targeting TNFα signaling. *Sci Rep* **6**, (2016).

104. Evans, J. T. *et al.* How long does a knee replacement last? A systematic review and meta-analysis of case series and national registry reports with more than 15 years of follow-up. *The Lancet* **393**, (2019).

105. Cook, R., Davidson, P. & Martin, R. More than 80% of total knee replacements can last for 25 years. *The BMJ* **367**, (2019).

106. Brittberg, M. *et al.* Treatment of Deep Cartilage Defects in the Knee with Autologous Chondrocyte Transplantation. *New England Journal of Medicine* **331**, (1994).

107. Pestka, J. M., Salzmann, G. M., Südkamp, N. P. & Niemeyer, P. Cartilage biopsy for autologous chondrocyte implantation (ACI). *Z Orthop Unfall* **151**, (2013).

108. Minas, T., Von Keudell, A., Bryant, T. & Gomoll, A. H. The John Insall Award: A minimum 10-year outcome study of autologous chondrocyte implantation knee. in *Clinical Orthopaedics and Related Research* (2014). doi:10.1007/s11999-013-3146-9.

109. Whittaker, J. P. *et al.* Early results of autologous chondrocyte implantation in the talus. *Journal of Bone and Joint Surgery - Series B* **87**, (2005).

110. Ghosh, S. *et al.* Dedifferentiation alters chondrocyte nuclear mechanics during in vitro culture and expansion. *Biophys J* **121**, (2022).

111. Niethammer, T. R. *et al.* Graft maturation of autologous chondrocyte implantation: Magnetic resonance investigation with T2 mapping. *American Journal of Sports Medicine* **42**, (2014).

112. Kaszkin-Bettag, M. Is autologous chondrocyte implantation (ACI) an adequate treatment option for repair of cartilage defects in paediatric patients? *Drug Discovery Today* vol. 18 Preprint at https://doi.org/10.1016/j.drudis.2013.04.007 (2013).

113. Krishnan, S. P. *et al.* Who is the ideal candidate for autologous chondrocyte implantation? *Journal of Bone and Joint Surgery - Series B* **88**, (2006).

114. Eleftherios A. Makris, Andreas H. Gomoll, Konstantinos N. Malizos, Jerry C. Hu, A. & Athanasiou, K. A. Repair and tissue engineering techniques for articular cartilage. *Nat Rev Rheumatol.* **11**, 21–34 (2015).

115. Migliorini, F., Eschweiler, J., Goetze, C., Tingart, M. & Maffulli, N. Membrane scaffolds for matrix-induced autologous chondrocyte implantation in the knee: a systematic review. *British Medical Bulletin* vol. 140 Preprint at https://doi.org/10.1093/bmb/ldab024 (2021).

116. Intini, C. *et al.* A highly porous type II collagen containing scaffold for the treatment of cartilage defects enhances MSC chondrogenesis and early cartilaginous matrix deposition. *Biomater Sci* **10**, (2022).

117. Schuette, H. B., Kraeutler, M. J. & McCarty, E. C. Matrix-Assisted Autologous Chondrocyte Transplantation in the Knee: A Systematic Review of Mid- to Long-Term Clinical Outcomes. *Orthopaedic Journal of Sports Medicine* vol. 5 Preprint at https://doi.org/10.1177/2325967117709250 (2017).

118. Caron, M. M. J. *et al.* Redifferentiation of dedifferentiated human articular chondrocytes: Comparison of 2D and 3D cultures. *Osteoarthritis Cartilage* **20**, (2012).

119. Bartlett, W. *et al.* Autologous chondrocyte implantation versus matrix-induced autologous chondrocyte implantation for osteochondral defects of the knee. A prospective, randomised study. *Journal of Bone and Joint Surgery - Series B* (2005) doi:10.1302/0301-620X.87B5.15905.

120. Zeifang, F. *et al.* Autologous chondrocyte implantation using the original periosteum-cover technique versus matrix-associated autologous chondrocyte implantation: A randomized clinical trial. *American Journal of Sports Medicine* **38**, (2010).

121. Barié, A. *et al.* Prospective Long-term Follow-up of Autologous Chondrocyte Implantation With Periosteum Versus Matrix-Associated Autologous Chondrocyte Implantation: A Randomized Clinical Trial. *American Journal of Sports Medicine* **48**, (2020).

122. Jeon, J. E., Schrobback, K., Hutmacher, D. W. & Klein, T. J. Dynamic compression improves biosynthesis of human zonal chondrocytes from osteoarthritis patients. *Osteoarthritis Cartilage* **20**, (2012).

123. Martinez, I., Elvenes, J., Olsen, R., Bertheussen, K. & Johansen, O. Redifferentiation of in vitro expanded adult articular chondrocytes by combining the hanging-drop cultivation method with hypoxic environment. *Cell Transplant* (2008) doi:10.3727/096368908786576499.

124. Cheng, O. T., Souzdalnitski, D., Vrooman, B. & Cheng, J. Evidence-Based Knee Injections for the Management of Arthritis. *Pain Medicine (United States)* Preprint at https://doi.org/10.1111/j.1526-4637.2012.01394.x (2012).

125. Matzkin, E. G. *et al.* Efficacy and Treatment Response of Intra-articular Corticosteroid Injections in Patients with Symptomatic Knee Osteoarthritis. *Journal of the American Academy of Orthopaedic Surgeons* (2017) doi:10.5435/JAAOS-D-16-00541.

126. Arroll, B. & Goodyear-Smith, F. Corticosteroid injections for osteoarthritis of the knee: Meta-analysis. *Br Med J* (2004) doi:10.1136/bmj.38039.573970.7c.

127. Okike, K. *et al.* Rapidly Destructive Hip Disease Following Intra-Articular Corticosteroid Injection of the Hip. *Journal of Bone and Joint Surgery* **103**, (2021).

128. do Amaral, R. J. F. C. *et al.* Platelet-Rich Plasma Obtained with Different Anticoagulants and Their Effect on Platelet Numbers and Mesenchymal Stromal Cells Behavior In Vitro. *Stem Cells Int* **2016**, (2016).

129. Karolczak, K. & Watala, C. Blood platelets as an important but underrated circulating source of tgfβ. *International Journal of Molecular Sciences* vol. 22 Preprint at https://doi.org/10.3390/ijms22094492 (2021).

130. Harrison, S. *et al.* Platelet activation by collagen provides sustained release of anabolic cytokines. *American Journal of Sports Medicine* **39**, (2011).

131. Roman-Blas, J. A., Stokes, D. G. & Jimenez, S. A. Modulation of TGF-β signaling by proinflammatory cytokines in articular chondrocytes. *Osteoarthritis Cartilage* **15**, (2007).

132. Shen, L., Yuan, T., Chen, S., Xie, X. & Zhang, C. The temporal effect of platelet-rich plasma on pain and physical function in the treatment of knee osteoarthritis: Systematic review and meta-analysis of randomized controlled trials. *J Orthop Surg Res* **12**, (2017).

133. Patel, S., Dhillon, M. S., Aggarwal, S., Marwaha, N. & Jain, A. Treatment with platelet-rich plasma is more effective than placebo for knee osteoarthritis: A prospective, double-blind, randomized trial. *American Journal of Sports Medicine* vol. 41 Preprint at https://doi.org/10.1177/0363546512471299 (2013).

134. Bennell, K. L. *et al.* Effect of Intra-Articular Platelet-Rich Plasma vs Placebo Injection on Pain and Medial Tibial Cartilage Volume in Patients with Knee Osteoarthritis: The RESTORE Randomized Clinical Trial. *JAMA - Journal of the American Medical Association* **326**, (2021).

135. Gato-Calvo, L., Magalhaes, J., Ruiz-Romero, C., Blanco, F. J. & Burguera, E. F. Platelet-rich plasma in osteoarthritis treatment: Review of current evidence. *Therapeutic Advances in Chronic Disease* vol. 10 Preprint at https://doi.org/10.1177/2040622319825567 (2019).

136. Sfikakis, P. P. & Tsokos, G. C. Towards the next generation of anti-TNF drugs. *Clinical Immunology* vol. 141 Preprint at https://doi.org/10.1016/j.clim.2011.09.005 (2011).

137. I., A. *et al.* Sustained clinical benefit with multiple courses of rituximab in second line for all rheumatoid arthtritis patients irrespective to the inhibitor of tumour necrosis factor previously used. *Arthritis and Rheumatology* vol. 66 S677–S678 Preprint at http://ovidsp.ovid.com/ovidweb.cgi?T=JS&PAGE=reference&D=emed12&NEWS=N&AN=71737533 (2014).

138. Chevalier, X., Eymard, F. & Richette, P. Biologic agents in osteoarthritis: Hopes and disappointments. *Nature Reviews Rheumatology* vol. 9 Preprint at https://doi.org/10.1038/nrrheum.2013.44 (2013).

139. Kloppenburg, M. *et al.* Etanercept in patients with inflammatory hand osteoarthritis (EHOA): A multicentre, randomised, double-blind, placebo-controlled trial. *Ann Rheum Dis* **77**, (2018).

140. Aitken, D. *et al.* A randomised double-blind placebo-controlled crossover trial of HUMira (adalimumab) for erosive hand OsteoaRthritis – the HUMOR trial. *Osteoarthritis Cartilage* **26**, (2018).

141. Davidson, D. *et al.* Fibroblast growth factor (FGF) 18 signals through FGF receptor 3 to promote chondrogenesis. *Journal of Biological Chemistry* **280**, (2005).

142. Yao, X. *et al.* Fibroblast growth factor 18 exerts anti-osteoarthritic effects through PI3K-AKT signaling and mitochondrial fusion and fission. *Pharmacol Res* **139**, (2019).

143. Eckstein, F. *et al.* Long-term structural and symptomatic effects of intra-articular sprifermin in patients with knee osteoarthritis: 5-year results from the FORWARD study. *Ann Rheum Dis* **80**, (2021).

144. Hunter, D. J. *et al.* The symptoms of OA and the genesis of pain. *Rheum Dis Clin North Am.* **34**, (2009).

145. Abhishek, A. & Doherty, M. Diagnosis and Clinical Presentation of Osteoarthritis. *Rheumatic Disease Clinics of North America* vol. 39 Preprint at https://doi.org/10.1016/j.rdc.2012.10.007 (2013).

146. Kohn, M. D., Sassoon, A. A. & Fernando, N. D. Classifications in Brief: Kellgren-Lawrence Classification of Osteoarthritis. *Clin Orthop Relat Res* **474**, (2016).

147. KELLGREN, J. H. & LAWRENCE, J. S. Radiological assessment of osteo-arthrosis. *Ann Rheum Dis* **16**, (1957).

148. Stachowiak, G. W., Wolski, M., Woloszynski, T. & Podsiadlo, P. Detection and prediction of osteoarthritis in knee and hand joints based on the X-ray image analysis. *Biosurf Biotribol* **2**, (2016).

149. Hawker, G. A. & Lohmander, L. S. What an earlier recognition of osteoarthritis can do for OA prevention. *Osteoarthritis Cartilage* **29**, (2021).

150. Kundu, S. *et al.* Enabling early detection of osteoarthritis from presymptomatic cartilage texture maps via transport-based learning. *Proc Natl Acad Sci U S A* **117**, (2020).

151. Urish, K. L. *et al.* T2 texture index of cartilage can predict early symptomatic OA progression: Data from the osteoarthritis initiative. *Osteoarthritis Cartilage* **21**, (2013).

152. Nguyen, L. T. *et al.* Review of prospects of biological fluid biomarkers in osteoarthritis. *International Journal of Molecular Sciences* vol. 18 Preprint at https://doi.org/10.3390/ijms18030601 (2017).

153. Stannus, O. *et al.* Circulating levels of IL-6 and TNF-α are associated with knee radiographic osteoarthritis and knee cartilage loss in older adults. *Osteoarthritis Cartilage* **18**, (2010).

154. Attur, M. *et al.* Increased interleukin-1β gene expression in peripheral blood leukocytes is associated with increased pain and predicts risk for progression of symptomatic knee osteoarthritis. *Arthritis Rheum* **63**, (2011).

155. Özler, K. *et al.* Serum and knee synovial fluid matrixmetalloproteinase-13 and tumor necrosis factor-alpha levels in patients with late stage osteoarthritis. *Acta Orthop Traumatol Turc* **50**, (2016).

156. Okuhara, A. *et al.* Changes in microRNA expression in peripheral mononuclear cells according to the progression of osteoarthritis. *Mod Rheumatol* **22**, (2012).

157. Lao, T. D. & Le, T. A. H. Data integration reveals the potential biomarkers of circulating micrornas in osteoarthritis. *Diagnostics* vol. 11 Preprint at https://doi.org/10.3390/diagnostics11030412 (2021).

158. Ramos, Y. F. M. *et al.* Circulating micrornas highly correlate to expression of cartilage genes potentially reflecting oa susceptibility—towards identification of applicable early oa biomarkers. *Biomolecules* **11**, (2021).

159. Bay-Jensen, A. C., Mobasheri, A., Thudium, C. S., Kraus, V. B. & Karsdal, M. A. Blood and urine biomarkers in osteoarthritis - an update on cartilage associated type II collagen and aggrecan markers. *Current Opinion in Rheumatology* vol. 34 Preprint at https://doi.org/10.1097/BOR.0000000000000845 (2022).

160. Arunrukthavon, P. *et al.* Can urinary CTX-II be a biomarker for knee osteoarthritis? *Arthroplasty* **2**, (2020).

161. Mao, A. S. & Mooney, D. J. Regenerative medicine: Current therapies and future directions. *Proc Natl Acad Sci U S A* **112**, (2015).

162. Zein, I., Hutmacher, D. W., Tan, K. C. & Teoh, S. H. Fused deposition modeling of novel scaffold architectures for tissue engineering applications. *Biomaterials* **23**, (2002).

163. Bose, S., Tarafder, S. & Bandyopadhyay, A. Effect of Chemistry on Osteogenesis and Angiogenesis Towards Bone Tissue Engineering Using 3D Printed Scaffolds. *Ann Biomed Eng* (2017) doi:10.1007/s10439-016-1646-y.

164. Russias, J. *et al.* Fabrication and in vitro characterization of three-dimensional organic/inorganic scaffolds by robocasting. *J Biomed Mater Res A* **83**, (2007).

165. Chen, X. *et al.* 3D printed porous PLA/nHA composite scaffolds with enhanced osteogenesis and osteoconductivityin vivo for bone regeneration. *Biomedical Materials (Bristol)* **14**, (2019).

166. Du, R. *et al.* A Systematic Approach for Making 3D-Printed Patient-Specific Implants for Craniomaxillofacial Reconstruction. *Engineering* **6**, (2020).

167. Johnstone, B. *et al.* Tissue engineering for articular cartilage repair - The state of the art. *Eur Cell Mater* **25**, (2012).

168. Im, G. I. Current status of regenerative medicine in osteoarthritis. *Bone and Joint Research* vol. 10 Preprint at https://doi.org/10.1302/2046-3758.102.BJR-2020-0517.R1 (2021).

169. Datta, P. *et al.* Bioprinting of osteochondral tissues: A perspective on current gaps and future trends. *Int J Bioprint* **3**, (2017).

170. Monaco, G., El Haj, A. J., Alini, M. & Stoddart, M. J. Ex vivo systems to study chondrogenic differentiation and cartilage integration. *Journal of Functional Morphology and Kinesiology* vol. 6 Preprint at https://doi.org/10.3390/jfmk6010006 (2021).

171. Poole, A. R. *et al.* Composition and structure of articular cartilage: A template for tissue repair. in *Clinical Orthopaedics and Related Research* vol. 391 (2001).

172. Vanderploeg, E. J., Wilson, C. G. & Levenston, M. E. Articular chondrocytes derived from distinct tissue zones differentially respond to in vitro oscillatory tensile loading. *Osteoarthritis Cartilage* **16**, (2008).

173. Sophia Fox, A. J., Bedi, A. & Rodeo, S. A. The basic science of articular cartilage: Structure, composition, and function. *Sports Health* **1**, (2009).

174. S., N., A., D. & Carlos, J. Mechanical Behavior of Articular Cartilage. in *Injury and Skeletal Biomechanics* (2012). doi:10.5772/48323.

175. Darling, E. M., Hu, J. C. Y. & Athanasiou, K. A. Zonal and topographical differences in articular cartilage gene expression. *Journal of Orthopaedic Research* **22**, (2004).

176. Youn, I., Choi, J. B., Cao, L., Setton, L. A. & Guilak, F. Zonal variations in the three-dimensional morphology of the chondron measured in situ using confocal microscopy. *Osteoarthritis Cartilage* **14**, (2006).

177. Finnilä, M. A. J. *et al.* Mineral Crystal Thickness in Calcified Cartilage and Subchondral Bone in Healthy and Osteoarthritic Human Knees. *Journal of Bone and Mineral Research* **37**, (2022).

178. Mente, P. L. & Lewis, J. L. Elastic modulus of calcified cartilage is an order of magnitude less than that of subchondral bone. *Journal of Orthopaedic Research* **12**, (1994).

179. Sanchez-Adams, J., Leddy, H. A., McNulty, A. L., O'Conor, C. J. & Guilak, F. The Mechanobiology of Articular Cartilage: Bearing the Burden of Osteoarthritis. *Current Rheumatology Reports* vol. 16 Preprint at https://doi.org/10.1007/s11926-014-0451-6 (2014).

180. Choi, J. B. *et al.* Zonal changes in the three-dimensional morphology of the chondron under compression: The relationship among cellular, pericellular, and extracellular deformation in articular cartilage. *J Biomech* **40**, (2007).

181. Bader, D. L., Salter, D. M. & Chowdhury, T. T. Biomechanical Influence of Cartilage Homeostasis in Health and Disease. *Arthritis* **2011**, (2011).

182. Houard, X., Goldring, M. B. & Berenbaum, F. Homeostatic mechanisms in articular cartilage and role of inflammation in osteoarthritis. *Curr Rheumatol Rep* **15**, (2013).

183. Dowthwaite, G. P. *et al.* The surface of articular cartilage contains a progenitor cell populations. *J Cell Sci* **117**, (2004).

184. Khan, I. M., Bishop, J. C., Gilbert, S. & Archer, C. W. Clonal chondroprogenitors maintain telomerase activity and Sox9 expression during extended monolayer culture and retain chondrogenic potential. *Osteoarthritis Cartilage* **17**, (2009).

185. Haller, R. *et al.* Notch1 signaling regulates chondrogenic lineage determination through Sox9 activation. *Cell Death Differ* **19**, (2012).

186. Levato, R. *et al.* The bio in the ink: cartilage regeneration with bioprintable hydrogels and articular cartilage-derived progenitor cells. *Acta Biomater* **61**, (2017).

187. Chen, S. S., Falcovitz, Y. H., Schneiderman, R., Maroudas, A. & Sah, R. L. Depth-dependent compressive properties of normal aged human femoral head articular cartilage: Relationship to fixed charge density. *Osteoarthritis Cartilage* **9**, (2001).

188. Saito, T. The superficial zone of articular cartilage. *Inflammation and Regeneration* vol. 42 Preprint at https://doi.org/10.1186/s41232-022-00202-0 (2022).

189. Zheng, Q. *et al.* Type X collagen gene regulation by Runx2 contributes directly to its hypertrophic chondrocyte-specific expression in vivo. *Journal of Cell Biology* **162**, (2003).

190. Da, H. *et al.* The Impact of Compact Layer in Biphasic Scaffold on Osteochondral Tissue Engineering. *PLoS One* **8**, (2013).

191. Shim, J. H. *et al.* Three-dimensional bioprinting of multilayered constructs containing human mesenchymal stromal cells for osteochondral tissue regeneration in the rabbit knee joint. *Biofabrication* (2016) doi:10.1088/1758-5090/8/1/014102.

192. Mekhileri, N. v. *et al.* Automated 3D bioassembly of micro-tissues for biofabrication of hybrid tissue engineered constructs. *Biofabrication* **10**, (2018).

193. Cui, X. *et al.* 3D bioassembly of cell-instructive chondrogenic and osteogenic hydrogel microspheres containing allogeneic stem cells for hybrid biofabrication of osteochondral constructs. *Biofabrication* **14**, (2022).

194. Liu, Y. *et al.* 3D-bioprinted BMSC-laden biomimetic multiphasic scaffolds for efficient repair of osteochondral defects in an osteoarthritic rat model. *Biomaterials* **279**, (2021).

195. Steele, J. A. M. *et al.* In vitro and in vivo investigation of a zonal microstructured scaffold for osteochondral defect repair. *Biomaterials* **286**, (2022).

196. Little, C. B. & Hunter, D. J. Post-traumatic osteoarthritis: From mouse models to clinical trials. *Nature Reviews Rheumatology* vol. 9 Preprint at https://doi.org/10.1038/nrrheum.2013.72 (2013).

197. Kuyinu, E. L., Narayanan, G., Nair, L. S. & Laurencin, C. T. Animal models of osteoarthritis: Classification, update, and measurement of outcomes. *Journal of Orthopaedic Surgery and Research* vol. 11 Preprint at https://doi.org/10.1186/s13018-016-0346-5 (2016).

198. Moreau, M. *et al.* A posteriori comparison of natural and surgical destabilization models of canine osteoarthritis. *Biomed Res Int* **2013**, (2013).

199. Jakus, A. E. *et al.* Hyperelastic 'bone': A highly versatile, growth factor-free, osteoregenerative, scalable, and surgically friendly biomaterial. *Sci Transl Med* (2016) doi:10.1126/scitranslmed.aaf7704.

200. Wang, L. *et al.* Key considerations on the development of biodegradable biomaterials for clinical translation of medical devices: With cartilage repair products as an example. *Bioactive Materials* vol. 9 Preprint at https://doi.org/10.1016/j.bioactmat.2021.07.031 (2022).

201. He, T. *et al.* Multi-arm Avidin nano-construct for intra-cartilage delivery of small molecule drugs. *Journal of Controlled Release* **318**, (2020).

202. Brown, B. N., Sicari, B. M. & Badylak, S. F. Rethinking regenerative medicine: A macrophage-centered approach. *Frontiers in Immunology* vol. 5 Preprint at https://doi.org/10.3389/fimmu.2014.00510 (2014).

203. Wang, Y. *et al.* Macrophage-derived extracellular vesicles: diverse mediators of pathology and therapeutics in multiple diseases. *Cell Death and Disease* vol. 11 Preprint at https://doi.org/10.1038/s41419-020-03127-z (2020).

204. Stein, M., Keshav, S., Harris, N. & Gordon, S. Interleukin 4 potently enhances murine macrophage mannose receptor activity: A marker of alternative immunologic macrophage activation. *Journal of Experimental Medicine* **176**, (1992).

205. M., N., Dasgupta, P., J., N., P., S. & D., A. The Type I and Type II Receptor Complexes for IL-4 and IL-13 Differentially Regulate Allergic Lung Inflammation. in *Allergic Diseases - Highlights in the Clinic, Mechanisms and Treatment* (2012). doi:10.5772/25650.

206. Keegan, A. D., Leonard, W. J. & Zhu, J. Recent advances in understanding the role of IL-4 signaling. *Fac Rev* **10**, (2021).

207. Atri, C., Guerfali, F. Z. & Laouini, D. Role of human macrophage polarization in inflammation during infectious diseases. *International Journal of Molecular Sciences* vol. 19 Preprint at https://doi.org/10.3390/ijms19061801 (2018).

208. Vogel, D. Y. S. *et al.* Human macrophage polarization in vitro: Maturation and activation methods compared. *Immunobiology* **219**, (2014).

209. Iqbal, S. & Kumar, A. Characterization of In vitro Generated Human Polarized Macrophages. *J Clin Cell Immunol* **06**, (2015).

210. Schraufstatter, I. U., Zhao, M., Khaldoyanidi, S. K. & Discipio, R. G. The chemokine CCL18 causes maturation of cultured monocytes to macrophages in the M2 spectrum. *Immunology* **135**, (2012).

211. Rapp, M. *et al.* CCL22 controls immunity by promoting regulatory T cell communication with dendritic cells in lymph nodes. *Journal of Experimental Medicine* **216**, (2019).

212. Ren, G., Al-Jezani, N., Railton, P., Powell, J. N. & Krawetz, R. J. CCL22 induces pro-inflammatory changes in fibroblast-like synoviocytes. *iScience* **24**, (2021).

213. Roszer, T. Understanding the mysterious M2 macrophage through activation markers and effector mechanisms. *Mediators of Inflammation* vol. 2015 Preprint at https://doi.org/10.1155/2015/816460 (2015).

214. Yue, Y. *et al.* M2b macrophages reduce early reperfusion injury after myocardial ischemia in mice: A predominant role of inhibiting apoptosis via A20. *Int J Cardiol* **245**, (2017).

215. Wang, L. xun, Zhang, S. xi, Wu, H. juan, Rong, X. lu & Guo, J. M2b macrophage polarization and its roles in diseases. *Journal of Leukocyte Biology* vol. 106 Preprint at https://doi.org/10.1002/JLB.3RU1018-378RR (2019).

216. Anderson, C. F. & Mosser, D. M. A novel phenotype for an activated macrophage: the type 2 activated macrophage. *J Leukoc Biol* **72**, (2002).

217. Keeler, G. D., Durdik, J. M. & Stenken, J. A. Effects of delayed delivery of dexamethasone-21-phosphate via subcutaneous microdialysis implants on macrophage activation in rats. *Acta Biomater* **23**, (2015).

218. Lu, J. *et al.* Discrete functions of M2a and M2c macrophage subsets determine their relative efficacy in treating chronic kidney disease. *Kidney Int* **84**, (2013).

219. Ferrante, C. J. *et al.* The adenosine-dependent angiogenic switch of macrophages to an M2-like phenotype is independent of interleukin-4 receptor alpha (IL-4Rα) signaling. *Inflammation* **36**, (2013).

220. Duque, G. A. & Descoteaux, A. Macrophage cytokines: Involvement in immunity and infectious diseases. *Frontiers in Immunology* vol. 5 Preprint at https://doi.org/10.3389/fimmu.2014.00491 (2014).

221. Hessian, P. A. & Fisher, L. The heterodimeric complex of MRP-8 (S100A8) and MRP-14 (S100A9). *Eur J Biochem* **268**, (2001).

222. Bhardwaj, R. S. *et al.* The calcium-binding proteins MRP8 and MRP14 form a membrane-associated heterodimer in a subset of monocytes/macrophages present in acute but absent in chronic inflammatory lesions. *Eur J Immunol* **22**, (1992).

223. Wang, S. *et al.* S100A8/A9 in inflammation. *Frontiers in Immunology* vol. 9 Preprint at https://doi.org/10.3389/fimmu.2018.01298 (2018).

224. Zhou, Y. *et al.* Different distributions of M1 and M2 macrophages in a mouse model of laser-induced choroidal neovascularization. *Mol Med Rep* **15**, (2017).

225. Hamilton, T. A., Zhao, C., Pavicic, P. G. & Datta, S. Myeloid colony-stimulating factors as regulators of macrophage polarization. *Front Immunol* **5**, (2014).

226. Ushach, I. & Zlotnik, A. Biological role of granulocyte macrophage colony-stimulating factor (GM-CSF) and macrophage colony-stimulating factor (M-CSF) on cells of the myeloid lineage. *J Leukoc Biol* **100**, (2016).

227. Murray, P. J. *et al.* Macrophage Activation and Polarization: Nomenclature and Experimental Guidelines. *Immunity* vol. 41 Preprint at https://doi.org/10.1016/j.immuni.2014.06.008 (2014).

228. Nahrendorf, M. & Swirski, F. K. Abandoning M1/M2 for a network model of macrophage function. *Circulation Research* vol. 119 Preprint at https://doi.org/10.1161/CIRCRESAHA.116.309194 (2016).

229. McWhorter, F. Y., Wang, T., Nguyen, P., Chung, T. & Liu, W. F. Modulation of macrophage phenotype by cell shape. *Proceedings of the National Academy of Sciences* (2013) doi:10.1073/pnas.1308887110.

230. Yu, W. P. *et al.* Titanium dioxide nanotubes promote M2 polarization by inhibiting macrophage glycolysis and ultimately accelerate endothelialization. *Immun Inflamm Dis* **9**, (2021).

231. Wang, M. *et al.* Regulation of macrophage polarization and functional status by modulating hydroxyapatite ceramic micro/nano-topography. *Mater Des* **213**, (2022).

232. Saleh, B. *et al.* Local Immunomodulation Using an Adhesive Hydrogel Loaded with miRNA-Laden Nanoparticles Promotes Wound Healing. *Small* **15**, (2019).

233. Li, T. *et al.* 3D-printed IFN-γ-loading calcium silicate-β-tricalcium phosphate scaffold sequentially activates M1 and M2 polarization of macrophages to promote vascularization of tissue engineering bone. *Acta Biomater* (2018) doi:10.1016/j.actbio.2018.03.012.

234. Díez-Tercero, L., Delgado, L. M., Bosch-Rué, E. & Perez, R. A. Evaluation of the immunomodulatory effects of cobalt, copper and magnesium ions in a pro inflammatory environment. *Sci Rep* **11**, (2021).

235. Rostam, H. M. *et al.* Immune-Instructive Polymers Control Macrophage Phenotype and Modulate the Foreign Body Response In Vivo. *Matter* **2**, (2020).

236. Anderson, J. M., Rodriguez, A. & Chang, D. T. Foreign body reaction to biomaterials. *Seminars in Immunology* Preprint at https://doi.org/10.1016/j.smim.2007.11.004 (2008).

237. McNally, A. K. & Anderson, J. M. Interleukin-4 induces foreign body giant cells from human monocytes/macrophages: Differential lymphokine regulation of macrophage fusion leads to morphological variants of multinucleated giant cells. *American Journal of Pathology* **147**, (1995).

238. MacLauchlan, S. *et al.* Macrophage fusion, giant cell formation, and the foreign body response require matrix metalloproteinase 9. *J Leukoc Biol* **85**, (2009).

239. Noskovicova, N., Hinz, B. & Pakshir, P. Implant fibrosis and the underappreciated role of myofibroblasts in the foreign body reaction. *Cells* vol. 10 Preprint at https://doi.org/10.3390/cells10071794 (2021).

240. Haas, A. The phagosome: Compartment with a license to kill. *Traffic* vol. 8 Preprint at https://doi.org/10.1111/j.1600-0854.2006.00531.x (2007).

241. Brown, B. N. *et al.* Macrophage phenotype as a predictor of constructive remodeling following the implantation of biologically derived surgical mesh materials. *Acta Biomater* **8**, (2012).

242. Madden, L. R. *et al.* Proangiogenic scaffolds as functional templates for cardiac tissue engineering. *Proc Natl Acad Sci U S A* **107**, (2010).

243. Deng, Y. *et al.* 3D printed scaffolds of calcium silicate-doped β-TCP synergize with co-cultured endothelial and stromal cells to promote vascularization and bone formation. *Sci Rep* **7**, (2017).

244. Spiller, K. L. *et al.* Sequential delivery of immunomodulatory cytokines to facilitate the M1-to-M2 transition of macrophages and enhance vascularization of bone scaffolds. *Biomaterials* (2015) doi:10.1016/j.biomaterials.2014.10.017.

245. Louiselle, A. E., Niemiec, S. M., Zgheib, C. & Liechty, K. W. Macrophage polarization and diabetic wound healing. *Translational Research* vol. 236 Preprint at https://doi.org/10.1016/j.trsl.2021.05.006 (2021).

246. Hesketh, M., Sahin, K. B., West, Z. E. & Murray, R. Z. Macrophage phenotypes regulate scar formation and chronic wound healing.

International Journal of Molecular Sciences vol. 18 Preprint at https://doi.org/10.3390/ijms18071545 (2017).

247. Tsuchiya, S. *et al.* Establishment and characterization of a human acute monocytic leukemia cell line (THP-1). *Int J Cancer* **26**, (1980).

248. Genin, M., Clement, F., Fattaccioli, A., Raes, M. & Michiels, C. M1 and M2 macrophages derived from THP-1 cells differentially modulate the response of cancer cells to etoposide. *BMC Cancer* **15**, (2015).

249. Abuawad, A., Mbadugha, C., Ghaemmaghami, A. M. & Kim, D. H. Metabolic characterisation of THP-1 macrophage polarisation using LC–MS-based metabolite profiling. *Metabolomics* **16**, (2020).

250. Baxter, E. W. *et al.* Standardized protocols for differentiation of THP-1 cells to macrophages with distinct M(IFNγ+LPS), M(IL-4) and M(IL-10) phenotypes. *J Immunol Methods* **478**, (2020).

251. Gažová, I. *et al.* The Transcriptional Network That Controls Growth Arrest and Macrophage Differentiation in the Human Myeloid Leukemia Cell Line THP-1. *Front Cell Dev Biol* **8**, (2020).

252. Chanput, W., Mes, J. J., Savelkoul, H. F. J. & Wichers, H. J. Characterization of polarized THP-1 macrophages and polarizing ability of LPS and food compounds. *Food Funct* **4**, (2013).

253. Murray, P. J. & Wynn, T. A. Obstacles and opportunities for understanding macrophage polarization. *J Leukoc Biol* **89**, (2011).

254. Shiratori, H. *et al.* THP-1 and human peripheral blood mononuclear cell-derived macrophages differ in their capacity to polarize in vitro. *Mol Immunol* **88**, (2017).

255. Tedesco, S. *et al.* Convenience versus biological significance: Are PMA-differentiated THP-1 cells a reliable substitute for blood-derived macrophages when studying in vitro polarization? *Front Pharmacol* **9**, (2018).

256. Schildberger, A., Rossmanith, E., Eichhorn, T., Strassl, K. & Weber, V. Monocytes, peripheral blood mononuclear cells, and THP-1 cells exhibit different cytokine expression patterns following stimulation with lipopolysaccharide. *Mediators Inflamm* **2013**, (2013).

257. Feige, M. J. & Hendershot, L. M. Disulfide bonds in ER protein folding and homeostasis. *Current Opinion in Cell Biology* vol. 23 Preprint at https://doi.org/10.1016/j.ceb.2010.10.012 (2011).

258. Comstock, M. J. *et al.* Direct observation of structure-function relationship in a nucleic acid -processing enzyme. *Science (1979)* **348**, (2015).

259. Ritchie, K. P., Keller, B. M., Syed, K. M. & Lepock, J. R. Hyperthermia (heat shock)-induced protein denaturation in liver, muscle and Lens tissue as determined by differential scanning calorimetry. *International Journal of Hyperthermia* **10**, (1994).

260. Yang, A. S. & Honig, B. On the pH dependence of protein stability. *J Mol Biol* **231**, (1993).

261. Ruzza, P., Honisch, C., Hussain, R. & Siligardi, G. Free radicals and ros induce protein denaturation by uv photostability assay. *Int J Mol Sci* **22**, (2021).

262. England, J. L. & Haran, G. Role of solvation effects in protein denaturation: From thermodynamics to single molecules and back. *Annu Rev Phys Chem* **62**, (2011).

263. Dill, K. Denatured States Of Proteins. *Annu Rev Biochem* **60**, (1991).

264. Li, W., Fan, Z., Lin, Y. & Wang, T. Y. Serum-Free Medium for Recombinant Protein Expression in Chinese Hamster Ovary Cells. *Frontiers in Bioengineering and Biotechnology* vol. 9 Preprint at https://doi.org/10.3389/fbioe.2021.646363 (2021).

265. Pulix, M., Lukashchuk, V., Smith, D. C. & Dickson, A. J. Molecular characterization of HEK293 cells as emerging versatile cell factories. *Current Opinion in Biotechnology* vol. 71 Preprint at https://doi.org/10.1016/j.copbio.2021.05.001 (2021).

266. Zhou, M. *et al.* Production of bioactive recombinant human fibroblast growth factor 12 using a new transient expression vector in E. coli and its neuroprotective effects. *Appl Microbiol Biotechnol* **105**, (2021).

267. Kesik-Brodacka, M. Progress in biopharmaceutical development. *Biotechnology and Applied Biochemistry* vol. 65 Preprint at https://doi.org/10.1002/bab.1617 (2018).

268. Usmani, S. S. *et al.* THPdb: Database of FDA-approved peptide and protein therapeutics. *PLoS One* **12**, (2017).

269. Gillman, C. E. & Jayasuriya, A. C. FDA-approved bone grafts and bone graft substitute devices in bone regeneration. *Materials Science and Engineering C* vol. 130 Preprint at https://doi.org/10.1016/j.msec.2021.112466 (2021).

270. Burkus, J. K., Transfeldt, E. E., Kitchel, S. H., Watkins, R. G. & Balderston, R. A. Clinical and radiographic outcomes of anterior lumbar interbody fusion using recombinant human bone morphogenetic protein-2. *Spine (Phila Pa 1976)* **27**, (2002).

271. Deutsch, H. High-dose bone morphogenetic protein-induced ectopic abdomen bone growth. *Spine Journal* **10**, (2010).

272. Epstein, N. Complications due to the use of BMP/INFUSE in spine surgery: The evidence continues to mount. *Surg Neurol Int* **4**, (2013).

273. Epstein, N. Pros, cons, and costs of INFUSE in spinal surgery. *Surgical Neurology International* vol. 2 Preprint at https://doi.org/10.4103/2152-7806.76147 (2011).

274. G. Marx, J. & P. Lorio, M. Class III Spine Grafts. in *Clinical Implementation of Bone Regeneration and Maintenance* (2021). doi:10.5772/intechopen.87706.

275. Sreekumar, V. *et al.* BMP9 a possible alternative drug for the recently withdrawn BMP7? New perspectives for (re-)implementation by personalized medicine. *Arch Toxicol* **91**, (2017).

276. Nevins, M. *et al.* Platelet-Derived Growth Factor Promotes Periodontal Regeneration in Localized Osseous Defects: 36-Month Extension

Results From a Randomized, Controlled, Double-Masked Clinical Trial. *J Periodontol* **84**, (2013).

277. Berraondo, P. *et al.* Cytokines in clinical cancer immunotherapy. *British Journal of Cancer* vol. 120 Preprint at https://doi.org/10.1038/s41416-018-0328-y (2019).

278. Floros, T. & Tarhini, A. A. Anticancer Cytokines: Biology and Clinical Effects of Interferon-α2, Interleukin (IL)-2, IL-15, IL-21, and IL-12. *Seminars in Oncology* vol. 42 Preprint at https://doi.org/10.1053/j.seminoncol.2015.05.015 (2015).

279. Zhang, B. *et al.* Site-specific PEGylation of interleukin-2 enhances immunosuppression via the sustained activation of regulatory T cells. *Nat Biomed Eng* **5**, (2021).

280. Gupta, V. *et al.* Protein PEGylation for cancer therapy: bench to bedside. *Journal of Cell Communication and Signaling* vol. 13 Preprint at https://doi.org/10.1007/s12079-018-0492-0 (2019).

281. Huang, X. & Brazel, C. S. On the importance and mechanisms of burst release in matrix-controlled drug delivery systems. *Journal of Controlled Release* vol. 73 Preprint at https://doi.org/10.1016/S0168-3659(01)00248-6 (2001).

282. Yasmin, F., Chen, X. & Eames, B. F. Effect of process parameters on the initial burst release of protein-loaded alginate nanospheres. *J Funct Biomater* **10**, (2019).

283. Kim, H. K. & Park, T. G. Microencapsulation of human growth hormone within biodegradable polyester microspheres: Protein aggregation stability and incomplete release mechanism. *Biotechnol Bioeng* **65**, (1999).

284. Raza, F. *et al.* A review on recent advances in stabilizing peptides/proteins upon fabrication in hydrogels from biodegradable polymers. *Pharmaceutics* vol. 10 Preprint at https://doi.org/10.3390/pharmaceutics10010016 (2018).

285. Paillard-Giteau, A. *et al.* Effect of various additives and polymers on lysozyme release from PLGA microspheres prepared by an s/o/w emulsion technique. *European Journal of Pharmaceutics and Biopharmaceutics* **75**, (2010).

286. Li, J. & Mooney, D. J. Designing hydrogels for controlled drug delivery. *Nature Reviews Materials* Preprint at https://doi.org/10.1038/natrevmats.2016.71 (2016).

287. Lin, C. C. & Anseth, K. S. PEG hydrogels for the controlled release of biomolecules in regenerative medicine. *Pharmaceutical Research* vol. 26 Preprint at https://doi.org/10.1007/s11095-008-9801-2 (2009).

288. Fairbanks, B. D., Schwartz, M. P., Bowman, C. N. & Anseth, K. S. Photoinitiated polymerization of PEG-diacrylate with lithium phenyl-2,4,6-trimethylbenzoylphosphinate: polymerization rate and cytocompatibility. *Biomaterials* **30**, (2009).

289. Tibbitt, M. W., Kloxin, A. M., Sawicki, L. A. & Anseth, K. S. Mechanical properties and degradation of chain and step-polymerized photodegradable hydrogels. *Macromolecules* **46**, (2013).

290. Krutkramelis, K., Xia, B. & Oakey, J. Monodisperse polyethylene glycol diacrylate hydrogel microsphere formation by oxygen-controlled photopolymerization in a microfluidic device. *Lab Chip* **16**, (2016).

291. Lin, J. T., Liu, H. W., Chen, K. T. & Cheng, D. C. Modeling the Kinetics, Curing Depth, and Efficacy of Radical-Mediated Photopolymerization: The Role of Oxygen Inhibition, Viscosity, and Dynamic Light Intensity. *Front Chem* **7**, (2019).

292. Rekowska, N. *et al*. Thermal, Mechanical and Biocompatibility Analyses of Photochemically Polymerized PEGDA250 for Photopolymerization-Based Manufacturing Processes. *Pharmaceutics* **14**, (2022).

293. Yoshii, E. Cytotoxic effects of acrylates and methacrylates: Relationships of monomer structures and cytotoxicity. *J Biomed Mater Res* **37**, (1997).

294. Browning, M. B., Cereceres, S. N., Luong, P. T. & Cosgriff-Hernandez, E. M. Determination of the in vivo degradation mechanism of PEGDA hydrogels. *J Biomed Mater Res A* **102**, (2014).

295. Lee, S., Tong, X. & Yang, F. Effects of the poly(ethylene glycol) hydrogel crosslinking mechanism on protein release. *Biomater Sci* **4**, (2016).

296. Cruise, G. M., Scharp, D. S. & Hubbell, J. A. Characterization of permeability and network structure of interfacially photopolymerized poly(ethylene glycol) diacrylate hydrogels. *Biomaterials* **19**, (1998).

297. Weber, L. M., Lopez, C. G. & Anseth, K. S. Effects of PEG hydrogel crosslinking density on protein diffusion and encapsulated islet survival and function. *J Biomed Mater Res A* **90**, (2009).

298. Sawhney, A. S., Pathak, C. P. & Hubbell, J. A. Bioerodible Hydrogels Based on Photopolymerized Poly(ethylene glycol)-co-poly (α-hydroxy acid) Diacrylate Macromers. *Macromolecules* **26**, (1993).

299. Tong, X., Lee, S., Bararpour, L. & Yang, F. Long-Term Controlled Protein Release from Poly(Ethylene Glycol) Hydrogels by Modulating Mesh Size and Degradation. *Macromol Biosci* **15**, (2015).

300. Lau, C. M. L., Jahanmir, G., Yu, Y. & Chau, Y. Controllable multi-phase protein release from in-situ hydrolyzable hydrogel. *Journal of Controlled Release* **335**, (2021).

301. Stillman, Z., Jarai, B. M., Raman, N., Patel, P. & Fromen, C. A. Degradation profiles of poly(ethylene glycol)diacrylate (PEGDA)-based hydrogel nanoparticles. *Polym Chem* **11**, (2020).

302. Zarrintaj, P. *et al.* Poloxamer: A versatile tri-block copolymer for biomedical applications. *Acta Biomaterialia* vol. 110 Preprint at https://doi.org/10.1016/j.actbio.2020.04.028 (2020).

303. Bohorquez, M., Koch, C., Trygstad, T. & Pandit, N. A study of the temperature-dependent micellization of pluronic F127. *J Colloid Interface Sci* **216**, (1999).

304. Diniz, I. M. A. *et al.* Pluronic F-127 hydrogel as a promising scaffold for encapsulation of dental-derived mesenchymal stem cells. *J Mater Sci Mater Med* **26**, (2015).

305. Wang, P. L. & Johnston, T. P. Sustained-release interleukin-2 following intramuscular injection in rats. *Int J Pharm* **113**, (1995).

306. Argueta, L. B. *et al.* Platforms to test the temporospatial capabilities of carrier systems in delivering growth factors to benefit vascular bioengineering. *Nanomedicine* **36**, (2021).

307. Sultan, M. H., Mahdi, W. A. & Kwon, Y. M. Insulin release from nph insulin-loaded pluronic® f127 hydrogel in the presence of simulated tissue enzyme activity. *Processes* **8**, (2020).

308. Geng, H., Song, H., Qi, J. & Cui, D. Sustained release of VEGF from PLGA-nanoparticles mbedded thermo-sensitive hydrogel in full-thickness porcine bladder acellular matrix. *Nanoscale Res Lett* **6**, (2011).

309. Capila, I. & Linhardt, R. J. Heparin - Protein interactions. *Angewandte Chemie - International Edition* vol. 41 Preprint at https://doi.org/10.1002/1521-3773(20020201)41:3<390::AID-ANIE390>3.0.CO;2-B (2002).

310. Audain, E., Ramos, Y., Hermjakob, H., Flower, D. R. & Perez-Riverol, Y. Accurate estimation of isoelectric point of protein and peptide based on amino acid sequences. *Bioinformatics* **32**, (2016).

311. Conlon, P. J., Tyler, S., Grabstein, K. H. & Morrissey, P. Interleukin-4 (B-cell stimulatory factor-1) augments the in vivo generation of cytotoxic cells in immunosuppressed animals. *Biotechnol Ther* **1**, (1989).

312. Jeon, O., Powell, C., Solorio, L. D., Krebs, M. D. & Alsberg, E. Affinity-based growth factor delivery using biodegradable, photocrosslinked heparin-alginate hydrogels. *Journal of Controlled Release* **154**, (2011).

313. Noushi, F., Richardson, R. T., Hardman, J., Clark, G. & O'Leary, S. Delivery of neurotrophin-3 to the cochlea using alginate beads. *Otology and Neurotology* **26**, (2005).

314. Claaßen, C., Sewald, L., Tovar, G. E. M. & Borchers, K. Controlled release of vascular endothelial growth factor from heparin-functionalized gelatin type a and albumin hydrogels. *Gels* **3**, (2017).

315. Fareed, J. *et al.* Biochemical and Pharmacologic Heterogeneity in Low Molecular Weight Heparins. Impact on the Therapeutic Profile. *Curr Pharm Des* **10**, (2005).

316. Estrada, C. A., Mansfield, C. J. & Heudebert, G. R. Cost-effectiveness of low-molecular-weight heparin in the treatment of proximal deep vein thrombosis. *J Gen Intern Med* **15**, (2000).

317. Liu, H., Zhang, Z. & Linhardt, R. J. Lessons learned from the contamination of heparin. *Natural Product Reports* vol. 26 Preprint at https://doi.org/10.1039/b819896a (2009).

318. Monakhova, Y. B., Diehl, B. W. K. & Fareed, J. Authentication of animal origin of heparin and low molecular weight heparin including ovine, porcine and bovine species using 1D NMR spectroscopy and chemometric tools. *J Pharm Biomed Anal* **149**, (2018).

319. Oduah, E. I., Linhardt, R. J. & Sharfstein, S. T. Heparin: Past, present, and future. *Pharmaceuticals* vol. 9 Preprint at https://doi.org/10.3390/ph9030038 (2016).

320. Nilasaroya, A., Martens, P. J. & Whitelock, J. M. Enzymatic degradation of heparin-modified hydrogels and its effect on bioactivity. *Biomaterials* **33**, (2012).

321. Hunt, N. C., Shelton, R. M., Henderson, D. J. & Grover, L. M. Calcium-alginate hydrogel-encapsulated fibroblasts provide sustained release of vascular endothelial growth factor. *Tissue Eng Part A* **19**, (2013).

322. Freeman, I., Kedem, A. & Cohen, S. The effect of sulfation of alginate hydrogels on the specific binding and controlled release of heparin-binding proteins. *Biomaterials* (2008) doi:10.1016/j.biomaterials.2008.04.025.

323. Park, J., Lee, S. J., Lee, H., Park, S. A. & Lee, J. Y. Three dimensional cell printing with sulfated alginate for improved bone morphogenetic protein-2 delivery and osteogenesis in bone tissue engineering. *Carbohydr Polym* **196**, (2018).

324. Yorimitsu, M. *et al.* Intra-articular injection of interleukin-4 decreases nitric oxide production by chondrocytes and ameliorates subsequent destruction of cartilage in instability-induced osteoarthritis in rat knee joints. *Osteoarthritis Cartilage* **16**, (2008).

325. Zhao, D. W. *et al.* Interleukin-4 assisted calcium-strontium-zinc-phosphate coating induces controllable macrophage polarization and promotes osseointegration on titanium implant. *Materials Science and Engineering C* **118**, (2021).

326. van Helvoort, E. M. *et al.* IL4-10 Fusion Protein Shows DMOAD Activity in a Rat Osteoarthritis Model. *Cartilage* **13**, (2021).

327. von Kaeppler, E. P. *et al.* Interleukin 4 promotes anti-inflammatory macrophages that clear cartilage debris and inhibits osteoclast development to protect against osteoarthritis. *Clinical Immunology* **229**, (2021).

328. Reeves, A. R. D., Spiller, K. L., Freytes, D. O., Vunjak-Novakovic, G. & Kaplan, D. L. Controlled release of cytokines using silk-biomaterials for macrophage polarization. *Biomaterials* **73**, (2015).

329. Li, M. *et al.* Controllable release of interleukin-4 in double-layer sol-gel coatings on TiO 2 nanotubes for modulating macrophage polarization. *Biomedical Materials (Bristol)* **13**, (2018).

330. Kumar, M., Gupta, P., Bhattacharjee, S., Nandi, S. K. & Mandal, B. B. Immunomodulatory injectable silk hydrogels maintaining functional islets and promoting anti-inflammatory M2 macrophage polarization. *Biomaterials* **187**, (2018).

331. Li, Q., Liang, B., Wang, F. & Wang, Z. Delivery of Interleukin 4 from a Titanium Substrate Coated with Graphene Oxide for Enhanced Osseointegration by Regulating Macrophage Polarization. *ACS Biomater Sci Eng* **6**, (2020).

332. Gong, L. *et al.* An interleukin-4-loaded bi-layer 3D printed scaffold promotes osteochondral regeneration. *Acta Biomater* **117**, (2020).

333. Yue, K. *et al.* Synthesis, properties, and biomedical applications of gelatin methacryloyl (GelMA) hydrogels. *Biomaterials* vol. 73 Preprint at https://doi.org/10.1016/j.biomaterials.2015.08.045 (2015).

334. Liu, Y. & Chan-Park, M. B. A biomimetic hydrogel based on methacrylated dextran-graft-lysine and gelatin for 3D smooth muscle cell culture. *Biomaterials* **31**, (2010).

335. Suvarnapathaki, S., Nguyen, M. A., Wu, X., Nukavarapu, S. P. & Camci-Unal, G. Synthesis and characterization of photocrosslinkable hydrogels from bovine skin gelatin. *RSC Adv* **9**, (2019).

336. Li, R. *et al.* Expression of recombinant human IL-4 in Pichia pastoris and relationship between its glycosylation and biological activity. *Protein Expr Purif* **96**, (2014).

337. Lin, C. C., Sawicki, S. M. & Metters, A. T. Free-radical-mediated protein inactivation and recovery during protein photoencapsulation. *Biomacromolecules* **9**, (2008).

338. Lin, C. C. & Metters, A. T. Enhanced protein delivery from photopolymerized hydrogels using a pseudospecific metal chelating ligand. *Pharm Res* **23**, (2006).

339. Weber, L. M., Lopez, C. G. & Anseth, K. S. Effects of PEG hydrogel crosslinking density on protein diffusion and encapsulated islet survival and function. *J Biomed Mater Res A* **90**, (2009).

340. Lockman, L. E. Practice Tips: Knee joint injections and aspirations. The triangle technique. *Canadian Family Physician* vol. 52 Preprint at (2006).

341. Gill, H. S. & Prausnitz, M. R. Does needle size matter? *J Diabetes Sci Technol* **1**, (2007).

342. Yang, W., Yu, H., Liang, W., Wang, Y. & Liu, L. Rapid fabrication of hydrogel microstructures using UV-induced projection printing. *Micromachines (Basel)* **6**, (2015).

343. Mau, R., Reske, T., Eickner, T., Grabow, N. & Seitz, H. DLP 3D printing of Dexamethasoneincorporated PEGDA-based photopolymers: Compressive properties and drug release. *Current Directions in Biomedical Engineering* **6**, (2020).

344. Madzarevic, M. *et al.* Optimization and prediction of ibuprofen release from 3D DLP printlets using artificial neural networks. *Pharmaceutics* **11**, (2019).

345. Martinez, P. R., Goyanes, A., Basit, A. W. & Gaisford, S. Influence of Geometry on the Drug Release Profiles of Stereolithographic (SLA) 3D-Printed Tablets. *AAPS PharmSciTech* **19**, (2018).

346. Wang, P. *et al.* Controlled Growth Factor Release in 3D-Printed Hydrogels. *Adv Healthc Mater* **9**, (2020).

347. McGann, C. L., Dumm, R. E., Jurusik, A. K., Sidhu, I. & Kiick, K. L. Thiol-ene Photocrosslinking of Cytocompatible Resilin-Like Polypeptide-PEG Hydrogels. *Macromol Biosci* **16**, (2016).

348. Lo Conte, M., Pacifico, S., Chambery, A., Marra, A. & Dondoni, A. Photoinduced addition of glycosyl thiols to alkynyl peptides: Use of free-radical thiol-yne coupling for post-translational double-glycosylation of peptides. *Journal of Organic Chemistry* **75**, (2010).

349. Zhong, H., Chan, G., Yuanjia, H., Hao, H. & Defang, O. A Comprehensive Map of FDA-Approved Pharmaceutical Products. *Pharmaceutics* **263**, (2018).

350. Sarmadi, M. *et al.* Modeling, design, and machine learning-based framework for optimal injectability of microparticle-based drug formulations. *Sci Adv* **6**, (2020).

351. Whitaker, M. A., Langston, P., Naylor, A., Azzopardi, B. J. & Howdle, S. M. Particle size and shape effects in medical syringe needles: Experiments and simulations for polymer microparticle injection. *J Mater Sci Mater Med* **22**, (2011).

352. *The IUPAC Compendium of Chemical Terminology*. *The IUPAC Compendium of Chemical Terminology* (2019). doi:10.1351/goldbook.

353. AMC. What should be done with results below the detection limit? Mentioning the unmentionable. *AMC Technical Briefs* **5**, (2001).

354. Saadati, N. *et al.* Limit of detection and limit of quantification development procedures for organochlorine pesticides analysis in water and sediment matrices. *Chem Cent J* **7**, (2013).

355. Meneghetti, M. C. Z. *et al.* Heparan sulfate and heparin interactions with proteins. *Journal of the Royal Society Interface* Preprint at https://doi.org/10.1098/rsif.2015.0589 (2015).

356. Nie, T., Baldwin, A., Yamaguchi, N. & Kiick, K. L. Production of heparin-functionalized hydrogels for the development of responsive and controlled growth factor delivery systems. *Journal of Controlled Release* **122**, (2007).

357. Arlov, Ø., Aachmann, F. L., Sundan, A., Espevik, T. & Skjåk-Bræk, G. Heparin-like properties of sulfated alginates with defined sequences and sulfation degrees. *Biomacromolecules* **15**, (2014).

358. Mhanna, R., Becher, J., Schnabelrauch, M., Reis, R. L. & Pashkuleva, I. Sulfated Alginate as a Mimic of Sulfated Glycosaminoglycans: Binding of Growth Factors and Effect on Stem Cell Behavior. *Adv Biosyst* **1**, (2017).

359. Arlov, Ø. & Skjåk-Bræk, G. Sulfated alginates as heparin analogues: A review of chemical and functional properties. *Molecules* vol. 22 Preprint at https://doi.org/10.3390/molecules22050778 (2017).

360. McAlindon, T. E. *et al.* Effect of intra-articular triamcinolone vs saline on knee cartilage volume and pain in patients with knee osteoarthritis a randomized clinical trial. *JAMA - Journal of the American Medical Association* **317**, (2017).

361. Gómez-Aristizábal, A., Gandhi, R., Mahomed, N. N., Marshall, K. W. & Viswanathan, S. Synovial fluid monocyte/macrophage subsets and their correlation to patient-reported outcomes in osteoarthritic patients: A cohort study. *Arthritis Res Ther* **21**, (2019).

362. Almer, G. *et al.* Interleukin 10-coated nanoparticle systems compared for molecular imaging of atherosclerotic lesions. *Int J Nanomedicine* **9**, (2014).

363. Pellaud, J., Schote, U., Arvinte, T. & Seelig, J. Conformation and self-association of human recombinant transforming growth factor-β3 in aqueous solutions. *Journal of Biological Chemistry* **274**, (1999).

364. Wu, H. *et al.* Purification and characterization of recombinant human lysozyme from eggs of transgenic chickens. *PLoS One* **10**, (2015).

365. Wetter, L. R. & Deutsch, H. F. Immunological iv. immunochemical. *J Biol Chem* **192**, (1951).

366. Powers, R. *et al.* The High-Resolution, Three-Dimensional Solution Structure of Human Interleukin-4 Determined by Multidimensional

Heteronuclear Magnetic Resonance Spectroscopy. *Biochemistry* **32**, (1993).

367. Powell, M. J., Thompson, S. A. J., Tone, Y., Waldmann, H. & Tone, M. Posttranscriptional Regulation of IL-10 Gene Expression Through Sequences in the 3′-Untranslated Region. *The Journal of Immunology* **165**, (2000).

368. Miyazono, K., Hellman, U., Wernstedt, C. & Heldin, C. H. Latent high molecular weight complex of transforming growth factor β1. Purification from human platelets and structural characterization. *Journal of Biological Chemistry* **263**, (1988).

369. Balkani, S., Shamekhi, S., Raoufinia, R., Parvan, R. & Abdolalizadeh, J. Purification and characterization of bovine serum albumin using chromatographic method. *Adv Pharm Bull* **6**, (2016).

370. Zomer Volpato, F. *et al.* Preservation of FGF-2 bioactivity using heparin-based nanoparticles, and their delivery from electrospun chitosan fibers. *Acta Biomater* **8**, (2012).

371. Gäbler, S. *et al.* Determination of the viscoelastic properties of hydrogels based on polyethylene glycol diacrylate (PEG-DA) and human articular cartilage. *International Journal of Materials Engineering Innovation* **1**, (2009).

372. Setton, L. A., Elliott, D. M. & Mow, V. C. Altered mechanics of cartilage with osteoarthritis: Human osteoarthritis and an experimental model of joint degeneration. *Osteoarthritis Cartilage* (1999) doi:10.1053/joca.1998.0170.

373. Fu, R. *et al.* Effectiveness and harms of recombinant human bone morphogenetic protein-2 in spine fusion: A systematic review and meta-analysis. *Annals of Internal Medicine* vol. 158 Preprint at https://doi.org/10.7326/0003-4819-158-12-201306180-00006 (2013).

374. Feige, M. J., Braakman, I. & Hendershot, L. M. CHAPTER 1.1. Disulfide Bonds in Protein Folding and Stability. in (2018). doi:10.1039/9781788013253-00001.

375. Kamiya, T. A procedure for the detection of free thiol-containing proteins on a polyvinylidene difluoride membrane. *J Immunoassay* **18**, (1997).

376. Rombouts, I., Lagrain, B., Scherf, K. A., Koehler, P. & Delcour, J. A. Formation and reshuffling of disulfide bonds in bovine serum albumin demonstrated using tandem mass spectrometry with collision-induced and electron-transfer dissociation. *Sci Rep* **5**, (2015).

377. Li, R., Wu, Z., Wangb, Y., Ding, L. & Wang, Y. Role of pH-induced structural change in protein aggregation in foam fractionation of bovine serum albumin. *Biotechnology Reports* **9**, (2016).

378. Hinck, A. P., Mueller, T. D. & Springer, T. A. Structural biology and evolution of the TGF-β family. *Cold Spring Harb Perspect Biol* **8**, (2016).

379. Kim, S. K. *et al.* An engineered transforming growth factor β (TGF-β) monomer that functions as a dominant negative to block TGF-β signaling. *Journal of Biological Chemistry* **292**, (2017).

380. Wongkongkathep, P. *et al.* Enhancing protein disulfide bond cleavage by UV excitation and electron capture dissociation for top-down mass spectrometry. *Int J Mass Spectrom* **390**, (2015).

381. Rigo, A. *et al.* Interaction of copper with cysteine: Stability of cuprous complexes and catalytic role of cupric ions in anaerobic thiol oxidation. *J Inorg Biochem* **98**, (2004).

382. Mistry, P. *et al.* Bioprinting Using Mechanically Robust Core–Shell Cell-Laden Hydrogel Strands. *Macromol Biosci* **17**, (2017).

383. Chanput, W., Mes, J. J. & Wichers, H. J. THP-1 cell line: An in vitro cell model for immune modulation approach. *International Immunopharmacology* vol. 23 Preprint at https://doi.org/10.1016/j.intimp.2014.08.002 (2014).

384. Daigneault, M., Preston, J. A., Marriott, H. M., Whyte, M. K. B. & Dockrell, D. H. The identification of markers of macrophage differentiation in PMA-stimulated THP-1 cells and monocyte-derived macrophages. *PLoS One* **5**, (2010).

385. Mulder, R., Banete, A., Seaver, K. & Basta, S. M(IL-4) tissue macrophages support efficient interferon-gamma production in antigen-specific CD8+ T cells with reduced proliferative capacity. *Front Immunol* **8**, (2017).

386. Luiz, J. P. M. *et al.* MEK5/ERK5 signaling mediates IL-4-induced M2 macrophage differentiation through regulation of c-Myc expression. *J Leukoc Biol* **108**, (2020).

387. Soldano, S. *et al.* Alternatively activated (M2) macrophage phenotype is inducible by endothelin-1 in cultured human macrophages. *PLoS One* **11**, (2016).

388. Kar, M., Sengupta, J., Kumar, S., Bhargava, V. L. & Ghosh, D. Immunohistochemical localization of macrophage CD68+, HLA-DR+, L1+ and CD44+ subsets in uterine endometrium during different phases of menstrual cycle. *Indian J Physiol Pharmacol* **48**, (2004).

389. Shardlow, E., Mold, M. & Exley, C. The interaction of aluminium-based adjuvants with THP-1 macrophages in vitro: Implications for cellular survival and systemic translocation. *J Inorg Biochem* **203**, (2020).

390. Forrester, M. A. *et al.* Similarities and differences in surface receptor expression by THP-1 monocytes and differentiated macrophages polarized using seven different conditioning regimens. *Cell Immunol* **332**, (2018).

391. Madhvi, A., Mishra, H., Leisching, G. R., Mahlobo, P. Z. & Baker, B. Comparison of human monocyte derived macrophages and THP1-like macrophages as in vitro models for M. tuberculosis infection. *Comp Immunol Microbiol Infect Dis* **67**, (2019).

392. Sukegawa, S., Miyagi, E., Bouamr, F., Farkašová, H. & Strebel, K. Mannose Receptor 1 Restricts HIV Particle Release from Infected Macrophages. *Cell Rep* **22**, (2018).

393. Vigerust, D. J., Vick, S. & Shepherd, V. L. Characterization of functional mannose receptor in a continuous hybridoma cell line. *BMC Immunol* **13**, (2012).

394. Hind, L. E., Lurier, E. B., Dembo, M., Spiller, K. L. & Hammer, D. A. Effect of M1–M2 Polarization on the Motility and Traction Stresses of Primary Human Macrophages. *Cell Mol Bioeng* **9**, (2016).

395. Albina, J. E., Cui, S., Mateo, R. B. & Reichner, J. S. Nitric oxide-mediated apoptosis in murine peritoneal macrophages. *The Journal of Immunology* **150**, (1993).

396. Sarih, W., Souvannavong, V. & Adam, A. Nitric oxide synthase induces macrophage death by apoptosis. *Biochem Biophys Res Commun* **191**, (1993).

397. Tan, H., Shen, Q., Jia, X., Yuan, Z. & Xiong, D. Injectable nanohybrid scaffold for biopharmaceuticals delivery and soft tissue engineering. *Macromol Rapid Commun* **33**, (2012).

398. Spieler, V. *et al.* Targeting interleukin-4 to the arthritic joint. *Journal of Controlled Release* **326**, (2020).

399. Wang, M. *et al.* MMP13 is a critical target gene during the progression of osteoarthritis. *Arthritis Res Ther* **15**, (2013).

400. Muñoz-Rojas, A. R., Kelsey, I., Pappalardo, J. L., Chen, M. & Miller-Jensen, K. Co-stimulation with opposing macrophage polarization cues leads to orthogonal secretion programs in individual cells. *Nat Commun* **12**, (2021).

Appendix 1 – Supplementary data

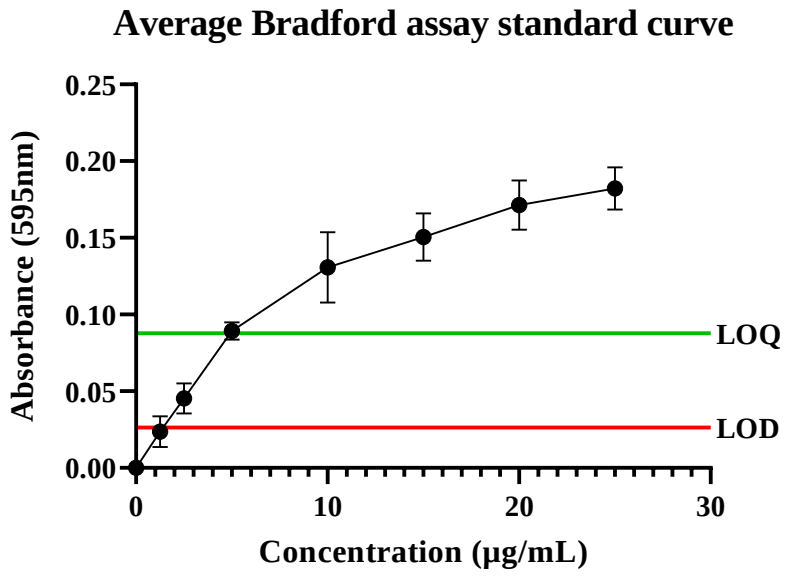

Figure S.1: Average Bradford assay standard curve. Values presented as mean ± standard deviation (N=7, n=3).

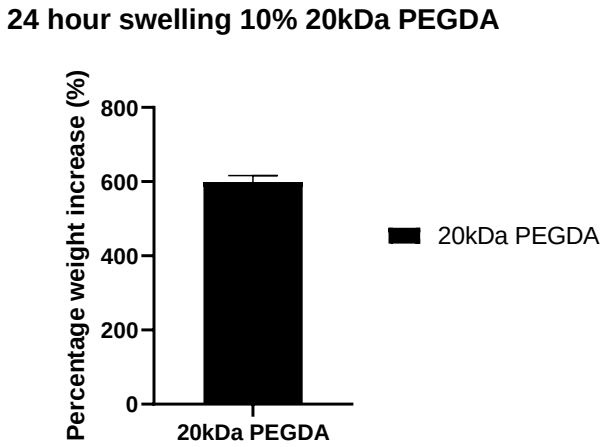

Figure S.2: Percentage weight increase of 10% 20kDa PEGDA hydrogels following 24 hours incubation in PBS at 37ºC. Values presented as mean ± standard deviation (n=3).

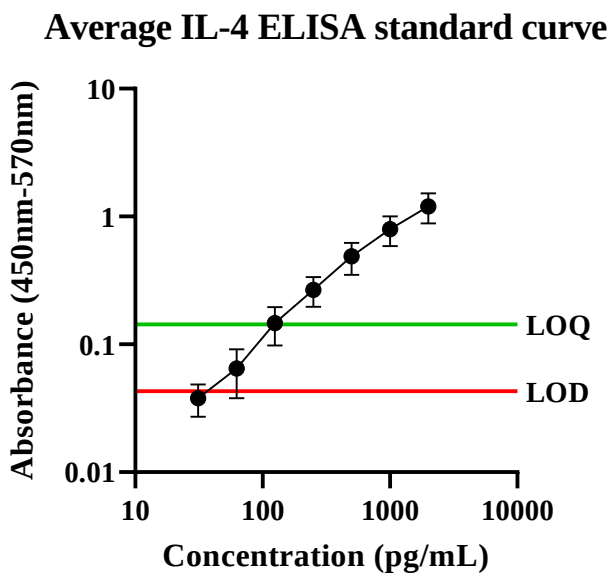

Figure S.3: Average IL-4 ELISA standard curve. Values presented as mean ± standard deviation (N=5, n=3).

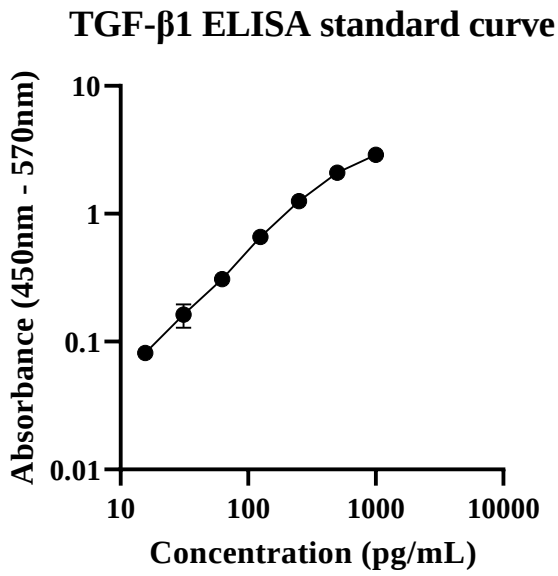

Figure S.4: TGF-β1 ELISA standard curve. Values presented as mean ± standard deviation (n=3).

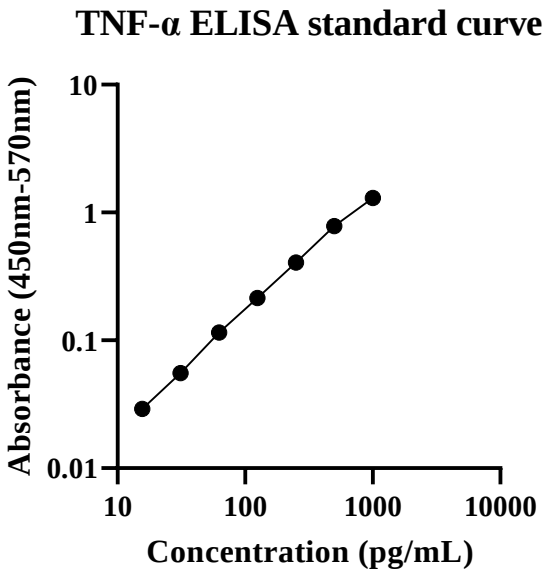

Figure S.5: TNF-α ELISA standard curve. Values presented as mean ± standard deviation (n=3).

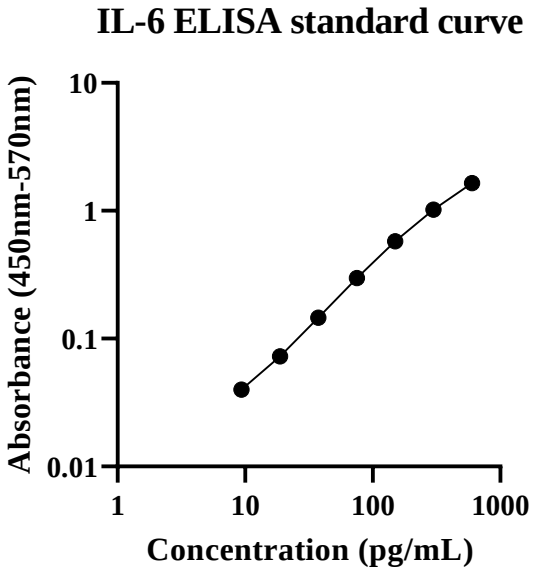

Figure S.6: IL-6 ELISA standard curve. Values presented as mean ± standard deviation (n=3).

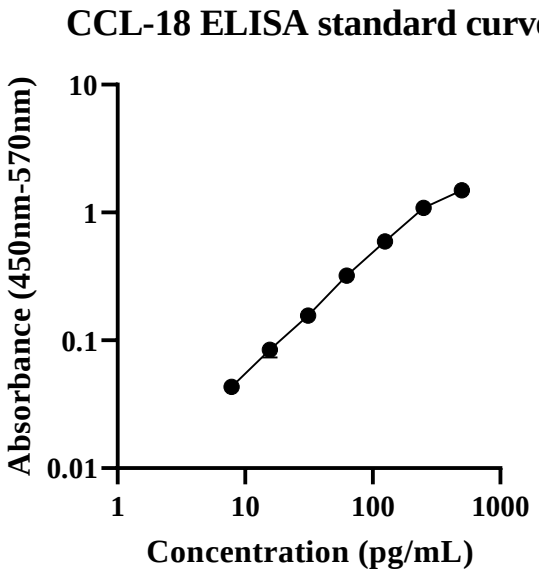

Figure S.7: CCL-18 ELISA standard curve. Values presented as mean ± standard deviation (n=3).

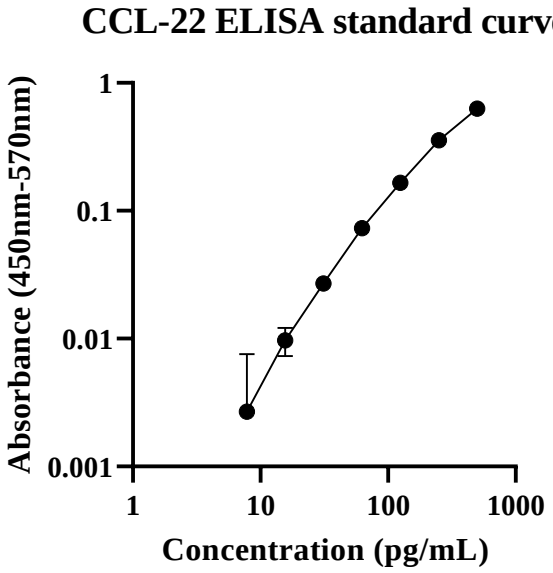

Figure S.8: CCL-22 ELISA standard curve. Values presented as mean ± standard deviation (n=3).

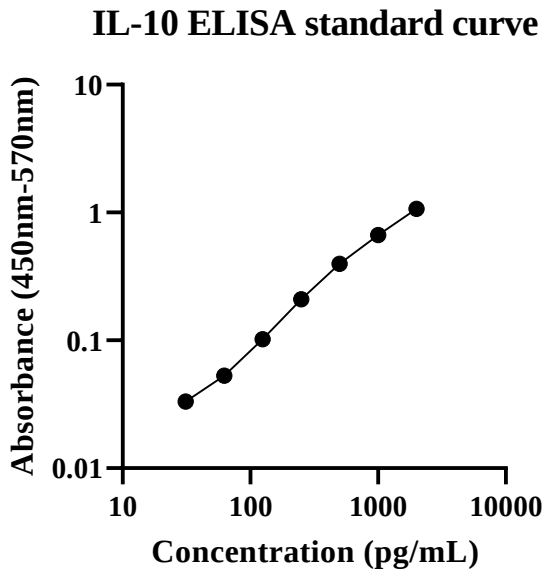

Figure S.9: IL-10 ELISA standard curve. Values presented as mean ± standard deviation (n=3).

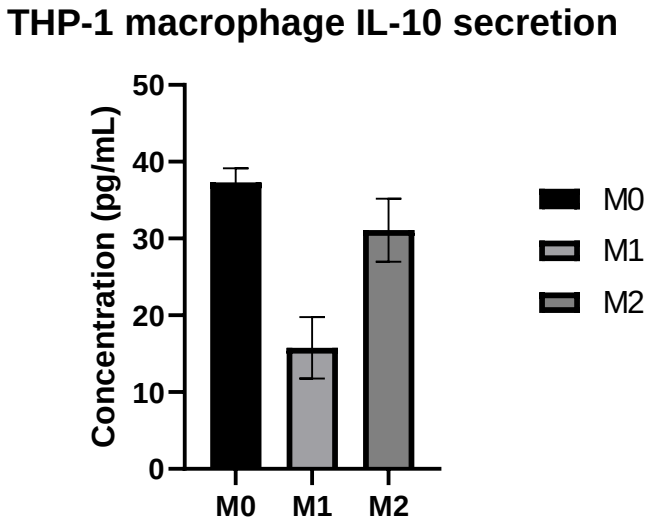

Figure S.10: IL-10 secretion from THP-1 macrophages following 6 days of culture. M0 was polarised with 50ng/mL M-CSF, M1 was polarised with 50ng/mL GM-CSF + 20ng/mL IFN-γ, M2 was polarised with 50ng/mL M-CSF + 20ng/mL IL-4. Values presented as mean ± standard deviation (n=3).

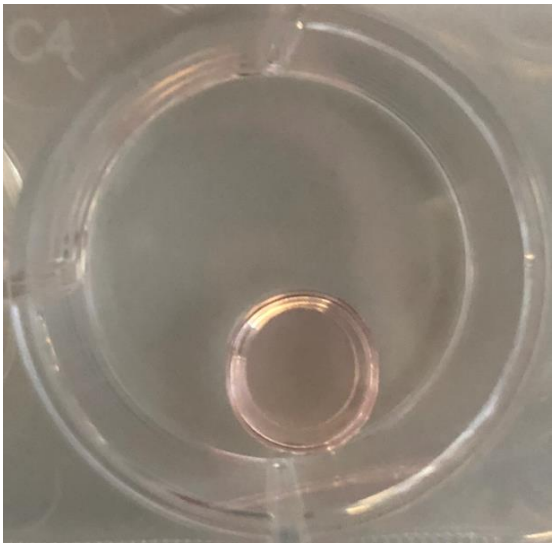

Figure S.11: Macroscopic image of a 5% SPAK 10% PEGDA hydrogel in a 12-well tissue culture plate. This is a visual representation of the set-up for THP-1 macrophage polarisation using direct incubation with IL-4 releasing hydrogels.

LAP (%w/v)	575Da PEGDA (%w/v)	SPAK (%w/v)	Tartrazine (%w/v)	Bottom exposure (seconds x layers)	Exposure (seconds)	Observed Result
0.5	10	0	0	20x2	10	Overexposure
0.5	10	2	0	10x2	5	Overexposure in pore base
0.5	10	5	0	10x2	5	Overexposure in pore base
0.5	10	2	0.1	45x2	20	Print failed
0.5	10	2	0.1	120x2	35	Low fidelity print
0.5	10	2	0.00085	60x2	9	Overexposure
0.5	10	2	0.00085	60x2	7	Overexposure
0.5	10	2	0.00255	60x2	4	Warped hydrogel
0.5	10	2	0.00255	30x2	4	High fidelity
0.5	10	5	0.00255	60x3	6	Warped hydrogel
0.5	10	5	0.00255	30x3	4	Slightly warped
0.5	10	5	0.00255	30x2	4	High fidelity
0.5	10	5	0.00255	20x2	3	Print failed

Table S.1: 3D printing parameter optimisation for DLP printing of SPAK PEGDA hydrogels